UNIVERSIDAD COMPLUTENSE DE MADRID
FACULTAD DE CIENCIAS QUÍMICAS

TESIS DOCTORAL

Protección Activa de Aleaciones de Magnesio

Active protection of magnesium alloys

MEMORIA PARA OPTAR AL GRADO DE DOCTOR

PRESENTADA POR

Borja Pillado Ríos

Directores

Raúl Arrabal Durán
Marta Mohedano Sánchez

Madrid

UNIVERSIDAD COMPLUTENSE DE MADRID
FACULTAD DE CIENCIAS QUÍMICAS

TESIS DOCTORAL

Protección Activa de Aleaciones de Magnesio
Active protection of magnesium alloys

MEMORIA PARA OPTAR AL GRADO DE DOCTOR

PRESENTADA POR

Borja Pillado Ríos

DIRECTORES

Dr. Raúl Arrabal Durán
Dra. Marta Mohedano Sánchez

Vida antes que muerte.

Fuerza antes que debilidad.

Viaje antes que destino.

Agradecimientos

En primer lugar, me gustaría agradecer a mis directores de tesis Raúl y Marta. Vuestra incasable dedicación y capacidades científicas han sido la mejor guía durante todo este camino que jamás hubiera podido pedir. Pero, sobre todo, gracias por la cercanía, compresión y disponibilidad, todo cuanto me habéis enseñado y el tiempo que me habéis dedicado. Siempre estaré en deuda con vosotros.

A todo el grupo de investigación, a Endzhe, tus disposición e ideas me han sacado de más atolladeros de los que soy capaz de contar, pero sobre todo por tu insaciable curiosidad científica. Y toda la gente que ha pasado por el grupo durante estos años (Hugo, David, Gonzalo, Yanira, Ewa, Pedro, Morty, etc.), pero muy especialmente a Rubén y Lara, habéis sido los mejores compañeros que hubiera podido pedir.

I would like to express my gratitude to the people from the Materials Science Department at UMONS (Belgium) for making the research stay much more rewarding. Especially to Prof. Marjorie Olivier, Sajjad Akbarzadeh and Isis Tournay–Dufrenne for their priceless support.

A mis padres, por el esfuerzo que habéis hecho para traerme hasta aquí, por no rendiros nunca conmigo y haber echado todas las horas necesarias ayudándome a estudiar. Sois el ejemplo para todo lo bueno que hay en mí. Espero que encontréis aquí un digno final a la lista de verbos irregulares. A mi hermana, gracias por entenderme mejor que yo mismo y encontrar siempre las palabras adecuadas. Ser la persona que crees que soy es casi tan difícil como una tesis, pero estoy en ello.

A mis amigos, los de siempre y lo nuevos, gracias por todos los buenos momentos. Habéis sido un gran apoyo durante estos años aun sin tener ni idea de qué iba todo esto. Pero de nuevo muy especialmente a Lara, mi confidente y compañera, por estar conmigo en todo momento gracias.

A Esther por haber compartido los momentos más duros de este periodo, tu cariño y amor son bases fuertes sobre las que mirar siempre hacia arriba.

Por último, agradecer al personal de la UCM y de otras instituciones colaboradoras (URJC, CENIM, Cidaut, UoM, TuDelft, NEU, etc.), por su inestimable ayuda.

Table of contents

Abstract

The transport sector is currently facing a complete overhaul due to ever increasing restrictions on greenhouse gas emissions. As described in the European Green Deal, the main goal is to achieve net zero emissions by 2050 and to limit global warming to 1.5–2ºC above pre–industrial levels. Owing to their low density, magnesium alloys could become a turning point in light vehicle design and therefore, drastically reduce the energy consumption and gas emissions in this sector. At present, the most promising strategies to increase the range of applications of magnesium alloys are concerned with the development of new alloys and protection systems with higher corrosion resistance.

Commercial protection mechanisms for magnesium alloys are often based on the use of Cr(VI) compounds, which is known to be toxic and carcinogenic. Therefore, the development of Cr(VI)–free surface treatments has become one of the main research lines in recent years. The alternatives should also provide active corrosion protection and be environmentally friendly.

The **Introduction** in this Thesis provides an overview of magnesium alloys and their corrosion behaviour as well as a literature review on protection strategies, including trends on smart surface engineering approaches which have been postulated as potential replacements for Cr(VI)–based treatments.

The **Hypothesis** of the present work is that environmentally friendly treatments based on plasma electrolytic oxidation, layered double hydroxides and sol–gel coatings should provide a sound basis for active corrosion protection of magnesium alloys.

The **Objectives** are divided into four chapters that are mainly concerned with the incorporation of corrosion inhibitors and/or the development of multistep protection systems.

Chapter 1 explores the synthesis of layered double hydroxides (LDH) coatings and the incorporation of inorganic corrosion inhibitors. Two separate LDH coatings on AZ31 alloy, Zn–Al LDH and Li–Al LDH, are produced *in–situ* under hydrothermal conditions. The chapter includes inhibitor screening by electrochemical impedance spectroscopy (EIS), characterization of the inhibitor–free and inhibitor–loaded coatings and assessment of the active protection by immersion corrosion tests with scribed specimens.

Abstract

In **Chapter 2**, coatings fabricated by flash plasma electrolytic oxidation (flash–PEO) are investigated as an energy efficient and environmentally friendly corrosion protection strategy for the AZ31 alloy. The feasibility of using electrolytes loaded with Ca species as an anti–corrosion species is evaluated. In this study, an electrolyte based on phosphate and sodium aluminate is used. Two calcium compounds are added independently, calcium oxide and calcium glycerophosphate, both in the presence of EDTA (ethylenediaminetetraacetic acid) complexing agent. The chapter includes coating characterization, paint adhesion tests and corrosion testing by EIS and salt spray.

Chapter 3 is focused on the development of sealing post–treatments on PEO coatings on two magnesium alloys: a MgYZn alloy with long period stacking ordered (LPSO) phases and AZ91D alloy. Different sealing procedures based on Ca and Ce species are selected and evaluated. In both cases, conditions with the highest corrosion resistance are characterized and evaluated by corrosion tests such as EIS and potentiodynamic polarization.

Chapter 4 deals with the morphology, composition and corrosion behaviour of hybrid PEO/sol–gel coatings on AZ31 alloy. The incorporation of a corrosion inhibitor is approached by following two strategies: immersion post–treatment after PEO and sol–gel precursor with incorporated inhibitor. The chapter includes inhibitor screening by EIS, coating characterization and assessment of the active protection by immersion corrosion tests with scribed specimens.

Overall, findings reveal that the corrosion resistance of magnesium alloys can be significantly improved by using PEO, LDH and sol–gel systems in combination with corrosion inhibitors.

Resumen

El sector del transporte afronta en la actualidad una renovación completa debido al incremento en las emisiones de los gases de efecto invernadero. De acuerdo con el Pacto Verde Europeo, el principal objetivo es conseguir cero emisiones netas para 2050 y limitar el calentamiento global a 1.5–2 ºC sobre las condiciones previas a la época industrial. Debido a su baja densidad, el empleo de aleaciones de magnesio podría suponer un punto de inflexión en el diseño de vehículos ligeros, reduciendo enormemente el consumo energético y las emisiones de los mismos. El desarrollo de nuevas aleaciones y sistemas de protección con mejor resistencia a corrosión son las estrategias más prometedoras en la actualidad para ampliar el rango de aplicaciones de las aleaciones de magnesio.

Actualmente los mecanismos de protección comerciales sobre magnesio se basan en el empleo de compuestos de Cr(VI), cuyas características tóxicas y carcinogénicas son ampliamente conocidas. En este contexto, el desarrollo de nuevos tratamientos superficiales libres de Cr(VI) se ha convertido en una de las principales líneas de investigación en los últimos años. Las alternativas deben presentar además capacidades de protección activa y ser respetuosas con el medio ambiente.

En la **Introducción** de esta Tesis se presenta una visión general de las aleaciones de magnesio y su comportamiento a corrosión. También se recoge una revisión bibliográfica sobre las estrategias de protección, incluyendo tendencias sobre recubrimientos inteligentes como posibles sustitutos de tratamientos basados en Cr(VI).

La **Hipótesis** del presente trabajo es que tratamientos respetuosos con el medio ambiente basados en oxidación electrolítica por plasma, hidróxidos dobles laminares y capas sol–gel deberían proporcionar una base sólida para la protección activa contra la corrosión de las aleaciones de magnesio.

Los **Objetivos** se dividen en cuatro capítulos centrados en la incorporación de inhibidores de corrosión y/o en el desarrollo de sistemas de protección híbridos.

El **Capítulo 1** explora la síntesis de recubrimientos de hidróxidos dobles laminares (LDH) y la incorporación de inhibidores de corrosión inorgánicos. Se producen *in–situ* y bajo condiciones hidrotermales dos recubrimientos sobre la aleación AZ31, Zn–Al LDH y Li–Al LDH. El capítulo incluye el cribado de los inhibidores mediante espectroscopía de impedancia

electroquímica (EIS), la caracterización de los recubrimientos sin y con inhibidores y la evaluación de la protección activa mediante ensayos de corrosión por inmersión con probetas que incluyen defecto artificial.

En el **Capítulo 2**, se investigan recubrimientos fabricados mediante oxidación electrolítica por plasma de corta duración (flash–PEO), como estrategia energéticamente eficiente y respetuosa con el medio ambiente, para la protección de la aleación AZ31. Se evalúa la viabilidad de utilizar electrolitos cargados con especies de Ca como especie anticorrosiva. En este estudio, se utiliza un electrolito basado en fosfato y aluminato de sodio. Se añaden dos compuestos de calcio de forma independiente, óxido de calcio y glicerofosfato de calcio, ambos en presencia del agente complejante EDTA (ácido etilendiaminotetraacético). El capítulo incluye la caracterización del recubrimiento, los ensayos de adhesión de pintura y pruebas de corrosión por EIS y niebla salina.

El **Capítulo 3** se centra en el desarrollo de post–tratamientos de sellado sobre recubrimientos de PEO en dos aleaciones de magnesio: una aleación MgYZn con estructuras ordenadas con apilamiento de periodo largo (LPSO) y la aleación AZ91D. Se seleccionan y evalúan diferentes procedimientos de sellado basados en especies de Ca y Ce. En ambos casos, se caracterizan las condiciones que proporcionan la mayor resistencia a la corrosión y se evalúan mediante ensayos de corrosión como EIS y polarización potenciodinámica.

En el **Capítulo 4** se estudian recubrimientos híbridos PEO/sol–gel sobre la aleación AZ31 en términos de morfología, composición y comportamiento frente a la corrosión. La incorporación de un inhibidor de corrosión se aborda siguiendo dos estrategias: postratamiento por inmersión tras PEO y precursor sol–gel con inhibidor incorporado. El capítulo incluye cribado de inhibidores mediante EIS, la caracterización del recubrimiento y la evaluación de la protección activa mediante ensayos de corrosión por inmersión con probetas rayadas.

En general, los resultados revelan que la resistencia a la corrosión de las aleaciones de magnesio puede mejorarse significativamente utilizando sistemas PEO, LDH y sol–gel en combinación con inhibidores de corrosión.

List of Figures

List of Figures

List of Figures

List of Figures

List of Figures

List of Figures

List of Tables

List of Tables

List of Tables

Disclosure and Acknowledgements

The Author has carried out most of the experimental work in this Thesis, including experiment design, sample preparation, surface treatments, corrosion tests (electrochemical impedance spectroscopy, potentiodynamic polarization, hydrogen evolution measurements). The Author has also participated in the characterization and analysis of the specimens by optical microscopy, SEM, TEM, XRD, FTIR, UV–Vis and XPS as well as coating thickness measurements, surface metrology, wettability, and paint adhesion tests. The Author significantly contributed to the dissemination of the obtained results in manuscripts and conferences/seminars.

XRD and FTIR measurements were conducted at the X–ray diffraction and Spectroscopy and Correlation Units at UCM (Madrid, Spain). SEM and TEM facilities were located at National Centre for Electron Microscopy (ICTS). XPS measurements were performed at University of Vigo (Pontevedra, Spain) and Northeastern University (Shenyang, China) with the help of Dr. Xiaopeng Lu. UV–Vis spectra were obtained and analysed by the Author at the *Faculte Polytechnique de Mons* (Mons, Belgium). Hybrid sol–gel coatings were developed during a 3–month stay at *Faculte Polytechnique de Mons* (Mons, Belgium) in collaboration with Dr. Marjorie Olivier. SVET measurements were performed at Delft University of Technology (Delft, The Netherlands) with the collaboration of Dr. Yaiza González.

The data analysis was carried out in collaboration with Dr. Raúl Arrabal, Dr. Marta Mohedano and Dr. Endzhe Matykina.

This Thesis was enabled by funding from the following projects and scholarships, which are gratefully acknowledged:

- ALMAGIC project (EU, H2020 Clean Sky 2, Grant agreement N° 755515).
- MAT2015–66334–C3–3–R, MAT2015–73355–JIN, RTI2018–096391–B–C33, RYC–2017–21843 (MCIU/AEI/FEDER, UE), PID2021-1243410B-C22.
- Erasmus+ programme Scholarship of Complutense University of Madrid.

List of Publications

The results of this Thesis have been included in several scientific manuscripts for their publication in peer–reviewed journals:

Chapter 1

- **B. Pillado**, B. Mingo, R. del Olmo, E. Matykina, A. M. Kooijman, Y. Gonzalez–Garcia, R. Arrabal, M. Mohedano, *LDH conversion films for active protection of AZ31 Mg alloy.* Journal of Magnesium and Alloys *(accepted), DOI: 10.1016/j.jma.2022.09.014.*

Chapter 2

- E. Wierzbicka, **B. Pillado**, M. Mohedano, R. Arrabal, E. Matykina, *Calcium Doped Flash–PEO Coatings for Corrosion Protection of Mg Alloy*. Open Access. Metals, Volume 10, 2020, 916, *DOI: 10.3390/met10070916.*

Chapter 3

- M. Mohedano, P. Pérez, E. Matykina, **B. Pillado**, G. Garcés, R. Arrabal, *PEO coating with Ce–sealing for corrosion protection of LPSO Mg–Y–Zn alloy*. Surface and Coatings Technology, Volume 383, 2020, 125253, *DOI: 10.1016/j.surfcoat.2019.125253.*
- X. Lu. J. Ma, M. Mohedano, **B. Pillado**, R. Arrabal, K. Qian, Y. Li, T. Zhang, F. Wang, *Ca–based sealing of plasma electrolytic oxidation coatings on AZ91 Mg alloy*. Open Access. Surface and Coatings Technology, Volume 417, 2021, 127220, *DOI: 10.1016/j.surfcoat.2021.127220.*

The outcomes have also been presented at various international conferences:

- I. Tournay–Dufrenne, **B. Pillado**, M. Mohedano, M.–G Olivier, *Effect of the fluoride species and content of the PEO electrolyte on corrosion properties of the layers obtained on AZ31 for biomedical purposes.* EUROCORR 2022, Berlin (Germany).
- **B. Pillado**, M. Mohedano, R. del Olmo, B. Mingo, E. Matykina, R. Arrabal, *Corrosion of AZ31 with LDH conversion coatings loaded with inorganic inhibitors.* CDMWC 2022, Online.

List of Publications

- **B. Pillado**, M.–G. Olivier, I. Tournay–Dufrenne, E. Matykina, R. Arrabal, M. Mohedano, *Functionalized hybrid PEO/Sol–gel Coatings for corrosion protection of Mg alloys.* CDMWC 2022, Online.
- **B. Pillado**, R. del Olmo, E. Matykina, R. Arrabal, M. Mohedano, *LDH coatings on AZ31 Mg alloy: characterization and corrosion performance*. 3CIC 2022, Online.
- **B. Pillado**, B. Mingo, R. del Olmo, E. Matykina, A.M. Kooijman, Y. Gonzalez–Garcia, R. Arrabal, M. Mohedano, *Corrosion of inhibitor–loaded Li–Al– and Zn–Al–LDH coatings on AZ31 Mg alloy.* EUROCORR 2021, Online.
- M. Mohedano, P. Pérez, E. Matykina, **B. Pillado**, G.Garcés, R. Arrabal, *PEO coating with Ce–sealing for corrosion protection of LPSO Mg–Y–Zn alloy*. EUROCORR 2021, Online.
- **B. Pillado**, M. Mohedano, R. del Olmo, B. Mingo, E. Matykina, R. Arrabal, *Corrosion of AZ31 with LDH conversion coatings loaded with inorganic inhibitors.* Brain Wars, 2019, Madrid (Spain).
- R. Del Olmo, **B. Pillado**, M. Mohedano, R. Arrabal, E. Matykina, *Alternativas libre de Cr (VI) para aleaciones ligeras en transporte.* La noche de los investigadores, 2019, Madrid (Spain).
- **B. Pillado**, M. Mohedano, E. Matykina, R. Arrabal, *Corrosion of Inhibitor–loaded Phosphate Conversion Coatings on AZ31 Alloy*. EUROCORR 2019, Sevilla (Spain).

List of Abbreviations

3C Computer, communications and consumer electronics

8HQ 8–Hydroxyquinoline

AC Alternating current

AFM Atomic Force Microscopy

AHE Anomalous hydrogen evolutionion

AM Additive manufacturing

AZ Aluminium–Zink magnesium alloy

CC Conversion coating

CCC Chromium conversion coating

CPE Constant phase element

DC Direct current

DFT Density functional

DI deionized water

E Elastic modulus

EDS Energy–dispersive X–ray spectroscopy

EIS Electrochemical impedance spectroscopy

FTIR Fourier–transform infrared spectroscopy

CaGlyP Calcium glycerophosphate

GTS GPTMS–TEOS–Silica

GPTMS (3–Glycidyloxypropyl)trimethoxysilane

HE Hydrogen evolution

IREs Internal reflection elements

LDH Layered double hydroxide

LPSO Long period stacking ordered structures

NDE Negative difference effect

NSST Neutral salt spray test

OCP Open circuit potential

OM Optical microscopy

PEO Plasma electrolytic oxidation

PCL Polycaprolactone

RE Rare earths

SCC Stress–corrosion cracking

SDS Sodium dodecyl sulphate

SCE Saturated calomel electrode

SEM Scanning electron microscope

SG sol–gel

SVET Scanning vibrating electrode technique

TEM Transmission Electron Microscope

TEOS Tetraethyl orthosilicate

V_{SHE} Standard hydrogen electrode

XRD X–ray diffraction

XPS X–ray photoelectron spectroscopy

|Z| impedance modulus

1 Introduction

1.1 Magnesium alloys: general properties and corrosion behaviour

1.1.1 Overview of Mg alloys

Magnesium (Mg) is the 8th most abundant element in the Earth's crust and is also present in seawater. Therefore, there are plenty of resources to cover the needs of multiple engineering sectors. A timeline of the main scientific and technological developments on Mg is presented in Figure 1. Mg was isolated and prepared in coherent form in the 19th century and nowadays is produced either by electrolysis of molten $MgCl_2$ or by thermal reduction of MgO [1]. The production of primary Mg is an energy–intensive process with a large carbon footprint, e.g. 360 GJ and 5.2 t CO_2 per ton of Mg obtained via thermal reduction [2]. Secondary or recycled Mg accounts for about 20% of the total production and requires much less energy (10 GJ/t) [3, 4]. World production has reached ~1.2 Mt/year and is expected to grow at 4.9% during the next 5 years and reach 1.6 Mt by 2027, with China being the main producer [5-7].

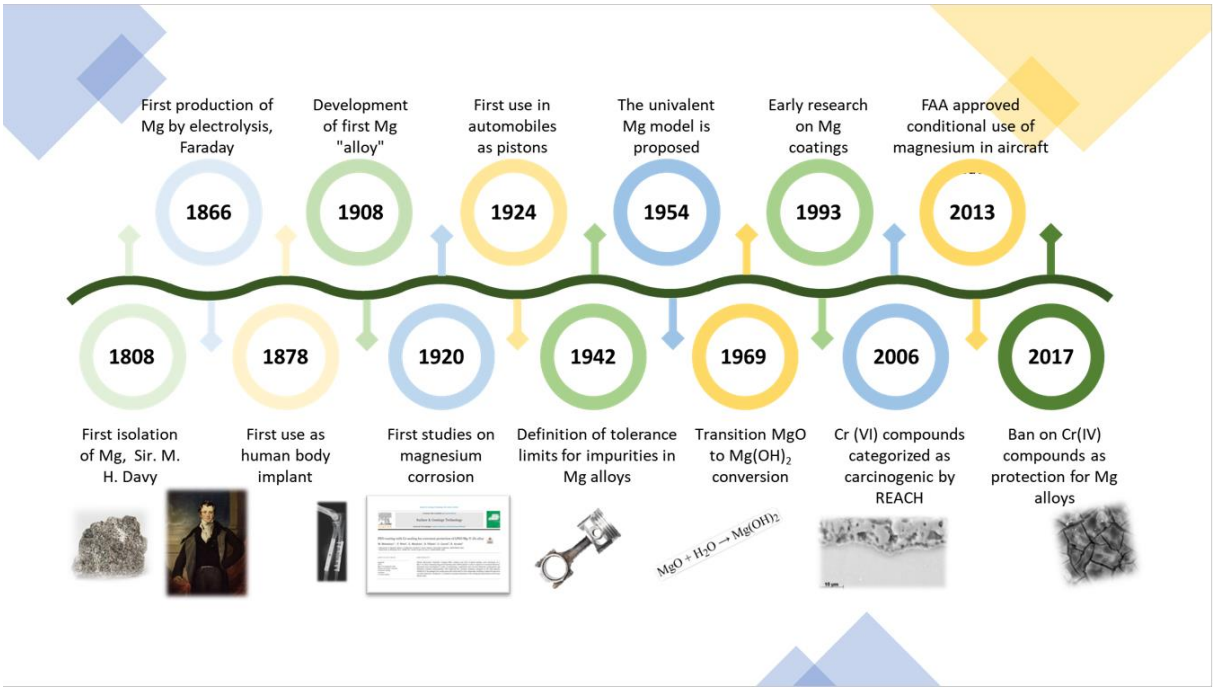

Figure 1. Scientific and technological developments on Mg [7].

Society's growing environmental awareness has resulted in an increased number of stringent regulations, leading to significant challenges for the transport sector. For instance, in 2016, the European Union ratified the Paris Agreement and targeted to reduce emissions by at least 55% by 2030 from 1990 levels [8]. In this framework, magnesium –the lightest structural metal– has attracted huge attention as an effective way to reduce demands on fuel resources, increase

energy efficiency and decrease CO_2 emissions. With a density of ~1.7 g/cm^3, Mg is significantly lighter than Al (2.7 g/cm^3), Ti (4.5 g/cm^3) and Fe (7.9 g/cm^3) [9], and compared with other engineering materials has a higher specific strength, being similar to that of composite materials (Figure 2).

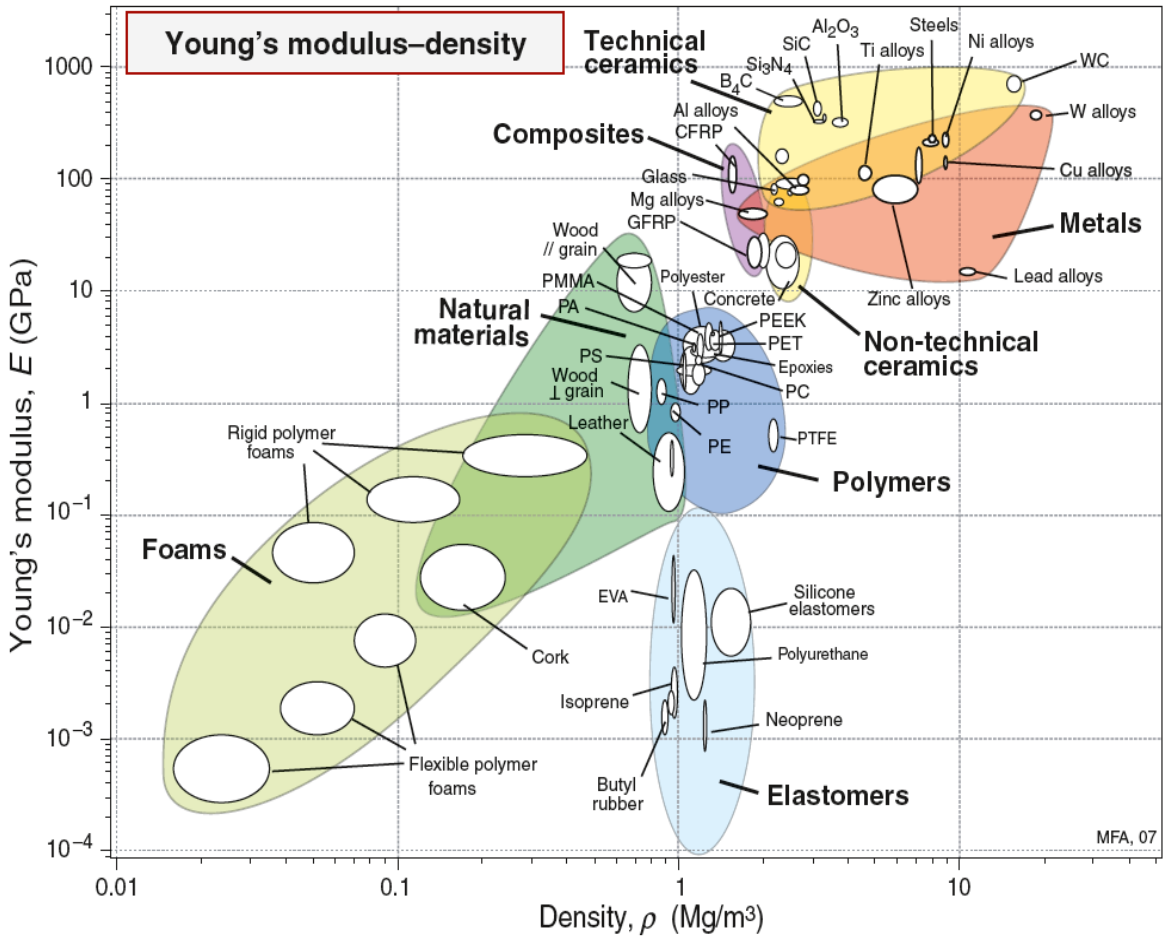

Figure 2. Young's modulus (E) – density (ρ) chart for various engineering materials [9].

The good castability and damping capacity of Mg–based materials are also sought after in the transport industry (Figure 3). However, issues regarding formability and in–service performance are restricting their wider use in this sector [10]. In any case, Mg alloys still find many applications in aerospace and military industries as well as in consumer electronics and sporting goods.

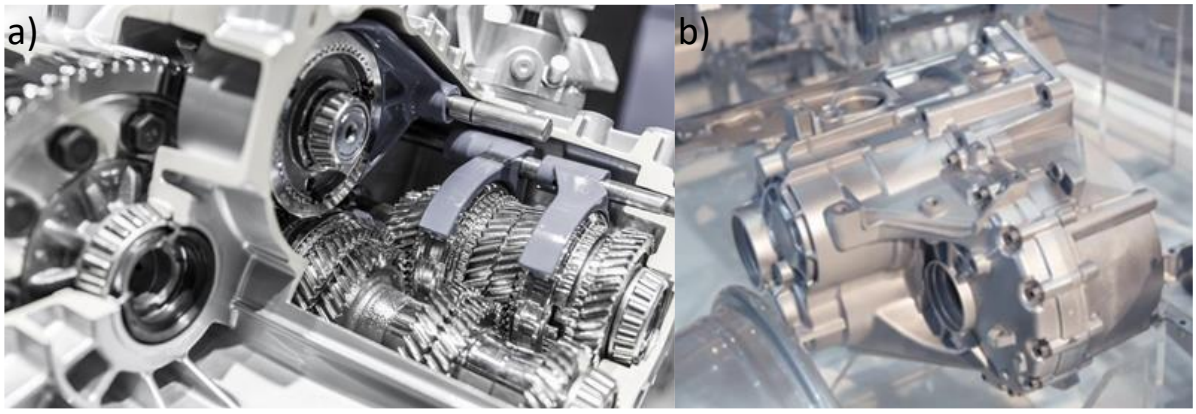

Figure 3. Examples of potential applications of Mg alloys in the transport industry. (a) Forging gear box, and (b) Cast steering box housing.

The use of cast magnesium alloys is far more extensive than that of wrought alloys, which only accounts for up to 10–15% of all products. This is again explained by the low formability of Mg alloys. Many strategies have been developed for multiple applications to overcome that pure Mg is soft and mechanically weak [10]. Aluminium was the first alloying element commercialised and nowadays Mg–Al alloys are still one of the most widely used. AZ91, AM60, AM50 and AZ31 are examples of the most commonly used Mg–Al alloys [11, 12]. Aluminium improves the castability and induces hardening by precipitation. It is usually combined with zinc since it increases melt fluidity and strength at ambient temperature [13]. Manganese is also added in small quantities to counteract the detrimental effect of impurities (e.g. Fe, Cu, Ni).

Magnesium alloys containing rare earths (REs) are more expensive than Mg–Al alloys, but they offer advantages such as high creep strength, pressure tightness and weldability. Mg–RE alloys such as WE43, EV31, EZ33 and ZE41 are currently being used in the aeronautic and aerospace industries for high temperature components (>175ºC). An example of recent developments in alloy design for structural applications include cast and wrought Mg–systems with long period stacking ordered structures (LPSOs), which are obtained by combining REs elements and transition metals [14].

In the last decade, Mg alloys are increasingly being used for biomedical applications. AZ31 and WE43 alloys have already been commercialized [15], although new alloys with biocompatible elements such as Ca, Zn, Ag and Si are being developed [16]. The main advantage of Mg alloys is that they can be used as temporary implants. Therefore, a second surgery would not be necessary since the implant would be reabsorbed once its purpose has been fulfilled. However,

rapid biodegradation of magnesium alloys under physiological conditions has delayed their use in therapeutic applications. Complications are mostly related to excessive hydrogen evolution, local alkalinisation and early loss of mechanical integrity [17].

Figure 4 shows some of the most relevant properties of magnesium alloys that justify their use in the transport, 3C (computer, communications and consumer electronics) and medical sectors.

Figure 4. Main applications of magnesium alloys [18].

Magnesium alloys still face some important challenges that limit a wider acceptance. These include poor corrosion resistance in saline environments (an example of corrosion is shown in Figure 5), low creep strength above 175ºC, poor stiffness, limited formability and price variability. Therefore, great efforts are being carried out to improve manufacturing and processing routes as well as to design new Mg alloys and surface treatments with improved properties.

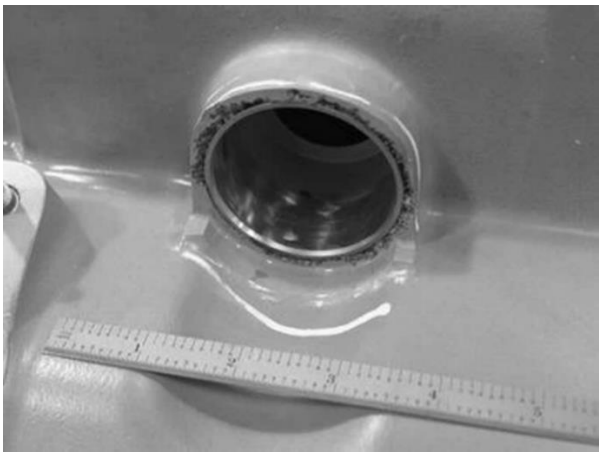

Figure 5. Repair of a corroded magnesium rotorcraft component by cold spray [19].

1.1.2 Corrosion behaviour of magnesium alloys

1.1.2.1 Thermodynamics

In the absence of water, Mg exothermically reacts with oxygen (1) and develops a MgO film with a thickness of a few nanometres [20]:

$$2Mg(s) + O_2(g) \rightarrow 2MgO(s) \quad (1)$$

A discontinuous or defective MgO layer is likely to form due to its relatively low Pilling–Bedworth ratio of 0.81 [21]. In dry air at room temperature, the MgO film provides adequate protection and, thereby, Mg shows good corrosion resistance. In the presence of water, hydroxylation (2) of the MgO surface occurs:

$$MgO(s) + H_2O(l) \rightarrow 2Mg(OH)_2(s) \quad (2)$$

This reaction is thermodynamically favourable. Accordingly, a bilayer film is formed consisting of a $Mg(OH)_2$ upper layer and a bottom MgO layer (Figure 6).

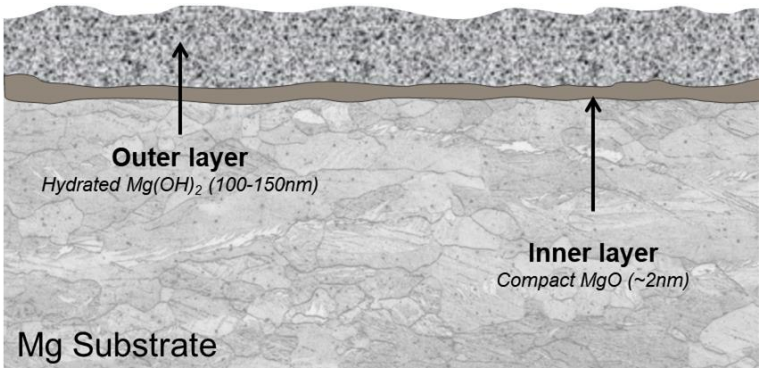

Figure 6. Schematic representation of the corrosion layer on Mg in the presence of atmospheric H_2O.

The $MgO/Mg(OH)_2$ film is non–protective in neutral and acidic aqueous solutions. Thus, dissolution of this "quasi–passive" film eventually exposes the metal to the solution and, as a result, Mg, which is highly active, corrodes in accordance with the following reactions [22, 23].

Anodic reaction	$Mg(s) \rightarrow Mg^{2+}(aq) + 2e^-$	(3)
Cathodic reaction	$2H_2O(l) + 2e^- \rightarrow H_2(g) + 2OH^-(aq)$	(4)
Precipitation reaction	$Mg^{2+}(aq) + 2OH^-(aq) \rightarrow Mg(OH)_2(s)$	(5)
Overall reaction	$Mg(s) + 2H_2O(l) \rightarrow Mg(OH)_2(s) + H_2(g)$	(6)

Magnesium oxidation half reaction releases two electrons (3), although some authors defend that an intermediate state of univalent magnesium also comes into play [24, 25]. The released electrons reduced water molecules and hydrogen gas is produced (4). This is because magnesium is a very active metal and, in neutral and low pH aqueous solutions, is well below the water stability region. In addition to molecular hydrogen, OH^- is also released, which causes the pH to rise. Finally, magnesium hydroxide precipitates (5). Thus, the overall corrosion reaction could be expressed as (6).

In summary, the poor corrosion resistance of pure Mg can be mainly attributed to two factors: (i) the highly electronegative potential of Mg (–2.4 V_{SHE}), and (ii) the poorly protective properties of the $MgO/Mg(OH)_2$ surface film. In case of Mg alloys and/or multimaterial designs, additional corrosion issues arise due to formation of galvanic couples. This is because most metals, inclusions and second phases are more noble than Mg and serve as cathodes.

1.1.2.2 Effect of the environment

There are several environmental variables that affect the corrosion susceptibility of magnesium alloys such as pH, temperature and the nature of aggressive species (e.g. Cl^-, SO_2). It has also recently been stated that oxygen concentration may also be relevant under specific conditions [26, 27]. It is known that the presence of Cl^- is always associated with a higher corrosion rate for the entire pH range. In alkaline saline environments, especially above pH 11.5, corrosion rate is somewhat lower since a semi–protective layer of $Mg(OH)_2$ is formed on the surface [28].

Pourbaix's diagram in Figure 7 shows the most stable Mg species as a function of water pH and electrode potential. In neutral saline environments, the corrosion potential usually lies around ~ –1.5 V_{SHE}, as a $Mg(OH)_2$ film is formed on the surface. Oxygen reduction should be negligible in comparison to the more thermodynamically favourable water reduction [28]. It can also be inferred from this diagram that there is a higher tendency towards corrosion in neutral and acidic

media. Indeed, magnesium rapidly dissolves in aqueous solutions below pH 11, the equilibrium pH value for $Mg(OH)_2$.

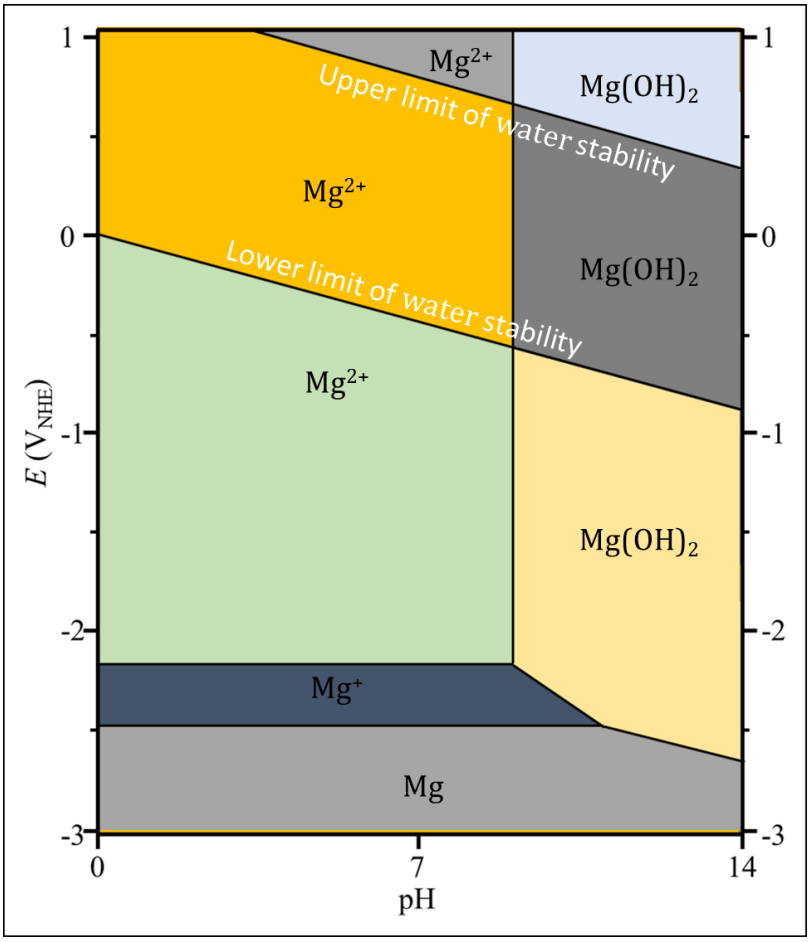

Figure 7. Pourbaix's diagram for magnesium, adapted from [29].

1.1.2.3 Effect of alloying elements and microstructure

Most alloying elements show a rather limited solubility in Mg. This translates into minimal effects in the corrosion potential. However, corrosion rates may spread over several orders of magnitude. This is mostly due to enhanced cathodic kinetics in combination with the very low anodic Tafel slope of Mg [30].

The Mg–Al–Zn or AZ system is probably one of the most studied and by far the most commercially interesting one. The microstructure of AZ alloys typically consists of α–Mg and β–$Mg_{17}Al_{12}$ phases as well as some small polygonal Al–Mn inclusions (e.g. Al_8Mn_5). Figure 8a and 8b show the microstructure of the slowly cooled AZ80 alloy as an example [31-37]. However, this microstructure is not found in commercial systems that are solidified under non–equilibrium conditions. For the latter, α–Mg dendritic grains and a partially or fully divorced

eutectic network at the grain boundaries is more common [31]. In these alloys, impurity control is important as heavy metals (Fe, Ni and Cu) can cause severe galvanic corrosion [31].

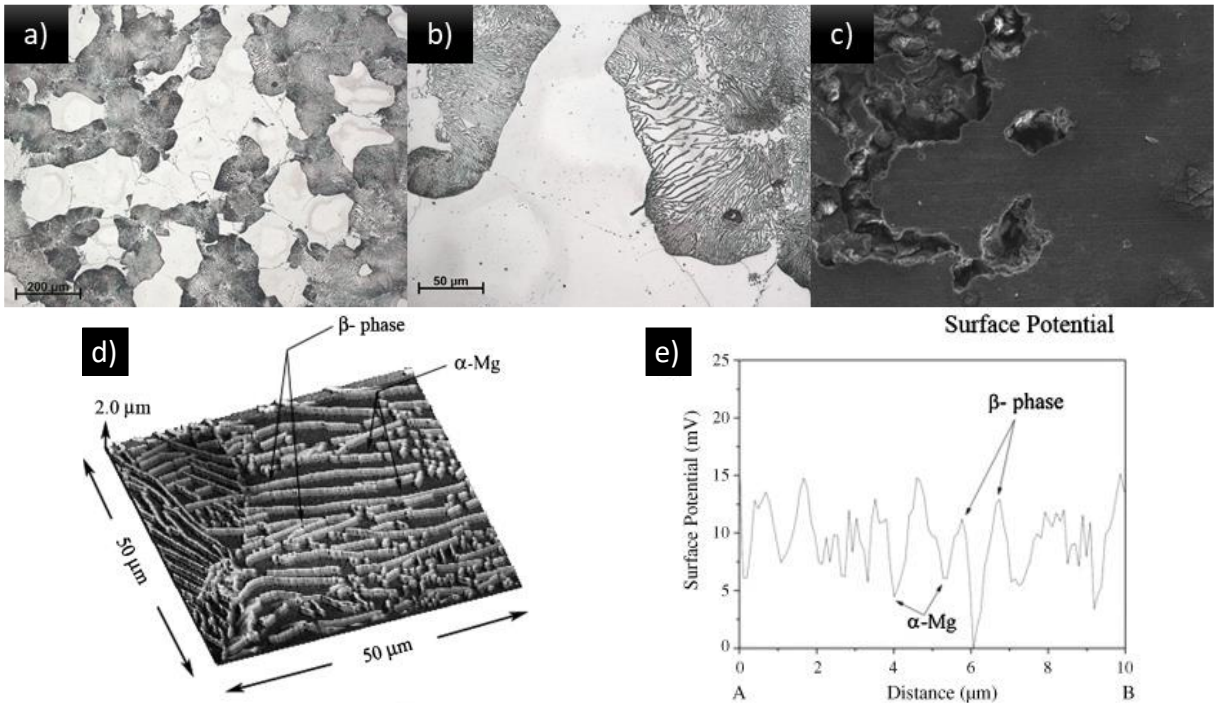

Figure 8. (a,b) Microstructure of AZ80 alloy at two different magnifications. The alloy shows a microstructure of α–Mg matrix grains and grains of a lamellar α–Mg + β–$Mg_{17}Al_{12}$ aggregate in higher proportion. (c) Surface image of AZ80 after immersion in aggressive media for 28 days. SKPFM study: (d) topography image; (e) profile–line analysis. Adapted from [31].

The corrosion resistance of AZ alloys mainly depends on the distribution of aluminium. Under atmospheric conditions, Al alloying has a positive effect [22, 31], whereas contradictory results are usually found for immersion tests [20]. This is mostly explained by the role of the β–phase. The β–phase is known to have a cathodic behaviour, causing the acceleration of anodic metal dissolution from the α–phase, but it can also act as an anodic barrier when the volume fraction is high enough, thus decreasing the overall corrosion [28, 31, 34, 35, 38-46] (Figure 8c,d,e).

In case of other alloy systems, the common observation is an increased corrosion rate in comparison to pure Mg due to the presence of secondary phases acting as cathodes. This detrimental effect can be illustrated with the example of Mg–Y–Zn alloys that contain LPSO phases. LPSO–Mg alloys possess superior mechanical properties and plastic formability than conventional Mg alloys [47-52]. LPSO phases show different morphologies depending on the heat treatment and reveal different stacking sequences, although 18R and 14H structures are the most common ones (Figure 9). However, it has been shown that these cathodic phases

accelerate the corrosion attack and that their volume fraction, orientation and distribution greatly affect the corrosion morphology in Mg–Zn–Y alloys [53-56].

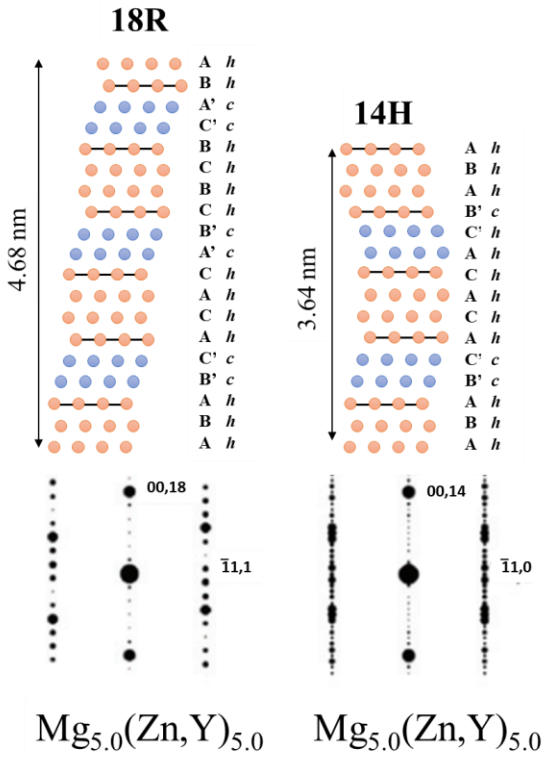

Figure 9. Structure models of the Mg–Zn–Y LPSO polytype structures. Blue and red circles represent the Mg site and Zn/Y occupation site, respectively. Adapted from [52].

1.1.2.4 Corrosion mechanisms and morphology

The corrosion mechanism of magnesium is still object of discussion among researchers such as Fajardo [57, 58], Lamaka [59], Birbilis [60, 61], Frankel [62, 63], and many others [64, 65]. It is widely accepted that the primary cathodic reaction on Mg corrosion reaction is the reduction of water molecules with the liberation of hydrogen gas. This process is known as hydrogen evolution (HE). Counterintuitively, anodic polarization of Mg increases both Mg dissolution and hydrogen liberation. This unexpected behaviour has been termed negative difference effect (NDE) or, more recently, anomalous HE (AHE), and is in contradiction with the Butler–Volmer equation [Eq. 1], which is the well–accepted expression to describe activation–controlled kinetics [66-68] (Table 1).

$$i_{HER} = i_{0,H,Mg}\left[exp\left(\frac{(E-E_{rev,H})}{b_a}\right) - exp\left(\frac{-(E-E_{rev,H})}{|b_c|}\right)\right] \qquad \text{[Eq. 1]}$$

Table 1. Components of Butler–Volmer equation.

Parameter	Units	Description
i_{HER}	A/cm^2	current density associated with the HER
$i_{0,H,Mg}$	A/cm^2	exchange current density for the evolution of H_2 on Mg
E	V	electrode potential
$E_{rev,H}$	V	reversible potential for the HER
b_a	V/dec	value of the anodic Tafel slope
$\lvert b_c \rvert$	V/dec	absolute value of the cathodic Tafel slope

Different theories have been proposed to explain the discrepancy between predicted and experimental results in regard to hydrogen evolution. According to the *univalent Mg theory*, AHE can be explained by a mechanism of dissolution in two steps; i) Mg is dissolved as Mg^+ (7) and ii) Mg^+ undergoes a homogeneous chemical reaction with water to form Mg^{2+} and H_2 (8). This implies that a greater dissolution of the metal produces more H_2. Although some authors still defend this theory, it is mostly discarded today as Mg^+ ion has not been experimentally detected [69].

$$Mg\,(s) \rightarrow Mg^{+}(aq) + e^{-} \quad (7)$$

$$Mg^{+}(aq) + H_2O(l) \rightarrow Mg^{2+}(aq) + \tfrac{1}{2}\,H_2(g) + 2OH^{-}(aq) \quad (8)$$

The *enhanced catalytic activity theory* [70] is another popular explanation for anomalous HE. This model assumes that there are some catalytic active sites on the Mg surface during anodic dissolution, which enhance HE. However, the catalyst has not been theoretically asserted or experimentally detected [71].

A more recent approach involving first–principles density functional (DFT) simulations was presented by Yuwono *et al.* [68]. In accordance with this model, Mg*H intermediates undergo oxidation upon anodic polarisation, resulting in hydrogen evolution and Mg dissolution. This causes AHE at the regions where anodic dissolution occurs, due to the reaction of Mg*H with water. However, this model has also been criticized based on the complexity of its multi–electron elementary reactions.

Corrosion of magnesium alloys in neutral aqueous solutions generally takes the form of shallow wells or pits that grow laterally until they merge longitudinally. However, stress–corrosion cracking (SCC), filiform and pitting corrosion as well as other forms of corrosion have also been reported in magnesium literature (Table 2).

Table 2. Different corrosion mechanism on Mg alloys.

Alloy	Media	Mechanism	Ref
Mg–4.0Zn–0.2Ca	Hank's solution	Uniform corrosion	[72]
AZ91	1 N (5.4 wt.%) NaCl Immersion test	Localised corrosion	[44]
WE43	3.5 wt.% NaCl immersion test	Intergranular corrosion	[73]
AE44	3.5 wt.% NaCl spray at 35 °C	Pitting corrosion	[74]
AZ91	3 wt.% NaCl Immersion	Filiform	[75]
Mg (>99.99% purity)	3.3 wt.% NaCl + 2 wt.% K_2CrO_4	SCC	[76]
AM60B	Water vapour	Corrosion fatigue	[77]

1.2 Protection of Mg alloys

1.2.1 Overview

Coatings are the most common approach to prevent corrosion. In addition to their barrier effect, coatings can also provide active protection when corrosion inhibitors are incorporated into them. When mechanical damage is likely to occur, the best coatings are those that are uniform, pore free, well–adhered and with self–healing ability.

It is known since early 1920s that Cr–based treatments provide a high level of protection to steel, galvanized steel and Mg and Al alloys. However, chromates are highly toxic and carcinogenic, according to REACH regulation [78]. Therefore, Cr–based treatments have to be replaced by environmental–friendly and equally effective alternatives in terms of corrosion, fatigue and paintability performance.

As shown in Figure 10, there is a clear growing research interest in coatings for corrosion protection of Mg and its alloys. It is worth noticing that over 200 influential review articles and several book chapters related to coating technology for Mg alloys have been published in the last decade [20, 79-92]. There are a number of coating technologies available, including electrochemical plating, conversion coatings, anodizing, hydride coatings, organic coatings, ion implantation, hot pressing and vapor–phase processes [79]. Two Cr–free coating alternatives which are addressed in the present work deserve particular attention due to their versatility and combination of properties: plasma electrolytic oxidation (PEO) and conversion coatings. To give an idea of their relevance, in the last 10 years and according to the Scopus database, these two topics have been the focus of more than 13000 publications in JCR journals.

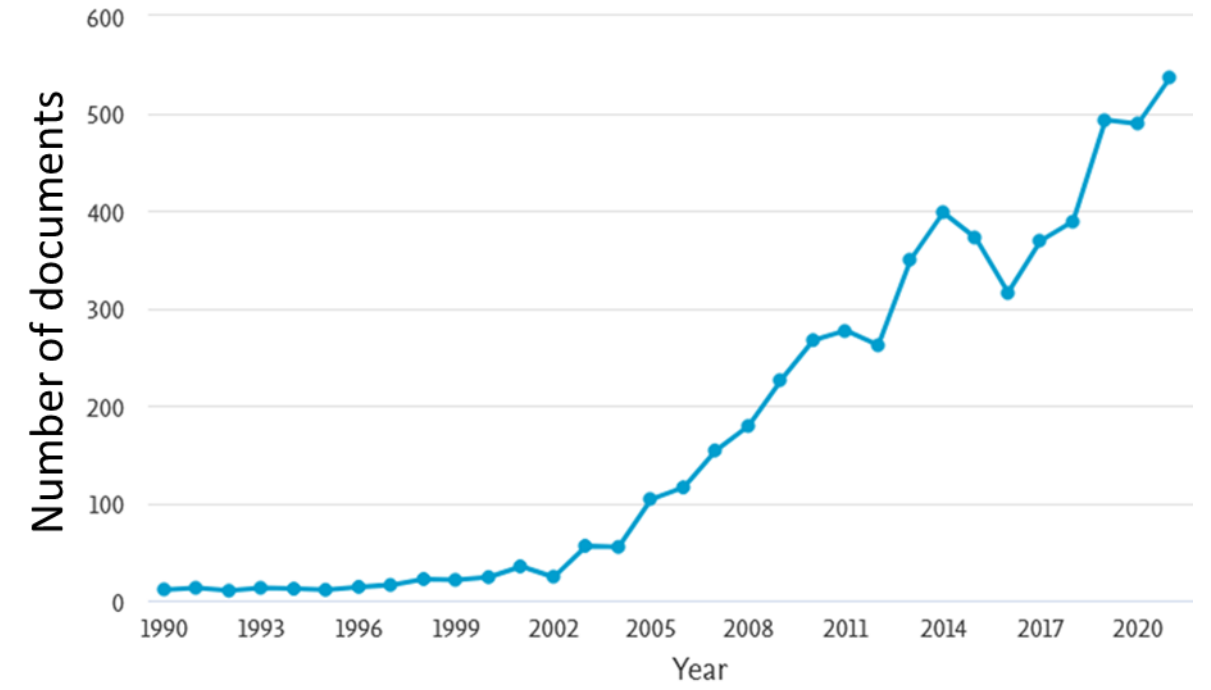

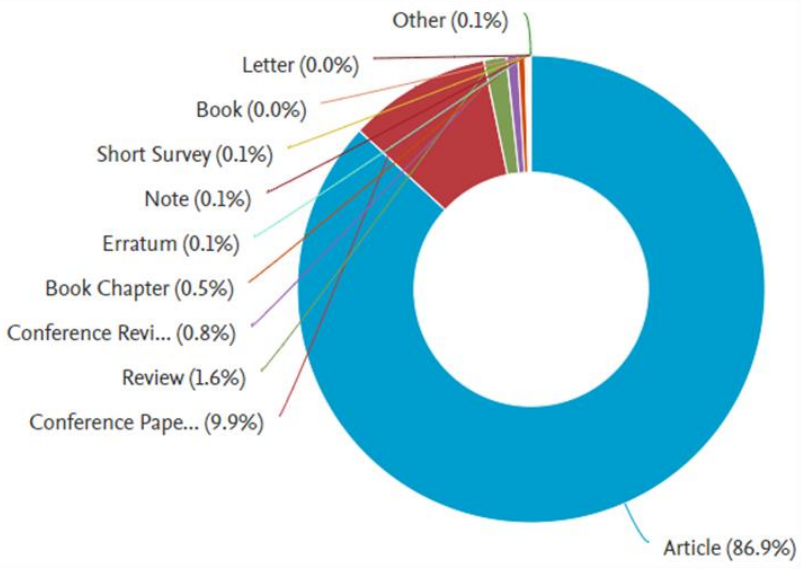

Document type	Documents
Article	13757
Conference Paper	1566
Review	246
Conference Review	124
Book Chapter	78
Erratum	19
Note	15
Short Survey	9
Book	5
Letter	5
Editorial	3
Report	2
Retracted	2
Data Paper	1
Undefined	3

Figure 10. Publications in relation to "magnesium", "corrosion" and “coating” over the last 30 years and analysis of the results for the documents published since 2012 (Source: Scopus).

1.2.2 Smart surface engineering on Mg alloys

In recent years, physical barrier coatings are being replaced by smart approaches. The main advantage of smart surfaces is that they modulate their response as requested. Self–cleaning, self–healing, active protection, anti–fouling, pollution–absorbing and sensing are often linked to smart coating technologies. The common ground is that the response of the surface is driven by a stimulus (e.g. chemical, mechanical, thermal, electrical or biological changes in the

material or surrounding environment). The response to the stimuli can be global or local depending on the applied technology (Figure 11).

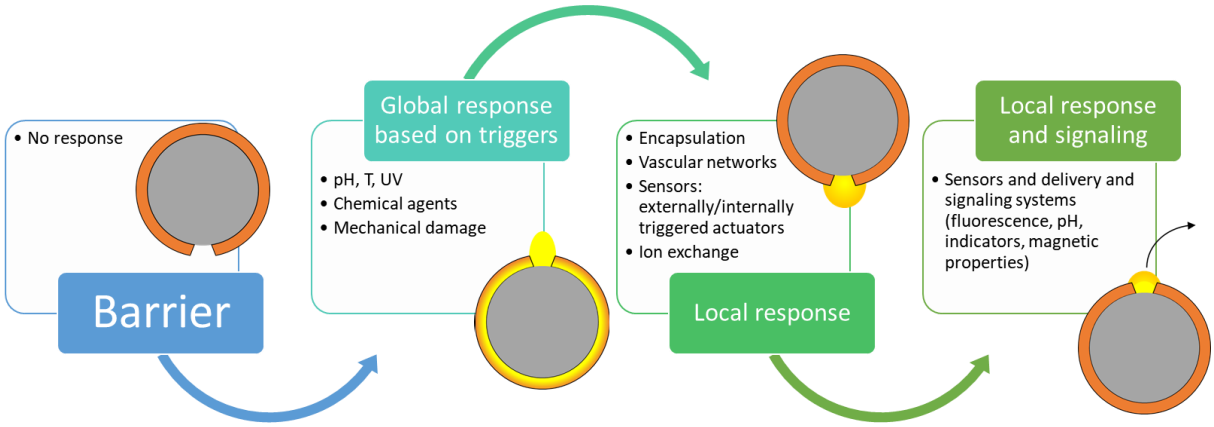

Figure 11. Classification of coatings according to the response to stimuli and its complexity.

In the particular case of Mg alloys, smart surface engineering is mainly devoted to the enhancement of corrosion resistance [93], particularly through the application of smart–coatings because they are available in a wide range of compositions and can provide other desirable properties such as wear resistance, aesthetics, paint adhesion and electrical insulation.

In the transport sector, the state–of–the–art for corrosion protection of Mg alloys is based on conversion films as primers and sealing top coats (e–coats, paints, etc.). Conversion coatings (CCs) are thin and offer limited protection, but they provide good compatibility with top layers. Chromate conversion coatings (CCCs) are considered the best option. However, formulations that contain chromates are heavily regulated due to Cr(VI) toxicity [94]. Currently, CCs on Mg alloys are based on phosphates, permanganates and fluorozirconates, but they are less effective than CCCs as they do not provide the same self–healing capacity that comes with Cr(VI) species. As a result, critical components in the aeronautic sector still rely on CCCs. A similar situation is found for anodizing of Mg alloys, although promising Cr–free treatments with self–healing capacity have been recently developed by plasma electrolytic oxidation (PEO) [95], which is an advanced anodizing technology.

Based on the above information, it becomes evident that smart–coatings are in demand for transport applications. Smart–coatings for Mg alloys often seek self–healing properties. That is, when the surface is damaged during use, the coating self–repairs entirely or partially and restores its functionality. During the last decade, several self–healing approaches have been

investigated for different surface modification techniques. The most relevant ones include: (1) active agent; (2) encapsulation coatings; and (3) layer–by–layer (LBL) assembled coatings (Figure 12).

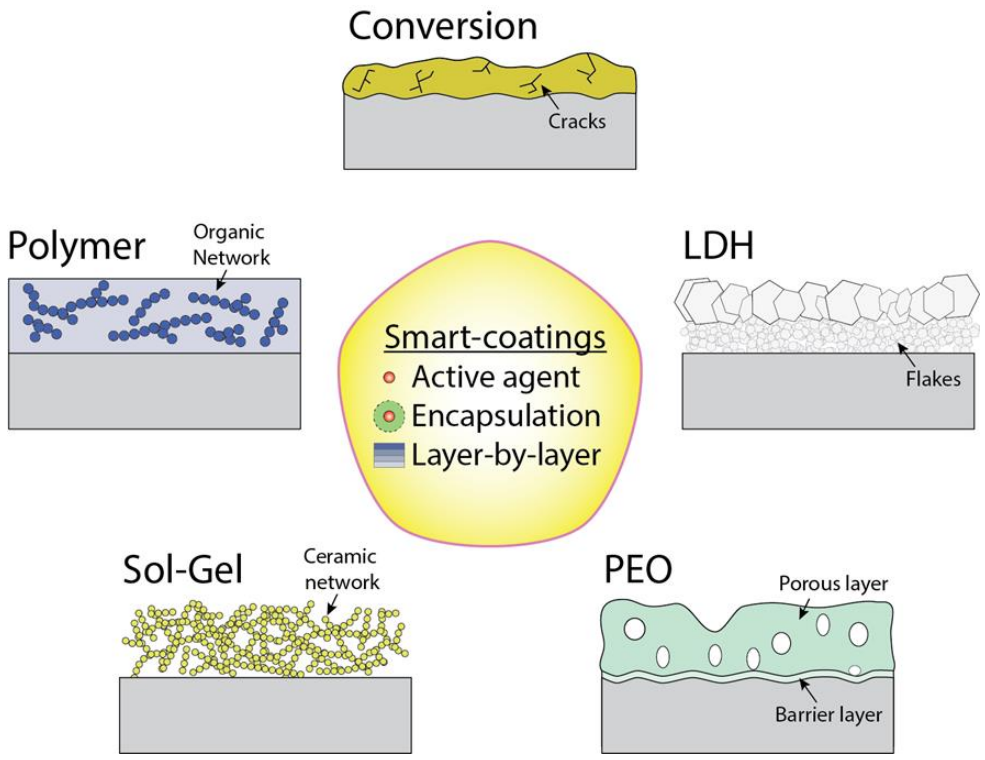

Figure 12. Smart coatings typically applied on Mg alloys.

1.2.2.1 Active agents

Active agents for corrosion protection of Mg alloys typically involve inorganic and organic inhibitors. There are many classification systems for corrosion inhibitors. One of the most common ones is based on the effect on the cathodic and anodic reactions. Cathodic, anodic and mixed inhibitors are distinguished. The inhibition mechanism is based on retarding the cathodic or anodic reaction of the corrosion process or both of them. As a result, they cause a shift of the corrosion potential of the inhibited metal toward respectively either the cathodic or the anodic directions or they substantially leave the metal corrosion potential more or less unchanged [96-98].

Another classification system is based on the type of interaction with the metallic surface (Figure 13): (i) adsorption film, (ii) passivation film, and (iii) precipitation of protective compounds. Inhibitors that interact forming an adsorption protective film are mainly organic compounds and normally have a molecular structure of a surfactant, with a hydrophilic group capable to bond with the metal surface and a hydrophobic part toward the solution. To form a

passivation film conventional inhibitors include oxidizing species (e.g. chromates and nitrites) and also non–oxidizing inhibitors, (e.g. tungstates and molybdates). It is worth mentioning that some of these species, in particular chromates based, are being abandoned because of toxicity concerns. In the case of precipitation of protective compounds, inhibitors are chemicals forming insoluble protective films by reaction with soluble species in the environment (e.g., phosphonates and polyphosphates forming protective films with calcium ions in solution) or with the protected metal ions (e.g. copper–benzotriazole (BTA) salt film).

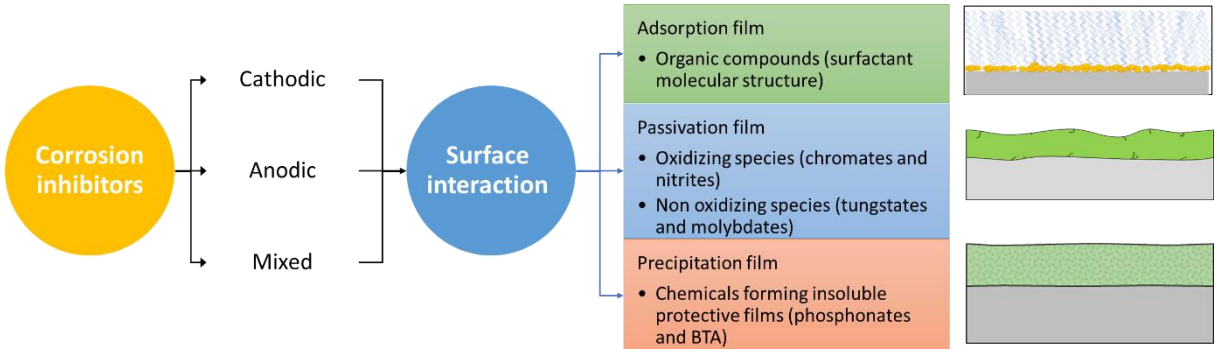

Figure 13. Corrosion inhibitor interaction mechanisms with magnesium surfaces.

Focusing on Mg alloys, the scientific community is making a great effort to find effective and environmentally friendly inhibitors [97, 98] that also fulfil the technical and legal requirements. Table 3 collects some of the most representative inhibitors for Mg alloys based on the interaction with the metallic surface. In addition, a long list of inhibitors for Mg alloys can be found in a recent review [98].

Table 3. Suitable inhibitors for Mg alloys.

Alloy	Inhibitor	Corrosion performance			Ref
		Medium	i_{corr} (A cm^{-2})	$\|Z\|_{10mHz}$ (Ω cm^2)	
Adsorption–type inhibitors					
ZK30	Sodium dodecylbenzenesulphonate (SDBS)	50 mM NaCl 51 h		4×10^4	[99]
AZ91	Lactobionic–acid (LTA)	50% aqueous ethyleneglycol	10.8×10^{-6}		[100]
AZ91	6–Ring organic compounds containing N–heteroatom	50% aqueous ethyleneglycol	42.5×10^{-6}		[100]
Mg–Al–Zn	Aliphatic amino acids, aromatic amino acids and sulphur containing amino acids	chloride–free naturally aerated solutions	$(8.5 – 29.9) \times 10^{-6}$		[101]

Table 3. Suitable inhibitors for Mg alloys. (cont.)

Alloy	Inhibitor	Corrosion performance			
		Medium	i_{corr} (A cm^{-2})	$\|Z\|_{10mHz}$ (Ω cm^2)	Ref
Passivation–type inhibitors					
AZ81	Phosphate–permanganate conversion coatings	ASTM D1384–87 water	~7×10^{-5}		[102]
AM60	Phosphate coatings	phosphating bath	1×10^{-3}		[103]
Precipitation–Type inhibitors					
Mg–Ca–Zn–Co alloy foam	Fluorides	Simulated body fluid	10^{-5}		[104]
WE43	Molybdate	0.5 M NaCl	4.6×10^{-6}		[105]
Mg–10Gd–3Y–0.5Zr	Sodium aminopropyltriethoxysilicate (APTS–Na)	ASTM D1384–87 solution	5×10^{-7}		[106]
Mg–10Gd–3Y–0.5Zr	Zinc nitrate	ASTM D1384–87 solution	6×10^{-6}		[106]
Mg–10Gd–3Y–0.5Zr	Sodium phosphate	50 vol% ethylene glycol	8×10^{-7}		[107]
Mg–10Gd–3Y–0.5Zr	5,10,15,20–Tetraphenylporphyrin (TPP)	50 vol% ethylene glycol	2×10^{-6}		[107]

1.2.2.2 Encapsulation systems

One of the main challenges of corrosion inhibitors is the fading effect due to uncontrolled release into the active corrosion spots. Encapsulation systems provide an effective way for controlled–release of inhibitors. The encapsulation systems are based on load–release mechanisms of active repair agents. The release mechanism is based on a specific trigger (e.g. pH, UV light, mechanical damage). These coatings require multiple steps, but a greater level of protection is achieved. *In–situ* and *ex–situ* incorporation of inhibitors into the host coating are both possible. The host coating is typically a polymer, sol–gel, layered double hydroxides (LDHs), PEO coatings and their combination [108]. These procedures are referred to as *in–situ* when the inhibitor agent is loaded during coating formation. In *ex–situ* coatings the inhibitor is loaded in a different step, for instance by pre–loading the inhibitor into a container which then goes into the coating. Encapsulation of inhibitors into nanoparticles and microcontainers works similarly to direct encapsulation. However, it has the added benefit of improved mechanical properties of the coating and smarter release of inhibitors that otherwise may be released too quickly. All sorts of containers have been used in the literature. TiO_2, CeO_2, SiO_2, carbon

nanotubes, LDHs, organic microspheres, zeolites and natural clays are some examples [108]. Figure 14 shows examples of common approaches of encapsulation systems.

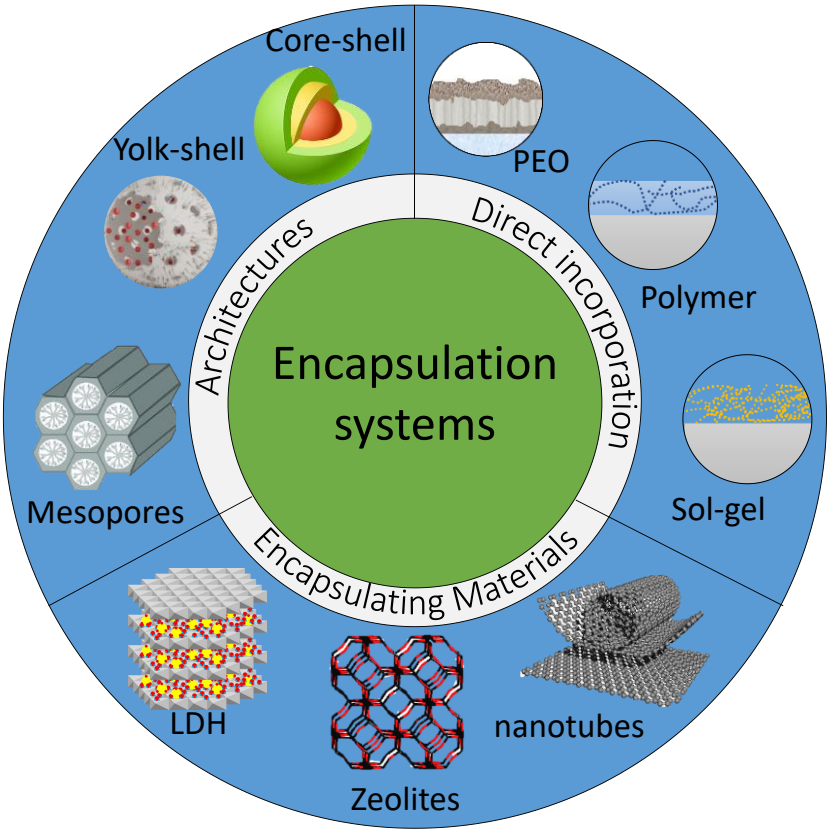

Figure 14. Common approaches of encapsulation systems.

In the case of Mg alloys, inorganic and organic inhibitors such as $Ce^{3+/4+}$, La^{3+}, VO^{3-}, PO_4^{3-}, MO_4^{2-}, benzotriazole, 2–mercaptobenzothiazole and 8–hydroxiquinoline have been investigated using different encapsulation systems to improve the corrosion performance. Table 4 gathers the most relevant systems including information about the alloy type, coating system, corrosion inhibitors and the incorporation method.

Table 4. Examples of inhibitor incorporation into coatings on Mg alloys.

Alloy	Coating	Corrosion inhibitor	Incorporation system	Corrosion performance	Ref
AZ91D	Sol–Gel	8–Hydroxiquinoline	Halloysite nanotubes	2.67×10^{-7} A cm^{-2}	[109]
AZ91D	Sol–Gel	Ce^{3+}/Zr^{4+}	Nanotubes	7.03×10^{-7} A cm^{-2}	[110]
AZ31B	Epoxy	Mercaptabenzimidazole	Magnesium–Silicate nanotubes	3.34×10^{-7} A cm^{-2}	[111]
ZE21B	Sol–Gel	Paeonol condensation tyrosine	Direct incorporation	3.64×10^{-6} A cm^{-2}	[112]
AZ31	PEO	Ciprofloxacin	Post–treatment	7.03×10^{-8} A cm^{-2}	[113]

Table 4. Examples of inhibitor incorporation into coatings on Mg alloys. (cont.)

Alloy	Coating	Corrosion inhibitor	Incorporation system	Corrosion performance	Ref
AZ31	Mg–Al LDH		LDH intercalation	1.70×10^{-9} A cm^{-2}	[114]
AZ91D	Mg–Al LDH	Ce^{3+}	Direct incorporation	2.32×10^{-5} A cm^{-2}	[115]

1.2.2.3 Layer–by–Layer (LBL)

LBL assemblies are very versatile due to their multilayer design. The assembly depends on chemical/physical bonding interactions between the layers and can be obtained with a wide range of methods (e.g. dip, spin, spray, multi–step). The most common approach is the deposition of multiple polymer layers with incorporated repair agents. In the case of Mg alloys, examples of polymers include PCL (polycaprolactone), poly (ethylene imine), poly (acrylic acid) and polymethyltrimethoxysilane, and examples of active agents are similar to those previously mentioned. However, LBL self–healing coatings show poor mechanical stability and they still remain at the lab scale (Figure 15) [108].

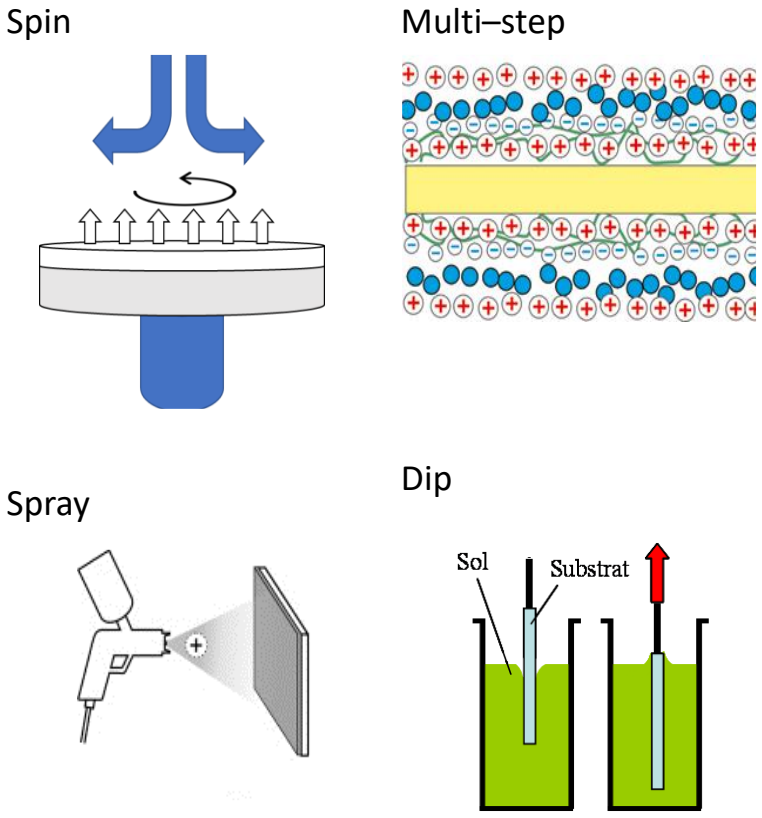

Figure 15. LBL methods schematic representation [108].

1.2.3 Conversion and plasma electrolytic oxidation coatings

1.2.3.1 Chromium conversion coatings

Since early 1920s, chromium conversion coatings (CCC) have efficiently been used for corrosion protection of various types of alloys including Mg [95]. The typical treatment conditions are gathered in Table 5.

Table 5. Typical composition and procedures for CCCs on Mg alloys.

Chemical Composition (aqueous solution)	Conditions	Thickness (µm)
H_2CrO_4 or $H_2Cr_2O_7$ + activators (sulphates, chlorides, fluorides, phosphates and complex cyanides)	pH: 1~2 Low T (RT) ~3 min	0.05–2

As shown in Table 5, the precursor solution is acidic. This favors the dissolution of Mg followed by a local pH increase, which triggers the reaction between Mg^{2+} ions and chromate ions and, therefore, the formation of insoluble and adherent compounds [116, 117]. The conversion process is quite fast and can take place at room temperature [118]. The result is usually a very thin layer of a few microns. CCC provides high corrosion protection with a self–healing and inhibition effect, due to the presence of trace amounts of Cr(VI) species that have a high repassivation capacity of the damaged areas through the formation of mixed oxides of Mg^{2+} and Cr^{3+}. Even today, Cr(VI)–free coatings are far from matching these good corrosion protection properties, with perhaps a few notable exceptions based on V and Mo oxides [119].

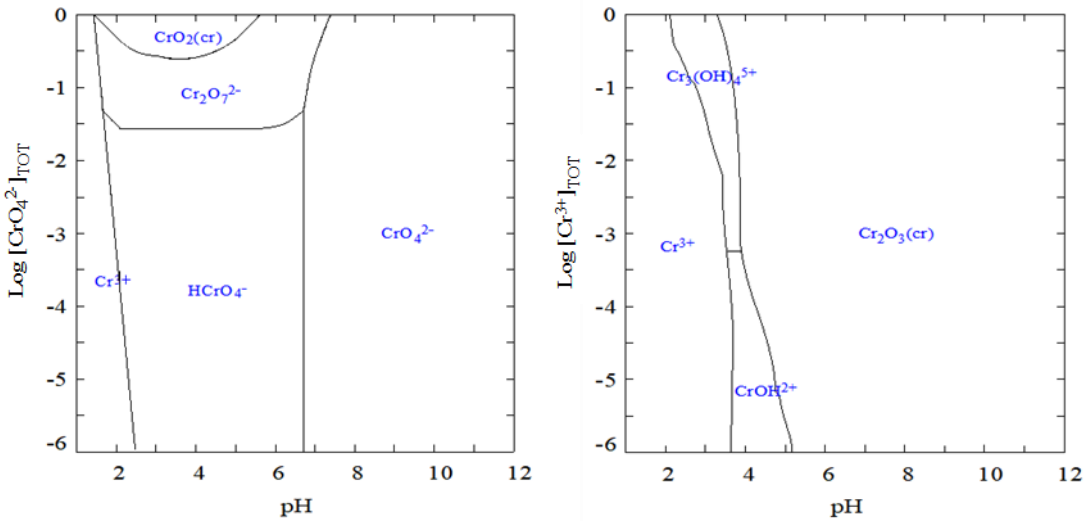

Figure 16. Cr species predominance diagrams for (a) hexavalent and (b) trivalent oxidation states. Diagrams calculated using the MEDUSA software package developed by KTH Chemistry department. Adapted from [120-122].

In solution, the stable species for hexavalent chromium are hydrochromate ($HCrO^{4-}$), chromate (CrO_4^{2-}), and dichromate ($Cr_2O_7^{2-}$) ionic species (Figure 16). The proportion of each ion in solution depends on the specific pH and concentration. The formation mechanism of the CCC on Mg goes as follows according to Pommiers–Belin *et al.* [123].

Redox reaction: $$Cr_2O_7^{2-}(aq) + 14H^+(aq) + 3Mg(s) \rightarrow \rightarrow 2\,Cr^{3+}(aq) + 7H_2O + 3Mg^{2+}(aq) \quad (9)$$

Magnesium deposition: $$Mg^{2+}(aq) + 2OH^-(aq) \rightarrow Mg(OH)_2(s) \quad (10)$$

Chromium deposition: $$Cr^{3+}(aq) + 3H_2O(l) \rightarrow Cr(OH)_3\,(s) + 3H^+(aq) \quad (11)$$

The main advantages of these layers are based on the simplicity of the process and low operating cost along with a significant improvement of corrosion properties with self–healing characteristics. However, according to recent REACH regulation, Cr(VI) is highly toxic and carcinogenic and must be withdrawn from use and replaced by new environmental–friendly substitutes.

Currently, commercial alternatives to CCCs are based on phosphates, permanganates and fluorozirconates, but they are less effective than CCCs as they do not provide the same self–healing capacity that comes with Cr(VI) species [124-128].

1.2.3.2 Layered double hydroxides

I. Fundamentals

Recently, a lot of attention has been drawn to innovative conversion coatings based on layered double hydroxides (LDHs) as an environmentally friendly alternative to CCC due to their unique structure and versatility from a corrosion protection point of view [84].

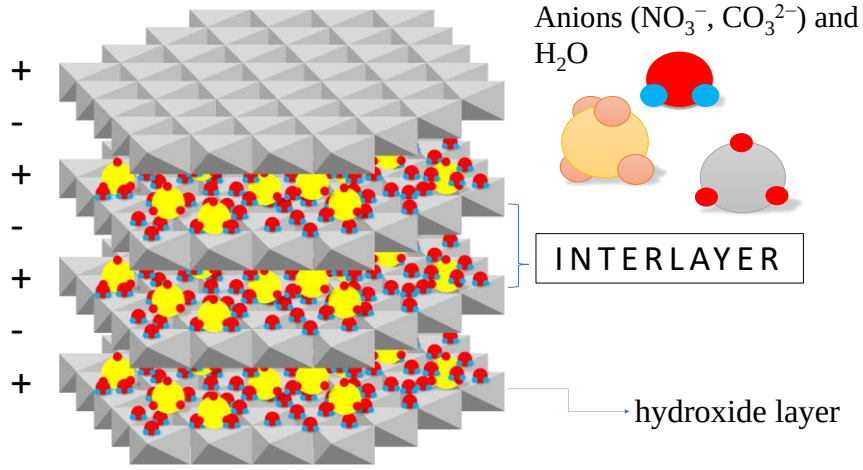

Figure 17. Schematic representation of a hydrotalcite like structure.

LDH systems, also known as hydrotalcite–like systems or anionic clays, can be described as positively charged mixed metal (M^{2+} – M^{3+}) hydroxide layers and interlayers occupied by anions (A^{m-}) and water molecules.

The general formula of LDHs can be represented as $[M^{2+}_{(1-x)}\ M^{3+}_{x}(OH)_2]^{x+}\ [(A^{m-})_{x/m}\cdot nH_2O]^{x-}$ [129]. The atomic structure (Figure 17) is close to a brucite–like structure similar to hydrotalcite (HT), where a fraction of divalent cations (M^{2+}) has been substituted by trivalent cations (M^{3+}). The nature of cations can be very diverse: Mg^{2+}, Ca^{2+}, Cu^{2+}, Mn^{2+}, Zn^{2+} and Al^{3+}, Cr^{3+}, Fe^{3+}, Co^{3+} [84, 130]. The positive charge of the sheets (x^+) caused by the partial substitution of the divalent cations is defined by the ratio $M^{2+}/(M^{2+} + M^{3+})$ which usually varies in the range of 0.20 to 0.33 [131]. Anions allocated in the interlayer galleries (e.g. NO_3^-, PO_4^{3-}, CO_3^{2-}) balance this positive charge and provide the coatings with ion–exchange ability. In fact, the intercalated anions can be exchanged under controlled conditions with other species from the environment (e.g. corrosion inhibitors).

There are different synthesis methods for LDHs including *in–situ* growth, co–precipitation, electrochemical deposition, spinning, etc. Table 6 shows the features of the most common LDH routes [130, 132].

Table 6. Features of several LDH synthesis methods.

Method	Features/Advantages	Challenges/Disadvantages
***In–situ* growth**	• Simple operation • Strong adhesion • Size control • Adaptability	• Substrate as only source • Time consuming • Limited to alkaline conditions
Co–precipitation	• Simple operation • High adaptability • Controllable chemical compositions • Compatible with hydrothermal process	• Long treatment times • Weak adhesion • Heterogeneous coatings (aggregates)
Electrochemical deposition	• High deposition rate • Adaptable to complex geometries • Simple equipment	• Complex operation • High cost • Several steps required

The co–precipitation process is the most widely used, particularly for the Mg–Al alloys. During the process, over–saturated conditions and alkaline pH are necessary for the correct formation

of LDH. Typically, nitrates, sulphates and chlorides are used as precursors. Under these conditions, a colloid of LDH particles is formed. Then, the immersion of the Mg specimen triggers the crystallisation process on the surface of the alloy due to partial dissolution of the alloy, which supplies Mg^{2+} and Al^{3+} ions. This effect is more pronounced around the intermetallic precipitates due to two phenomena: i) micro–galvanic corrosion between the inclusions and the surrounding matrix; and ii) selective Al dissolution within the Al–Mn inclusions due to the highly alkaline conditions (pH 10) during treatment [133]. Hydrothermal conditions assist the formation of LDH crystals, but also cause the formation of irregular coatings due to the precipitation of large aggregates of LDH flakes [84, 129].

II. State of the art and challenges of LDH coatings on Mg

The ion exchange capacity of LDHs is the most important quality from a corrosion point of view. It allows the structure to act as a nano–trap for corrosive anions such as Cl^- or as a nano–container for molecules with corrosion–inhibiting properties. This anion exchange capacity is due to the lack of cross–linking between the hydrotalcite layers [129, 134] and can be controlled, resulting in a tuneable intergallery size. It is also possible to control the charge ratio between the hydrotalcite layers and the intergalleries as well as the amount of water molecules, thus modifying the capacity of the structure to store inhibitors and/or corrosive ions [84, 130, 132]. Table 7 [135-152] summarizes corrosion results reported for Mg alloys with LDH coatings. In general, LDH coatings improve the corrosion performance by up to 4 orders of magnitude in terms of corrosion current density and impedance modulus. Most studies focus on Mg–Al LDH. Other systems include Mg–Fe, Zn–Al and Li–Al.

Table 7. Synthesis method and corrosion performance of different LDH coatings on Mg alloys.

Alloy	LDH	Synthesis method	Corrosion performance [NaCl][a]	i_{corr} (A cm^{-2})	$\|Z\|_{10mHz}$	Ref.
AZ31	Mg–Al 1 µm	Two–step *in–situ*	0.1M	4.5×10^{-6}	3.2×10^{4}	[135]
AZ91D	Mg–Al	Hydrothermal	3.5 %	1.1×10^{-7}	–	[136]
Mg–Nd–Zn–Zr	Mg–Al	Hydrothermal	PBS	3.6×10^{-7}	–	[137]
AZ31	Mg–Al 25–50 µm	Urea hydrolysis	3.5 %	5.8×10^{-6}	1.8×10^{3}	[138]
AZ31	Mg–Al 28 µm	Steam coating	0.86 M	2.1×10^{-9}	–	[139]
AZ31	Mg–Al	Steam coating	5 %	1.4×10^{-10}	–	[140]

[a]in wt.%

Table 7. Synthesis method and corrosion performance of different LDH coatings on Mg alloys. (cont).

Alloy	LDH	Synthesis method	Corrosion performance [NaCl][a]	i_{corr} (A cm^{-2})	$\|Z\|_{10mHz}$	Ref.
AMCa 602	Mg–Al 53–308 µm	Steam coating	5 %	9.6×10^{-11}	–	[141]
AZ31	Mg–Al 20 µm	Hydrothermal	3.5 %	1.5 × 10–6	–	[142]
AZ31	Mg–Al 7 µm	Co–precipitation and hydrothermal	3.5 %	6.5×10^{-8}	4.8×10^{5}	[143]
AZ31	Li–Al 0.82 µm	Electrochemical deposition	0.1 M	1.5×10^{-6}	–	[144]
AZ31	Mg–Al 180 µm	Co–precipitation and hydrothermal	0.86 M	2.1×10^{-9}	–	[139]
AZ31	Mg–Al 17 µm	Co–precipitation and hydrothermal Intercalation MoO_4	3.5 %	Mg–Al 4.5×10^{-6} MoO_4^{2-} 1.6×10^{-7}	– 1.10×10^{4}	[145]
AZ31	Ni–Al 7 µm	Co–precipitation and hydrothermal Intercalation Na_2SiO_3	3.5 %	Ni–Al 4.8×10^{-5} Na_2SiO_3 8.2×10^{-6}	– –	[146]
AZ31	Mg–Al	Co–precipitation and hydrothermal Intercalation Aspartic acid	3.5 %	Mg–Al 5.6×10^{-7} Aspartic acid 5.7×10^{-8}	 2.5×10^{4} 1.3×10^{11}	[147]
AZ31	Mg–Al	Co–precipitation and hydrothermal Intercalation 8–HQ	3.5 %	4.9×10^{-6} 8–HQ 1.7×10^{-7}	 1.9×10^{3} 5.0×10^{3}	[150]
AZ31	Zn–Al 9–16 µm	Co–precipitation and hydrothermal Intercalation Na_3PO_4 Na_2MoO_4 Na_3VO_4	3.5 %	Zn–Al 2.1×10^{-5} Na_3PO_4 3.7×10^{-6} Na_2MoO_4 3.4×10^{-6} Na_3VO_4 3.0×10^{-7}	 1.1×10^{3} 1.5×10^{4} 2.1×10^{4} 3.4×10^{4}	[151]

[a]in wt.%

As shown in Table 7, there are no many studies on the ion–exchange capacity and inhibitor intercalation for Mg alloys. Up to now, only a few studies have brought this intercalation to fruition. Therefore, although results so far are promising, more research is required to find suitable inhibitor–coating combinations with self–healing properties.

1.2.3.3 Plasma electrolytic oxidation

I. Fundamentals

Plasma electrolytic oxidation (PEO) or micro–arc oxidation (MAO) is a plasma–assisted electrochemical surface treatment or advanced anodizing process where high voltages are applied (100–600 V). The treatment can be carried out under current, voltage or power input control. A typical experimental set up is shown in Figure 18. Anodic polarization above the breakdown potential results in short–lived microdischarges and formation of ceramic–like coatings. PEO coatings are typically hard and enriched in substrate– and electrolyte–derived constituents [153, 154].

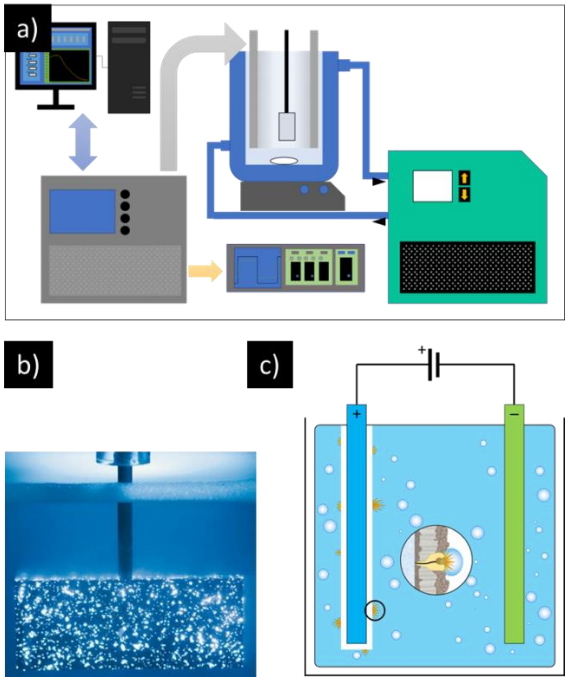

Figure 18. (a) Simplified representations of a typical set–up for a PEO electrolytic cell, (b) Micro–discharges during PEO process [155] and (c) schematic representation of PEO process mechanism.

The mechanism of formation of PEO coatings is rather complex. It involves processes such as ionic migration, electrolyte vaporization, high temperature reactions and solidification of molten material [154, 156]. *Oxide film dielectric breakdown*, *discharge–in–pore model*, and *contact glow electrolysis* are examples of models that have been used to describe PEO [157-159]. *Dielectric breakdown* is the most cited one. At the location of film breakdown there is a current surge that is followed by electron avalanches and formation of new coating material after the discharges fade out [160]. As shown in Figure 19, PEO coatings exhibit a layered structure comprising a nanometer barrier layer (close to the substrate), an outer porous layer

and, in some cases, a dense intermediate layer. The latter is typical of alternating current regimes and shows smaller pores.

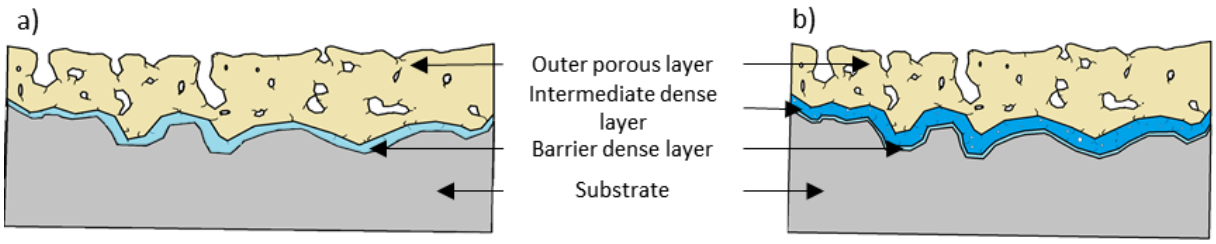

Figure 19. Schematic representation of a (a) two– and (b) tree–layered PEO coating structure and were pores and cracks can be observed.

II. State of the art and challenges of PEO on Mg

The history of PEO studies on Mg can be separated into three stages or periods (Figure 20). Anodizing on Mg began in the early 1920s. Then, many commercial processes were introduced between 1930 and 1960. Examples are the 'hard anodizing' processes known as Dow 17 and HAE. Nowadays, anodizing above the breakdown potential (PEO) is much more common. During the 80 and 90s, commercial PEO processes were developed, especially in Russia [161, 162]. The breakthroughs in the last ten years are mainly related to coating functionalization and compositional design [163-169].

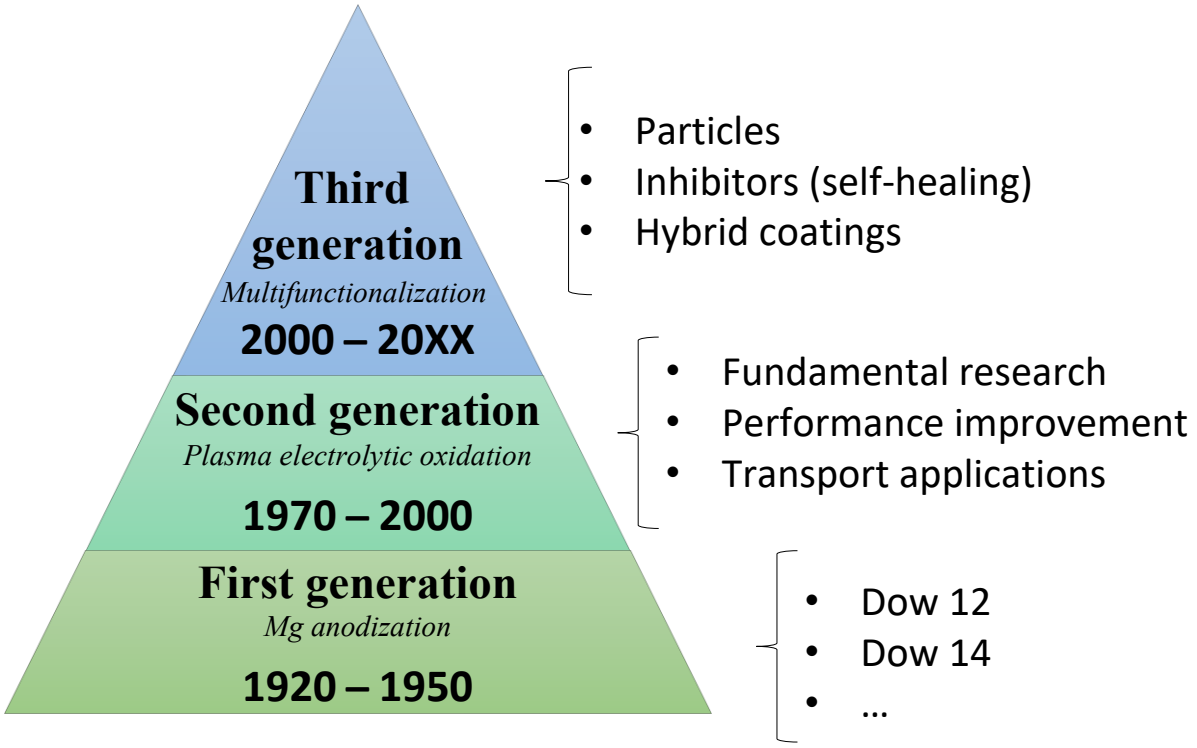

Figure 20. Chronology of the main scientific advances on PEO of Mg. Adapted from [95].

The incorporation of electrolytes species opens many possibilities for PEO coating design and tailoring of the surface properties. Silicates, phosphates, aluminates, fluorides and their combinations in alkaline solutions constitute the most common approach. Acidic electrolytes with fluorozirconate or fluorotitanate are less common [170, 171]. Figure 21 presents a general overview of PEO electrolytes and the phases that are formed on Mg.

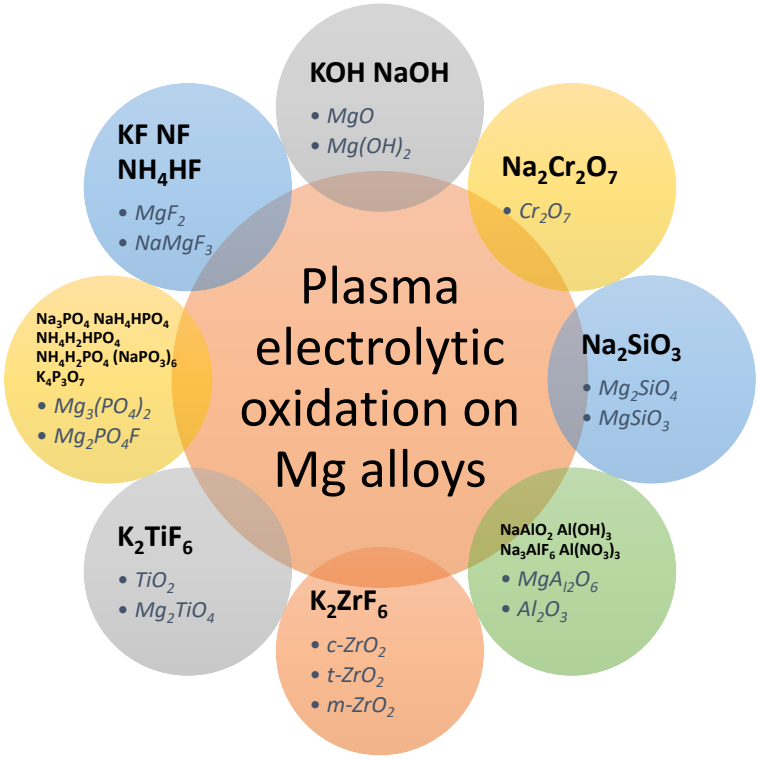

Figure 21. Electrolytes and crystalline phases in PEO processing of Mg alloys.

Most PEO coatings consist of MgO, $Mg(OH)_2$, Mg_2SiO_4, $Mg_3(PO_4)_2$, Mg_2AlO_4 or MgF_2 crystalline phases. F–rich phases are closer to the substrate as the migration of small fluoride ions is relatively easy. Ca–, Si–, Al–, P–rich compounds are more likely to be located in the outer coating layer.

From a corrosion perspective, the outer layer only provides short–term protection due to the easy access of aggressive species through the pores. That is why the inner barrier layer is mostly responsible for the corrosion performance of PEO films, despite being only a few hundreds of nanometres thick. However, when exposed to neutral and acidic media, the barrier layer rapidly dissolves, leading to localized corrosion [172] or other failure mechanisms such as undercoating corrosion and coating hydration/dissolution [173, 174].

Detailed strategies to improve the corrosion performance of PEO layers have been compiled in a detailed review [153] and include: i) selection of electrolyte; ii) fine–tuning the process parameters; iii) incorporation of nanoparticles; and iv) additives.

The most recent studies on PEO processing of Mg are focused on aspects related to reduction of energy consumption, sealings, active protective response and hybrid or duplex coatings. The following list provides a brief summary:

- High voltages (~300–400 V) and relatively long treatment times (15–30 min) are commonly needed for PEO of Mg. This implies a high cost and energy consumption, thus limiting the acceptance of PEO technology in large–scale industrial production [7, 9]. A recent strategy is the development of short treatment times in order to produce "flash–PEO" coatings [175, 176]. Thin or flash–PEO has already demonstrated to be a cost–effective approach with thicknesses and corrosion protection comparable to CCCs.

- Long–term corrosion protection is a challenge for PEO coatings. Strategies to tackle this goal are focused on "self–healing" functionality or the ability to "heal" surface defects. For instance, improvement of the corrosion properties of a PEO–coated Mg alloy was obtained after immersion in a solution containing inhibitor species such as 8–hydroxyquinoline [177] and Ce(III) [178]. Other strategies to incorporate active agents are based on electrophoretic deposition [179, 180], electrodeposition [181], thermosetting polymers [182, 183] and hydrothermal post–treatment [184, 185].

- Hybrid or duplex coatings combining PEO and sol–gel have been recently identified as a viable option for improving the long–term corrosion protection [186-188]. Sol–gel formulations range from conventional inorganic silane–based structures to more advanced hybrid organic–inorganic systems [189, 190]. Silane–based coatings offer good mechanical properties and adhesion; however, this system requires high curing temperatures leading to micropores and microcracks on the surface [189, 191]. In recent years, hybrid sol–gel coatings are becoming more common. They are formed from the interaction of an inorganic precursor, usually a silane, with an organic one. The organic part provides low curing temperatures, but also provides adaptability to the system while maintaining good mechanical properties [190-192]. The positive effect of PEO coating as pre–treatment for sol–gel layer has been reported in several studies [186, 193]. The PEO layer improves the uniformity and durability of the sol–gel top layer. In addition,

the benefits of combining a PEO coating impregnated with organic and corrosion inhibitors and a sol–gel sealing have also been recently demonstrated. [178, 194-196].

2 Hypotheses and Objectives

2.1 Hypotheses

The following hypotheses are the base of this research work:

H1. Environmentally friendly coatings based on PEO, flash–PEO, LDH and sol–gel can be developed for corrosion protection of magnesium alloys. These coatings should provide a sound basis for post–treatment and/or incorporation of inhibitors.

H2. It is possible to provide active protection to the fabricated coatings, thus improving their corrosion performance. This should be possible by incorporating inorganic or organic corrosion inhibitors following *in–situ* or post–treatment approaches.

2.2 Objectives

In order to confirm the abovementioned hypotheses, the following specific objectives were defined.

O1. To develop LDH conversion coatings with incorporated inhibitors.

The goal is to provide active protection to LDH conversion coatings formed on the AZ31 alloy. For this purpose, different LDH systems are evaluated and modified by incorporating several corrosion inhibitors. Electrochemical impedance spectroscopy is used to evaluate the best LDH–inhibitor combinations. Active protection tests are performed by immersion and SVET measurements. A detailed morphological and compositional characterization of the developed systems is carried out. These systems are intended as an alternative for chromium conversion coatings used in transport applications.

O2. To develop flash–PEO coatings doped with Ca.

The main objective is to develop flash–PEO coatings on the AZ31 alloy that are doped *in–situ* with inhibitive cations. These thin PEO coatings containing Ca should be a promising alternative to chromium conversion coatings in transport applications due to their compact and resistive ceramic–like nature. Identification and detailed characterization of the best candidates is performed for stand–alone and painted components. Their corrosion performance is also evaluated in saline aqueous environments.

Hypotheses and Objectives

O3. To develop Ce– or Ca–based sealings for PEO coatings.

The first goal is to apply a Ce–based sealing to improve the corrosion performance of a PEO–coated Mg–Y–Zn alloy that contains long period stacking order (LPSO) phases. This protection system is intended for transport applications. The second goal is to develop a Ca–based sealing for a PEO–treated AZ91 Mg alloy. The use of Ca is intended for both transport and biomedical applications. In both cases, the influence of sealing conditions on the corrosion resistance is investigated. The corrosion behaviour is evaluated by electrochemical and hydrogen measurements. Detailed characterization of the PEO and post–treated PEO coatings is also performed.

O4. To develop hybrid PEO/Sol–Gel coatings.

In this objective the aim is to seal PEO coatings on the AZ31 alloy by applying sol–gel post–treatments based on TEOS and GPTMS precursors that are modified with corrosion inhibitors. The duplex or multi–layer systems are characterized in detail (FTIR, SEM, paint adhesion, etc.) and their long–term electrochemical corrosion performance is evaluated by electrochemical impedance spectroscopy and immersion tests. These advanced treatments are intended for corrosion–critical applications in the transport sector.

3 Materials and Methods

3.1 Materials

3.1.1 Magnesium alloys

3.1.1.1 AZ31B

The AZ31B alloy was acquired from two different suppliers in the form of sheets (~1 m^2). The chemical compositions are specified in Table 8. Sheets were cut into specimens of 40×20×3 mm^3 and 40×30×2 mm^3 for Magnesium Elektron Ltd. and FamiMetal SL., respectively. The designation "B" refers to the second generation of this alloy in which a better control of impurities is achieved. The alloy was supplied in the “H24” condition, which corresponds to a strain hardened and partially annealed version of AZ31B. The number “2” applies to products that are strain hardened more than the desired final amount, whereas the number "4" (half hard) indicates a strength about midway between “0” (annealed) and “8” (full hard) conditions.

Table 8. Nominal composition in wt.% of AZ31B studied alloys (compositions supplied by the manufacturer).

AZ31B–H24	Mg	Al	Zn	Mn	Fe	Si	Ce	Ca	Cu	Si
Magnesium Elektron Ltd.	Bal.	2.72	0.76	0.19	0.0028	0.0103	0.24	0.0008	–	–
FamiMetal SL	Bal	2.5	0.6	0.2	0.005	0.009	–	0.0007	0.05	0.031

3.1.1.2 AZ91D

AZ91D specimens (30×15×5 mm^3), with the nominal composition shown in Table 9, were supplied by the Northeastern University (China). The designation "D" in the AZ91 alloy refers to the fourth generation of this alloy in which a better control of impurities is achieved. This alloy was produced by standard gravity casting.

Table 9. Nominal composition in wt.% of AZ91D alloy determined by X–ray fluorescence analysis at Northeastern University.

AZ91D	Mg	Al	Zn	Mn	Fe	Ce	Si	Cu
Northeastern University	Bal.	9.02	0.55	0.19	0.002	0.008	0.027	0.002

3.1.1.3 Mg–Y–Zn

The LPSO Mg–Y–Zn alloy was manufactured and supplied by CENIM (Spain). The alloy was cast in a resistance melting furnace and extruded at 400 °C employing an extrusion ratio of 18:1

and a rectangular profile of 4×20 mm^2. The composition of the alloy is given in Table 10. Specimens of 40×10×2 mm^3 were used in this work.

Table 10. Nominal composition in wt.% determined by X–ray fluorescence analysis at CENIM.

Mg–Y–Zn	Mg	Y	Zn	Fe	Mn
CENIM	Bal.	6.8	2.2	0.02	<0.01

3.2 Specimen preparation

3.2.1 Surface preparation for metallographic characterization

For the metallographic characterization of the studied alloys, specimens were ground to grade P1200 with silicon carbide abrasive papers and polished until a mirror–like finish with successive cloths containing 3, 2 and 1 μm diamond pastes. Unless otherwise stated, the microconstituents were revealed on the polished samples by immersion for up to 30 s in the following acid mixture: 5 g picric acid (CAS number 88–89–1), 100 mL ethanol (CAS number 64–17–5), 5 mL acetic acid (CAS number 200–580–7) and 10 mL deionized water.

3.2.2 Surface pretreatment

AZ31B specimens were pre–treated following a two–step commercial procedure from Henkel. The first step consists of cleaning in an alkaline surfactant solution (Bonderite C–AK 4181 L, 90 g/L) at 80–90 °C for 15 min, followed by water rinsing. The second step involves acid etching at room temperature for 3 min (Bonderite C–IC 3610, 10 g/L), also followed by water rinsing. The required etching rate limit of 10 g/cm^2 was maintained for the Mg substrates. Each 1 L solution was used to clean a total surface of 500 cm^2 (8 – 9 samples). After etching, specimens were washed with deionised water, dried with alcohol and warm air and stored in a desiccator for at least 24 h before use.

Mg–Y–Zn specimens were wet ground using increasing grades of silicon carbide abrasive papers from P120 to P1200, followed by water rinsing, drying with alcohol and warm air and storage in a desiccator for at least 24 h. The AZ91D specimens followed a similar procedure, although a P2000 SiC finish was selected in this case.

3.3 Surface treatments

3.3.1 Plasma electrolytic oxidation coatings

The studied PEO coatings were produced by using the electrolytes and the conditions specified in Table 11 and Table 12. The PEO set up is presented in Figure 22. Both DC and AC power supplies were used to produce the coatings (DC power supply: SM400–AR–8, Delta Elektronika; AC power supply: EAC–S2000, ET Systems Electronic). The DC power supply was connected to a PC for acquisition of the current and voltage values with a time resolution of ~0.1 s. For the AC power supply, a 2–channel Tektronix TDS 2012B oscilloscope was used for recording the instantaneous voltage and current signals. Complementarily, a Keithley KUSB–3116 data acquisition card (500 kS/s) was used to record the root mean square (rms) values of the current and voltage during treatment (time resolution ~0.1 s).

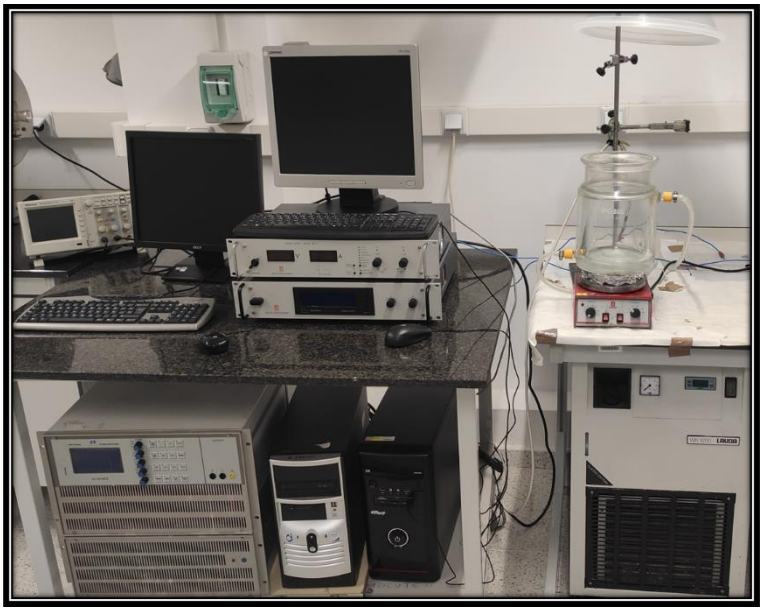

Figure 22. Experimental system used for the fabrication of PEO coatings.

Both AC and DC PEO stations use a 2 L double–jacketed glass cell connected to a closed–loop water cooling system (WK 120 LAUDA) to maintain a constant temperature (~21ºC). A cylindrical AISI 316L stainless steel mesh (length 265 mm × width 145 mm × height 265) was used as the counter–electrode. During the PEO process, constant stirring was maintained at 300 rpm. After PEO, the specimens were washed with deionised water and dried with alcohol and warm air. Specimens were kept in a desiccator for at least 24 h before further manipulation.

Table 11. Range of studied variables for PEO alloy under AC conditions.

Alloy	Electrolyte	CAS number	Electrical signal	Chapter
Mg–Y–Zn	$Na_2SiO_4 \cdot H_2O$ (water glass) 10.5 g/L	1344–09–8	20 ± 1 °C 400 V/–30 V square signal	3
	NaOH 6 g/L	1310–73–2	400 mA cm^{-2}	
	NaF 2 g/L	7681–49–4	500 Hz 15 min 60 s ramp	
AZ91D	$Na_3PO_4 \cdot 12H_2O$ 30 g/L	10101–89–0	20 ± 1 °C	3
	KF·2 H_2O 4 g/L		500 V	
	NaOH 2 g/L	7789–23–3	200 mA cm^{-2}	
		1310–73–2	500 Hz 15 min 60 s ramp duty cycle 30%	
AZ31B	Na_2SiO_3 10.5 g/L	10213–79–3	20 ± 1 °C	4
	KOH 8.5 g/L	1310–48–3	400/–30 V	
	NaF 2 g/L	7681–49–4	100 mA cm^{-2} 50 Hz 4 min 60 s ramp	

Table 12. Range of studied variables for PEO alloy under DC conditions.

Alloy	Electrolyte	CAS number	Electrical data	Chapter
AZ31	$Na_2SiO_3 \cdot 5H_2O$ 5 g/L	10213–79–3	200 V	2
	$Na_3PO_4 \cdot 12H_2O$ 5 g/L	10101–89–0	100 mA cm^{-2}	
	KOH, 14 g/L		20 ± 1 °C	
	KF 3 g/L	1310–48–3	20 and 45 s	
	Na_2EDTA 0–2 mM	7789–23–3		
	CaO 0–1.5 mM	6381–92–6		
	CaGlyP 0–1.5 mM	1305–78–8		
		1336–00–1		
AZ31	$Na_3PO_4 \cdot 12H_2O$ 4 g/L	10101–89–0	400 V	4
	$NaAlO_2$ 5g/L	11138–49–1	200 mA cm^{-2}	
	KF 3 g/L	7789–23–3	90 s (10 s slope+80s)	
	KOH 0.5 g/L	1310–48–3		

3.3.2 Ce–, Ca– and 8HQ–sealings of PEO coatings

The PEO–coated Mg–Y–Zn alloy was sealed at (30 ± 1) ºC by immersion for 5 or 60 min in an aqueous acid solution containing 10 g/L $Ce(NO_3)_3.6H_2O$ (CAS number 10294–41–4), 0.3 g/L hydrogen peroxide (CAS number 7722–84–1) and 1 g/L boric acid (CAS number 10043–35–

3). The treatment is carried out in batches of 12 samples, each in a volume of 250 mL of fresh solution.

Ca–based sealings of the PEO–coated AZ91D alloy were carried out for 60 min at (80 ± 2) ºC in a solution composed of 70 g/L $Ca(NO_3)_2$ (CAS number10294–41–4) and 0.1 mol/L sodium dodecyl sulphate (SDS) (CAS number 151–21–3). The solution was adjusted to different pH values (3, 4 and 5) by dripping dilute HNO_3 (CAS number 7697–37–2). The treatment is carried out in batches of 12 samples, each in a volume of 500 mL of fresh solution.

8HQ–based sealings of the PEO–coated AZ31B alloy were carried out at room temperature for increasing times up to 30 min in aqueous solutions of 8–hydroxyquinoline (8HQ) (CAS numbers 148–24–3) and concentrations ranging from 0.01 to 0.1 M at a total volume of 250 mL. A fresh solution was used every 4 samples.

3.3.3 Layered double hydroxide conversion coatings

The LDH coatings were synthesized via the hydrothermal route. The latter term refers to a synthesis process where chemical reactions occur in an aqueous solution above ambient temperature and pressure. Table 13 shows the concentrations for each of the LDH precursors. Each solution was prepared by dissolving the corresponding species in a small amount of water, then the pH of the solution was raised by adding 1 M NaOH solution up to a pH value between 9.5 and 10.5. The stirred 500 mL aqueous solution was then transferred to a PTFE–lined stainless–steel autoclave in which the samples were vertically immersed during 24 h at 125 ºC. Synthesis conditions were defined according to [131] in order to ensure the optimal crystallization of the LDH flakes. A schematic representation of the process is presented in Figure 23.

After the LDH synthesis, the inhibitor incorporation step (Li^+; WO_4^{2-}) was conducted by immersion in the corresponding solution according to the conditions shown in Table 14. Finally, the specimens were rinsed in deionized water, dried with warm air and stored in a desiccator for at least 24 h before use.

Materials and Methods

Table 13. Solutions used for hydrothermal synthesis of the studied LDH coatings.

Coating	Cations	CAS number	pH
Li–Al LDH	$LiNO_3$ 0.0625 M	7790–69–4	10
	$Al(NO_3)_3 \cdot 9H_2O$ 0.125 M	7784–27–2	
	Na_2CO_3 0.0625 M	497–19–8	
Zn–Al LDH	$Zn(NO_3)_2 \cdot 6H2O$ 0.25M	10196–18–6	10
	$Al(NO_3)_3 \cdot 9H_2O$ 0.125 M	7784–27–2	
	Na_2CO_3 0.0625 M	497–19–8	

Table 14. LDH post–treatment for inhibitor loading.

Coating	Inhibitor	CAS number	Synthesis
Li–Al LDH Li	$LiNO_3$ 0.1 M	7790–69–4	10 pH 2 h 45 ºC
Zn–Al LDH W	Na_2WO_4 0.1 M	10213–10–2	10 pH 2 h 45 ºC

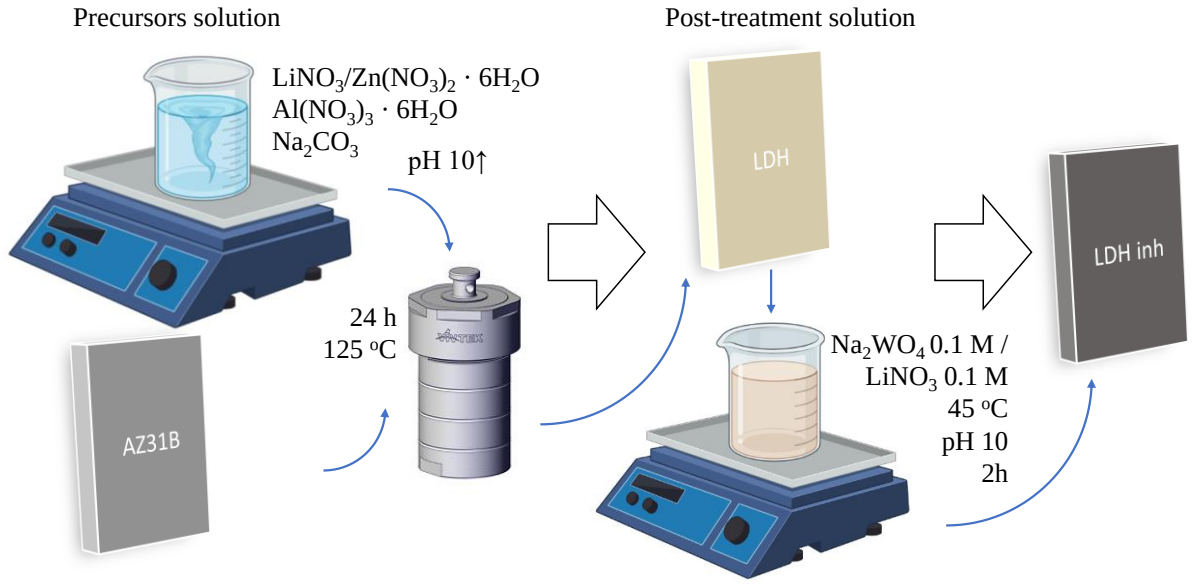

Figure 23. Scheme of the hydrothermal LDH growth method for the studied LDH conversion coatings.

3.3.4 Sol–Gel post–treatments

Two different sol–gel formulations were used for producing the hybrid PEO/SG coatings on the AZ31B alloy. Both of them are based on the GPTMS [(3–glycidyloxypropyl) methyldiethoxysilane, CAS number 2897–60–1] and TEOS (tetraethyl oxysilicate, CAS number 78–10–4) precursors (Figure 24). The difference between them is the presence or absence of inhibitor.

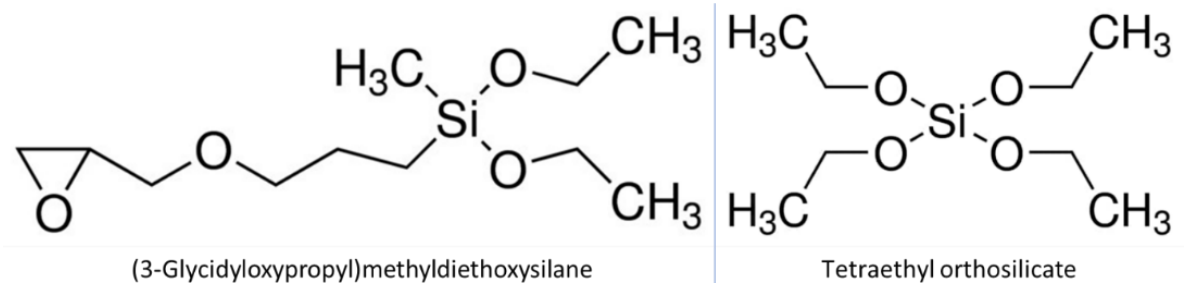

Figure 24. Chemical structures of GPTMS and TEOS.

The sol–gel sealings was based on a hybrid sol–gel (HSG) system consisting of GPTMS–TEOS. The sealing studied in this work was composed of (% v/v) TEOS 20%, GPTMS 10 %, ethanol 10 %, DI water 58 % and acetic acid until pH 2 was reached. Separately, the inhibitor was dissolved in a stirred water for 30 min. The precursors were mixed in the order presented. The solution was then placed in agitation under magnetic stirring for 24 h at room temperature. After that period, the sol–gel solution was stored at (4 ± 2) °C until application. The corrosion inhibitor 8HQ was introduced into this sol–gel formulation up to a maximum of 50 mM (Table 15).

For sol–gel sealings, a constant immersion and withdraw rate of 100 mm/min was ensured by using the automated dip–coating method. A KSV Nima dip–coater was used in this study in collaboration with the Department of Materials Science Department at UMONS (Mons, Belgium). Finally, specimens were air dried for 10–20 min and heated in a furnace to 125 and 150 °C for 1 h, respectively.

Table 15. Sol–gel precursors solution composition.

Coating	Composition	Volume ratio
GS	TEOS (tetraethoxysilane)	20 %
	GPTMS (3–(glycidyloxypropyl)trimethoxy silane)	10%
	Ethanol	10 %
	DI water	58%
	Acetic acid to adjust pH 2	
GS–8HQ	TEOS (tetraethoxysilane)	20 %
	GPTMS (3–(glycidyloxypropyl)trimethoxy silane)	10%
	Ethanol	10%
	8HQ aqueous solution (8–hydroxiquinoline 0.05 M)	58%
	Acetic acid to adjust pH 2	

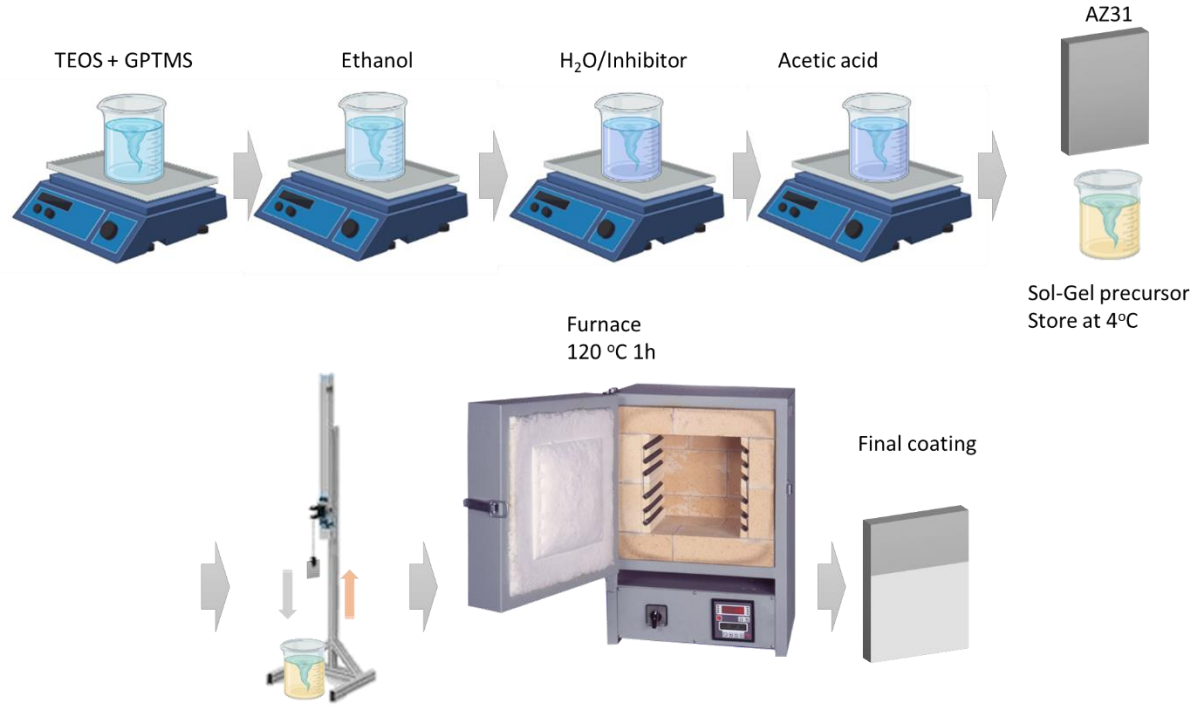

Figure 25. Synthesis route followed for the hybrid sol–gel post–treatments.

3.4 Characterization techniques

3.4.1 Optical microscopy (OM)

The Mg alloys and coatings studied in this work were examined by optical microscopy (OM) by using a Leica DMi8 optical microscope with a FlexaCam C1 digital camera. Micrographs were obtained in bright field mode at different magnifications (between ×50 and ×1000). When necessary, polarized light in combination with a lambda plate was used for enhancing the contrast between microconstituents.

3.4.2 Scanning electron microscopy (SEM)

Electron microscopy in tandem with an energy dispersive (EDS) X–ray analyser and a backscatter electron (BSE) detector is a powerful tool for the study of surfaces at high magnification and the analysis of their composition. One of the key advantages is the larger depth of field in comparison to optical microscopy. SEM uses a focalised electron beam that follows a vertical path from the electron gun through the microscope to finally hit the surface of the sample. This beam is highly energetic, so it penetrates the surface atomic layers. The supplied energy causes a series of elastic and inelastic collisions. A billiard–ball effect is observed then as the elastic scattering alters the trajectory but not the kinetic energy of the

electrons. By detecting the different signals resulting from this collision, useful information can be obtained: characteristic X–rays for chemical composition, escaping secondary electrons for surface topography and backscattered electrons for atomic contrast.

Planar and cross–section samples were examined with a JEOL JSM 6400 microscope equipped with an EDS spectrometer, for semi–quantitative analysis (OXFORD LINK PENTAFET 6506); and a backscattered scanning electron (BSE) detector. For higher magnifications, a field emission scanning electron microscope (FESEM, JEOL JSM 6335F) was also used. Operating voltages ranged between 3 and 20 kV. When not specified, the operating voltage and working distance were 20 kV and 15 mm respectively.

3.4.3 Surface metrology (3D focus–variation microscopy)

Focus–variation microscopy is a relatively popular method when measuring surface topography due to its ability to capture high tilt angles but being reasonably robust to variation in optical properties. This technique combines a depth–of–field limited optic with a vertical scanning process [197], where a sequence of images is recorded as the optic is moved vertically along the optical axis, resulting in a stack of vertical images. The contrast of each pixel is compared between the different images in the vertical stack to estimate the so–called contrast stack from which the height location of that pixel is estimated, while the RGB colour information associated with the point of maximum contrast at each location is used to generate a fully focused map of the surface. The software can then calculate the roughness parameters such as S_a (the difference in height of each point compared to the arithmetical mean of the surface), S_z (the sum of the largest peak height value and the largest pit depth value within the defined area) and S_{10z} (difference between the mean surface for the five highest local maxima plus the average height below the mean surface for the five lowest local minima). In this work, an InfiniteFocusSL optical profilometer (ALICONA, Gmbh) equipped with ×10 and ×50 objectives were used. The IF–Measure Suite software was used to extract roughness parameters.

3.4.4 Atomic force microscopy and Scanning Kelvin probe force microscopy (AFM–SKPFM)

Atomic force microscopy (AFM) belongs to the field of scanning probe microscopy (SPM) which, as the name implies, is based on the movement of a small probe for reproducing the surface features. AFM can determine the local properties of a surface (e.g. height, hardness,

friction, roughness) by employing a cantilever with an extremely sharp tip at its end. When this tip is positioned close enough to the surface, attractive forces cause the cantilever to deflect and move towards the surface (Figure 26). This deflection can be measured with a laser system, thus providing excellent lateral and vertical resolutions. Scanning Kelvin probe force microscopy (SKPFM), also known as surface potential microscopy, is a variant of the AFM. SKPFM measures the Volta potential difference between the AFM tip and the specimen under study [198, 199]. The most common configuration is based on a two–pass strategy. The first scan gathers topographical data, whereas the second one is performed at constant height for measuring the Volta potential without artefacts coming from variations in the tip–to–sample distance. Therefore, potential and topographic analysis can be carried almost simultaneously in the same area.

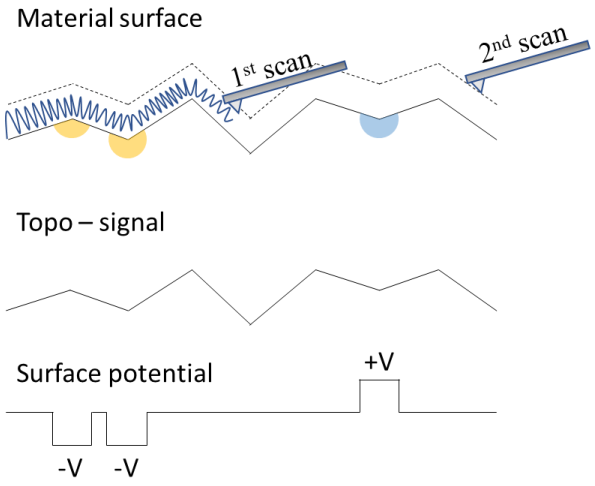

Figure 26. Schematic representation of the double scanning technique used in SKPFM. Note that during the first scan the tip works in Tapping® mode for the acquisition of the topographic signal.

In this work, prior to SKPFM measurements, the specimens (1 cm^2) were polished with diamond paste to a 0.1 μm finish and stored for 24 h in a desiccator. Volta potential maps were obtained with a Nanoscope IIIA MultiMode AFM microscope (SKPFM) equipped with a 20 nm platinum coated Si OSCM–PT tip. Temperature and relative humidity were maintained at 20–23 ºC and 40–65%, respectively.

3.4.5 X–ray diffraction (XRD)

X–ray diffraction analysis is probably the most useful tool for identification of crystalline phases. The Bragg–Brentano [Eq. 2] gives the relation between the spacing of crystallographic planes and the incidence angles at which these planes produce constructive interference (Figure

27). Where n is the order of the reflection, λ is the wavelength of the X–ray beam, d is the interplanar spacing of the atomic planes (d_{hkl}) and θ is the angle of incidence.

$$2d \cdot sen(\theta) = n\lambda \qquad \text{[Eq. 2]}$$

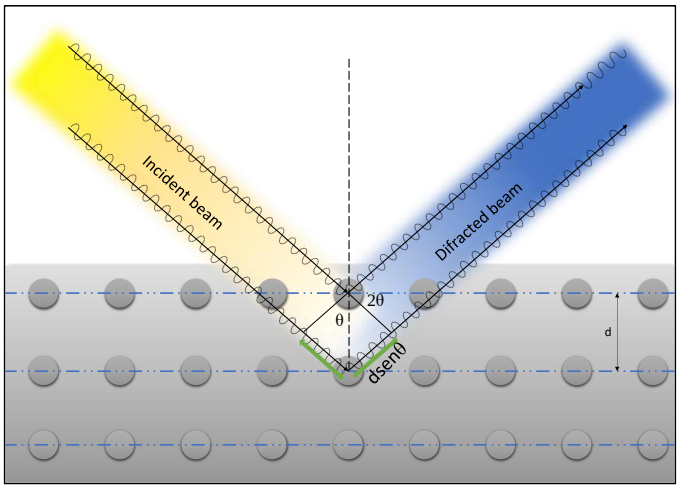

Figure 27. Schematic representation of the X–ray beam with material basal planes when the Bragg's law is fulfilled.

In this work, a Philips X'Pert diffractometer in the range of 2θ from 10° to 90°, with a step size of 0.04° and a dwell time between 1 and 6 s per step, was used to acquire the XRD patterns. Phase identification was performed with the X'Pert High Score software and the ICDD PDF4+ database. Normal (90º) and grazing incidences (1º) were used depending on the specimen. The latter was used to determine the composition of the outermost layers of the material surface.

3.4.6 X–ray photoelectron spectroscopy (XPS)

The X–ray photoelectron spectroscopy (XPS), also known as electron spectroscopy for chemical analysis (ESCA), is an ultra–high–vacuum (< 10^{-9} Torr, < 10^{-7} Pa) surface–sensitive semi–quantitative technique. XPS is based on the photoelectric effect, which refers to the release of electrons from a solid as a result of irradiation with a relatively short wavelength (Figure 28). In this technique, surface–released electrons and their kinetic energy are collected while irradiating the surface of the material with a soft X–ray beam, the penetration capability of the beam ranging from 1 to 10 nm. The electron binding energy can be calculated by the equation proposed by Rutherford [Eq. 3], where EB is the binding energy of the photoelectrons, $h\nu$ is the X–ray photons energy, Ek is the kinetic energy (eV) and Φ is the spectrometer work function:

$$EB = h\nu - Ek - \Phi \qquad \text{[Eq. 3]}$$

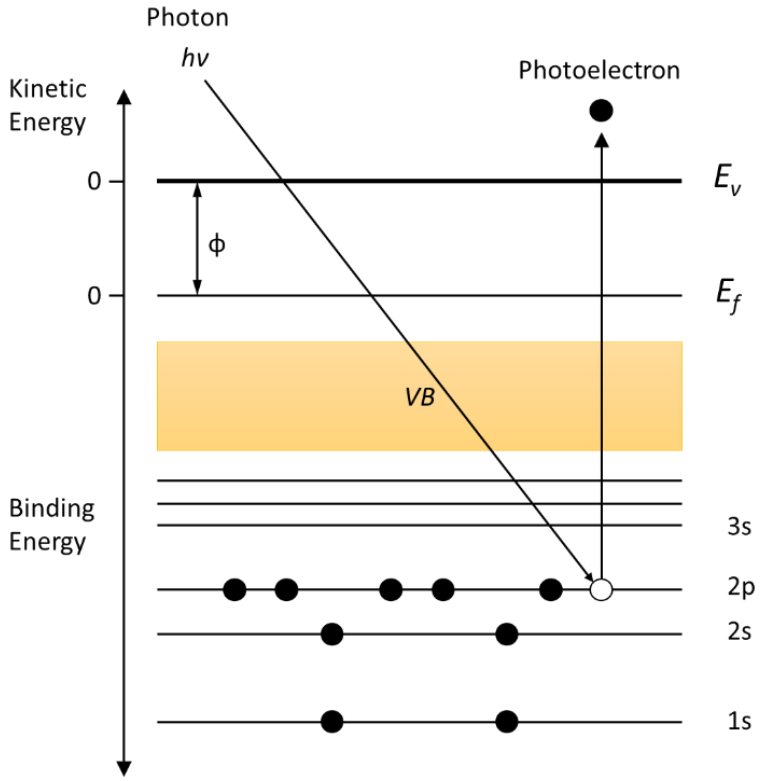

Figure 28. Schematic representation of photoelectron generation.

The XPS spectra in this work were acquired at the University of Vigo (Spain) using a Thermo Scientific K–Alpha ESCA instrument equipped with monochromatic Kα aluminium radiation at 1486.6 eV. An electron flood gun was used to minimise the surface charge on the ceramic layers as well as a low energy flood gun (electrons in the range of 0 to 14 eV) and a low energy Argon ion gun.

The atomic ratios were calculated from the integration of the peaks with respect to the background curve fitted to a function with varying proportions of Gaussian and Lorentzian contributions. The C1s peak at 285.0 eV was taken as a reference for the calculation of binding energies. To remove the shallowest layers, a sputtering cleaning was performed with an Argon gun operating at 5 kV, 10 mA and 10^{-7} torr for 10 min. The current through the sample during sputtering was maintained under 1 mA.

3.4.7 Fourier transform infrared spectroscopy (FTIR)

Fourier transform infrared spectroscopy (FTIR) is based on the fact that most molecules absorb light in the infrared region of the electromagnetic spectrum, resulting in molecular vibrations. The energy absorption is highly dependent on the chemical bonds that are present in the molecule. Consequently, this method is widely used in organic synthesis, petrochemical

engineering, the food industry and surface characterization. The nature of the molecules present in a sample can be deduced from the analysis of the FTIR spectrum as well as other properties of the molecules. Unlike scattered infrared measurements, a continuous infrared light source generates IR radiation over a wide range of wavelengths. The infrared light passes through an interferometer and is then targeted to the sample, resulting in an interferogram. The interferogram must be subsequently converted into an IR spectrum by means of a Fourier transform. Hence, all wavelengths can be collected at once without having separate wavelength scans for each one.

Fourier transform infrared spectroscopy – attenuated total reflectance (FTIR–ATR) provides information related to the chemical structure of polymeric materials. Samples are placed in contact with internal reflection elements (IREs). Different types of IREs can be used such as zinc selenide (ZnSe) or germanium (Ge). In this process, the IR radiation is focused to the end of the IRE and reflects several times along the length of the IRE. From the surface of the IRE into the specimens the IR radiation has a short penetration distance (~1 μm).

In this study, a Nicolet iS50 instrument (Thermo Fisher Scientific) was used to perform the FTIR analysis. This instrument is equipped with a KBr beam splitter and a DTSG–KBr detector tandem with ATR SpectraTech Performer (Thermo Electron Corporation) with a diamond crystal. MicroFTIR analysis was also carried out using a Nicolet iMX10 spectrophotometer (Thermo Fisher Scientific) with KBr beam splitter and MCT/A detector refrigerated with liquid nitrogen and with a germanium crystal MicroATR accessory. To avoid artefacts due to high roughness of the coatings, FTIR–ATR measurements were acquired on coatings generated on polished surfaces. The measurements were performed using 128 scans at 4 cm^{-1} and 256 scans and 8 cm^{-1} resolution, respectively.

3.4.8 Raman spectroscopy

Raman spectroscopy is a powerful tool for the characterization of materials. This technique is based on the interaction of an inelastic scattering of monochromatic light with the molecular vibrations, phonons, or other excitations in the system. A laser beam is often used as a monochromatic light source. The Raman effect results from the interaction of the sample and the light beam that causes the re–emission of photons. The energy shifts up or down compared to their original monochromatic frequency, providing information about vibrational, rotational and other low–frequency transitions in molecules. The MicroRaman analysis was collected by

using a NT–MDT NTEGRA Spectra spectrometer (NT-MDT SI, Moscow, Russia), equipped with a Solar TII MS5004i monochromator (SOL instruments Ltd., Minsk, Belarus), a CCD Andor iDUS DU–420 detector (1024 × 128 pixels) (Oxford Instruments, Abingdon, UK) and an Olympus modular BX–100 microscope (Olympus Corporation, Tokyo, Japan). The measurements were performed inside the pores of the coatings using an Olympus MPlanFL 20×/0.45NA objective (Olympus Corporation, Tokyo, Japan). A 532 nm wavelength, 20 mW solid state laser (with a 0.1% ND filter attenuation) was used as an excitation source. Grating of 600 L/mm and acquisition times of 300–600 s were used.

3.4.9 Wettability test (water drop contact angle)

A wettability test was carried out to determine the hydrophilicity/hydrophobicity of the coatings. The tests were carried out by water droplet contact angle. The measurements of the selected samples were evaluated with two different equipments: an FTA 1000/FTA instrument, controlled by FTA32 software; and KRÜSS instrument (GmbH Germany DSA10–Mk2). For each surface, a total of six drops of deionised water distributed in two different samples (three drops each) were analysed. Fifty pictures were taken at a frame rate of 0.5 s from the moment the drop is formed (after the drop has landed, 10 images are analysed).

3.4.10 Coating thickness measurements

A Fischer ISOSCOPE *FMP10* (Fischer) instrument with an *FTA3.3H* probe was used to determine the thickness of all studied coatings. This method is based on the measurement of eddy currents as specified in ISO 2360 [200]. Cited values are the average of 15 measurements per specimen and are confirmed by cross–sectional view on SEM.

3.4.11 pH and ionic conductivity

The pH was measured with a LP 21 pH–meter equipped with a 3M Ag/AgCl C.A.T 1000 reference electrode. The ionic conductivity was measured using a GLP 31 EC–Meter equipped with a 5070 conductivity cell (Crison, C: 1 cm^{-1}). The cited values are the average of at least two measurements.

3.4.12 Image analysis

Two different software packages, AxioVision 4.8 and ImageJ, were used for image analysis. AxioVision was used to perform thickness and size measurements of the different coatings

studied. The ImageJ software was used to identify regionally specific effects: porosity, number of defects, delamination in salt spray and corroded area. The ImageJ thresholding tool was used on 8 bit grayscale images. Thresholding is a technique for dividing an image into two (or more) classes of pixels. This tool separates all pixels according to whether or not they exceed a certain cut–off value. By selecting the correct value, surface defects can be separated from the unaffected areas. Defects are then measured with the particle analysis tool.

3.4.13 Paint adhesion

For the paint adhesion test a white epoxy primer provided by AzkoNobel (epoxy primer 37076, thinner C25/90s and hardener, XP–420) was used. The paint was applied with a metallic draw bar and cured in an oven at a temperature of 80 °C for 1 h. The evaluation of the paint was carried out in accordance with ISO 2409 standard [201]. According to this standard, the paint was cut with a standardized tool maintaining a spacing between the cuts of 1 mm, creating a cross–cut grid of 5×5 defects. Subsequently an adhesive tape was applied and removed after ~5 min. When none of the paint is detached, the result is considered to be 0, the best category. Complete paint detachment is categorized with the number 5. To ensure repetitively, triplicate specimens were evaluated. Wet adhesion tests were carried out following the same procedure but on samples immersed on deionized water for 7 days.

3.4.14 Rheology measurements

Rheology is the study of deformation and flow of materials. A key parameter is viscosity, which quantifies the resistance of the material to deformation or flow. Mathematically is given by the shear stress to shear rate ratio [202]:

$$Viscosity = \frac{Shear\ stress}{Shear\ rate}\ (dyn \cdot s/cm^2) \qquad \text{[Eq. 4]}$$

Shear stress and shear rate are defined as follows:

$$Shear\ stress = \frac{Force}{Area}(dyn/cm^2) \qquad \text{[Eq. 5]}$$

$$Shear\ rate = \frac{Velocity}{Thickness}(1/s) \qquad \text{[Eq. 6]}$$

A double–gap cylinder (DG–41) was used in the domain of 0 to 200 s^{-1} shear rate at a constant temperature of 26 °C in an Anton Paar MCR 302 instrument for characterization of the rheological behaviour of sol–gel solutions with and without inhibitors.

3.5 Corrosion experiments

3.5.1 Hydrogen evolution measurements

The hydrogen evolution test is based on the molar ratio relation between Mg and H_2 involved in the corrosion reaction of magnesium in aqueous solution (12). This relation is 1:1, meaning that one mol of evolved hydrogen gas corresponds to the dissolution of one mole of magnesium. Therefore, measuring the volume of hydrogen evolved during corrosion is equal to the weight–loss rate [203, 204].

$$Mg(s) + H_2O(l) \rightarrow Mg^{2+}(aq) + 2OH^-(aq) + \uparrow H_2(g) \qquad (12)$$

To carry out this test, a 1 cm^2 surface was exposed to ~100 mL of 0.5 wt.% aqueous NaCl solution. For the screening of the corrosion inhibitors, identical tests were performed in solutions containing 0.05 M of the corresponding chemical species. An upside–down burette was used for the collection of the generated H_2. A schematic representation of the system is shown in Figure 29. The relationship between the volume of H_2 collected (V_H, mL) and the corrosion rate of magnesium (P, mg cm^{-2} d^{-1}) is defined by [Eq. 7], where A and t are the area of the specimen and the immersion time, respectively.

$$P_{corr} = 1.0805 \cdot \frac{V_H}{A \cdot t} \qquad \text{[Eq. 7]}$$

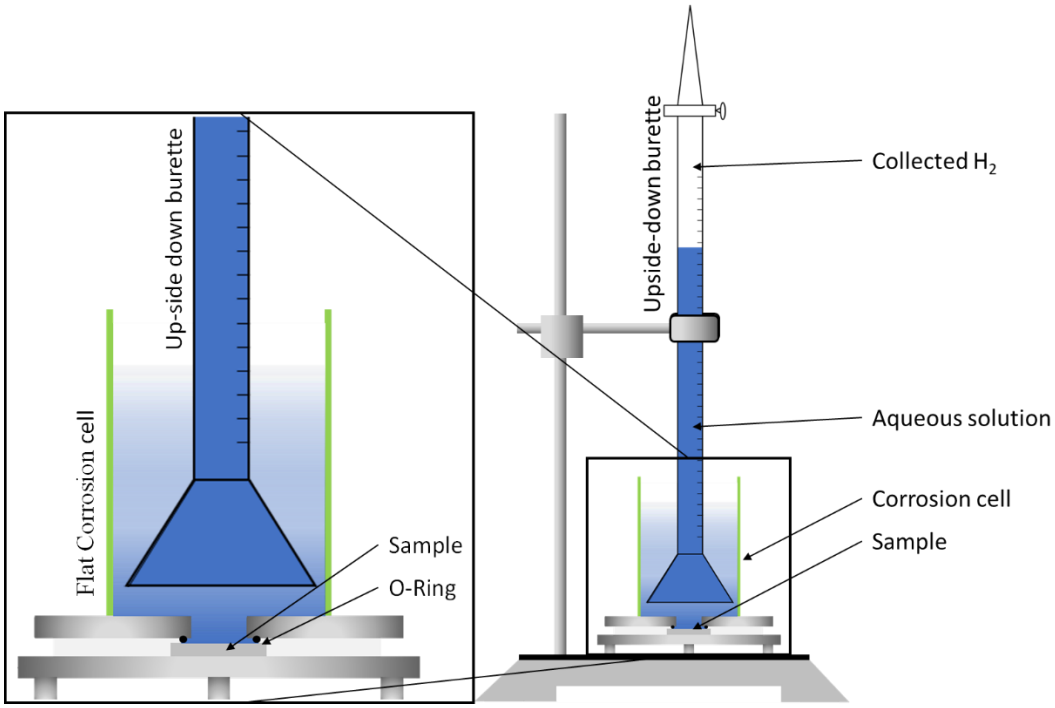

Figure 29. Schematic representation of the experimental setup for the measure of hydrogen evolution rates.

3.5.2 Potentiodynamic polarisation test

The potentiodynamic polarisation (PDP) measurements or polarisation tests are one of the most standard ones owing to their simplicity and reproducibility. In polarisation tests, after the open circuit potential or OCP is stable, the current response is measured by sweeping the potential at a constant speed. The scan ratio should be as slow as possible to obtain a near–to–stationary state [205]. Conventionally, a simple potential sweep from negative to positive values is performed, but different procedures such as cyclic polarisation can be followed. The following electrochemical parameters can be calculated from the polarisation curves by applying the Tafel intersection procedure: polarisation resistance (Rp), current density (i_{corr}) and corrosion and pitting potentials (E_{corr} and E_{pit}).

In this work, PDP measurements were performed in naturally aerated 0.5 wt.% NaCl solution at room temperature by using a computer–controlled potentiostat (GillAC, ACM Instruments). A three–electrode cell with a graphite counter–electrode and a silver–silver chloride 3M KCl reference electrode was used (Figure 30). In view of the great complexity of the reactions taking place during the magnesium corrosion process and on the assumption that the sweep rate is not slow enough to enable equilibrium, it is recommended by some authors [57] to perform the potential sweep in two steps: starting from the OCP towards more negative values for the cathodic branch and from the OCP towards more positive values for the anodic branch. Both branches were obtained after 1 h of immersion (during which OCP data were collected) with a scan rate of 0.3 mV s^{-1} and a current density limit of 5 mA cm^{-2}. The cathodic branch was measured from OCP to –100 mV_{OCP}, whereas the anodic branch was acquired from OCP to +3000 $mV_{OCP.}$

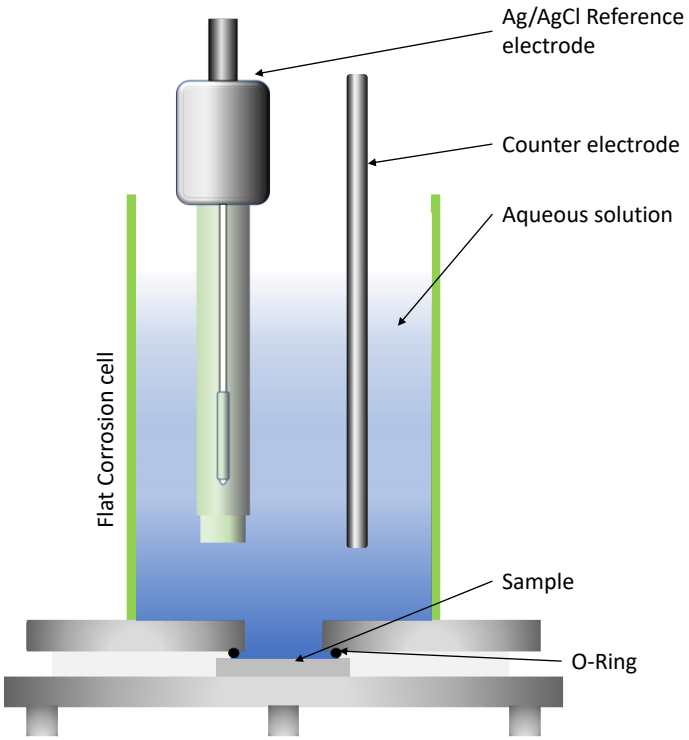

Figure 30. Set up used for the electrochemical tests.

3.5.3 Electrochemical impedance spectroscopy

EIS is an electrochemical technique widely used for studying electrochemical systems. This technique is based on the perturbation of the sample with a sinusoidal and small amplitude voltage signal in a wide range of frequencies. The analysis of the different frequency provides information on the mechanism and reaction kinetics at the metal/electrolyte interface. In opposition to polarisation curves, EIS is considered a non–destructive experiment that provides more realistic information since the system is kept close to equilibrium. Additionally, the frequency scan allows to distinguish between different processes such as diffusion–limited and electrochemical reactions.

In the present work, EIS measurements were performed using a GillAC (ACM Instruments) and a three–electrode cell as shown in Figure 30. Sodium chloride aqueous solutions of different concentrations were employed depending on the studied system. A 10 mV amplitude sinusoidal perturbation and a scan in the 10 kHz–0.01 Hz frequency range was applied after different immersion times. The analysis of the results was carried on by using Zview software and maintaining chi–squared values in the range between 0.001 and 0.0001.

3.5.4 Scanning Vibrating Electrode Technique (SVET)

The scanning vibrating electrode technique (SVET) was used to measure the local current density at the site of the artificial defects. Defects were produced with a scratcher instrument (CSM Revetest) with a 200 µm Rockwell C diamond indenter by applying a constant load of 4 N, which gives the possibility to prepare reproducible scratches with a controlled depth of ~5 µm and 1 mm length. A commercial SVET manufactured by Applicable Electronics™ and controlled with the software provided by Science Wares™ was used. The assembly uses an insulated microelectrode of Platinum–iridium manufactured by Microprobe™ with a Platinum black deposited on its tip of ø = ~20 µm as a vibrating electrode. The microelectrode was placed at 150 µm above the surface sample. The probe vibration frequency normal to the sample was 67 Hz and the peak–to–peak vibration amplitude was approximately 40 µm. Before the experiments, the microelectrode was calibrated in the working electrolyte following a common procedure described in detail elsewhere [206]. All the experiments were carried out in 0.05M NaCl solution. The area of interest surrounding the defect was masked using a thin layer of sealing lacquer (Electrolube Bloc Lube Red). SVET maps of, on average, 2 × 2.5 mm were recorded on grid of 31 × 31 points.

3.5.5 Immersion tests with scribed specimens

The long–term corrosion performance and self–healing capability of the developed coating systems were evaluated by immersion tests with scratched samples (the depth of the scratch was the necessary to expose the underlying substrate). Scribed samples were exposed to 0.05 M NaCl solution for 48 h. Specimens were manually scribed with a standard zirconia tip across the sample surface (a cross–shaped scribe, with a width of 0.1 mm and a length of 1 cm; the depth of the scribe was larger than the coating thickness and reached the underlying substrate).

For hybrid PEO/Sol–gel coatings, 1 cm–long scratches were produced with a standardized tool (ZEHTNER, ZVL–2190). Specimens were then immersed in a 0.5 wt.% NaCl solution and characterized after 14 days of immersion by SEM. The evolution of the corrosion process was also monitored by macroscopic photographs at different stages of the immersion test.

3.5.6 Neutral salt spray test

A CCI/CCM–MX cabinet was used to perform the neutral salt spray test (NSST). NSST was performed on painted specimens on which a 1 cm–long scratch defect was made with a

ZEHNTNER ZVL 2190 tool. According to ASTM B117 [207] the salt spray atmosphere was created using a 5 wt.% NaCl aqueous solution. The pH was kept in the range of 6.5 to 7.2 and the temperature at 35 ºC. The specimens were slightly inclined (~15º from the vertical) and exposed to the salt spray for up to 7 days. To remove the solid salt deposits, the samples were rinsed with water at ~38 °C and air dried. Classification numbers were defined under the ASTM D 1654–92 [208] by evaluating the area affected by corrosion.

4 Results and Discussion

Chapter 1

LDH conversion films for active protection of AZ31 Mg alloy

4.1 Chapter 1. Context and aim

The first chapter focuses on the chemical modification of the surface of the AZ31 Mg alloy by means of conversion coating systems consisting of layered double hydroxides (LDHs). As it was mentioned in the *Introduction*, LDHs coatings are emerging as an environmentally friendly approach for corrosion protection of metallic materials. In the particular case of Mg alloys, LDH coatings are commonly based on the Mg–Al system. Despite of the potential of LDHs to serve as nanocarriers for corrosion inhibitors the number of studies on this topic is still quite limited. On this basis, Chapter 1 focuses on the study of new LDH coatings produced by co–precipitation synthesis and incorporation of corrosion inhibitors by immersion post–treatment. The morphology, corrosion behaviour, self–healing ability and paintability of the developed systems are evaluated in a systematic way for a better understanding of their anticorrosion mechanism. The graphical abstract of Chapter 1 is shown in Figure 31.

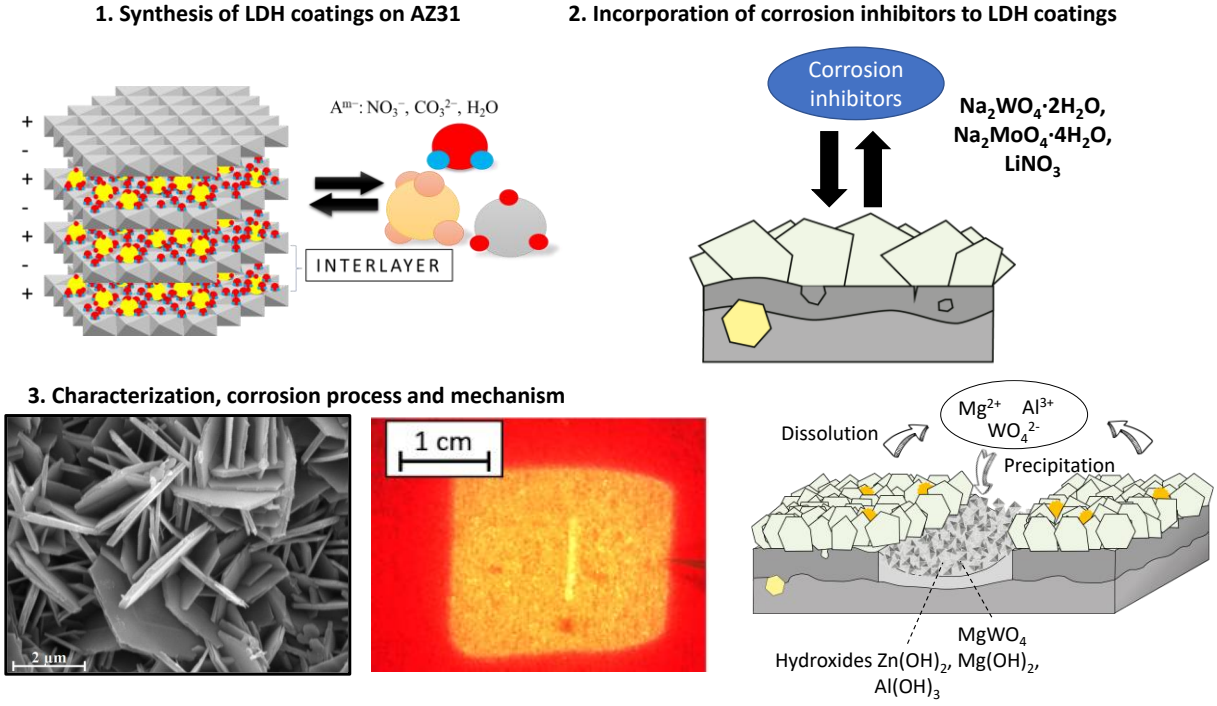

Figure 31. Chapter 1 graphical abstract: Study of LDH coatings on AZ31 without and with corrosion inhibitors.

4.1.1 Introduction

Conversion coatings are one of the most cost–effective approaches for preventing the degradation of metallic alloys [79]. LDH conversion coatings can improve the corrosion performance by up to 4 orders of magnitude in terms of corrosion current density and impedance modulus. Mg–Al LDH (other systems include Mg–Fe, Zn–Al and Li–Al) is the focus of most studies. LDH coatings are usually synthesised by hydrothermal route, although steam coating, two–step, and urea hydrolysis have also been used.

However, there is a lack of knowledge regarding intercalation of corrosion inhibitors species and, up to date, only a few the studies address this issue [145, 147, 150, 151]. Zeng *et al.* [145] synthesized a molybdate intercalated hydrotalcite coating with nanosized lamellar structures that, according to FTIR measurements, released MoO_4^{2-} which acted as anodic inhibitor. Chen *et al.* [147] found that Mg–Al–ASP–LDHs had better corrosion resistance than Mg–Al–NO_3–LDHs owing to the corrosion inhibition of aspartic acid (ASP) ions and the larger specific surface area to capture Cl^-. Anjum *et al.* [150] studied the effect of intercalation of 8–hydroxyquinoline (8HQ) corrosion inhibitor into Mg–Al based LDH coating. The enhancement of corrosion resistance was attributed to Cl^- and HQ^- ion exchange and the redeposition of $Mg(HQ)_2$. Tang *et al.* [151] intercalated Cl^-, VO_4^{3-}, PO_4^{3-}, and MoO_4^{2-}. The results showed that the corrosion resistance decreased in the following order: Zn–Al–VO_4^{3-} > Zn–Al–MoO_4^{2-} > Zn–Al–PO_4^{3-} > Zn–Al–Cl^- > Zn–Al–NO_3^-. The better corrosion behaviour of Zn–Al–VO_4^{3-}–LDHs was attributed to its greater ion–exchange ability.

In this section, new Zn–Al and Li–Al LDH coatings with incorporated inhibitors (W–, Mo– and Li–based species) are produced on AZ31 Mg alloy. After screening and ranking the coatings by electrochemical impedance spectroscopy (EIS), the best LDH coatings are investigated by X–ray photoelectron spectroscopy (XPS), X–ray diffraction (XRD), contact angle measurements and Fourier–transform infrared spectroscopy (FTIR). The corrosion performance is further evaluated by scanning vibrating electrode technique (SVET).

4.1.2 Results and Discussion

4.1.2.1 Inhibitor Screening

Two different LDH coatings (Zn–Al and Li–Al) were synthesized on the AZ31 alloy. The functionalization of the LDH layers with inhibitors was conducted by immersion post–

treatments in inhibitors–containing solutions (details are explained in section 3.3.3). Table 16 summarises the main information about the coatings formation conditions along with their labelling, which is based on the cations used to form the LDH and the inhibitor used in the post–treatment (when applicable).

Table 16. LDH coating and inhibitor post–treatment bath conditions.

LDH Coating	LDH precursors	Synthesis conditions	Post–treatment Solution	Conditions
Zn–Al LDH	$Zn(NO_3)_2{\cdot}6H_2O$ 0.25M $Al(NO_3)_3{\cdot}9H_2O$ 0.125 M Na_2CO_3 0.0625 M	125 ºC pH 10 24 h	–	–
Zn–Al LDH Li	$Zn(NO_3)_2{\cdot}6H_2O$ 0.25M $Al(NO_3)_3{\cdot}9H_2O$ 0.125 M Na_2CO_3 0.0625 M	125 ºC pH 10 24 h	$LiNO_3$ 0.1 M	pH 10 45 ºC 2 h
Zn–Al LDH Mo	$Zn(NO_3)_2{\cdot}6H_2O$ 0.25M $Al(NO_3)_3{\cdot}9H_2O$ 0.125 M Na_2CO_3 0.0625 M	125 ºC pH 10 24 h	$Na_2MoO_4{\cdot}4H_2O$ 0.1 M	pH 10 45 ºC 2 h
Zn–Al LDH W	$Zn(NO_3)_2{\cdot}6H_2O$ 0.25M $Al(NO_3)_3{\cdot}9H_2O$ 0.125 M Na_2CO_3 0.0625 M	125 ºC pH 10 24 h	Na_2WO_4 0.1 M	pH 10 45 ºC 2 h
Li–Al LDH	$LiNO_3$ 0.0625 M $Al(NO_3)_3{\cdot}9H_2O$ 0.125 M Na_2CO_3 0.0625 M	125 ºC pH 10 24 h	–	–
Li–Al LDH Li	$LiNO_3$ 0.0625 M $Al(NO_3)_3{\cdot}9H_2O$ 0.125 M Na_2CO_3 0.0625 M	125 ºC pH 10 24 h	$LiNO_3$ 0.1 M	pH 10 45 ºC 2 h
Li–Al LDH Mo	$LiNO_3$ 0.0625 M $Al(NO_3)_3{\cdot}9H_2O$ 0.125 M Na_2CO_3 0.0625 M	125 oC pH 10 24 h	$Na_2MoO_4{\cdot}4H_2O$ 0.1 M	pH 10 45 ºC 2 h
Li–Al LDH W	$LiNO_3$ 0.0625 M $Al(NO_3)_3{\cdot}9H_2O$ 0.125 M Na_2CO_3 0.0625 M	125 ºC pH 10 24 h	Na_2WO_4 0.1 M	pH 10 45 ºC 2 h

Eight different LDH systems, with and without inhibitor, were screened by EIS testing following 1 h of immersion in 3.5 wt.% NaCl solution (Figure 32). It is important to note that the comparison of the impedance modulus (|Z|) at low frequency response (0.01 Hz) is a common tool for ranking the corrosion performance of coatings [175], although it has some limitations as it does not always match the corrosion performance obtained by other methods such as salt spray testing.

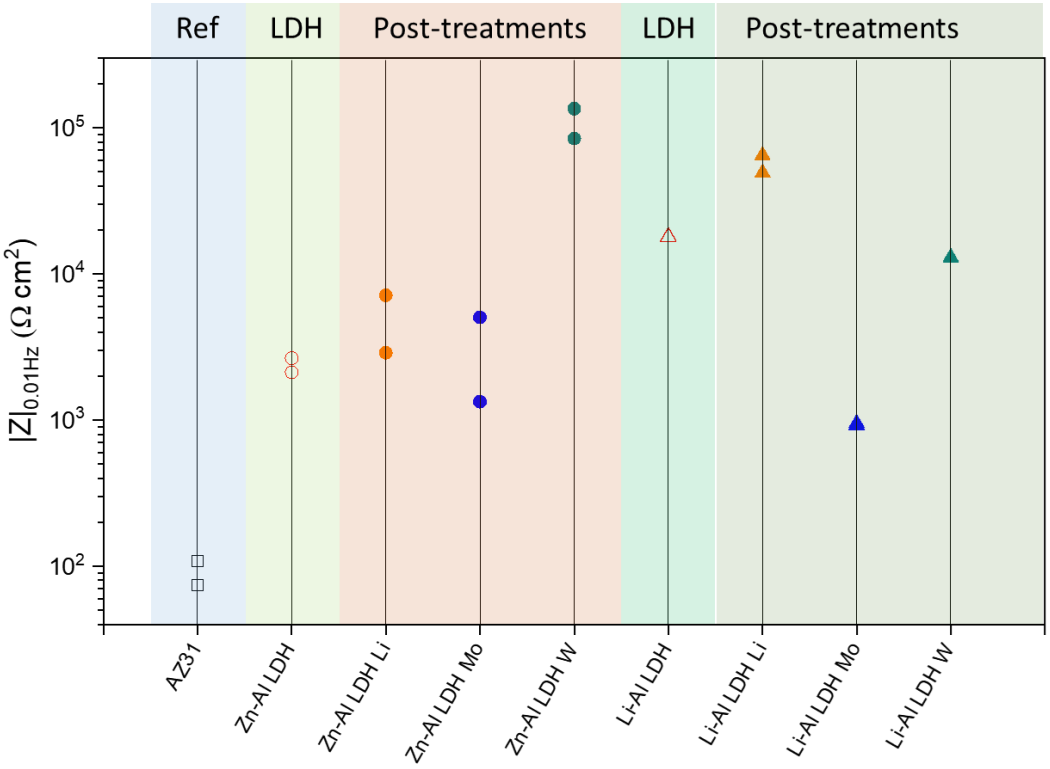

Figure 32. Scatter diagram of impedance modulus at 0.01 Hz for the AZ31 alloy with and without LDH coatings. Filled symbols correspond to the specimens loaded with corrosion inhibitors. Note that each system is measured twice, although some points overlap and only one symbol is observed.

Compared with the bare alloy, Zn–Al and Li–Al LDH coatings increase the impedance modulus by one and two orders of magnitude, respectively. Loading of Li–, Mo– and W–based corrosion inhibitors improved the corrosion resistance of Zn–Al LDH, with sodium tungstate yielding the highest impedance values ($|Z|_{0.01Hz}$ ~10^5 Ω cm^2). As for the Li–Al LDH system, only the Li–based inhibitor increased the impedance response ($|Z|_{0.01Hz}$ ~6×10^4 Ω cm^2).

Zn–Al LDH W and Li–Al LDH–Li systems were selected for further evaluation based on this initial corrosion screening. A quick comparison with the values reported in literature [139, 142, 147-151, 209-213] reveals that the selected systems are among the best in terms of low frequency impedance response. In the following sections, inhibitor–free LDH systems are also included for comparison.

4.1.2.2 Coating Morphology and Composition

Figure 33 shows the SEM characterization (plan view and cross–sections) of LDHs layers without inhibitors. Plan–view micrographs of Zn–Al and Li–Al LDHs reveal a flake–like morphology. Both coatings cover the entire surface and show LDH islands that are larger in the

Zn–Al system. The agglomeration of flakes that form the islands is attributed here to the increased amounts of available cations (i.e. Mg^{2+}, Al^{3+}), preferentially at the location of Al–Mn inclusions. Enhanced dissolution is expected to occur in these regions due to two phenomena: i) micro–galvanic corrosion between inclusions and the surrounding matrix; and ii) selective Al dissolution within the Al–Mn inclusions due to the highly alkaline conditions (pH 10) during treatment [214]. Figure 33f shows an example of partially dissolved Al–Mn inclusions surrounded by the thicker coating material.

EDS area and point analysis labelled in Figure 33 are shown in Table 17, along with the EDS results obtained for the bare substrate (not shown in Figure 33). Both coatings show increased Al content (6–8 at.%) in comparison with the AZ31 alloy (~2.4 at.%). This is consistent with the incorporation of this element into the LDH structure. Similarly, the Zn–Al LDH shows a higher amount of Zn on its surface (~2.9 at.%) compared with the as–received alloy (~0.4 at.%). Li was not observed in the Li–Al system due to the difficulties in detecting this element by EDS. Note the high amounts of Mn and Fe and the low Al/Mn ratio in point 2 in Figure 33f, which evidences the preferential dissolution of Al in the Al–Mn inclusion. It is worth mentioning that not all the islands show the presence of Al–Mn inclusions (e.g. point 2, Figure 33a).

Micrographs at higher magnification reveal that the flakes are mostly oriented perpendicularly to the surface, indicating a faster growth rate in the direction of the bulk solution (Figures 33c and 33g). This is typically observed in LDHs systems and is the result of their anisotropy (i.e. flakes growth in the ab–direction faster than in the c–direction) and the hampered growth of flakes oriented horizontally to the surface [213].

Flakes in the Zn–Al LDH are thicker and larger than those in the Li–Al system. Image analysis measurements (obtained from planar views micrographs) yielded thickness and surface area values of (300 ± 50) nm/(31.6 ± 0.5) μm^2 and (5 ± 3) nm/(560 ± 50) nm^2, for the coating flakes, respectively. Considering that similar conditions were used for both LDH treatments, it is evident that the differences in size are related to the characteristics of Zn^{2+} and Li^{+} cations.

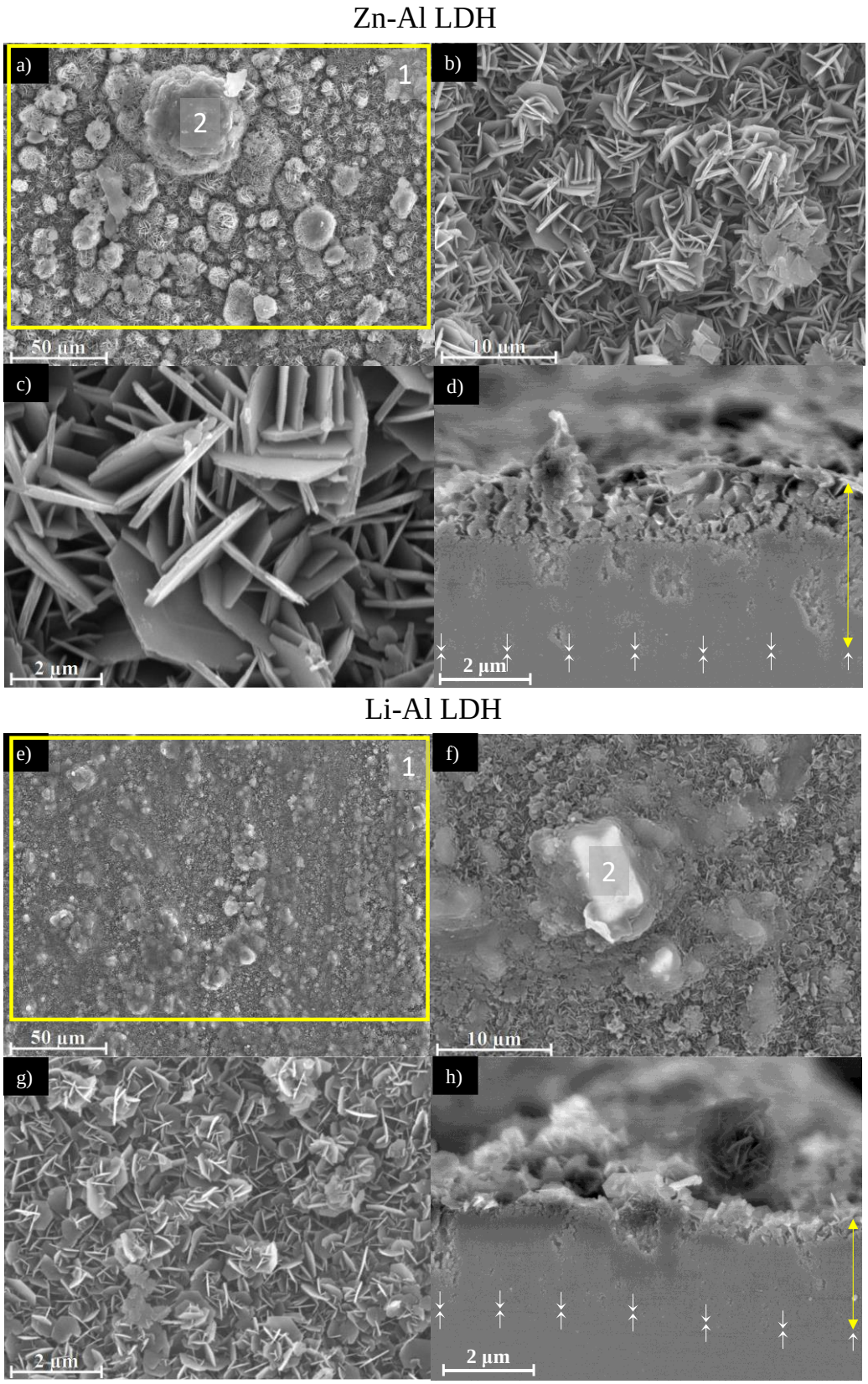

Figure 33. Planar view and cross sections micrographs of Zn–Al LDH (a,b,c,d) and Li–Al LDH (e,f,g,h) coatings. Yellow arrows mark the overall thickness of the LDH coatings and the interface between the coating and the bulk material is indicated by white arrows. The EDS analysis results are collected in Table 17.

Cross section examination of the LDH coatings shows a bi–layer structure composed of an outer part with loose flakes (~30 % of the layer) and a denser inner layer (Figure 33d and 33h). The overall LDH conversion layer is thicker when Zn cations are used (5.2 ± 0.5 µm) in comparison with the Li–based solution (3.8 ± 0.4 µm). This bi–layer structure is often seen in LDH conversion coatings [145, 149, 215] and is related to differences in flake–size and crystallinity of the coating material. For instance, Lin *et al.* [211] reported that the inner layer was less crystalline than the outer one in a Mg–Fe–LDH coating formed on a 99.9 % Mg. It is suggested here that the interface between the two layers roughly corresponds to the original surface as it shows a very flat profile (further studies are needed to confirm this).

Table 17. EDS quantification in at.% on AZ31, Zn–Al LDH (Figure 33a), Li–Al LDH (Figure 33e,g), Zn–Al LDH W (Figure 34a) and Li–Al LDH Li (Figure 34d) in the specified areas.

Sample	EDS	O	Al	Mg	Zn	Mn	Fe	W	Na
AZ31	Matrix	–	2.4	96.9	0.4	0.2	0.1	–	–
	Al–Mn	–	45.4	–	–	52.7	1.9	–	–
Zn–Al LDH	1 (area)	57.1	8.2	31.9	2.8	–	–	–	–
	2 (point)	55.2	6.1	36.2	2.5	–	–	–	–
Li–Al LDH	1 (area)	54.5	7.5	37.0	1.0	–	–	–	–
	2 (point)	26.1	6.7	2.5	1.6	61.6	1.5	–	
Zn–Al LDH W	1 (area)	41.4	2.9	53.6	1.2	0.2	–	0.1	0.6
	2 (point)	73.4	1.6	23.5	0.5	–	–	0.5	0.5
Li–Al LDH Li	area	76.2	1.9	21.9	–	–	–	–	–

Figure 34 shows the SEM characterization of the studied LDH systems after post–treatment with W– and Li–based inhibitors. The Zn–Al LDH–W coating shows a smoother morphology than the Zn–Al LDH coating, although some small islands are still scattered over the surface (Figure 34a). The EDS analysis shows that these islands contain slightly more W (~0.5 at.%) than the surrounding coating material (~0.1 at.%). Some Na contamination is also present in the coating (~0.6 at.%) (Table 17). According to the Pourbaix diagram of W (298 K, $[WO_4^{2-}]= 10^{-6}$ mol L^{-1}) [216], tungstates are soluble in alkaline aqueous solutions. Therefore, W–rich precipitates such as WO_3 are not expected to form during post–treatment at pH 10. The precipitation of $Al_2(WO_4)_3$ can also be ruled out as the amount of Al in the deposits is quite small (0.2 at.%). Therefore, the presence of W in the coating is most likely due to the incorporation of WO_4^{2-} ion into the LDH structure or to the precipitation of $MgWO_4$ (pK_α= 6.46). Li–rich deposits or precipitates, if any, were not detected in the Li–Al LDH Li coating. The surface also appeared smoother than the inhibitor–free coating (Figure 34 d, e compared to Figure 33e,f,g).

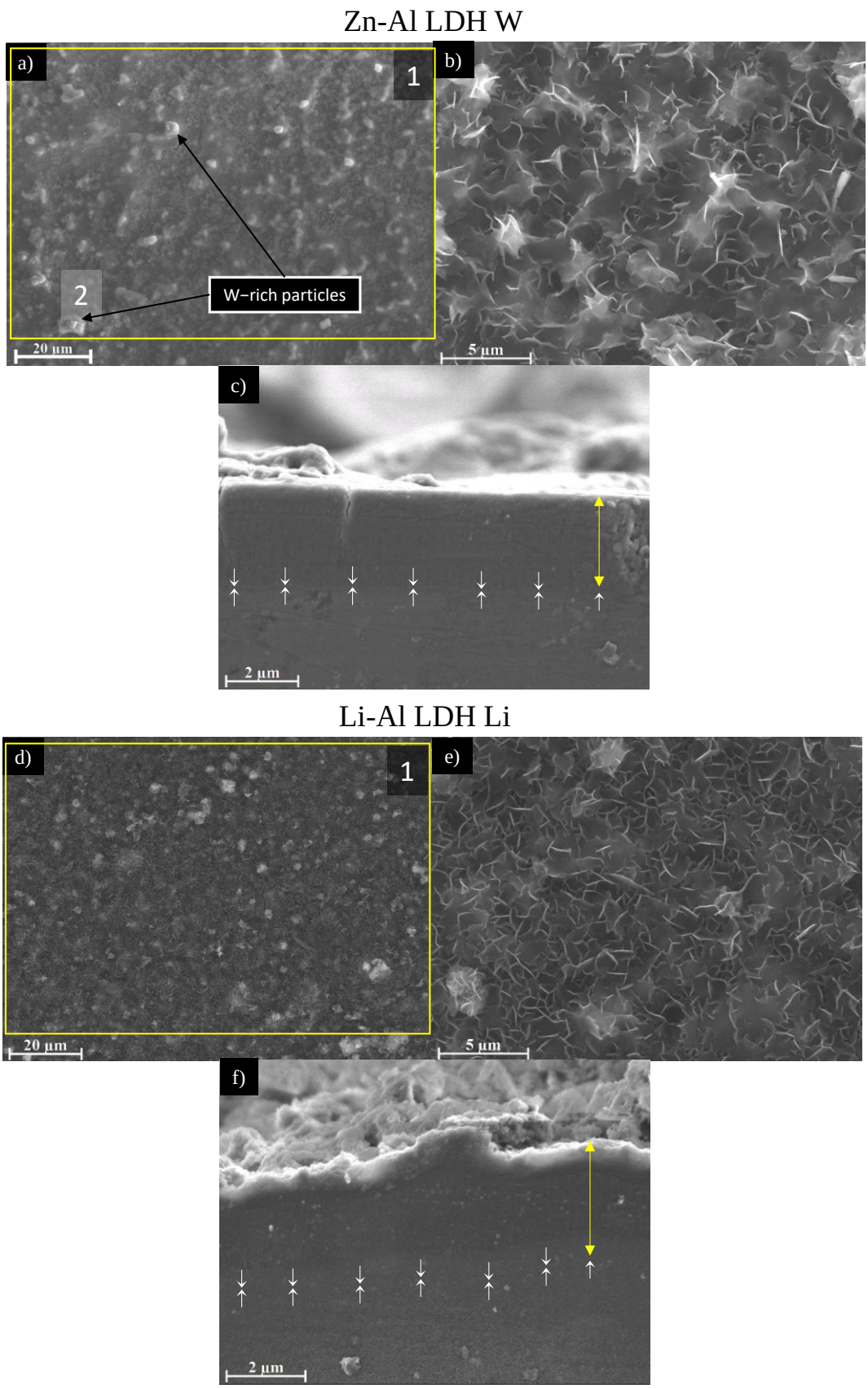

Figure 34. Plan view and cross section SEM micrographs after post–treatment. Zn–Al LDH plan–view (a,b) and cross–view (c). Li–Al LDH plan–view (d,e) and cross–view (f). The EDS analysis results are collected in Table 17.

High magnification plan views reveal that, after post–treatment with inhibitors, LDH flakes are smaller and are not very well–defined (Figures 34b,e). This is attributed to the partial dissolution of the outer layer, as evidenced by the cross sections (Figures 34c,f). During post–treatment at pH 10 and under the non–saturated conditions LDH flakes gradually dissolve, particularly those in the outer layer as they are loosely bonded to the surface. Note that some of the coating material from the dense inner layers was also lost during post–treatment, but the thickness loss can be considered negligible (<0.5 μm). After post–treatment, coating thicknesses were ~2.7 and ~2.5 μm for the Zn–Al LDH W and Li–Al LDH Li, respectively.

Figure 35 depicts the grazing angle X–ray diffraction (XRD) pattern for the studied coatings before and after post–treatment. All the coatings show the characteristic peaks of hydrotalcite–like LDH structure with a rhombohedral unit cell and R–3m space group [217]. $Mg(OH)_2$ was also identified, which is a common subproduct formed during the synthesis of LDH in alkaline conditions (pH>10.8) [218]. Despite using grazing angle for the measurement, and due to the low thickness of the studied coatings, peaks from the α–Mg phase in the substrate are also identified at 34, 36 and 47º.

Table 18 shows the basal plane spacing d calculated using Bragg's equation and the unit cell parameters a and c ($a=2d_{110}$; $c=3d_{003}$ [219]) of LDH structures calculated from (003), (006) and (110) reflections at ~11°, ~18.5° and 62°, respectively. The inhibitor–free structures present a d_{003} value of 0.8098 nm and 0.8058 nm, for Zn–Al LDH and Li–Al LDH, respectively, which are consistent with hydrotalcite–like systems intercalated with NO_3^- anions [219]. The shoulder peaks identified for (003) and (006) reflexions at slightly higher 2–theta values suggest the partial intercalation of CO_3^{2-}/OH^- ions between the LDH layers [220]. The d_{003} values correspond to the basal spacing of two consecutive hydrotalcite–like layers, therefore, it is possible to calculate the intergallery height by subtracting the basal spacing of the cationic layer (brucite–like, 4.8 Å) (Table 18). The intergallery height of both systems is comparable, being 3.298 Å and 3.258 Å for Zn–Al LDH and Li–Al LDH, respectively.

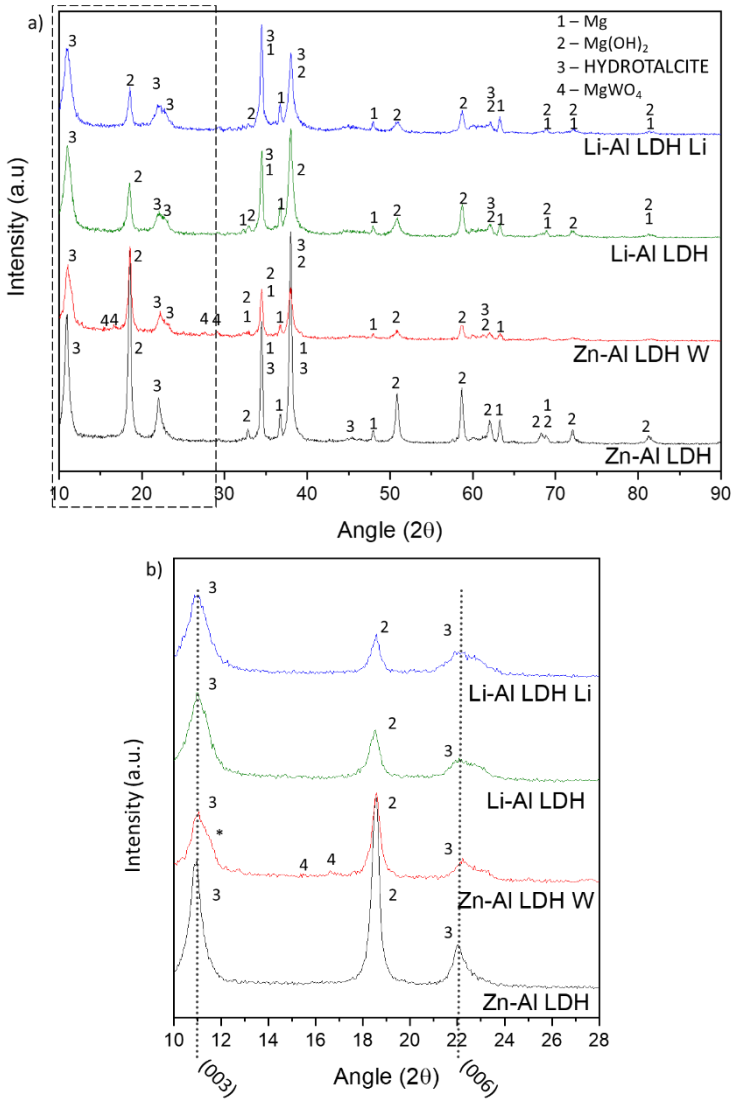

Figure 35. (a) XRD patterns for the studied LDH coatings. (b) Region of interest from 10 to 28º.

Table 18. XRD peak indexing results for the (003) and (006) planes of the LDH structures.

Sample	a (nm)	c (nm)	d (nm)	Intergallery height (nm)
Zn–Al LDH	0.2989	0.2429	0.8098	0.3298
Zn–Al LDH W	0.2991	0.2415	0.8051	0.3251
Li–Al LDH	0.2987	0.2417	0.8058	0.3258
Li–Al LDH Li	0.2994	0.2409	0.8029	0.3229

After the post–treatment, the characteristic LDH reflections (003) and (006) of both LDH systems show a lower intensity and remain at a relatively invariable 2θ (Figure 35b). The lower intensity is related to the removal of the external loose layer of the coating during the post–treatment. It is worth mentioning that the shoulder peak identified for (003) reflexion at slightly higher 2–theta values became clearer in the case of Zn–Al LDH–W (labelled * in Figure 35b)

which is probably related to a significant intercalation of CO_3^{2-}/OH^- ions, with smaller size compared to NO_3^-, between the LDH layers during the post–treatment.

The invariable reflection 2θ suggests that the corrosion inhibitors were not incorporated within the intergallery space. Therefore, the basal plane spacing, d, and the unit cell parameter c remained constant after the treatment. The ab–axis values also remained constant, which indicates that the inhibitors did not modify the cationic hydroxide layers. In Zn–Al LDH–W, W–rich particles in the form of $MgWO_4$ were detected at 12, 16.5 and 29º and observed on the SEM micrographs (Figure 34). This confirms their incorporation into the LDH system. Considering the low solubility of $MgWO_4$, these are likely to be physically adsorbed on the LDH's most external layers. The inhibitor Li^+ in the Li–Al LDH Li system is not likely to be incorporated between the LDH layers due to its positive charge. Li^+ is most probably located at the most external layers (top and bottom) of the LDH systems creating an electric double layer with the NO_3^- ions which remain attracted by electrostatic interactions to the LDH layers.

The FTIR spectra of the different LDH coatings with and without intercalated inhibitors are shown in Figure 36. The intense band located at 3683 cm^{-1} corresponds to O–H stretching mode of hydroxyl groups in the LDH layers (Zn–OH, Mg–OH, and Al–OH) [221]. The bands at 3650–3170 cm^{-1} and 1726–1505 cm^{-1} are assigned to tension and bending vibrations, respectively, of the O–H bonds of water molecules intercalated between the LDH layers. The bands at 1690–1480, 760 and 578 cm^{-1} correspond to the asymmetric stretching, out–of–plane, symmetric and antisymmetric deformation modes of NO_3^- ions intercalated between the LDH layers, respectively [220]. The band at 1690–1480 cm^{-1} could also be correlated to the symmetric stretching vibrations of O–C–O bond of CO_3^{2-} anions. The bands at lower wavenumbers (761–546 cm^{-1}) correspond to the stretching vibrations of M–O (M: Al, Zn) of the LDH [165]. The bands between 3000–2775 cm^{-1} correspond to C–H vibrations associated with the presence of superficial contamination in the form of hydrocarbons.

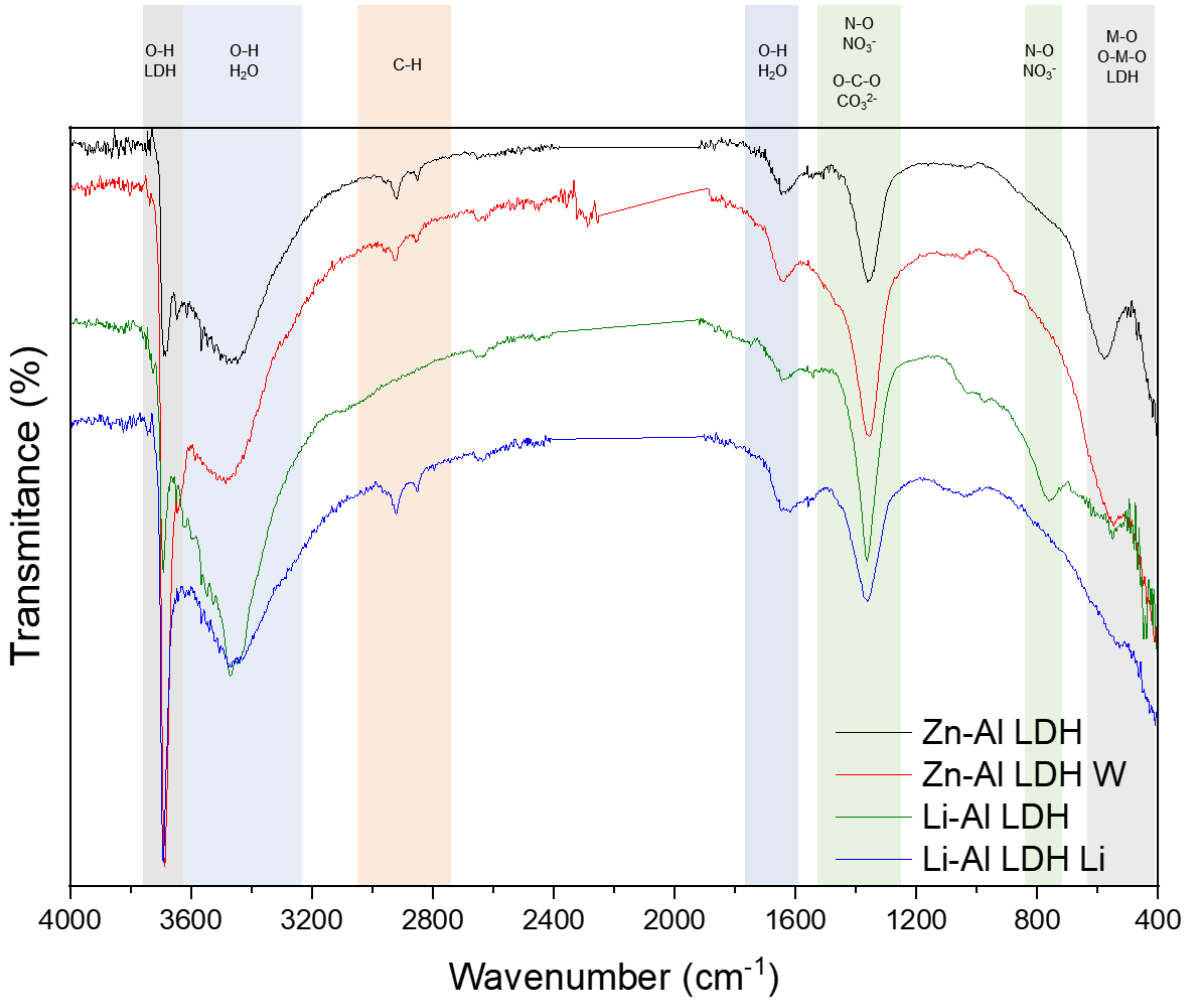

Figure 36. FTIR spectra of Zn–Al LDH, Zn–Al LDH W, Li–Al LDH and Li–Al LDH Li coatings on AZ31 Mg alloy.

XPS analysis (Figure 37) was carried out to obtain quantitative compositional information of the studied materials (Table 19). Figures 37a and 37b show the XPS spectra of the LDH systems before and after 10 min of argon sputtering, respectively. Figure 37c shows the high–resolution XPS spectra of elements Zn, W and Li after sputtering.

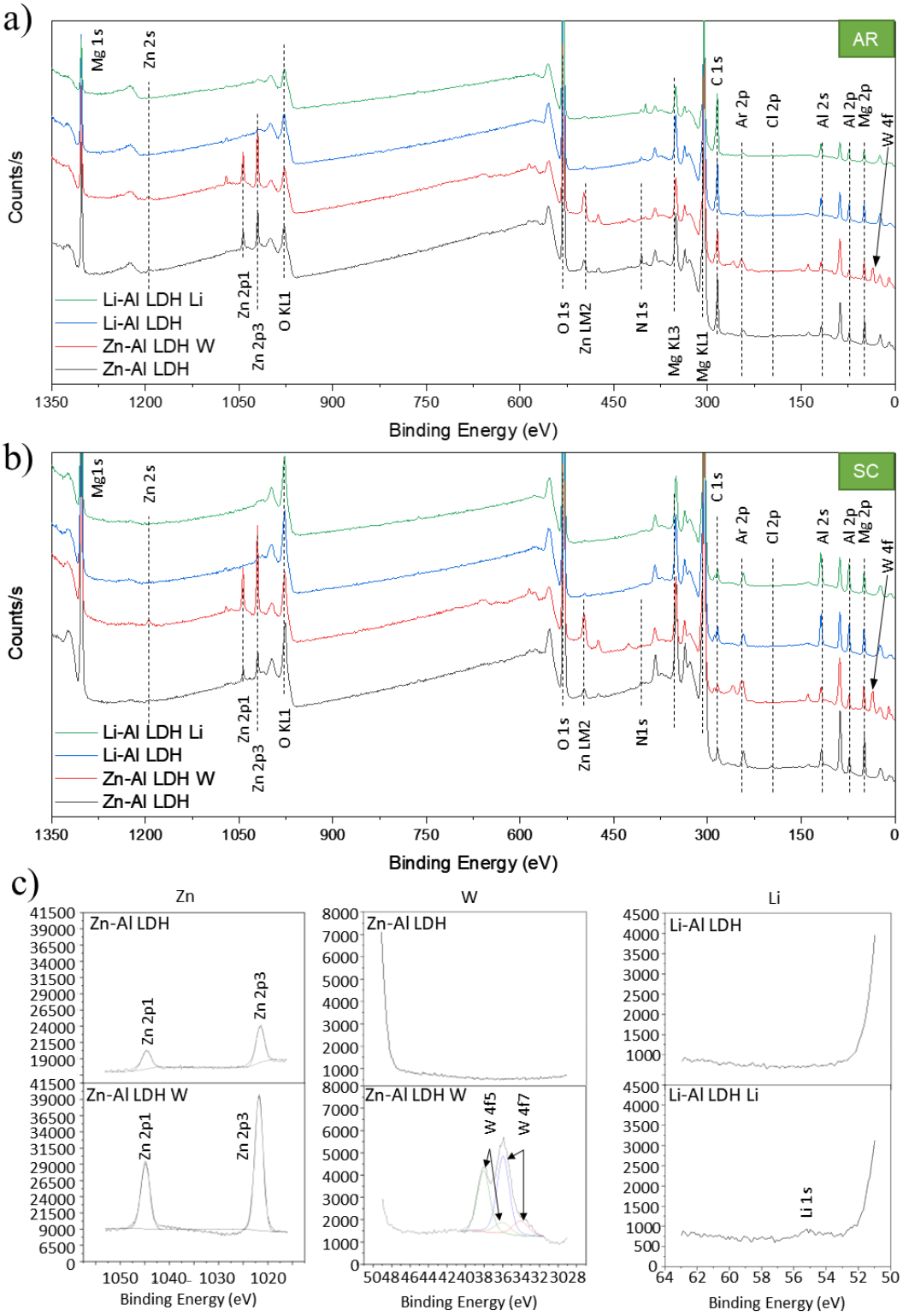

Figure 37. XPS spectra of the studied specimens (a) before (as received AR) and (b) after 10 min of argon sputtering (sputtering cleaning SC). (c) High–resolution Zn, W and Li spectra obtained after 10 min of argon sputtering of the LDH coatings on AZ31.

The most superficial layer for all the studied materials in the as–received condition shows varying amounts of adventitious C. The C 1s signals at 285 and 286 eV correspond to long

chain hydrocarbons (C–C, C–H) which were also evident in the FTIR analysis. After sputtering, the signals at 285 and 286 eV diminished and a small peak at ~290 eV, corresponding to carbonate ions, appeared (Figure 37b). This suggests the intercalation of CO_3^{2-} between the LDH galleries, as evidenced by shift of the (003) peak in XRD. The intensity of this signal increases for the deeper layers of the coating as the superficial contamination is sputtered away. In the as–received condition, only one O 1s signal is identified at ~532 eV which is assigned to O atom in metal–hydroxide species (or hydroxyl groups –OH) [222]. Another confirmation of the presence of magnesium hydroxides is the Auger parameters values of 997.23 eV to 997.47 eV (shown in Table 19). This parameter has been calculated by the difference between the kinetic energy (KE) of the Mg KLL Auger peak and the KE of the Mg 1s peak [223].

Table 19. Calculated Auger parameter for the studied coatings.

Auger Parameter Calculation			
Sample non–sputtered	Mg KLL (KE)	Mg1s (KE)	Auger Parameter*
Zn–Al LDH	1180.38	183.15	997.23
Zn–Al LDH W	1180.39	182.92	997.47
Li–Al LDH	1180.27	182.88	997.34
Li–Al LDH Li	1180.24	182.87	997.37

$$*\alpha = KE\ (Mg\ KLL) - KE\ (Mg\ 1s) \qquad \text{[Eq. 8]}$$

After sputtering, the Al 2p peak at ~74 eV is possibly related to the bonding energy of $Al(OH)_3$, but MgO peak was not observed (typically at ~1.5 eV of Mg 1s and Mg 2s binding energies [223, 224]). Zn is present in Zn–Al LDH samples; in the Li–Al LDH system, small amounts of Zn were also detected but disappeared after sputtering, suggesting superficial contamination. The twin peaks at ~1021 eV and ~1044 eV are assigned to Zn $2p_{3/2}$ and Zn $2p_{1/2}$ respectively (Figure 37c), suggesting that Zn is present in the LDH in the divalent oxidation state [225]. In the case of Zn–Al LDH W system, a peak associated with tungsten is observed at 50 eV. In the as–received condition, the W 4f high resolution spectra show a split peak at 35.48 and 37.58 eV, while after sputtering (Figure 37c), two doublets $4f_{7/2}$–$4f_{5/2}$ are fitted at 34.08–35.94 eV and 35.99–38.04 eV, respectively, which are associated with a tungsten oxidation state +6, probably in the form of WO_4^{2-} [226, 227]. Li was identified in Li–Al LDH and Li–Al LDH–Li systems at 55.33 eV (Li 1s). Table 20 shows the quantitative chemical analysis before and after sputtering of the studied materials. In the as received condition, for both Zn–Al LDH and Li–Al LDH systems, N is identified, from the intercalation of NO_3^- anions between the LDH layers. It is worth mentioning that Zn–Al LDH W did not present N, suggesting the partial intercalation

of CO_3^{2-} /OH^- ions between the LDH layers. This is in agreement with the shoulder peaks identified for (003) and (006) reflexions at slightly higher 2–theta values. In the case of Li–Al LDH system, the N content increased after the post–treatment in $LiNO_3$, where further NO_3^- ions are incorporated into the structure. Although a characteristic peak of Li was identified, the detected amount was below the limit of quantification.

Table 20. XPS elemental composition (at.%) of studied coatings.

Sample	C	O	Mg	Al	Zn	W	Li	N	Cl	Na	Mg/Al Ratio	(Zn+Mg)/Al Ratio
Non sputtered surface												
Zn–Al LDH	22.2	51.5	13.4	6.62	1.6	–	–	3.9	0.8	–	2.02	2.27
Zn–Al LDH W	20.8	52.9	13.7	7.38	2.8	0.8	–	–	–	1.5	1.86	2.24
Li–Al LDH	22.4	53	11.3	11.6	0.1	–	–	1.2	–	0.6	0.98	0.98
Li–Al LDH Li	34	46.7	5.89	9.62	0.1	–	**	3.3	–	0.5	0.61	0.61
After 10 min of sputtering												
Zn–Al LDH	5.94	47.2	36.1	9.52	0.7	–	–	–	0.5	–	3.8	3.87
Zn–Al LDH W	5.73	50.8	29.4	8.96	3.3	1.1	–	–	–	0.7	3.28	3.65
Li–Al LDH	8.19	51.2	24.1	16.2	*	–	–	–	–	0.4	1.49	1.49
Li–Al LDH Li	6.93	52.2	21.8	19.7	*	–	**	–	–	–	1.11	1.11

**A very weak peak of Zn2p3/2 was observed (not quantified)*
***A very low peak in the high–resolution spectrum is observed for the Li–Al LDH–Li; values are not included in the elemental table composition for both cases.*

In the as received condition, the (Mg+Zn)/Al ratios are ~2.3 and ~1.0 for Zn–Al and Li–Al LDH, respectively. After sputtering, the ratios increase as the surface contamination is removed (~3.9 and ~1.5) for Zn–Al and Li–Al LDH, respectively. In both systems, the specimens containing corrosion inhibitors show a slightly lower ratio which could be associated with the selective dissolution of Mg during the immersion post–treatment, where the most superficial layer of the coating is removed.

4.1.2.3 Corrosion Test: Immersion test and SVET measurements

To evaluate the corrosion protection efficiency offered by the encapsulated corrosion inhibitors, the coatings were artificially scratched, and their electrochemical response was analysed by SVET up to 6 days of immersion in 0.05 M NaCl. Figure 38 shows the optical images of the artificial defects and the SVET maps at the same location for different immersion times.

For Zn–Al LDH, right after the immersion, two features were observed: the discolouration of the surface and blurring of the defect, making it indistinguishable from the intact coating. At this stage, the current density values remained relatively low (±10 $\mu A/cm^2$) and no H_2 bubbles

were formed. This behaviour continued after 2 and 6 days of immersion and the corrosion response at the location of the defect remained relatively unchanged. This behaviour can be explained by the partial dissolution of the LDH flakes and redeposition of the coating material at the location of the artificial defect. The specimen containing the corrosion inhibitor (Zn–Al LDH W) showed a similar trend. The defect became indistinguishable in the optical image and low currents in the range of ±10 $\mu A/cm^2$ were registered.

It is worth noticing that two cathodic spots were detected at the location of the scratch after 2 days of immersion, indicating electrochemical activity during the initial stages of immersion, although the current values were relatively small. Interestingly, after 6 days of immersion, these two spots disappeared. This could be related to two phenomena: (i) the dissolution–redeposition of the LDH coating material (some liberation of Zn^{2+} ions from the LDH structure may also occur, which are likely to precipitate in the form of $Zn(OH)_2$) and, (ii) the dissolution/redeposition of $MgWO_4$. In both cases, these insoluble deposits would isolate the exposed magnesium substrate from the aggressive media, thus restating partially the passive properties of the coating while preventing corrosion propagation.

In the case of the Li–Al LDH system, with and without corrosion inhibitor, a high anodic activity (50 $\mu A/cm^2$) is identified at the location of the defect from the beginning of the immersion test. This is accompanied by an intense generation of H_2 bubbles. Over time, corrosion progresses through the exposed substrate and several initiation points are also developed outside the scribed area. This suggests that the barrier properties of this system are lower [228]. This can be explained by the composition of the LDH cationic layers; it seems that the presence of Zn is a requirement for the precipitation of insoluble hydroxides to achieve the partial recovery of the defect. Therefore, although the Li–Al LDH system increases the overall barrier properties of the material, it does not provide the same level of active corrosion protection when compared to the W–containing system.

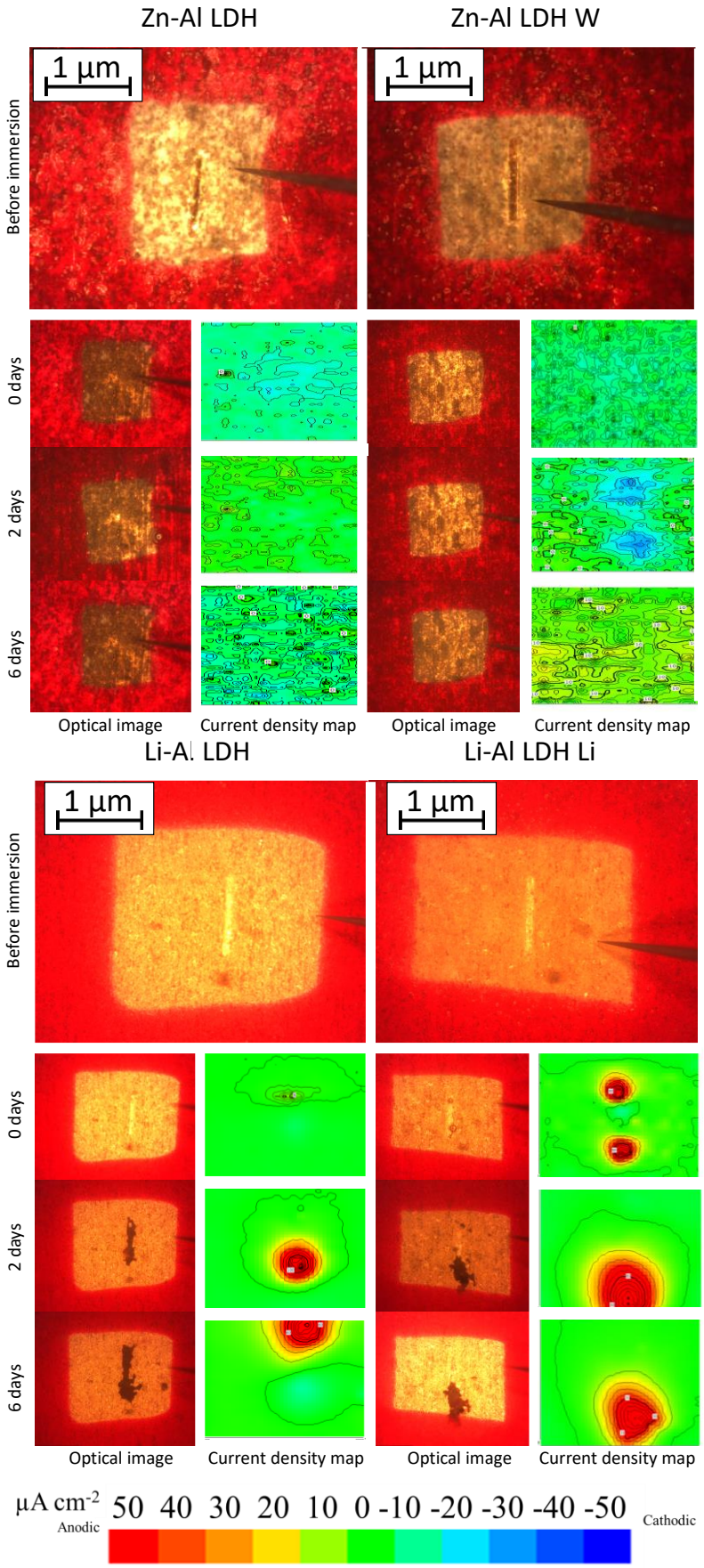

Figure 38. Optical images and SVET 2D current density maps of 1 mm scratch defect and the surrounding area up to 6 days of immersion in 0.05 M NaCl solution.

A more detailed analysis of the corrosion performance of the studied LDH systems includes SEM (Figure 39) and EDS (Table 21) results of the scratched regions for up to 6 days of immersion in 0.05 M NaCl.

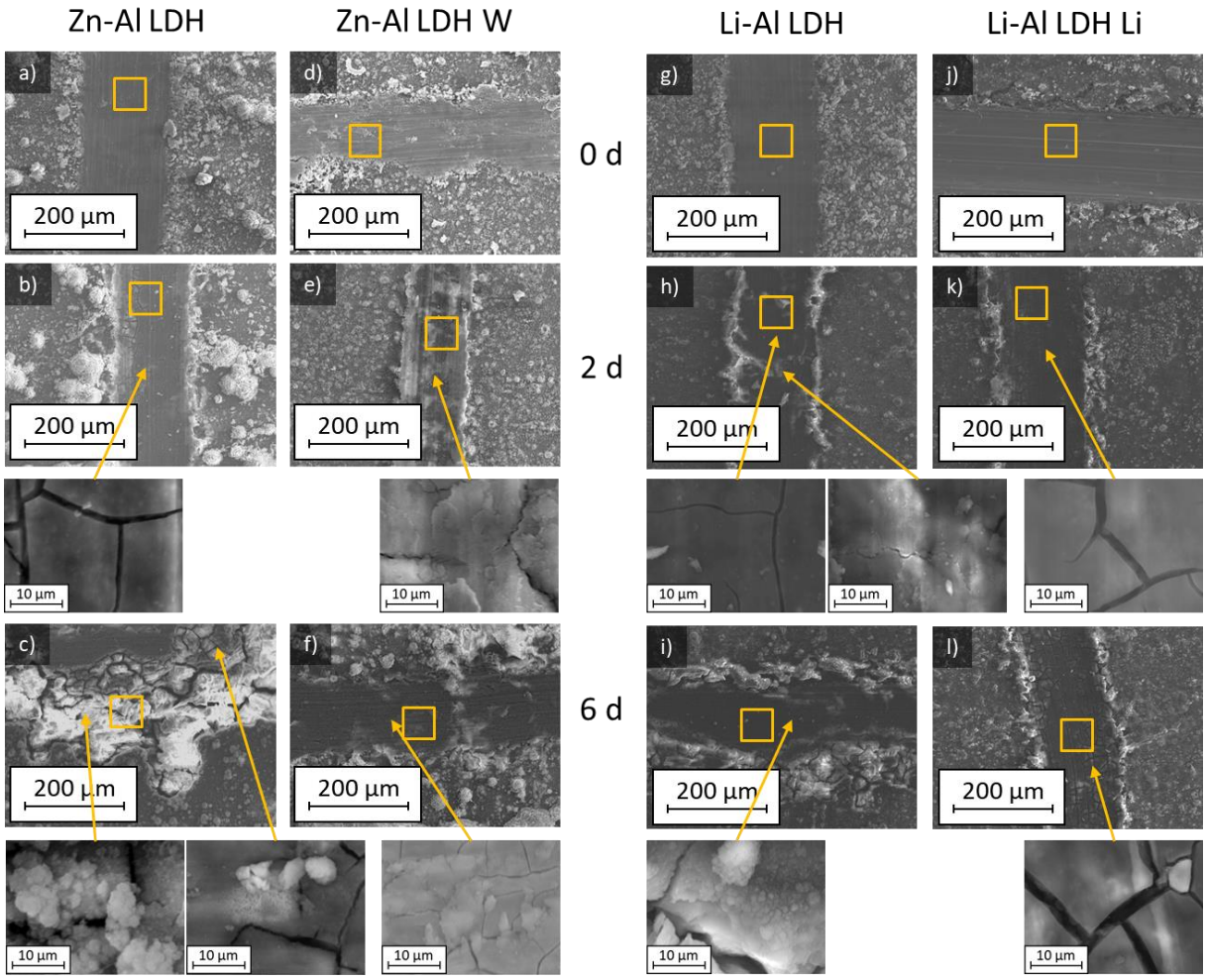

Figure 39. Scanning electron micrographs corresponding to the scribed planar views and details of (a,b,c) Zn–Al LDH, (d, e, f) Zn–Al LDH W, (g,h,i) Li–Al LDH and (j,k,l) Li–Al LDH Li coatings, up to 6 days immersion in 0.05 M NaCl solution. Squares represent the areas analysed by EDS.

Before immersion all the scratches are clean and with depth values greater than 7 µm. EDS results at the location of the scratches show high and low amounts of Mg and O, respectively, in comparison to non–scribed regions (Table 17), showing that the defect has reached the substrate.

After 6 days of immersion, the scratch of the Zn–Al LDH specimen shows voluminous corrosion products that are rich in O and Mg (Figure 39c). Contrarily, the Zn–Al–LDH W system shows a lesser amount of corrosion products in comparison (Figure 39f). It is noteworthy that the presence of W and Zn is detected inside the scribe after 2 days of immersion

and that their contents increase with time (Table 21). The presence of W inside the scribe (where there was none before the immersion) demonstrates the liberation of WO_4^{2-} from the intact coating zones and its subsequent precipitation at the defect.

The Li–Al LDH system also revealed voluminous corrosion products at the location of the artificial defect (not shown in the micrographs) and increased levels of Mg and O with increasing immersion times, possibly in the form of magnesium hydroxide. In the case of Li–Al LDH Li, better results were obtained, but some areas of the scribe were also covered by corrosion products. It is important to mention that, in the areas less affected by corrosion, the amount of Al and Zn increased significantly in comparison to the Li–Al LDH reference system suggesting some effect from the Li element. Therefore, the incorporation of $LiNO_3$ salt into the LDH coating has a beneficial effect on the corrosion performance, although the actual protection mechanism remains elusive. For instance, Zhang et al [229] reported that LDH films with a Li^+/Al^{3+} molar ratio of 1:2 showed better performance than those with 1:1 and 2:1 molar ratios due to the formation of less defective coatings, but they did not provide a detailed explanation on the role of Li. In case of Al alloys, previous studies on Li behaviour as corrosion inhibitor have shown the formation of a protective layer in artificial defects [230-234]. This layer usually has a composition of Al, O and Li and shows a compact three–layer morphology, thus providing long–term corrosion protection [233, 234]. A similar mechanism could be acting in the present case since Al–rich oxides/hydroxides (Table 21) are formed and these should provide a higher level of protection in comparison to magnesium oxides/hydroxides in neutral environments. Although further research is needed, this behaviour could be related to Li^+ promoting the distortion of the $Mg(OH)_2$ structure, thus reducing its stability [235].

Table 21. EDS analysis performed in the scratched regions of LDH coatings on AZ31 (at.%).

Coating	Time	Elements					
	Days	O	Mg	Al	Zn	Mn	W
Zn–Al LDH	0	32.1	64.9	1.7	1.3	–	–
	2	58.5	37.5	3.7	0.3	–	–
	6	67.9	28	3.5	0.6	–	–
Zn–Al LDH W	0	3.0	93.6	2.2	1.2	–	–
	2	54.4	40.7	2.1	1.7	0.4	0.7
	6	34.6	60.3	2.9	1.0	0.2	1.0
Li–Al LDH	0	15.1	82.2	1.7	1.0	–	–
	2	57.6	40.7	1.6	0.1	–	–
	6	34.4	60.9	3.4	1.3	–	–

Table 21. EDS analysis performed in the scratched regions of LDH coatings on AZ31 (at.%). (cont.)

Coating	Time	Elements					
	Days	O	Mg	Al	Zn	Mn	W
Li–Al LDH Li	0	1.5	96.1	2.0	0.4	–	–
	2	54.5	38.8	5.3	1.5	–	–
	6	57.8	34.8	5.5	1.9	–	–

In order to summarise the degradation and protection processes, simplified corrosion mechanisms are represented in Figure 40. These are based on the combination of three phenomena: ion–exchange, precipitation of hydroxides and competitive adsorption.

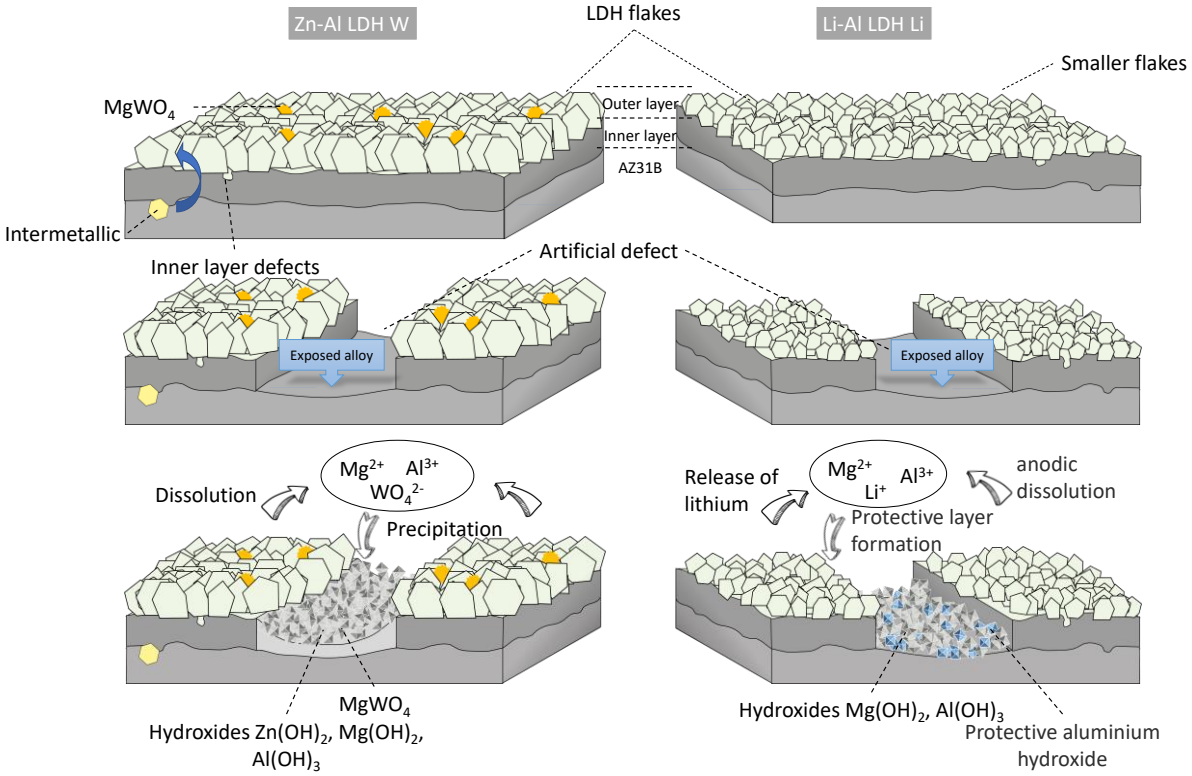

Figure 40. Schematic representation of the proposed mechanism for the corrosion protection on Zn–Al LDH W and Li–Al LDH Li.

4.1.2.4 Contact angle, Surface roughness and Paint adhesion

Contact angle measurements were performed to evaluate the hydrophilicity/hydrophobicity of the developed coatings (Figure 41). All the coatings show a hydrophilic behaviour. Zn–Al LDH shows a 0º contact angle and the water drop completely spread over the coating's surface. Li–Al LDH presents a slightly higher contact angle, 13º, which is also considered highly hydrophilic. In both systems, this behaviour can be explained by the presence of hydroxyl groups within the LDH structures that can easily interact with water molecules through

hydrogen bonding [185]. This extreme hydrophilicity may cause the aggregation of the LDH flakes and significant water adsorption, which may promote corrosion initiation if the aqueous environment reaches the substrate. Both specimens containing corrosion inhibitors show higher contact angles, 58º and 43º for Zn–Al LDH W and Li–Al LDH Li, respectively. This increase can be related to the loss of the outer layer that modifies the roughness of the coating and to the presence of inhibitor–containing species at the LDH surface that prevents the formation of hydrogen bonding. In case of Zn–Al LDH W, these could be W–rich solid precipitates, while in case of Li–Al LDH Li it could be associated with the adsorption of Li^+ cations.

The roughness values of the studied coatings are presented in Table 22. The analyses of Zn–Al LDH and Li–Al LDH reveal fundamental differences between them. The Zn–Al LDH shows the highest values among studied coatings. This may be related with the presence of agglomerated flakes on top of intermetallic particles, as observed in the SEM micrographs (Figure 33). This promotes the water adsorption, which is in accordance with the contact angle values. The post–treatment for that system results in the dissolution of the most external layer of the coating, including the above–mentioned agglomerations, leaving the dense and uniform inner layer exposed. As expected, this leads to a reduction of the superficial roughness (S_a and S_{10z}) and consequently a decrease in the hydrophilicity as observed in the increased contact angle values after the post–treatment. The differences in the surface roughness for the Li–Al LDH system before and after post–treatments were not significant, probably due to the lack of agglomerate flakes and their smaller size in comparison to Zn–Al LDH.

Table 22. Roughness parameters (S_a; arithmetical mean height and S_{10z}; ten–point height).

LDH coating	Roughness S_a (µm)	S_{10z} (µm)
Zn–Al LDH	3.8 ± 0.3	40.2 ± 0.5
Zn–Al LDH–W	2.6 ± 0.6	22 ± 4
Li–Al LDH	3.0 ± 0.1	20 ± 1
Li–Al LDH–Li	3.4 ± 0.1	22 ± 2

The paint adhesion property of the coatings was evaluated according to the EN ISO 2409 standard using a water–based paint, where scores are allocated to quantify the area affected by paint delamination. The scale ranges from 0 to 5, where 0 corresponds to a 0 % area delaminated, 1 to < 5 %, 2 to 5–15 %, 3 to 15–35 %, 4 to 35–65 % and 5 to an area > 65 %. Figure 41 shows the cross–cut test results and the allocated scores. Some differences are observed between the inhibitor–free and the inhibitor–containing LDH coatings. The Zn–Al

and Li–Al LDH specimens show a paint adhesion score of 1, since some detachment of small fakes of the coatings was observed at the intersection of the cuts. This indicates a relatively good paint adhesion property, which can be explained by the high hydrophilicity and roughness of the most superficial layer of the LDH coating prior to the immersion post–treatment that provides a high surface area for an optimal paint anchorage.

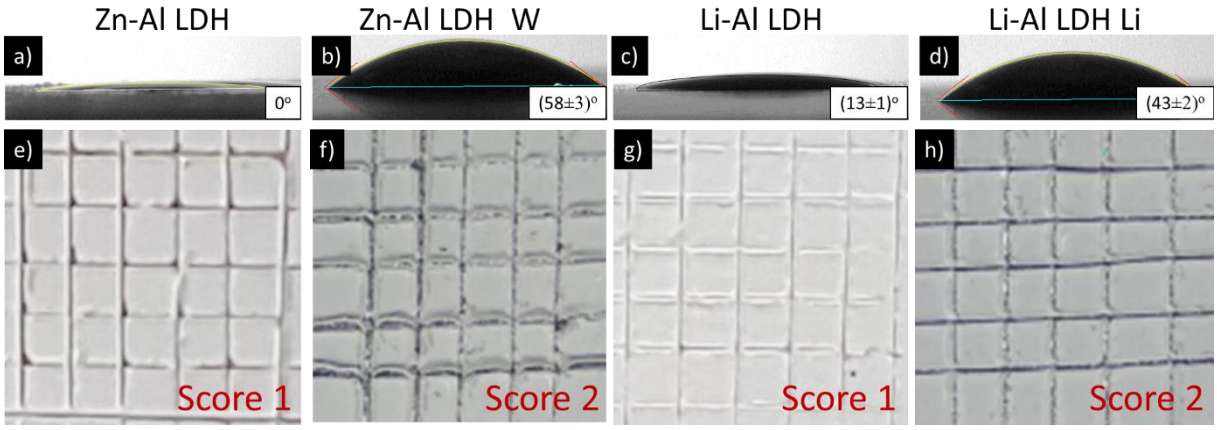

Figure 41. Water contact angle measurements and paint adhesion: (a,e) Zn–Al LDH, (b,f) Zn–Al LDH W, (c,g) Li–Al LDH and (d,h) Li–Al LDH Li.

The coatings containing corrosion inhibitors, Zn–Al LDH W and Li–Al LDH Li, obtained after the post–treatment, exhibit a slightly higher level of delamination (score 2). However, it remains in the lower range (~5 %). The coatings flake along the edges and at the intersections of the cuts. The slight decrease in paint adhesion is due to the physical and chemical changes suffered by the most external layer of the coating after the post–treatment that resulted in a smoother surface with slightly higher hydrophobicity. Consequently, the contact area available for the paint anchorage is reduced resulting in a decrease of the paint adhesion.

4.1.3 Concluding remarks on LDH coatings on AZ31 Mg alloy

The main conclusions obtained for the developed LDH systems are summarized as follows:

- Zn–Al and Li–Al LDH systems containing Li–, Mo– and W–based corrosion inhibitors were successfully synthesized and optimized in terms of corrosion resistance. The coatings with the highest corrosion resistance, Zn–Al LDH W and Li–Al LDH Li, were selected for further evaluation.
- XRD, FTIR and XPS analysis confirmed the incorporation of the inhibitors into the LDH structure. W is incorporated in the form of WO_4^{2-} and it is likely to be physically adsorbed on the LDH's most external layers. In contrast, Li is suggested

to be incorporated in the cationic form Li^+, remaining attached to the top and bottom layers of the LDH system due to electrostatic interactions with NO_3^-.

- The applied post–treatments result in the selective dissolution of the outermost layer of the LDH coatings, reducing hydrophilicity and paint adhesion of the coatings.
- The active corrosion properties of the developed coatings were confirmed by SVET analysis. The Zn–Al LDH W system revealed better active protection properties than Li–Al LDH Li.
- The inhibition corrosion mechanism is attributed to the combination of three phenomena: ion–exchange of aggressive Cl^- ions, dissolution–redeposition of protective deposits, including W–rich precipitates and aluminium hydroxides.

Chapter 2

Doped flash PEO coatings for corrosion protection of AZ31 Mg alloy

4.2 Chapter 2. Context and aim

PEO microdischarges allow for an efficient incorporation of electrolyte species into the coating. These are usually in the form of insoluble or corrosion–resistant phases, thus improving the coating barrier properties. Alternatively, electrolyte–derived phases may provide active corrosion protection by mechanisms such as dissolution/precipitation and inhibitor release. Ca is sometimes used in PEO coatings as its compounds typically lead to an improvement in the corrosion resistance of coated Mg alloys. Chapter 2 focuses on the study of a modified PEO electrolyte for Ca incorporation into a Flash–PEO coating on AZ31 alloy. Two compounds are considered as a source of Ca: calcium oxide (CaO) and calcium glycerophosphate ($C_3H_7CaO_6P$, CaGlyP). The goal is to synthesize thin, energy–efficient and corrosion resistant Ca–doped PEO coatings on the AZ31 Mg alloy. Chapter 2 graphical summary is shown in Figure 42.

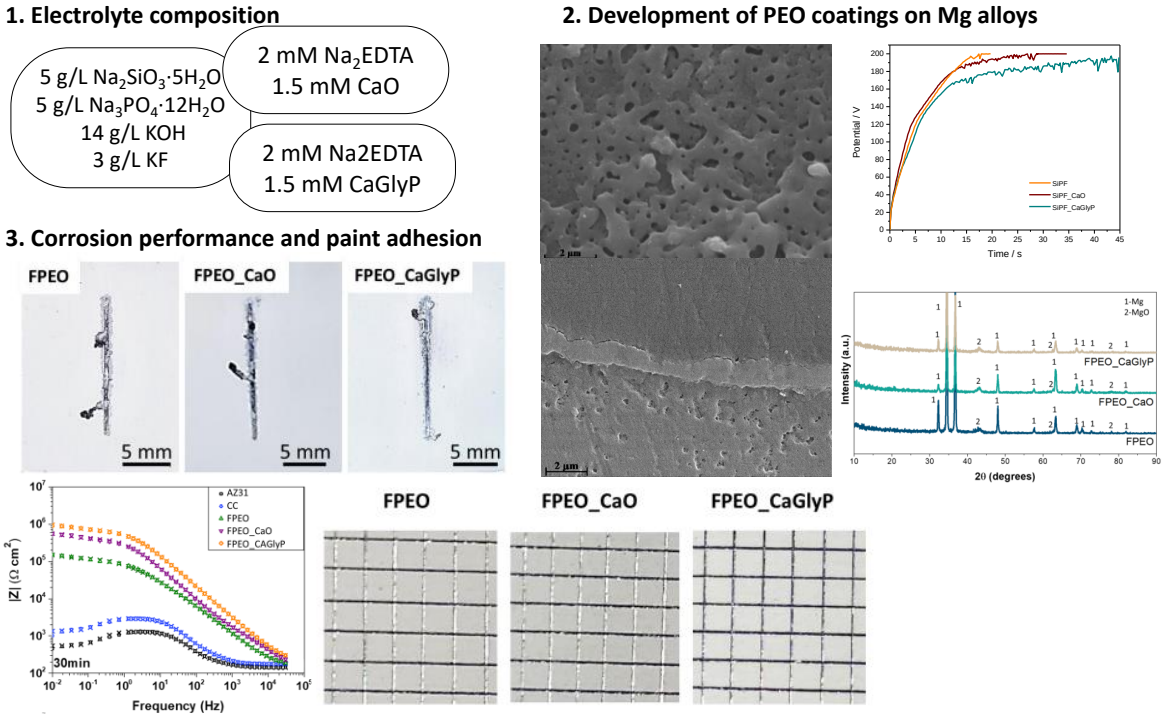

Figure 42. Chapter 2 graphical abstract: Study of Ca–doped PEO coatings on AZ31.

4.2.1 Introduction

The high temperature and pressure that develops within plasma microdischarges facilitate the incorporation of electrolyte species into PEO coatings [236]. The species then consolidate into corrosion–resistant phases and enhance the protection provided by the MgO layer which otherwise would not be that high, considering the low Pilling–Bedworth ratio ($V_{ox}/V_m = 0.81$) of MgO and its relatively high solubility in non–alkaline aqueous environments. It is worth mentioning that some cationic and anionic inorganic electrolyte species may provide active corrosion–inhibiting properties [237, 238], although this is usually achieved via a post–treatment. As a result, PEO is one of the most successful approaches for providing an enhanced corrosion protection of Mg components.

Ca is sometimes used in protective coatings produced by anodizing [239-251], electrodeposition [252-254], conversion [255, 256] or by mixed strategies (e.g. PEO with electrophoretic deposition [257] or hydrothermal treatment [258]). The formation of calcium phosphates, hydroxyapatite and other Ca–rich compounds typically leads to an improvement in the corrosion resistance of coated Mg alloys. The incorporation of Ca into PEO coatings is mostly focused on biological implant applications due to their great biocompatibility, especially in terms of hydroxyapatite–forming ability [259]. Reported studies on Ca–containing PEO coatings typically use high voltages (between 400 and 500 V) and long treatment times (5 to 30 min), resulting in thick coatings (up to 70–90 µm). Regarding corrosion properties, the studies revealed that the incorporation of Ca into the PEO oxide layers is beneficial for corrosion protection, leading to an increase in corrosion potential and corrosion resistance as well as a reduction in corrosion current [239, 241, 242, 249].

In this section, two compounds are considered as a source of calcium for PEO coatings on Mg; calcium oxide (CaO) and calcium glycerophosphate (CaGlyP). It is worth mentioning that CaO solubility is quite limited (approximately 1.18 g/L at 30 °C, pH 7.0 [260]), leading to difficulties with maintaining stable suspensions of CaO particles. Therefore, the present study also explores the viability of CaGlyP which shows a higher general solubility 5.7 g/L (pH 7.5) [255]. The effect of this compound on the coating properties is not clear since the number of studies using CaGlyP in the electrolyte are rather limited [242] and its influence on the coating performance is somehow unclear. It also needs to be addressed that the main drawback for the commercialization of PEO coatings is their considerable energy consumption. To overcome this limitation, this work presents the strategy of a thin coating formation by flash–PEO (FPEO)

with a much lower energy input (about 10 times lower) compared with typical PEO procedures. Thin PEO coatings obtained under such conditions can be a promising replacement for thin chromium conversion coatings (CC) due to their compact and resistive ceramic–like structure.

The PEO process parameters were optimized in order to reduce the treatment time and the applied voltage to a minimum, ensuring at the same time the best possible corrosion protection. The obtained coatings are thinner (~1 μm) in comparison to previous systems [261-268]. Another aim of the present work is to propose an alternative to thin CC treatments for industrial automobile or aircraft applications that would provide a superior corrosion protection. For such treatments, an excellent paint adhesion is mandatory. Therefore, special importance in this study is given to the evaluation of anticorrosion performance of the full system (PEO pre–treatment combined with epoxy primer layer) in neutral salt spray (NSST) and the paintability tests performed in accordance with ISO 17872 and ASTM D 1654 standards. Full system coating properties were compared with those for the untreated Mg AZ31B substrate and a commercially available CC product with similar coating thickness.

4.2.2 Results and Discussion

4.2.2.1 Electrical Response of Flash–PEO

Table 23 summarises the DC PEO parameters for the developed oxide layers. In order to maintain a low energy consumption, the PEO electrical parameters were optimized and kept as low as possible, simultaneously maintaining the shortest possible treatment times. Three different PEO coatings (FPEO, FPEO_CaO and FPEO_CaGlyP) were fabricated on the AZ31 alloy. It is noteworthy that the concentration of Ca ions was the same for both electrolytes.

Table 23. Electrolytes and PEO process conditions.

Name	Electrolyte	pH/ Conductivity (mS/cm)	Potential (V)	Time (s)	Current density (mA/cm^2)
FPEO	$Na_2SiO_3 \cdot 5H_2O$ 5g/L $Na_3PO_4 \cdot 12H_2O$ 5 g/L KOH 14 g/L KF 3 g/L	12.91/57.5	200	20	100

Table 23. Electrolytes and PEO process conditions. (cont.)

Name	Electrolyte	pH/ Conductivity (mS/cm)	Potential (V)	Time (s)	Current density (mA/cm^2)
FPEO_CaO	$Na_2SiO_3 \cdot 5H_2O$ 5 g/L $Na_3PO_4 \cdot 12H_2O$ 5 g/L KOH 14 g/L KF 3 g/L Na_2EDTA 2 mM CaO 1.5 mM	12.94/59.2	200	35	100
FPEO_CaGlyP	$Na_2SiO_3 \cdot 5H_2O$ 5 g/L $Na_3PO_4 \cdot 12H_2O$ 5 g/L KOH 14 g/L KF 3 g/L Na_2EDTA 2 mM CaGlyP 1.5 mM	12.91/57.8	200	45	100

The voltage–time curves acquired during the studied FPEO processes are presented in Figure 43. The curves exhibit shapes characteristic of galvanostatic anodizing conditions with an initial fast voltage increase corresponding to the growth of a barrier MgO layer and the subsequent voltage oscillations at a reduced slope associated with the initiation of plasma microdischarges until the finale set voltage was reached. Despite the fact that the pH and the conductivities of all the electrolytes were very similar (Table 23) the FPEO in base Ca–free electrolyte reached the top limiting potential (200 V) after only 20 s; the respective times were extended to 35 s and 45 s in the electrolytes with CaO and CaGlyP, respectively, in order to reach a similar final voltage. It should be remembered that both electrolytes contain Na_2EDTA, and both GlyP and EDTA are strong chelating agents not only with respect to Ca but with respect to Mg as well, which means that in their presence in the electrolyte Mg surface passivates with more difficulty, as the dissolution of Mg (through the formation of MgGlyP and MgEDTA complexes) competes with the formation of MgO. Consequently, this leads to a slower growth of the MgO layer and to the delay of the onset of microdischarges, more pronounced in a heavier chelated electrolyte. This also affects the energy consumption of the processes, which varied from ~0.8 kWh m^{-2} μm^{-1} for an Ca–free electrolyte to ~2.0 kWh m^{-2} μm^{-1} for CaGlyP (Table 24). Nevertheless, all three PEO processes can be considered as extremely short and, therefore, beneficial from the energy consumption point of view. For instance, the energy consumption of a typical 30 min PEO treatment is about 18 kWh m^{-2} μm^{-1} [269].

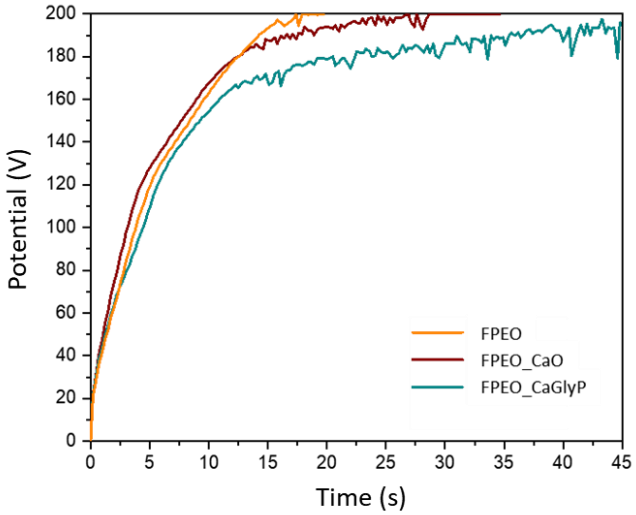

Figure 43. Voltage–time curves registered during the FPEO processes in the basic electrolyte and electrolytes doped with CaO or CaGlyP.

Table 24. Flash–PEO (FPEO) process and coating parameters.

Name	Energy ($kWh\ m^{-2}\ \mu m^{-1}$)	Pore Density (μm^{-2})	Pore Diameter (μm)
FPEO	0.8	3.1 ± 0.5	$(14\pm2) \times 10^{-3}$
FPEO_CaO	1.6	1.8 ± 0.3	$(8\pm3) \times 10^{-3}$
FPEO_CaGlyP	2.0	1.9 ± 0.8	$(10\pm4) \times 10^{-3}$

4.2.2.2 Coating Morphology and Composition

The plan–view electron–optic examination of the coatings did not reveal any significant differences in the surface morphologies (Figure 44). Specimens disclose flat regions with protruding irregularities which formed over the intermetallic inclusions; the latter are also observed in the AZ31 substrate, with and without commercial CC (Figure 45).

An EDS analysis of the pre–treated samples confirmed that these inclusions show an increased content of Al, Mn and Fe (17 ± 2, 4.8 ± 0.2, 0.10 ± 0.05 at.%, respectively). After the FPEO process, these inclusions were also covered with a passive layer. The flat regions of the surface disclose typical numerous sub–micron size pores with a uniform distribution for all FPEO coatings (Figure 44b,e,h).

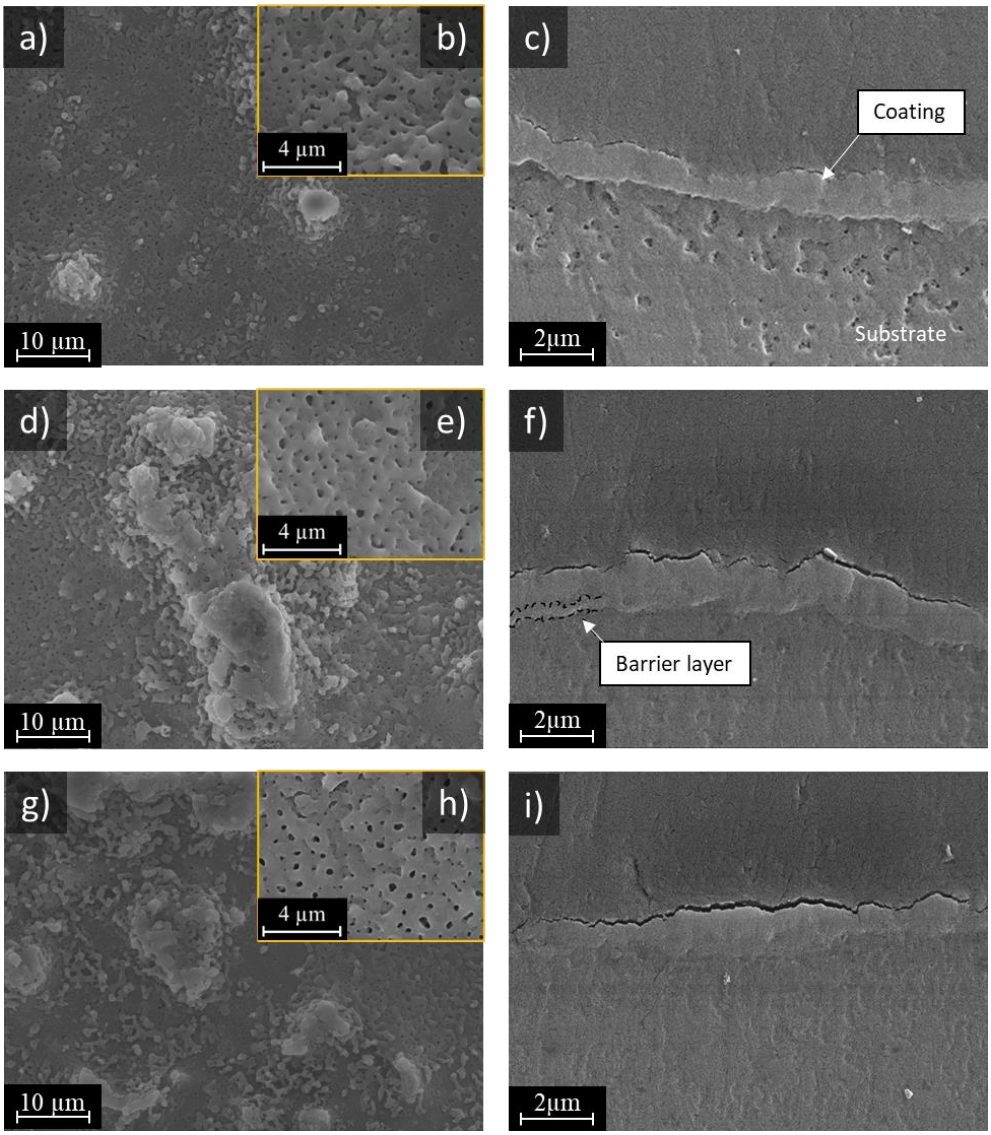

Figure 44. Secondary electron micrographs of the coating (a,b,d,e,g,h) plan views and the (c,f,i) cross–sections: (a–c) FPEO; (d–f) FPEO_CaO; (g–i) FPEO_CaGlyP. EDS surface analysis results for a,d,g images are collected on Table 25.

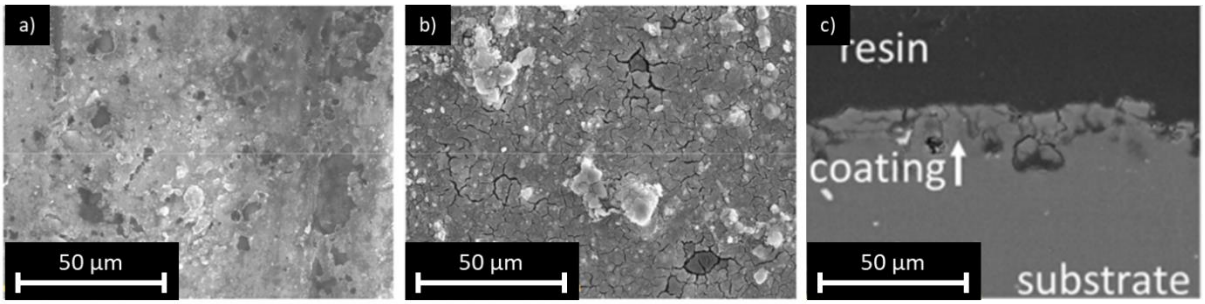

Figure 45. Secondary electron micrographs of surface morphologies of AZ31 substrate (a) without and with commercial CC (b) plan view and (c) cross view.

The porosity of the two Ca–doped coatings was found to be similar between them and about ~30% reduced with respect to the average pore size and pore population density of the base

FPEO coating (Table 24), due to the delayed onset of microdischarges. It is well known that the size and duration of the microdischarges tends to increase with the PEO processing time, producing larger pores [270], which did not have a chance to happen in the case of the present "flash" treatments. The chelating effect of EDTA on Mg, mentioned previously, facilitates the substrate dissolution making the growth of the passive layer slower: therefore, the dielectric breakdown of the latter and the initiation of the microdischarges occurs later and the number of the microdischarges, and hence pores, may be fewer too. From the corrosion resistance point of view, reduced porosity is expected to be a positive factor.

Table 25. Results of the local EDS surface analysis of the coatings (at.%).

Elements	Mg	Al	O	F	Si	P	Ca
FPEO	56.1	2.9	36.4	2.1	1.8	0.7	–
FPEO_CaO	50.6	3.2	39.6	3.5	2.3	0.9	0.1
FPEO_CaGlyP	52.4	2.5	39.6	2.6	2.0	0.7	0.1

Cross–sectional images (Figure 44c,f,i) exhibited a two–layered structure of the coatings: a thin barrier layer at the bottom and a relatively compact top layer; very few pores are discerned as a residue of microdischarge channels. This may be related to the small size of the discharges and their short life–time, both expected for a treatment of such a short duration [270]. Typically, prolonged PEO treatments of Mg alloys in DC and DC–pulsed regimes result in the formation of a so–called pore band that is located at the interface of the barrier and outer layer of the coating [271]. In the present case, this feature, predictably, is underdeveloped. All three FPEO coatings were of similar compactness and thickness (close to 1 μm). In comparison, the commercial CC (Figure 45) disclosed a uniformly cracked surface morphology; these kinds of cracks are known to be deeply penetrating throughout the CC thickness, negatively affecting the CC anticorrosive properties.

Surface texture is known to have a strong influence on the corrosion properties as well as on the paint adhesion to the coating. The three FPEO coatings exhibited very similar surface roughness parameters, with S_a and S_{10z}, between ~3.0–3.3 μm and ~21–23 μm, respectively (Figure 46). The intermetallic alloy inclusions are clearly visible on the 3D images of the surfaces and can be recognized as bright orange colour islands on the 2D maps.

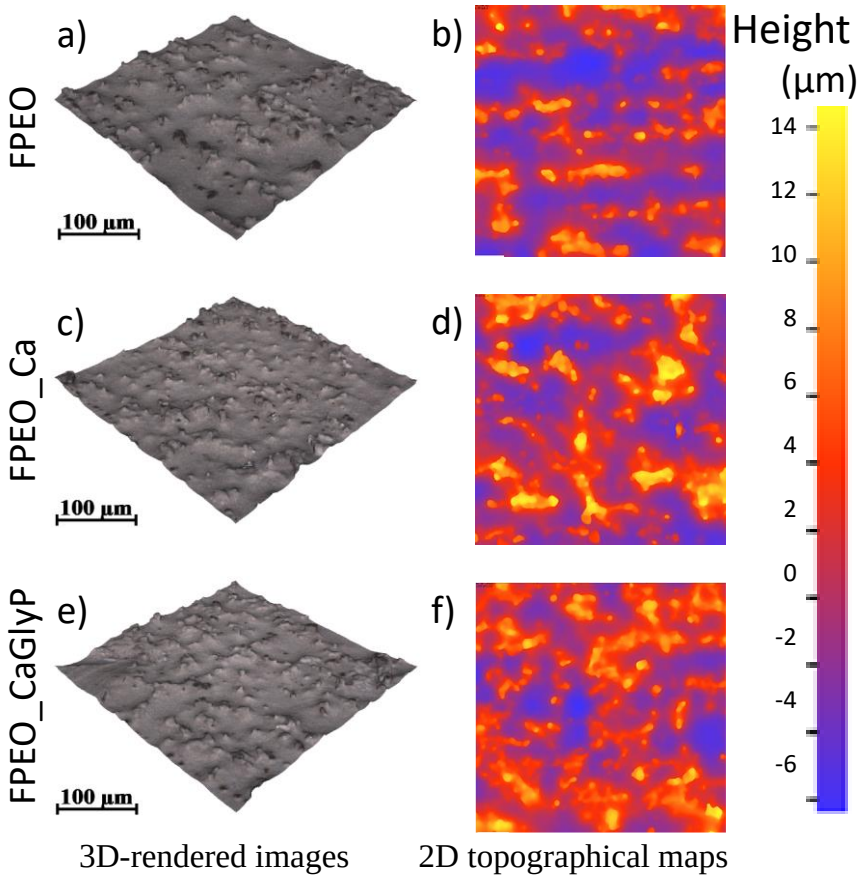

Figure 46. Optical profilometry micrographs and surface roughness parameters of the FPEO coatings, including the 3D–rendered images (a,c,e), 2D topographical maps (b,d,f). The corresponding calculated surface parameters are presented on Table 26.

Table 26. Average S_a, S_z and S_{10z} values for the FPEO coatings. The parameters represent the average height, maximum height and ten–point height of the selected area, respectively.

	S_a (µm)	S_z (µm)	S_{10z} (µm)
FPEO	3.2 ± 0.5	3.3 ± 0.4	3.0 ± 0.1
FPEO_Ca	21 ± 3	22 ± 3	24 ± 2
FPEO_CaGlyP	22 ± 3	23 ± 3	23 ± 6

The chemical compositions of all three FPEO coatings investigated by EDS were found to be relatively similar (Table 25) with regards to the incorporation of elements from the substrate (Al) and electrolyte (Si, P, F and Ca), although slightly higher Si content is observed in the Ca–containing coatings. The incorporation of Ca into the coatings from both electrolytes was equally small and non–uniform (Ca content varied from zero in some locations to 0.1 at.% in others). Grazing angle XRD detected MgO as the only crystalline phase (Figure 47). This indicates that the short PEO treatment time does not enable the evolution of longer lasting microdischarges with high enough plasma and gas temperature which could draw enough Ca

species into the discharge channels and form a significant amount of crystalline Ca–containing phases. CaO was introduced into the electrolyte as a powder which dissolves in the presence of EDTA and forms EDTA complexes which decompose and liberate Ca^{2+}. Given sufficiently long PEO treatment time, it would be reasonable to expect the formation of calcium phosphates, calcium fluoride or hydroxyapatite.

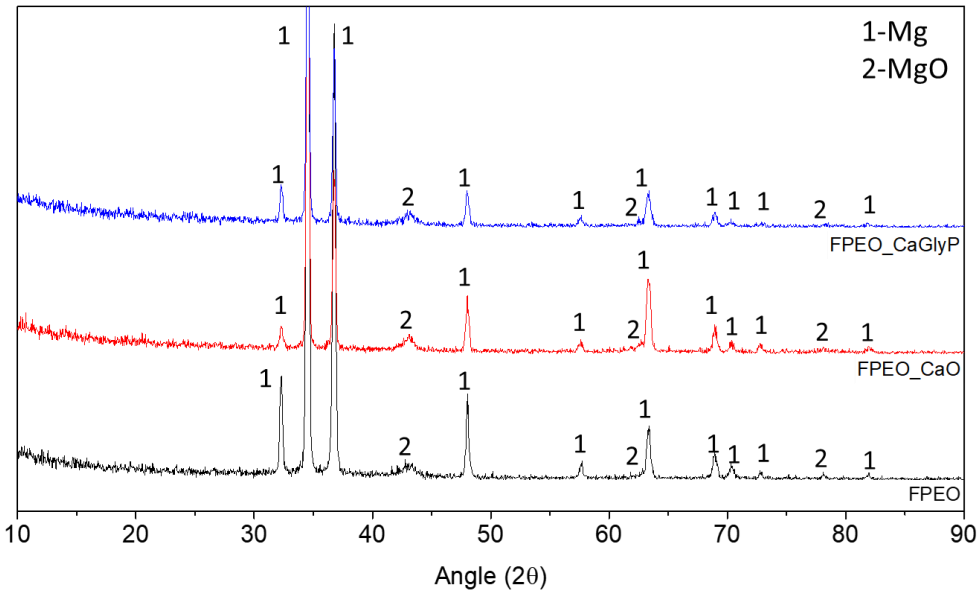

Figure 47. Grazing angle XRD patterns of the FPEO coatings.

Raman spectra (Figure 48) disclosed a dominant broad peak at ~630 cm^{-1} in all three coatings. Additionally, the Ca–containing coatings disclosed a weak intensity shoulder at about ~560–590 cm^{-1} and a broad and small peak at ~490 cm^{-1}, both of which were better defined in the case of the FPEO_CaGlyP coating. It should be noted that the fluorescence background masked the presence of peaks above 950 cm^{-1}. All the above mentioned bands are typically found in glasses and are mostly associated with silicate and orthophosphate groups [272-274]. Specifically, broad bands between 300 and 500 cm^{-1} are attributed to mixed stretching and bending modes of Si–O–Si units and bands in the 550–850 cm^{-1} region are commonly attributed to ring breathing modes [275, 276]. The band at 630 cm^{-1}, which corresponds to Si–O–Si bending, is more intense for the FPEO_CaO coating, which is in line with its slightly higher Si content, as shown by the EDS analysis [277]. The orthophosphate (Q0) group is represented by a 590 cm^{-1} band for the symmetric stretching of the P–O bonds [272]. All three coatings contain P in similar quantities; however, the shoulder at 590 cm^{-1} is less visible in the FPEO coating, suggesting a less ordered distribution of the PO_4^{3-} units.

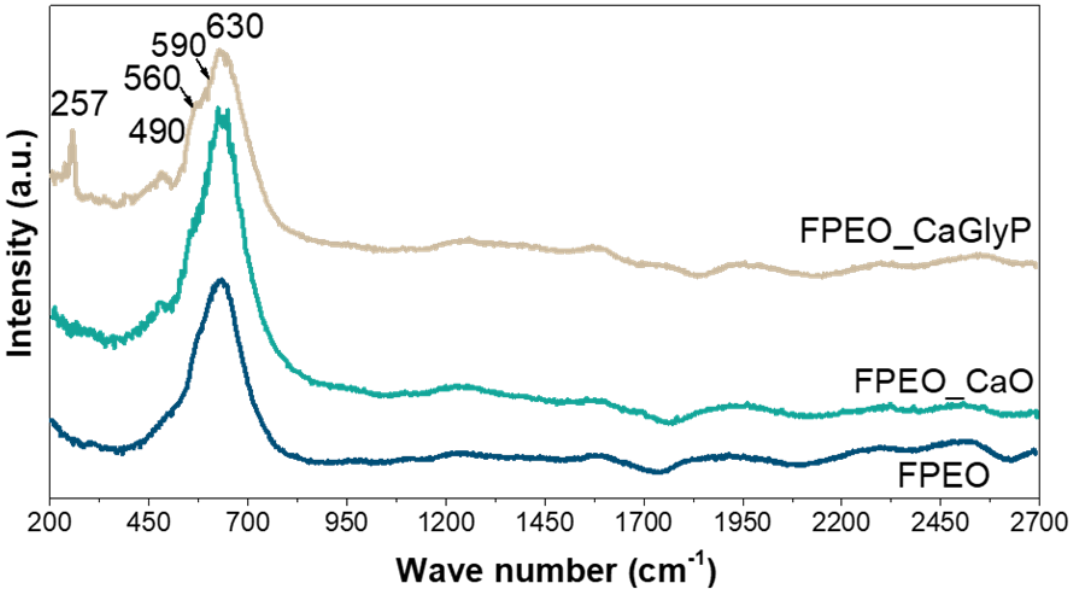

Figure 48. Raman spectra of the FPEO coatings.

Another important feature of the Ca–containing coatings spectra is the better defined peak at 490 cm^{-1}. This peak is also related to the Si–O–Si bonds (symmetric stretch oxygen vibration) and is also an indication of the higher Si content in the Ca–containing coatings.

Remarkably, only the Raman spectrum for the coating generated in the CaGlyP–doped electrolyte features a well–defined narrow peak at 257 cm^{-1}. The regions at <280 cm^{-1} in Ca–Si–O systems are associated with complex vibrations involving Ca–O polyhedra [277]. Therefore, the prominent 257 cm^{-1} peak suggests a more organized arrangement of the Ca ions in the structure of the FPEO_CaGlyP coating.

Complementary FTIR spectra (Figure 49) revealed a broad band at around a 937 cm^{-1} corresponding to the stretching of Si–O–NBO bonds in Q1 and Q2 type tetrahedral (with three and two non–bridging oxygen, NBO, atoms, respectively) of the silica depolymerized with dopant cations [278], which in the present case would be Mg^{2+} and Ca^{2+}. The broad band at 3390 cm^{-1} and 1608 cm^{-1} correspond to the –OH groups, commonly reported in the PEO–coatings on Mg [279-281] and originating from adsorbed water, due to the hydrophilic nature of MgO. The peak at 586 cm^{-1} in the FPEO coating can be attributed to Mg–O stretching vibrations; notably, it is further shifted to lower wavenumbers in Ca–doped coatings, which is not uncommon for O–Mg–O bonds in silica–modified MgO coatings [280, 281]. This is in agreement with the EDS results, where Ca–doped coatings revealed a slightly higher amount of Si. In this region there is also overlapping of O–Mg–O and P–O bond vibrations, as PO_4^{3-} antisymmetric bending is observed in the range of 570–600 cm^{-1} in crystalline MgO

surroundings [282, 283]. The weak peak at 1420 cm^{-1} can be associated with CO_3^{2-}; it is well known that hydroxylated MgO reacts with CO_2 from the atmosphere, forming magnesium hydroxyl carbonate [283, 284].

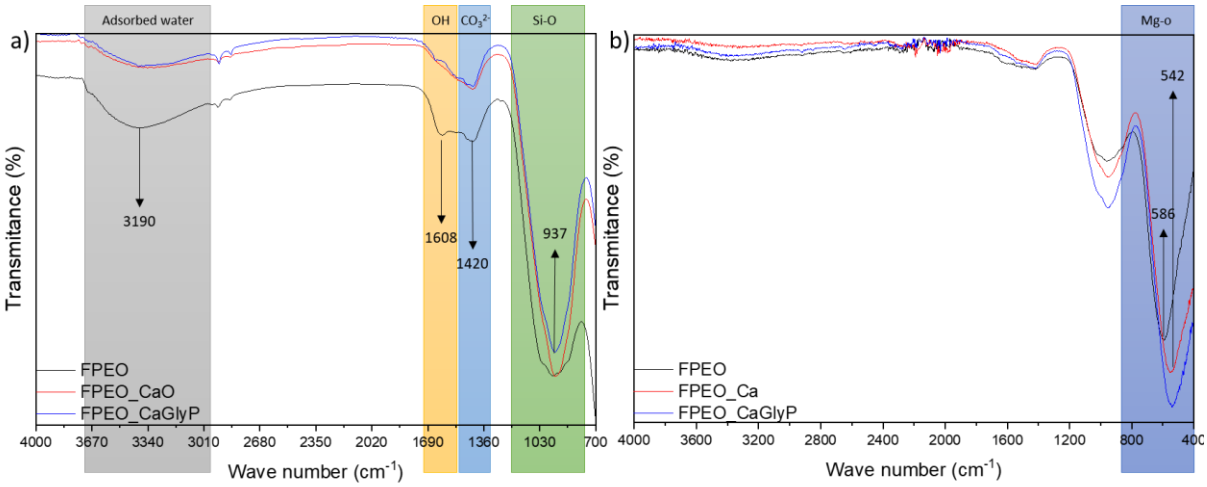

Figure 49. (a) ATR FTIR microscopy spectra and (b) the ATR FTIR spectra of the FPEO coatings.

4.2.2.3 Corrosion Test: EIS and NSST

Figure 50 depicts the values of total impedance modulus at low frequencies (0.01 Hz) after 30 min and 24 h of immersion in a 0.5 wt.% NaCl aqueous solution. This type of analysis is well known to be a strong indicator of the general corrosion resistance. The main observations can be summarized as follows:

- PEO coatings enhance the corrosion performance of the bulk material for both immersion times, showing higher values of the total impedance modulus (up to two orders of magnitude).
- A considerable decrease in the impedance modulus is observed after 24 h of immersion for the coated specimens. This reduction of the protective properties is associated with the penetration of the electrolyte through the cracks and pores of the oxide layer, leading to its chemical degradation.
- FPEO_CaGlyP coating reveals superior anticorrosion properties among the PEO coatings followed by FPEO_CaO and FPEO.

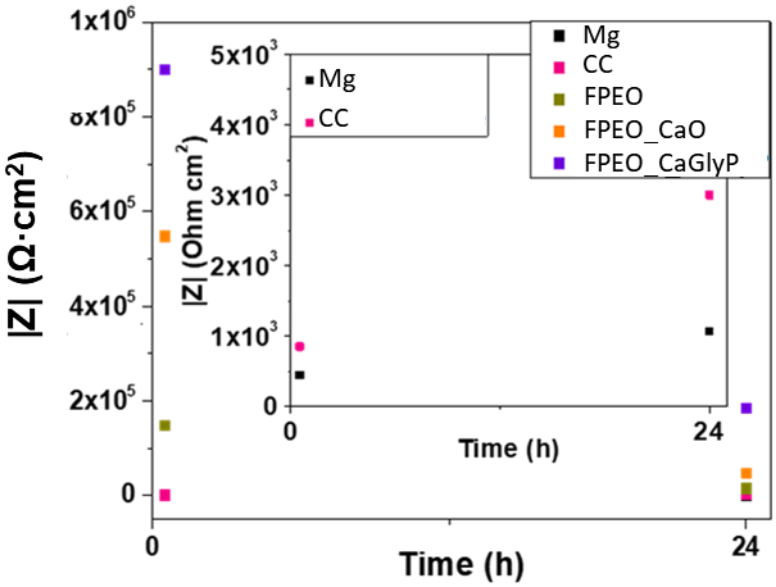

Figure 50. Evolution of the total impedance at 10 mHz for the studied systems. Inset shows the zoom–in on the difference between the bare substrate and the commercial CC.

A more detailed evaluation of the corrosion properties involved the equivalent circuit analysis of the impedance spectra and their correlation with the physical phenomena occurring in the coatings and substrate. The frequency dependent impedance response of the bare and coated materials after 30 min and 24 h of immersion in a 0.5 wt.% aqueous solution of NaCl is presented in Figure 51.

At early stages of immersion, the bare substrate reveals three relaxation processes defined by two capacitive responses (negative phase shift angles in Bode diagrams) at high and medium frequencies and an inductive response (positive phase shift angles) in the low frequency range. The time constants at high and medium frequencies present strong overlapping. The capacitive behaviour was ascribed to the charge transfer resistance and mass transport activities whereas the inductive response was related to processes involving adsorbed species [285].

After 24 h of immersion, there is a change in the impedance response of the bare material, mainly due to the formation of a corrosion product layer and the consequent variation of the free surface area (Figure 51d). Two relaxation processes associated with the presence of the corrosion products formed during immersion and the electrochemical activities in the substrate/electrolyte interface can be observed.

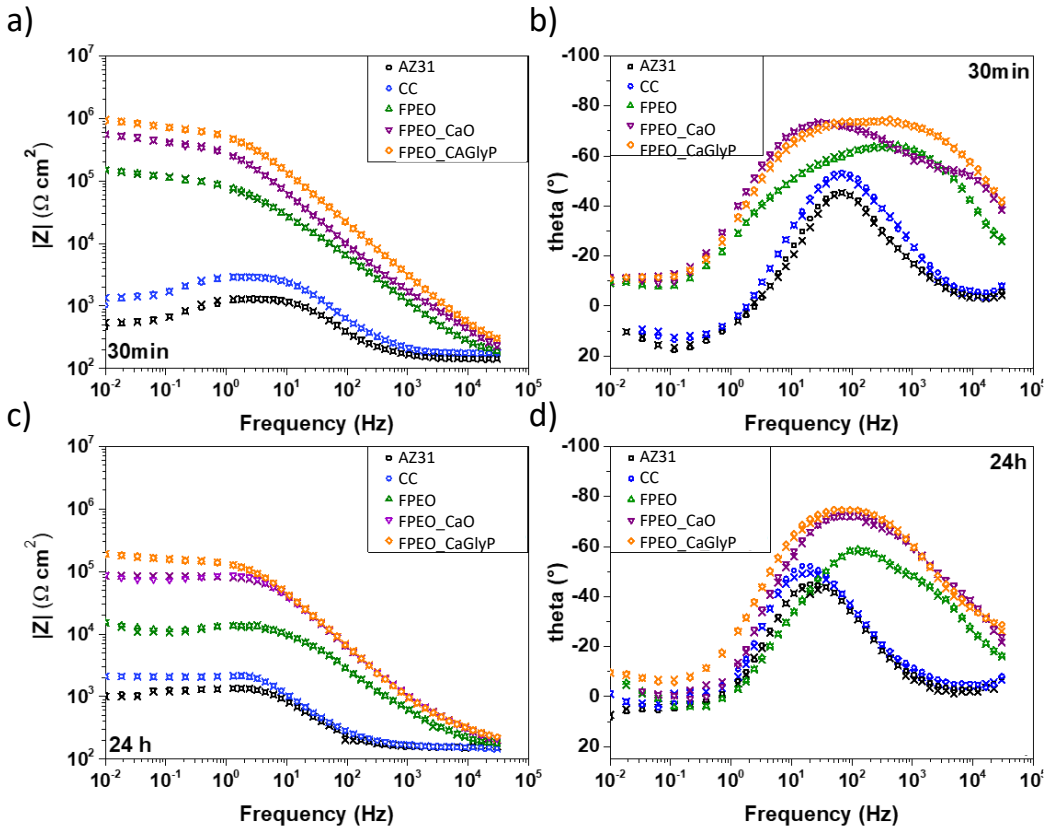

Figure 51. Bode plots for non–painted materials following 30 min (a,b) and 24 h (c,d) immersion in 0.5 wt.% NaCl. Empty symbols correspond to the experimental data and cross symbols to the fitting.

Considering the different physical processes discussed above, different equivalent circuits were used to fit the experimental data, depending on the exposure time (Figure 52); their corresponding electrochemical parameters are presented in Tables 27–30. In all the circuits, Rs accounts for the resistance of the electrolyte; constant phase elements (CPE) were used instead of capacitances in order to account for the non–ideal behaviour of the system. Good fits of the experimental data were obtained with the chi–squared values in the range of 0.001–0.0001.

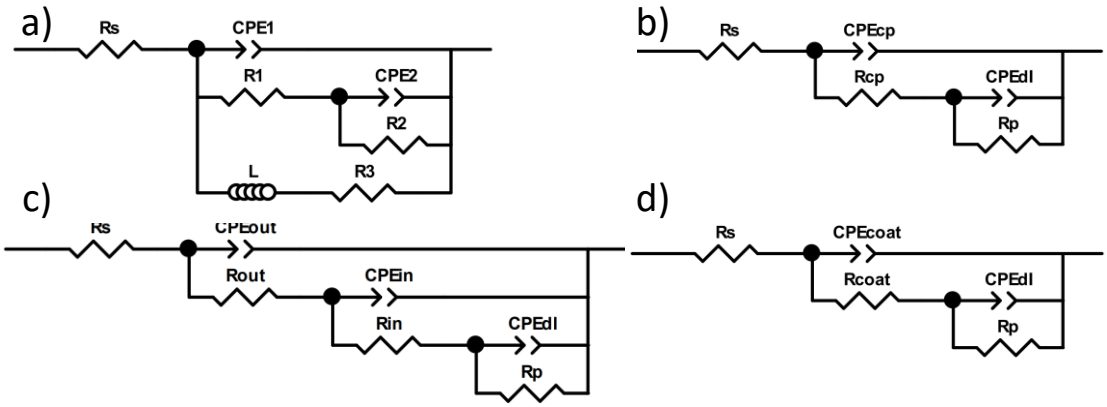

Figure 52. Equivalent electrical circuits used for fitting the EIS spectra of the AZ31B substrate (a) and the CC (b) and of the FPEO coatings after 30 min (c) and 24 h (d) of immersion in 0.5 wt.% NaCl.

For the uncoated materials, the corresponding elements of the equivalent electrical circuit at early immersion time are CPE_1/R_1 and CPE_2/R_2, associated with the capacitive and resistive behaviour of the response at high and medium frequencies, respectively; L/R_3 describes the inductive behaviour at low frequencies (Table 27 gathers the obtained fitted values). For a longer immersion time, the fitted equivalent circuit shows the resistance and the capacitive behaviour of the corrosion products formed on the alloy surface (R_{cp}/CPE_{cp}) and the electrochemical activities in the substrate/electrolyte interface represented by the capacitance of the double layer and the polarization resistance (R_p/CPE_{dl}).

Table 27. Fitted parameters of the EIS data for the Mg and CC specimens after 30 min of immersion in 0.5 wt.% NaCl. (R given in Ω cm^2; CPE given in S s^{-n} cm^{-2}; L given in Ω s cm^2).

Sample	R_s	CPE_1	n	R_1	CPE_2	n	R_2	L	R_3	R_{p*}
Mg	142.3	8.37×10^{-6}	0.87	320	1.7×10^{-6}	0.90	856	836.22	603	399
CC	178.1	1.06×10^{-6}	0.90	350	4.3×10^{-6}	0.90	2400	2873	2060	1178

**calculated according to King et al. [286]*

Specimens treated with CC showed relaxation processes and their evolution was similar to those of the bare substrate, indicating the negligible protection of the conversion layer. Therefore, the same equivalent circuits (Figure 52a,b) were used to fit the experimental data as the electrochemical response was mainly controlled by the substrate and the corrosion products layer. A slight increase in the total impedance values after 24 h of immersion in CC treatment and bare substrate are attributed to the protective effect of the corrosion product layer (Table 28), given that the R_p values with and without CC became very close.

Table 28. Fitted parameters of the EIS data for the Mg and CC specimens after 24 h of immersion in 0.5 wt.% NaCl. (R given in Ω cm^2; CPE given in S s^{-n} cm^{-2}).

Sample	R_s	CPE_{cp}	n	R_{cp}	CPE_{dl}	n	R_p
Mg	152.2	1.41×10^{-5}	0.90	120	6.37×10^{-6}	0.90	1047
CC	153.5	7.96×10^{-6}	0.94	228	8.73×10^{-6}	0.98	1173

For the PEO–coated specimens, the relaxation processes observed at the early immersion time can be ascribed to the response of the outer porous part of the oxide layer at high frequencies, the contribution of the inner barrier at medium frequencies and the initiation of the electrochemical activities on the alloy surface at low frequencies, hence the three–time constant equivalent circuit was used (Figure 52c). The corrosion processes can be described by the double layer capacitance on the electrolyte/metal interface and the polarization resistance. In fact, these two components are hard to distinguish at the early immersion stage because of the

strong overlapping. The inner barrier layer dominates the response of the system in this situation, as can be seen from high R_{in} values (Table 29). Which is far superior for FPEO_CaGlyP and FPEO_CaO contrasted to FPEO as it was suggested by increasing presence of Si.

Table 29. Fitted parameters of the EIS data for the PEO coatings after 30 min of immersion in 0.5 wt.% NaCl. (R given in Ω cm^2; CPE given in S s^{-n} cm^{-2}).

Sample	R_s	CPE_{out}	n	R_{out}	CPE_{in}	n	R_{in}	CPE_{dl}	n	R_p
FPEO	140.7	4.5×10^{-7}	0.83	70	1.46×10^{-6}	0.60	1.25×10^{5}	2.30×10^{-4}	0.97	0.37×10^{5}
FPEO_CaO	133.4	2.4×10^{-7}	0.83	2553	1.85×10^{-7}	0.86	4.02×10^{5}	2.23×10^{-5}	0.71	2.73×10^{5}
FPEO_CaGlyP	161.8	1.65×10^{-7}	0.84	2550	4.22×10^{-8}	0.83	6.79×10^{5}	1.06×10^{-5}	0.61	5.98×10^{5}

After 24 h of immersion, the time constant at high frequencies corresponding to the outer porous layer of the PEO coating has almost disappeared (Table 30 and Figure 51d). This indicates that the electrolyte can easily penetrate through the outer part of the PEO coating, and a chemical degradation of the coating (e.g. as result of species lixiviation and the hydration of the oxide) occurs to a certain degree, leading to the loss of the barrier properties of the outer layer. Since it became impossible to discriminate between the inner and outer coating part responses, a two time constant equivalent circuit was employed to fit the experimental data obtained after 24 h exposure time, where the general coating response was represented by the CPE_{coat}/R_{coat} unit. (Figure 52d). The improved response of FPEO_CaGlyP is attributed here to the presence of ordered CaO structures spread throughout the entire thickness of the protective layer, that may provide enhanced corrosion performance.

Table 30. Fitted parameters of the EIS data for the PEO coatings after 24 h of immersion in 0.5 wt.%. NaCl. (R given in Ω cm^2; CPE given in S s^{-n} cm^{-2}).

Sample	R_e	CPE_{coat}	n	R_{coat}	CPE_{dl}	n	R_p
FPEO	154.1	1.74×10^{-6}	0.77	2230	2.08×10^{-7}	1	0.11×10^{5}
FPEO_CaO	172.1	1.54×10^{-7}	0.94	8464	1.44×10^{-7}	0.92	0.76×10^{5}
FPEO_CaGlyP	152.6	3.61×10^{-7}	0.87	1.54×10^{5}	1.13×10^{-5}	0.68	1.14×10^{5}

In order to evaluate the degradation behaviour of the coated specimens, the changes in the total resistance ($R_{total} = R_{out} + R_{in} + R_p$) with immersion time are shown in Figure 53. The FPEO_CaGlyP coating showed the best corrosion performance, followed by the FPEO_CaO and FPEO, and maintained this tendency with the immersion time. The improved resistance of Ca–doped coatings can be partly caused by their reduced pore size and pore population density (Table 24). Notably, the resistance of the FPEO_CaGlyP coating as a whole after 24 h

immersion (R_{coat} = 154 kΩ cm^2) deteriorated considerably less (R_{in} + R_{out} = ~679 kΩ cm^2 after 30 min of immersion), compared with the other two coatings whose resistance deteriorated by two orders of magnitude.

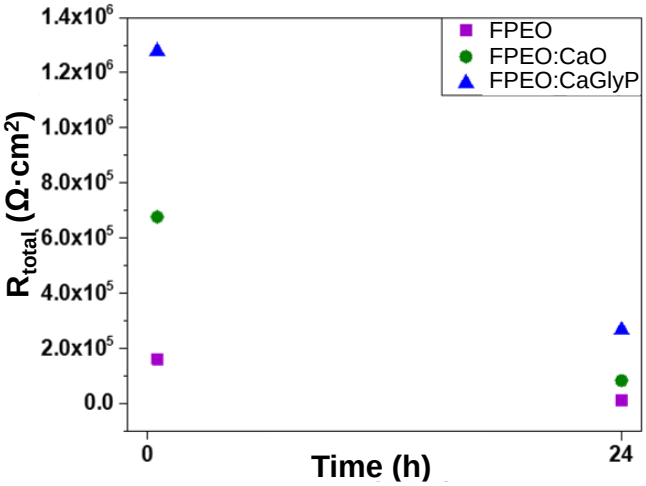

Figure 53. Total resistance for studied coatings FPEO, FPEO_CaO and FPEO_CaGlyP with immersion time.

The results of the cross–cut paint adhesion test (Figure 54) on all three flash–PEO coatings corresponded to the Score 0 in accordance with EN ISO 2409 both in dry and wet testing conditions, as no paint pull–off occurred along the cross–cut lines. This is expected since the inherent porosity of PEO coatings presents an excellent paint–absorbing base. Lower porosity and smaller pore size of Ca–doped coatings compared with base FPEO coating (Table 24) did not affect the paintability of the coatings.

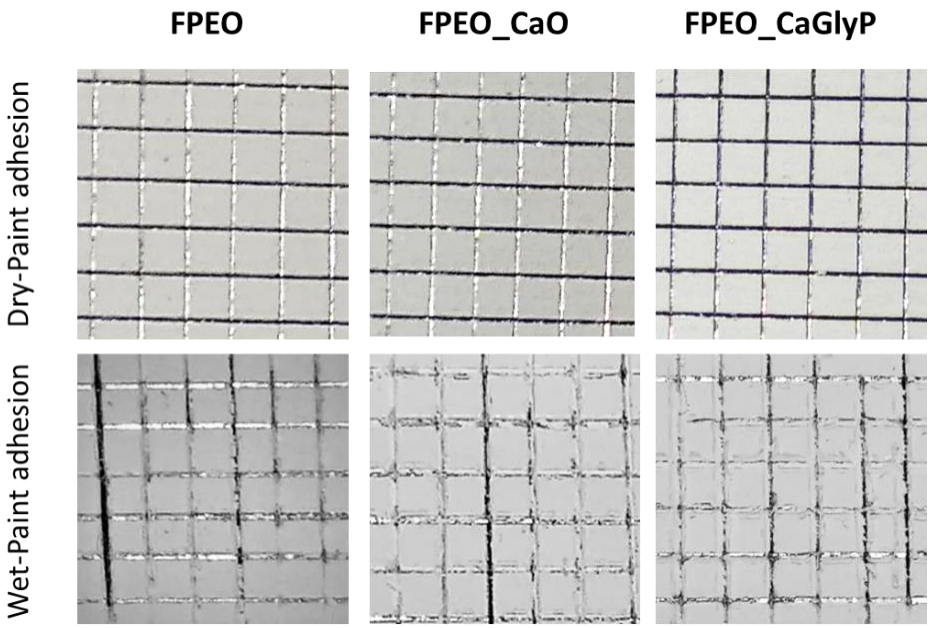

Figure 54. Cross–cut dry and wet paint adhesion test results on the flash–PEO coatings.

Macro–views of the corroded surface area of the painted and scribed specimens after NSST are shown in Figure 55, which also include an example of freshly scribed specimens before the exposure to salt fog and the related scores of the creepage.

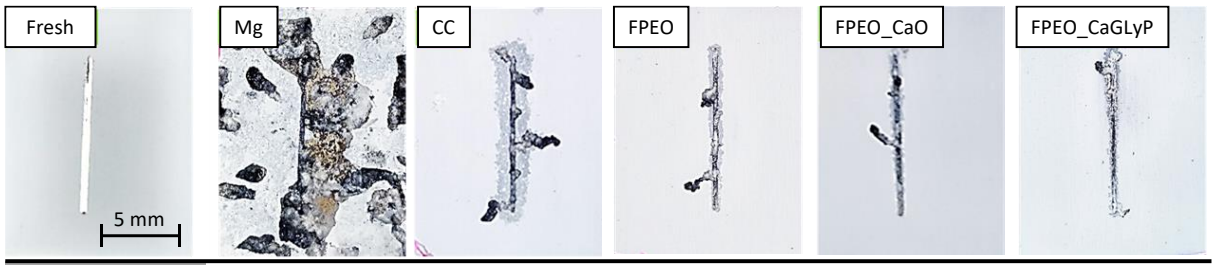

Length of corroded point (mm)	not applicable	4.1 ± 0.1	2 ± 1.5	2.3 ± 0.5	1.9 ± 0.3
Score ASTM D 1654	0	5	6	6	7
Corroded surface area (mm^2)	150 ± 41	11.0 ± 0.9	5 ± 2	4.1 ± 0.6	2.2 ± 0.5

Figure 55. Macrographs and summary results of the scribed area of the painted specimens before ("Fresh") and after 7 days of NSST, showing the creepage extent.

All the coatings revealed a clear improvement in the corrosion resistance compared with the untreated Mg substrate, which was heavily corroded, not only around the original scratch, but on the whole surface. According to the ASTM D 1654 standard, the rating related to the length of filiform corrosion filament (i.e. creepage) formed from the original scratch ranked the materials in the following order: Mg substrate < CC < FPEO < FPEO_CaO < FPEO_CaGlyP. All the FPEO coatings suffered a smaller average corroded surface area and exhibited greater corrosion resistance than CC (rating of 5). The FPEO_CaGlyP coating disclosed the highest score of 7 (lowest creepage and corroded surface area) among the investigated flash–PEO coatings, which was in line with the EIS results.

These findings suggest that the presence of even a slight amount of Ca (0.1 at.%) in a flash–PEO coating may be beneficial for improvement in protective properties. However, the source of Ca appears to be an important point affecting the corrosion resistance. Ca species in CaGlyP–doped electrolyte are chelated to a greater extent and although, semi–quantitatively, Ca content was found to be the same in both Ca–doped coatings, Ca–O bonds were detected in the FPEO_CaGlyP but not in the FPEO_CaO coating, according to the Raman analysis (Figure 48). Likewise, the FPEO_CaGlyP coating exhibited a more pronounced band around 490 cm^{-1} and

570 cm^{-1}, usually associated with PO_4^{3-} phosphate in a hydroxyapatite. It is evident, therefore, that Ca species formed more bonds (in terms of their type and complexity) with SiO_4^{4-} and PO_4^{3-} species within the MgO ceramic network during their *in–situ* incorporation from a double chelated electrolyte. That extended bonding network makes the hydrolysis of MgO and the hydration of the coating more difficult. Furthermore, the leaching of alkaline cations such as Ca during immersion modifies the SiO_2 network, giving rise to hydrolysis and the formation of $Si(OH)_4$ gel that seals the pores [287]. It is feasible that these phenomena may have led to the overall lesser resistance loss of FPEO_CaGlyP coating during immersion (R_{coat} = 154 kΩ cm^2) compared with the other two flash–PEO coatings.

4.2.3 Concluding remarks on Ca–doped PEO coatings on AZ31 Mg alloy

Considering the presented results on FPEO coatings on magnesium substrate, the most important conclusions are:

- DC flash–PEO 1 μm–thick coatings were developed from dilute alkaline electrolytes without and with added Ca species stabilized in the solution with glycerophosphate and EDTA chelating agents.
- Chelating agents delayed the onset of plasma microdischarges and the attainment of the set limiting voltage, which reduced the coating porosity but did not significantly alter the coating thickness.
- The coating obtained from the electrolyte doped with Ca in a highly soluble form of CaGlyP disclosed one and two orders of magnitude improvement in corrosion protection over 24 h of immersion in 0.5 wt.% NaCl compared with the coating generated from the CaO–doped and Ca–free electrolytes, respectively.
- All three flash–PEO coatings exhibited a score of 0 in a cross–cut dry and wait paint adhesion tests.
- Full system evaluation of the coatings in NSST for 7 days yielded ASTM D 1654 scores of 7 and 5 for FPEO_CaGlyP and commercial CC coatings, respectively.
- The enhanced corrosion resistance of FPEO_CaGlyP coating is attributed to the greater presence of covalent Si–O in the coating and ordered Ca–O structures within the MgO ceramic network.

Chapter 3

Active sealing post–treatments for PEO coatings on Mg alloys

4.3 Chapter 3. Context and aim

Recent developments in post–treatment or sealings for PEO coatings on Mg alloys are mainly driven by the need to improve their long–term corrosion resistance. The sealing procedures carried out by immersion in inorganic solutions appear to be an efficient and facile way since the high porosity of PEO coatings has the ability to act as a natural container for corrosion inhibitors. Chapter 3 aims for the development of inhibitor–containing post–treatments on PEO coatings on Mg alloys and their comparison with the non–sealed versions. The structure of the chapter is divided into two sections where each one is based on a different alloy–coating–inhibitor combination: (i) in the first section, a PEO coating on a highly novel Mg–Y–Zn alloy is studied, in which a post–treatment is applied based on the inhibition effect of Ce species; (ii) in the second section, the effect of several post–treatments based on Ca species are evaluated for a PEO–coated AZ91D alloy. Figure 56 shows the graphical abstract of Chapter 3. Also note that the sections in this chapter follow the same organization as in the corresponding publications.

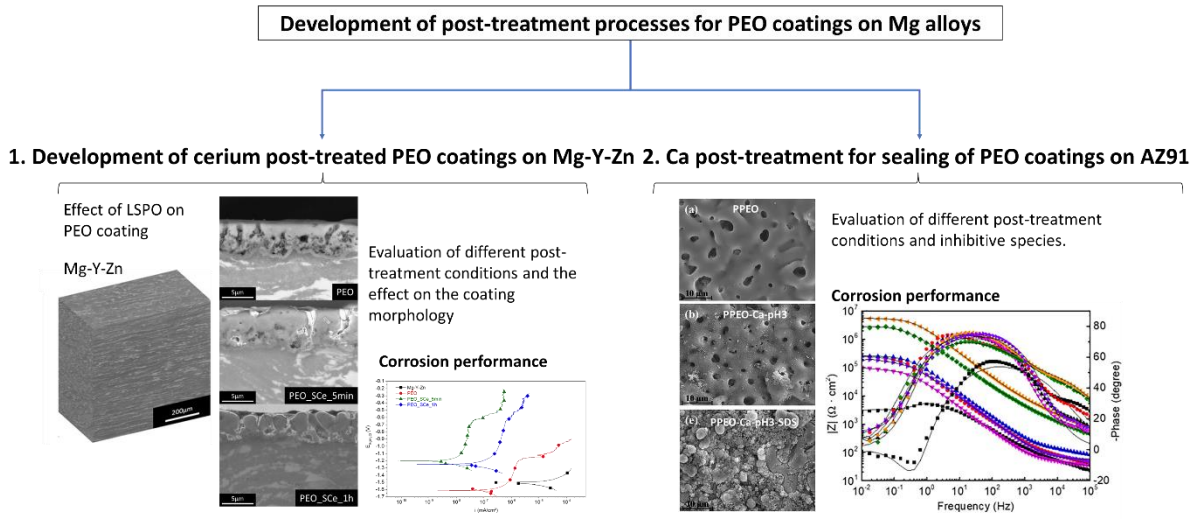

Figure 56. Chapter 3 graphical abstract: Study of sealed–PEO coatings on Mg alloys.

4.3.1 Introduction

The presence of pores is unavoidable in PEO coatings. This is highly relevant for Mg–based materials since pores worsen the coating barrier properties, thereby facilitating the corrosion of the substrate, particularly in the presence of Cl^- ions. Therefore, sealing of the outer part is required when PEO layers are exposed to highly corrosive media. Various post–treatments have been evaluated in the past, most of them adapted from sealing processes used in conventional anodizing [263, 288-290]. Examples include the use of silicate–, phosphate– and fluoride–based sealings. More recent approaches include the use of Ce– and Ca–containing solutions.

Post‑treatments in due to the efficient blockage of the coating defects by Ce–rich hydroxides and oxides and to the presence of Ce^{3+}/Ce^{4+} species which have been associated with self–healing mechanisms. For instance, Lim [291] and Laleh [292] reported an improvement in the corrosion resistance of PEO coated AZ31 alloy after post–treatment in cerium chloride solutions. Similarly, Mingo [288] and Sun [290] demonstrated the superior corrosion performance of PEO coatings sealed in cerium nitrate solutions when compared to other sealing procedures. It is generally accepted that the corrosion performance of PEO–coated specimens increases with increasing Ce concentration and sealing time due to a higher accumulation of Ce products within coating pores and cracks [178, 293]. However, this is not always the case, as reported by Phuong [293], who found that long post–treatments (phosphate–cerium based solution) led to a decrease in the corrosion resistance due to the dissolution of the PEO film during the sealing treatment.

PEO post–treatments in Ca–solutions are less explored, although it has been reported that the presence of Ca in oxide layers leads to a better corrosion performance [241, 253, 256]. Ca species that form in the coating usually include CaF_2 and $CaPO_4$, which are insoluble and significantly decrease the corrosion rate.

In addition to inorganic compounds, sealing procedures can also be used for the incorporation of organic compounds with active corrosion properties. In this regard, PEO coatings are ideal since their high porosity serves as a natural container for storing the corrosion inhibitor. A recent example is the work by Yang *et al.* [33], who added 3–methysalicylate via low vacuum environment and subsequently sealed a PEO coating by dip–coating in an epoxy resin. They found that the electrochemically active areas and corrosion current density were reduced to relatively low levels after incorporation of the corrosion inhibitor.

Chapter 3

Despite the recent advances on PEO sealing, there remain knowledge gaps. For instance, LPSO–based alloys remain almost unexplored in terms of surface treatments, let alone PEO and sealings. Also, the combination of precipitating species and active agents requires further investigation since most studies only focus on one or the other.

Considering the previous, this chapter is divided into two sections. The first one is focused on Ce–sealing of PEO coatings applied on an LPSO Mg alloy. The corrosion behaviour was evaluated in a NaCl solution by electrochemical and hydrogen measurements. The influence of the Ce–based sealing duration on the corrosion resistance was also investigated. The second part includes the investigations on Ca–based sealings for PEO coatings on AZ91D Mg alloy. Sodium dodecyl sulphate (SDS), which was previously found to be an effective corrosion inhibitor for AZ91D [294, 295], was evaluated as an active agent for improving the sealing performance. Since the dissolution/precipitation reaction during sealing is of vital importance for the coating properties, the effects of pH during Ca–based post–treatment were studied on the morphology, composition, and corrosion resistance of PEO coatings.

4.3.2 Results on Ce–sealing of a PEO coating on Mg–Y–Zn LPSO alloy

4.3.2.1 Substrate Characterization and Coating Morphology and Composition

I. Mg–Y–Zn alloy

Figure 57 shows the 3D SEM reconstruction and higher magnification micrographs along the extrusion direction for the Mg–Y–Zn alloy. The material shows fully recrystallized α–Mg grains surrounded by coarse and elongated α–Mg grains (98.3Mg, 0.6Zn, 1.1Y, in at.%) and bright contrast strings of LPSO phases (95.3Mg, 2.1Zn, 2.6Y, in at.%). Cuboid–shaped Y–rich intermetallics (46.5Mg, 0.9Zn, 52.6Y, in at.%) are also observed (Fig. 57b). Recrystallized fine α–Mg grains (~1 μm in diameter and ~60% area fraction) are the result of partial dynamic recrystallization during high temperature processing [296]. 3D characterization of this alloy in a previous study revealed that the volume fraction of the LPSO phase is close to 25% and that strings of this phase are composed of independent fibres of 200–300 μm in length [297].

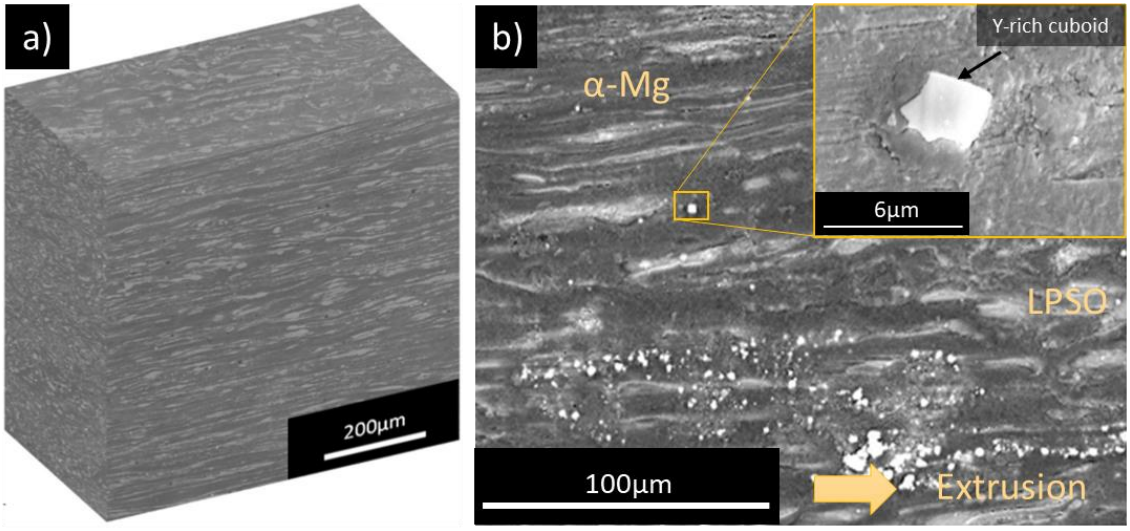

Figure 57. (a) 3D SEM reconstruction and (b) higher magnification micrographs along the extrusion direction of the Mg–Y–Zn alloy and detail of a cuboid–shaped Y–rich intermetallic.

Previous studies have pointed out the cathodic behaviour of LPSO phases based on the preferential corrosion of the surrounding α–Mg matrix, particularly for lamellar LPSO phases [55, 56], but only a few works have presented SKPFM results [298]. In this work, Volta potential differences are of the order of ~60 mV, confirming the cathodic activity of the LPSO phase (Figure 58a,c). This value is much lower than that reported by Li [55] in a Mg–Zn–Y cast alloy (250 mV). The latter result could be a misleading as it was determined right at the LPSO/α–Mg interface, where SKPFM artefacts are quite common [298].

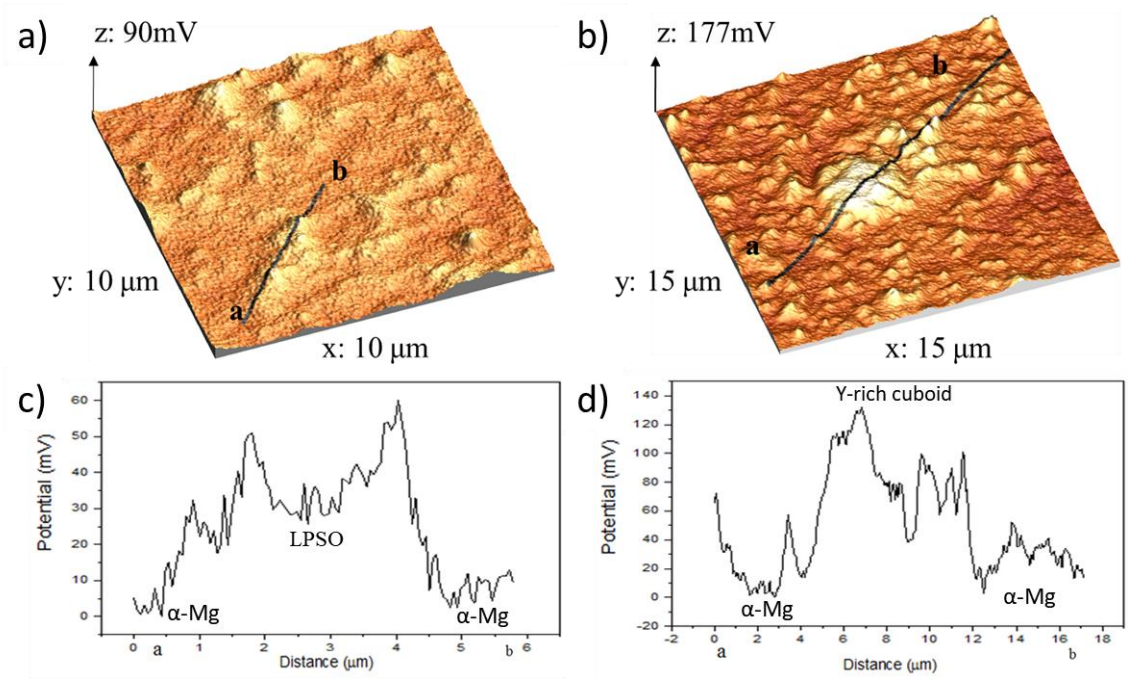

Figure 58. Surface potential maps and profiles of the (a,c) LPSO and (b,d) Y–rich phases.

Y–rich cuboid intermetallics reveal higher potential values (~140 mV) than the LPSO phase (Figure 58 b,d). This might be due to the higher Y+Zn/Mg ratio ratio (calculated based on at.%) of cuboids (~1.15) compared with that of LPSO phase (~ 0.03) which leads to a more noble potential [284, 299].

II. PEO coating

Table 31 shows the AC PEO parameters of the coating fabricated on the Mg–Y–Zn alloy along with the post–treatments details.

Table 31. PEO and post–treatments details for the LPSO–based Mg–Y–Zn alloy.

PEO Electrolyte	PEO conditions	Sealing solution	Sealing conditions
$Na_2SiO_4 \cdot H_2O$ (water glass) 10.5 g/L NaOH 6 g/L NaF 2 g/L	20 ± 1 °C 400 V/–30 V square signal 400 mA cm^{-2} 500 Hz 15 min 60 s ramp	$Ce(NO_3)_3 \cdot 6H_2O$ 10 g/L H_2O_2 0.3 g/L H_3BO_3 1 g/L	Room temperature 5 and 60 min pH 2

Surface morphologies of the PEO coated specimens before and after sealing are shown in Figure 59. The unsealed coating reveals a crater–like morphology with microcracks and micropores located at the sites of the discharge channels due to residual stresses and gas evolution during the coating formation [156] (Figure 60a,b). After post–treatment, a Ce–rich superficial layer is formed, mimicking the morphology of the PEO coating and decreasing the number and size of open pores (Figure 59c,d,e,f). Cracks observed in the Ce–rich layer may be associated with its dehydration (Figure 59d,f) [300]. The best sealing properties, based on surface porosity, pore size and number of pores, are obtained for the 5 min post–treatment (Table 32).

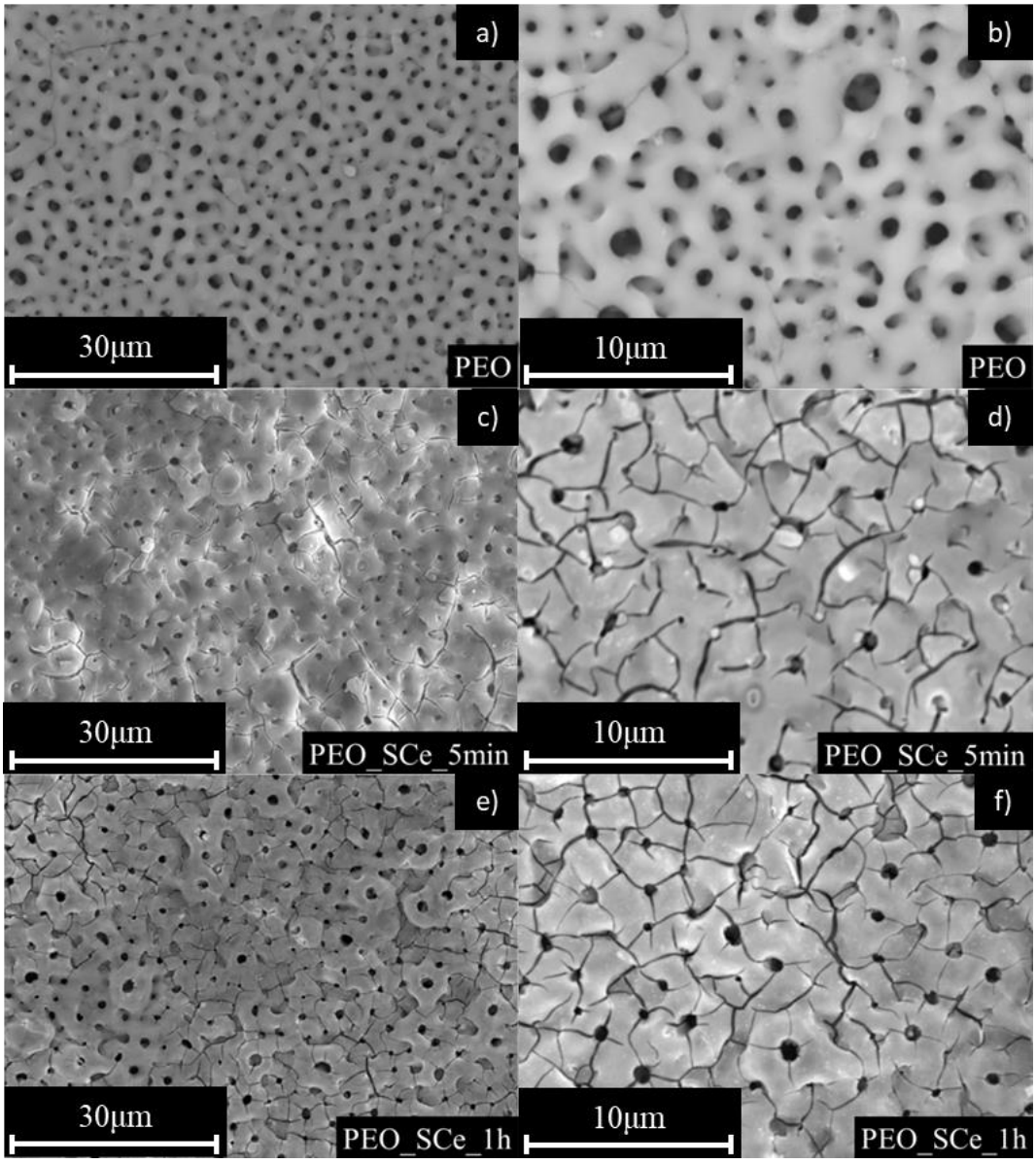

Figure 59. Plan view SEM micrographs of the coatings: (a,b) PEO, (c,d) PEO_SCe_5 min and (e,f) PEO_SCe_1h.

Table 32. Surface characteristics of the studied coatings.

	Surface porosity (%)	Pore size (µm)	Number of pores (Pores µm^{-2})
PEO	1.9 ± 1.0	0.38 ± 0.05	(4.29 ± 0.09) × 10^{-2}
PEO_SCe_5min	0.8 ± 0.2	0.19 ± 0.02	(0.38 ± 0.09) × 10^{-2}
PEO_SCe_1h	1.8 ± 0.9	0.28 ± 0.09	(4.1 ± 0.1) × 10^{-2}

The cross–sections of the unsealed PEO layer along with the Si, F, O and Y elemental maps are shown in Figure 60. Backscattered scanning electron (BSE) micrographs (Figure 60a,b) reveal a coating with a thickness of (5.4 ± 1.2) µm and a typical three–layered structure [90, 301-303], consisting of an outer part with through–going discharge channels, an intermediate section with smaller pores and a compact inner barrier layer (<500 nm).

X–ray elemental maps show Si species homogeneously distributed throughout the coating thickness (Figure 60c) and a F–rich inner region (Figure 60d), indicating a rapid inward migration of fluoride ions during the oxide formation [304]. LPSO phases are oxidized and incorporated into the coating in a localized manner, resulting in Y–rich regions. These regions did not significantly affect neither the coating thickness nor the morphology. This behaviour is quite different from that recently reported by Martin *et al.* [305], who observed a more defective coating at the location of intermetallics. The differences might be ascribed to the different anodizing conditions and composition of secondary phases.

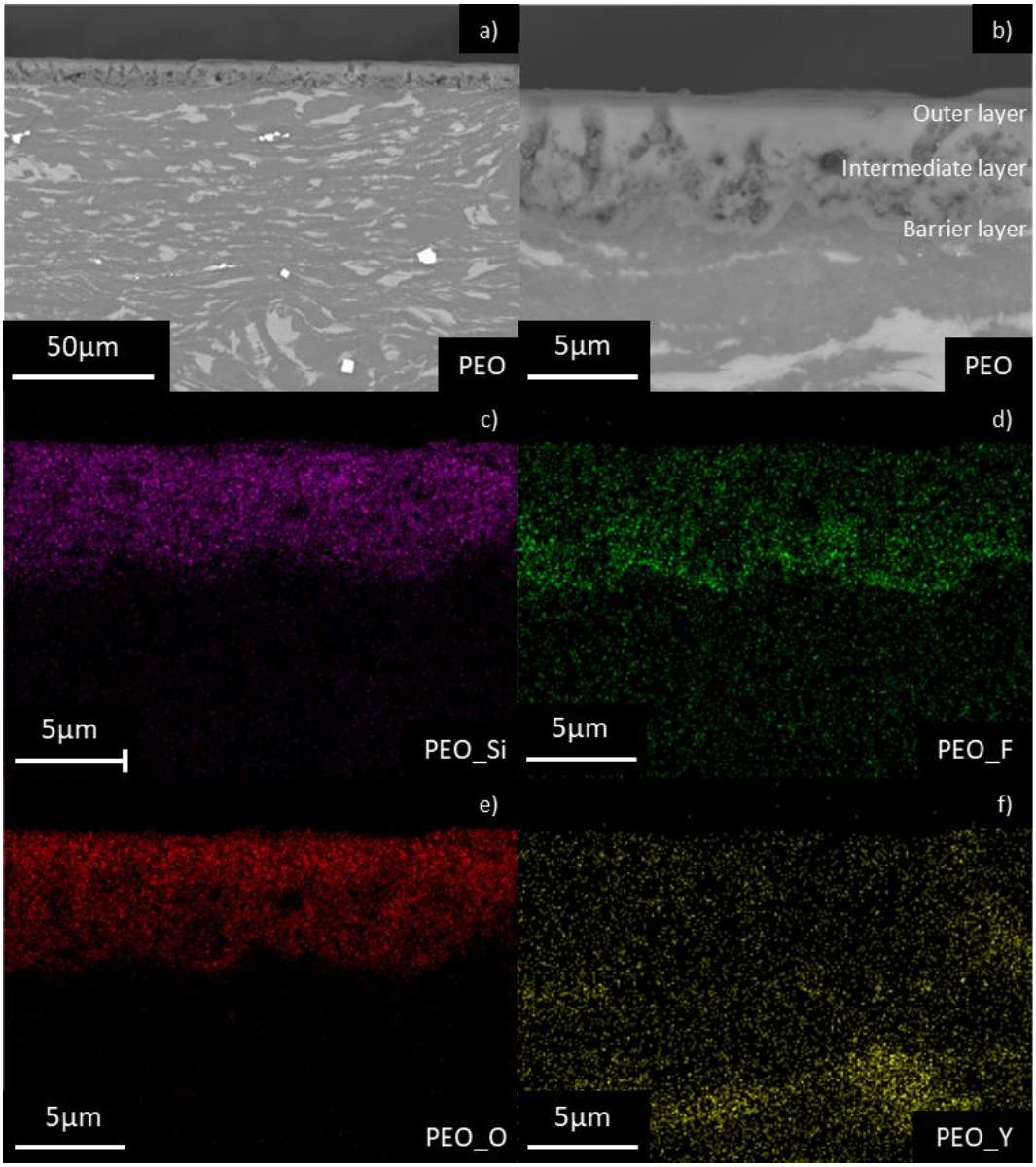

Figure 60. Cross–section examination of the unsealed PEO coating. (a,b) BSE micrographs and (c,d,e,f) X–ray elemental maps.

Figure 61 and Figure 62 show significant differences between the 5 min and 1 h sealed PEO coatings. After 5 min, the PEO layer does not undergo significant changes and, as marked by the brighter areas of the BSE micrograph and X–ray elemental maps, Ce–rich compounds are preferentially deposited within the crater–like pores [178] (Figure 61a). The BSE micrograph at higher magnification (Figure 61b) and the distribution of F (Figure 61d) suggest that the barrier inner layer remains intact and, therefore, the anticorrosion properties ascribed to this inner layer are not compromised. Sealing for 1 h (Figure 62), on the other hand, leads to important changes in the PEO coating. These are summarised as follows; i) decrease in the coating thickness up to 40% in some areas; ii) visible large pores through the film thickness; and iii) deterioration of the barrier layer which becomes hardly visible (Figure 62b). Indeed, the EDS map shows a depletion in F in the inner region (Figure 62d) indicating that the barrier layer has been partially dissolved.

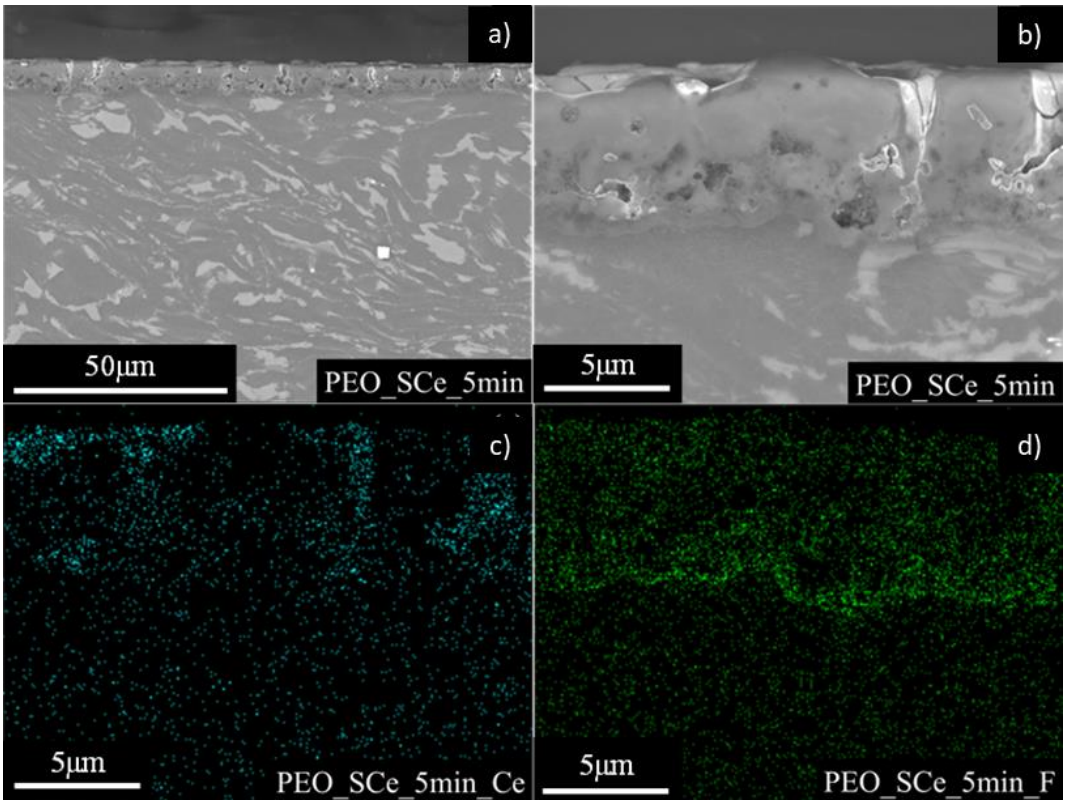

Figure 61. Cross section examination of the PEO_Ce_5min coating. (a,b) BSE micrographs and (c,d) X–ray elemental maps.

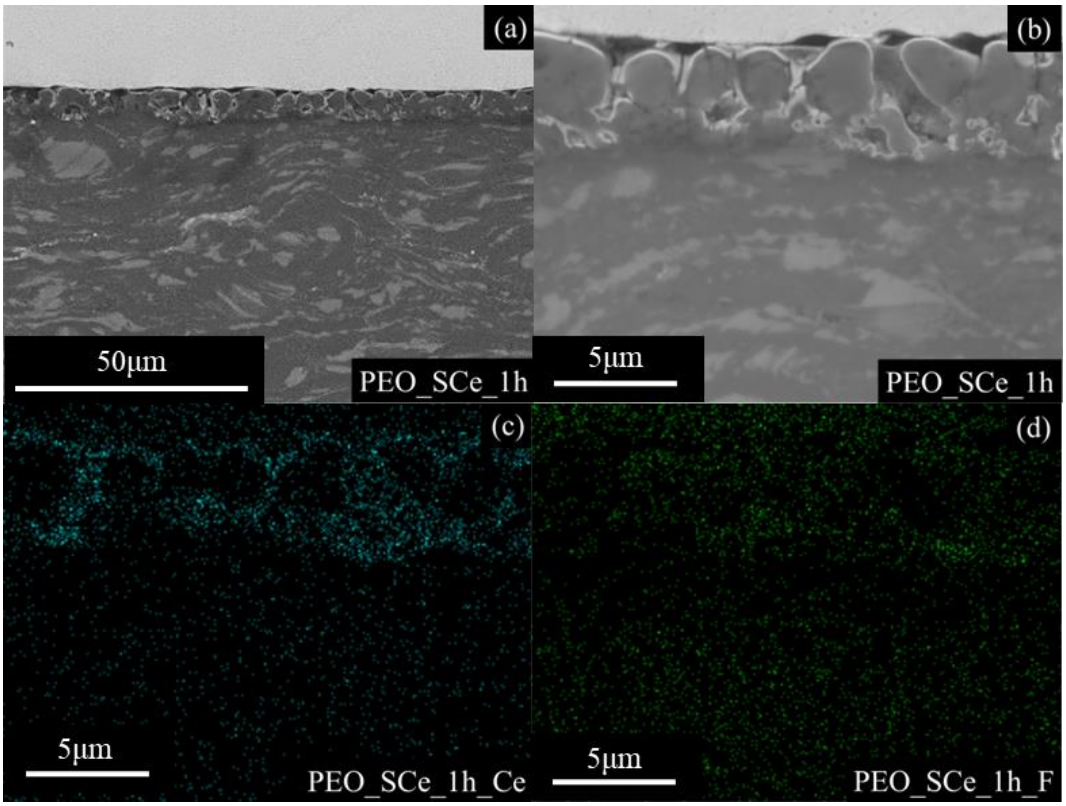

Figure 62. Cross section examination of the PEO_Ce_1h coating. (a,b) BSE micrographs and (c,d) X–ray elemental maps.

The XRD pattern of the unsealed PEO coating obtained at Bragg–Brentano geometry (Figure 63a) reveals only the presence of magnesium oxide (MgO). The formation of forsterite (Mg_2SiO_4) is detected using grazing angle geometry (Figure 63b) which indicates that Si element is incorporated as crystalline compound in the outer region of the coating. In the case of PEO_SCe_5min, CeO_2 compound is only detected using grazing angle (Figure 63b). After 1h sealing, CeO_2 diffraction peaks are revealed in both type of measurements. For both sealed coatings the peaks corresponding to Mg_2SiO_4 disappear for measurements obtained at 0.5º grazing angle, suggesting the dissolution of the coating during the post–treatment in acid solution. Other Ce–rich amorphous compounds may form, but they were not identified in the present study. In all the patterns, Mg peaks correspond to the substrate.

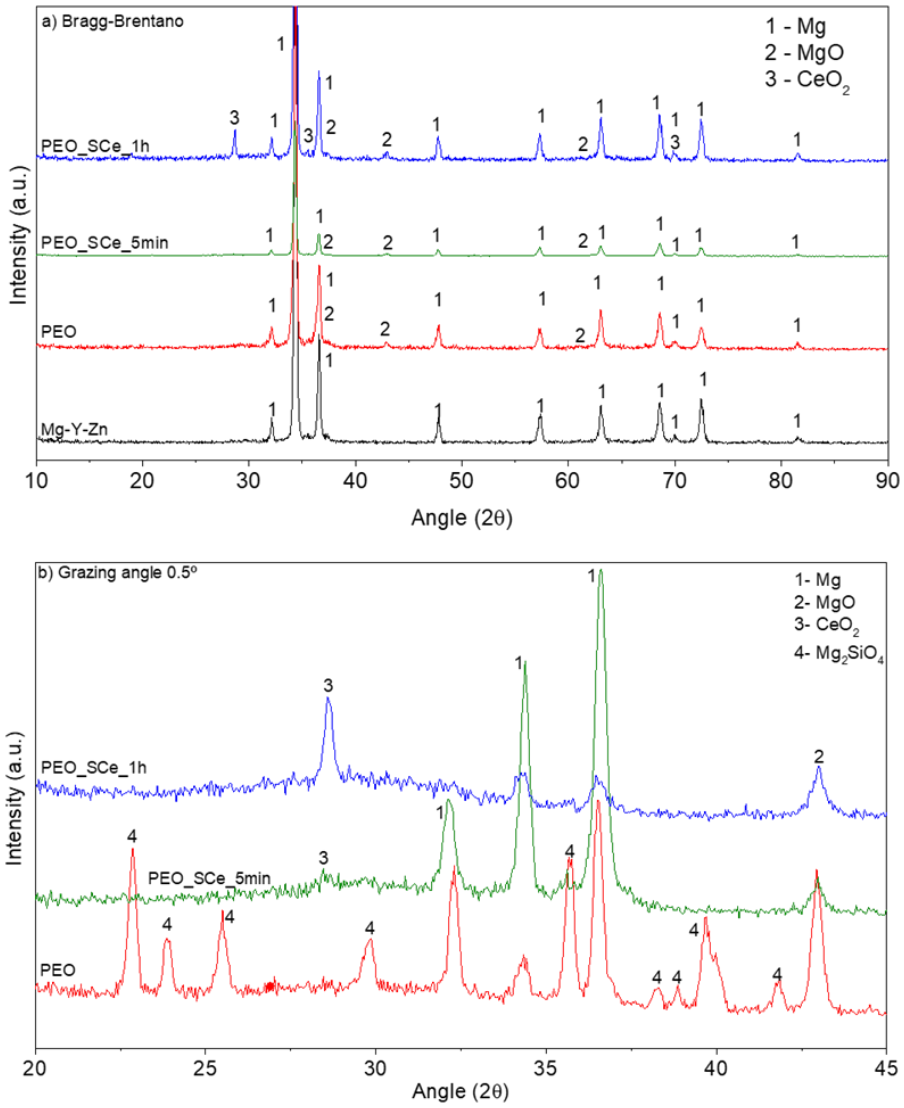

Figure 63. XRD patterns of studied materials. (a) Bragg–Brentano geometry and (b) grazing angle.

4.3.2.2 Corrosion Test: Polarization Curves and Hydrogen Evolution Test

The potentiodynamic polarization results obtained after immersion in 0.5 wt.% NaCl for 1 h are shown in Figure 64 and Table 33. The corrosion potential, E_{corr}, of the bulk material is higher (–1.50 $V_{Ag/AgCl}$) than that of the PEO coated specimen (–1.61 $V_{Ag/AgCl}$), although the latter is obviously more corrosion resistant. This is evidenced by the lower current densities of the anodic/cathodic branches and the well–defined passive region of ~400 mV between E_{corr} and the pitting potential, E_{pit} (–1.19 $V_{Ag/AgCl}$).

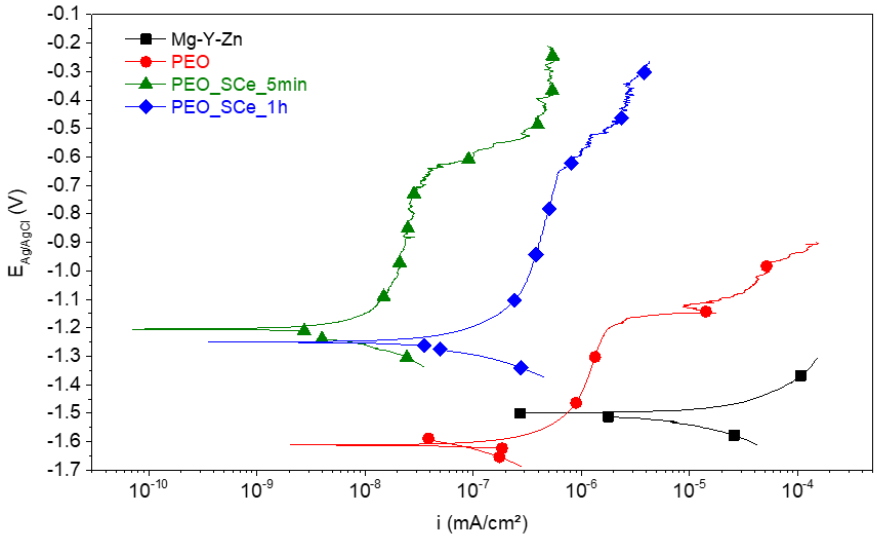

Figure 64. DC polarization curves of studied materials after 1h immersion in 0.5 wt.% NaCl.

Table 33. Parameters obtained from polarization curves in 0.5 wt.% NaCl.

Specimen	E_{corr} ($V_{Ag/AgCl}$)	i_{corr} (A cm^{-2})	E_{pit} ($V_{Ag/AgCl}$)
Mg–Y–Zn	–1.50	2.4×10^{-6}	–
PEO	–1.61	7.1×10^{-8}	–1.19
PEO_SCe_5min	–1.20	2.0×10^{-9}	–0.63
PEO_SCe_1h	–1.25	1.3×10^{-8}	–0.63

Ce–sealings yielded PEO coatings with higher E_{corr} and E_{pit} values (~ –1.2 $V_{Ag/AgCl}$ and –0.63 $V_{Ag/AgCl}$, respectively) and lower corrosion current densities, i_{corr}, namely, up to three orders of magnitude lower than the uncoated alloy (10^{-9} vs 10^{-6} A cm^{-2}). This was mainly associated with an increased surface passivity (~600 mV passive range) and further inhibition of the anodic reaction when compared to the unsealed coating. It needs to be noted that sealing for 1 h shifts the polarization curve towards higher current values for both the anodic and cathodic branches in comparison with the 5 min sealing. This is a clear indication of coating dissolution and insufficient blockage provided by the Ce–rich layer.

Figure 65 shows the collected hydrogen versus time for the studied materials up to 15 days of immersion in 0.5 wt.% NaCl. The kinetic laws calculated from the experimental data are gathered in Table 34 and were approximated by a linear equation $y = bt + a$, where y coordinate represents the collected hydrogen in mL cm^{-2} and t is the immersion time in days. As expected from the electrochemical measurements, the uncoated material reveals a high corrosion rate with significant amounts of hydrogen evolved from the surface. PEO coatings (without and with post–treatments) reduce considerably the hydrogen evolution when compared to the bulk

material (up to ~24 times in the best case for PEO_SCe_5min). Also, two trends can be distinguished depending on the immersion time: up to 3 days of immersion (short term) all the coatings show effective anticorrosion properties with values of accumulative hydrogen lower than 3 mL cm^{-2}. For longer immersion times, all the coated materials show some level of degradation, which is typical for this type of porous oxide layers without top layers such as paints. According to the total hydrogen collected, an opposite effect of Ce–based sealing post–treatments on the corrosion behaviour of PEO coating is observed: post–treatment conducted for 5 min reveals a beneficial effect whereas 1h sealing has a negative influence. This failure of the PEO_SCe_1h specimen was not observed in the short–term electrochemical tests, which shows the importance of carrying out long–term corrosion experiments.

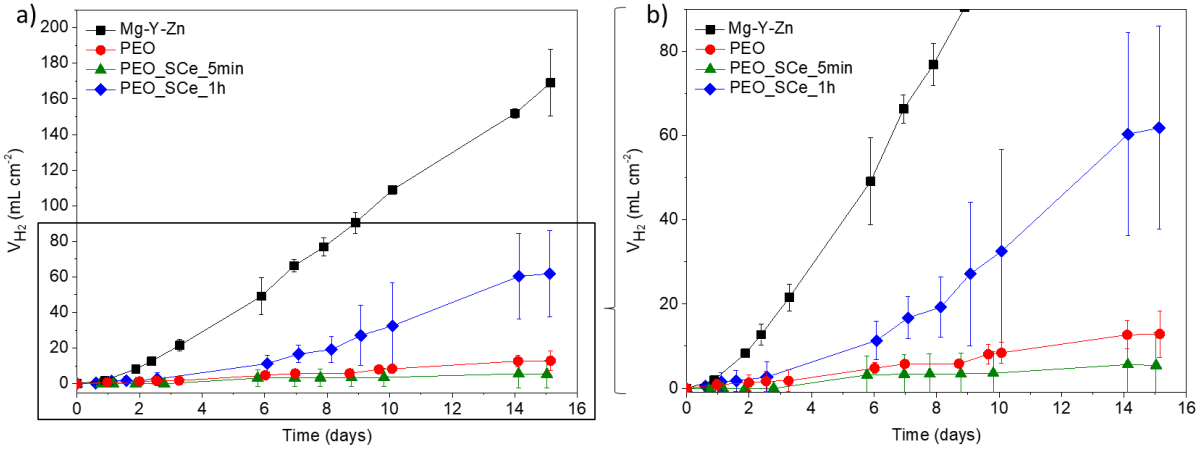

Figure 65. (a) Volume of hydrogen evolved from the cathodic reaction with immersion time of studied materials in 0.5 wt.% NaCl solution. (b) Detail for better comparison of PEO coated specimens.

Table 34. Kinetic laws calculated from hydrogen measurements.

Material	Kinetic law: y = *b t* + *a*; [y (mL cm^{-2}), t (days)]	Time (days)	R^2
Mg–Y–Zn	$y = 11.61t - 11.70$	0≤t≤15	0.99
PEO	$y = 0.88t - 0.46$	0≤t≤15	0.98
PEO_SCe_5min	$y = 0.48t - 0.38$	0≤t≤15	0.95
PEO_SCe_1h	$y = 2.17t$	0≤t≤8	0.83
	$y = 6.26t - 30.50$	8≤t≤15	0.99

4.3.3 Discussion on Ce–sealing of a PEO coating on Mg–Y–Zn LPSO alloy

LPSO Mg alloys are known to be highly susceptible to corrosion in aqueous media due to galvanic coupling between the cathodic LPSO phases and the α–Mg matrix. Therefore, the amount, composition and distribution of these phases are all factors needing consideration. Table 35 summarizes the influence of some of these factors and shows examples of literature

data on the corrosion of LPSO Mg alloys together with some of the experimental results obtained in the present study [55, 56, 297, 298, 306, 307].

Table 35. Examples of corrosion data for LPSO Mg alloys.

[Reference] Alloy	Corrosion data/Comments	
[298] Mg15Gd2Zn0.39Zr –As–cast –T4	3.5 wt.% NaCl	
	As–cast	T4
	E_{corr}* –1.57 $V_{Ag/AgCl}$	f_{LPSO} 27%
	i_{corr} 4.33 × 10^{-2} mA cm^{-2}	E_{corr}* –1.44 $V_{Ag/AgCl}$
	HER_{200h} 1.02 mL cm^{-2} d^{-1}	i_{corr} 1.16 × 10^{-1} mA cm^{-2}
	P* 2.32 mm y^{-1}	HER_{200h} 0.12 mL cm^{-2} d^{-1}
		P* 0.27 mm y^{-1}
	The improved long term corrosion behaviour of T4 treated alloy with LPSO structure was ascribed to: the lower VPD of LPSO vs α–Mg (in comparison with the eutectic phase) and the lower volume fraction of cathodic constituents.	
[307] Mg0.75Zn2Y –Gravity–cast –Injection–cast –Ribbon consolidated alloy (Mg0.75Zn2Y, Mg0.75Zn2Y0.5Al, Mg0.75Zn2Y1.5Al)	0.17 M NaCl (Hydrogen evolution)/ 0.1 M NaCl (Electrochemical measurements)	
	Mg0.75Zn2Y Gravity–cast	Mg0.75Zn2Y Injection–cast
	E_{corr}** –1.63 $V_{Ag/AgCl}$	E_{corr}** –1.72 $V_{Ag/AgCl}$
	P 2.8 mm y^{-1}	P 1.4 mm y^{-1}
	Mg0.75Zn2Y Ribbon–cons. alloy	Mg0.75Zn2Y0.5Al Ribbon–cons. alloy
	E_{corr}** –1.64 $V_{Ag/AgCl}$	E_{corr}** –1.71 $V_{Ag/AgCl}$
	P 1.0 mm y^{-1}	P 0.8 mm y^{-1}
	Mg0.75Zn2Y1.5Al Ribbon–cons. alloy	
	E_{corr}** –1.72 $V_{Ag/AgCl}$	
	P 0.6 mm y^{-1}	
	– Rapidly solidified alloys showed lower corrosion rate. – The best corrosion behaviour was achieved for the alloy combining aluminium addition and rapid solidification.	
[306] Mg15.24Gd4.75Zn –As cast –T4 –T6 –T6F	3.5 wt.% NaCl	
	As–cast	T4
	f_{LPSO} 19.68%	f_{LPSO} 18.74%
	E_{corr}* –1.53 $V_{Ag/AgCl}$	E_{corr}* –1.57 $V_{Ag/AgCl}$
	i_{corr} 8.942 × 10^{-2} mA cm^{-2}	i_{corr} 4.507 × 10^{-2} mA cm^{-2}
	P 323.39 mm y^{-1}	P 17.30 mm y^{-1}
	T6	T6F
	E_{corr}* –1.58 $V_{Ag/AgCl}$	E_{corr}* –1.63 $V_{Ag/AgCl}$
	i_{corr} 1.604 × 10^{-2} mA cm^{-2}	i_{corr} 2.630 × 10^{-2} mA cm^{-2}
	P 4.98 mm y^{-1}	P 9.75 mm y^{-1}
	LPSO phase was formed in T6 and T6F alloys and acted as corrosion barrier improving the degradation behaviour.	

P: corrosion rate

HER_{200h}: hydrogen evolution rate during 200 h immersion

**Calculated from the reported values*

***Obtained from graphical data*

Table 35. Examples of corrosion data for LPSO Mg alloys. (cont.)

[Reference] Alloy	Corrosion data/Comments	
[55]	0.1 M NaCl	
Mg0.9Zn1.6Y	Mg–0.9Zn–1.6Y	Mg–2.1Zn–5.2Y
Mg2.1Zn5.2Y	f_{LPSO} 3.6%	f_{LPSO} 20.3%
Mg3.1Zn7.6Y	E_{corr}* –1.64 $V_{Ag/AgCl}$	E_{corr}* –1.60 $V_{Ag/AgCl}$
–As cast	i_{corr} 1.2 × 10^{-2} mA cm^{-2}	i_{corr} 6.7 × 10^{-2} mA cm^{-2}
	P* 0.23 mm y^{-1}	P* 3.42 mm y^{-1}
	Weight loss** 0.5 mg cm^{-2} d^{-1}	Weight loss** 4.5 mg cm^{-2} d^{-1}
	Mg–3.1Zn–7.6Y	
	$\Delta V_{LPSO–matrix}$ 250 mV	
	f_{LPSO} 36.2%	
	E_{corr}* –1.61 $V_{Ag/AgCl}$	
	i_{corr} 2.6 × 10^{-2} mA cm^{-2}	
	P* 0.91 mm y^{-1}	
	Weight loss** 2.0 mg cm^{-2} d^{-1}	
	LPSO phase leads to micro galvanic activities increasing the corrosion rate.	
[297]	0.1 M NaCl	
Mg97Y2Zn1	Mg97Y2Zn1 transversal	Mg97Y2Zn1 longitudinal
	f_{LPSO} 25%	P 10(t<5h) mm y^{-1}
	P 40(t<5h) mm y^{-1}	P 30 mm y^{-1}
	P 20 mm y^{-1}	
	The corrosion resistance of extruded alloys is strongly influenced by the orientation of LPSO–phase alignments. Transversal samples showed a better long term corrosion performance associated with the corrosion front morphology.	
[56]	3.5 wt.% NaCl	
Mg4.59Zn8.92Y0.47Ti	As–cast	400 °C × 10 h
–As–cast	E_{corr}* –1.60 $V_{Ag/AgCl}$	E_{corr}* –1.62 $V_{Ag/AgCl}$
–400 °C × 10 h	i_{corr} 5.16 × 10^{-2} mA cm^{-2}	i_{corr} 8.77 × 10^{-2} mA cm^{-2}
–520 °C × 6 h	P** 6 mm y^{-1}	P** 16 mm y^{-1}
–520 °C × 6 h + 400 °C ×10 h	520 °C × 6 h	520 °C × 6 h + 400 °C × 10 h
	E_{corr}* –1.62 $V_{Ag/AgCl}$	E_{corr}* –1.61 $V_{Ag/AgCl}$
	i_{corr} 4.37 × 10^{-2} mA cm^{-2}	i_{corr} 7.52 × 10^{-2} mA cm^{-2}
	P** 2 mm y^{-1}	P** 8 mm y^{-1}
	Rod–like LPSO phases revealed a better performance with a more compact corrosion products film.	
Present study	0.5 wt.% NaCl	
	Mg–Y–Zn	
	$\Delta V_{LPSO–matrix}$ 60 mV	
	E_{corr} –1.50 $V_{Ag/AgCl}$	
	i_{corr} 2.4×10^{-3} mA cm^{-2}	
	P 26.46 mm y^{-1}	
	Low Volta potential differences obtained for the LPSO/α–Mg (~60 mV) do not promote the micro galvanic corrosion process. Moreover, inclusions Y–rich with higher Volta Potential Differences are expected to play a minor role in corrosion processes due to their negligible contribution to the total cathode area.	

P: corrosion rate

HER_{200h}: hydrogen evolution rate during 200 h immersion

**Calculated from the reported values*

***Obtained from graphical data*

Chapter 3

Detailing the corrosion performance of the bulk material is not the final goal of the present work, although it is worth to note that the studied Mg–Y–Zn alloy shows slightly lower corrosion rate in comparison with the available data. This is likely to be associated with the low Volta potential differences obtained for the LPSO/α–Mg (~60 mV) that do not promote the micro galvanic corrosion process. Moreover, Y–rich inclusions with higher Volta potential differences are expected to play a minor role in corrosion processes due to their negligible contribution to the total cathode area.

In this particular study, the combination of PEO processing and Ce–sealing was evaluated for the first time as a way for improving the corrosion performance of an LPSO Mg alloy. SEM/EDS and XRD characterization revealed that PEO processing can successfully be applied to a Mg alloy containing LPSO phases. The typical three–layered structure of AC PEO coatings is obtained and the intermetallics are oxidized/incorporated into the coating without disrupting its thickness or morphology (Figure 66a). The F–rich inner barrier layer (<500 nm) is the main responsible for the anticorrosion properties of the coating, whereas the outer layers with their interconnected porosity only serve as a short–term corrosion barrier [90, 308, 309].

Electrochemical (short–term) and hydrogen measurements (long–term) demonstrate that a short Ce–sealing of 5 min further improves the corrosion protection offered by the PEO coating, increasing its passive range and pitting potential. These effects were attributed to the precipitation of CeO_2 within the coating pores and cracks and the concomitant reduced surface porosity (Figure 66b). In addition to the blocking effect of Ce–rich compounds, there is also the possibility of a self–healing mechanisms related to the redox reactions involving Ce(III) and Ce(IV) [310-312]. For example, Ce(IV)–containing compounds may release Ce^{3+} ions, which then diffuse to the corroding areas and precipitate as $Ce(OH)_3$ and/or Ce_2O_3 when the pH increases. It is worth mention that if Ce^{3+} ions oxidize to Ce(IV) species, then these would precipitate at lower pH values.

The sealing mechanism of PEO coatings using cerium salts has been proposed in previous studies [178, 288] and can be summarized as follows: i) oxidation of Ce^{3+} ions to $Ce(OH)_2^{2+}$ due to the presence of H_2O_2 in the sealing solution (13), ii) partial dissolution in acidic media of the MgO and Mg_2SiO_4 phases, which consume protons and lead to local alkalinisation, (14) and (15); and, iii) precipitation of insoluble oxide/hydroxide Ce compounds ($Ce(OH)_4$ and CeO_2) due to the local pH increase (16).

$$2Ce^{3+}(aq) + H_2O_2(aq) + 2OH^-(aq) \rightarrow 2Ce(OH)_2^{2+}(aq) \quad (13)$$
$$MgO(s) + 2H^+(aq) \rightarrow Mg^{2+}(aq) + 2H_2O(l) \quad (14)$$
$$Mg_2SiO_4(s) + 4H^+(aq) \rightarrow 2Mg^{2+}(aq) + SiO_2(s) + H_2O(l) \quad (15)$$
$$Ce(OH)_2^{2+}(aq) + 2OH^-(aq) \rightarrow Ce(OH)_4(s) \rightarrow CeO_2(s) + 2H_2O(l) \quad (16)$$

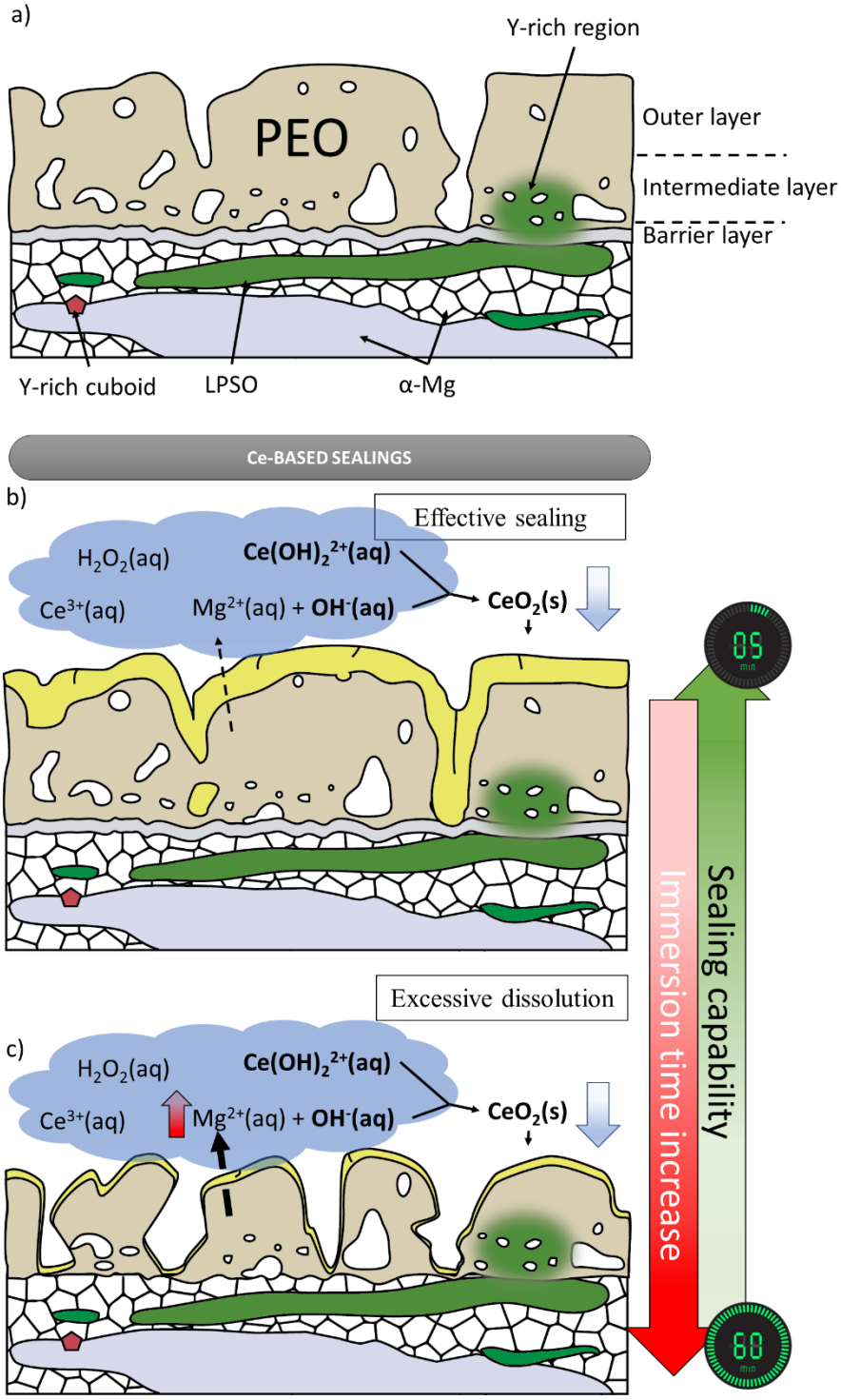

Figure 66. Protection mechanism: (a) PEO, (b) PEO_SCe_5min, (c) PEO_SCe_1h.

Increasing the sealing time (Figure 66c) leads to an excessive dissolution of the oxide layer in acidic media (15) and deterioration of the inner barrier layer which negatively influence the

corrosion performance. The lower corrosion resistance of PEO layers after long immersion time in acidic solution is in agreement with results obtained by Phuong *et al.* [293] and differ from author's previous work [178], pointing out the importance of the individual characteristics of the PEO layer (thickness, microstructure and composition) for achieving the optimum sealing time in Ce solutions which, due to their low pH, can become quite aggressive for MgO and other phases that typically constitute PEO coatings.

4.3.4 Concluding Remarks on Ce–sealed PEO coating on Mg–Y–Zn

The most important conclusions can be summarized as follows:

- The studied Mg–Y–Zn alloy shows fully recrystallized α–Mg grains, coarse and elongated α–Mg grains, strings of LPSO phases and Y–rich cuboids. The high–volume fraction of LPSO phases and their cathodic activity are the main factors contributing to the high corrosion rate of the uncoated alloy.
- LPSO phases are not an obstacle during PEO processing. The coating is mainly composed of MgO/Mg_2SiO_4 and shows a uniform three–layered structure with a <500 nm barrier layer. The enhanced surface passivity after PEO treatment significantly reduced the corrosion rate in comparison to the untreated alloy.
- Sealing of the PEO coating in an acidic Ce–containing solution for 5 minutes led to accumulation of CeO_2 on the surface, which partially blocked the coating pores and cracks. The combined effects of insoluble Ce–rich compounds and passivity of the PEO coating resulted in a much lower corrosion rate than that of the substrate (2.4×10^{-6} A cm^{-2} vs 2.0×10^{-9} A cm^{-2}). Electrochemical measurements also revealed a higher pitting potential in comparison to the unsealed coating (–1.19 $V_{Ag/AgCl}$ vs –0.63 $V_{Ag/AgCl}$).
- Sealing for 1 hour improved the short–term corrosion resistance of the PEO coating. However, long–term experiments revealed the opposite behaviour. This was associated with the excessive dissolution of the PEO coating during immersion in the acidic Ce–containing solution. This side effect of the dissolution/precipitation mechanism of Ce–sealings highlights the need for optimizing the sealing time in Mg/PEO systems.

4.3.5 Results and Discussion of Ca–sealings of a PEO coating on AZ91 Mg

4.3.5.1 Coating Morphology and Composition

PEO coatings were fabricated at Northeastern University of China according to conditions collected on Table 36, where the sealing details are also shown.

Table 36. PEO and Ca–based sealings –conditions for surface modification of AZ91D alloy.

PEO Electrolyte	PEO conditions	Sealing solution	Sealing conditions
$Na_3PO_4 \cdot 12H_2O$ 30 g/L $KF \cdot 2H_2O$ 4 g/L NaOH 2 g/L	Pulsed DC 30 ± 1 °C 2000 mA cm^{-2} 500 Hz 15 min 60 s ramp duty cycle 30%	$Ca(NO_3)_2$ 70 g/L Sodium dodecyl sulphate (SDS) 0.1 mol/L HNO_3	pH 3, 4 and 5 60 min (80 ± 2) ºC

Figures 67 and 68 show the surfaces and cross sections of the PEO coating before and after the studied sealing treatments. Cracks and open pores (2–5 μm in diameter) can be observed on the coating surface (Figure 67a). This is the typical morphology of PEO coated Mg alloys that is generated due to gas evolution and thermal stresses associated with discharges [313]. After the post–treatments, the surface of all PEO coatings is partially covered by newly formed precipitates. Precipitation is more prominent for lower pH values and in the presence of SDS, suggesting that coating or substrate dissolution under relatively acidic conditions plays a vital role in the sealing process. The effect of SDS on the reaction/precipitation process is quite significant as seen in the PPEO–Ca–pH3–SDS specimen, which is completely covered by Ca–rich deposits making difficult to distinguish the initial crater–like morphology and microcracks of the initial PEO coating (Figure 67e,f).

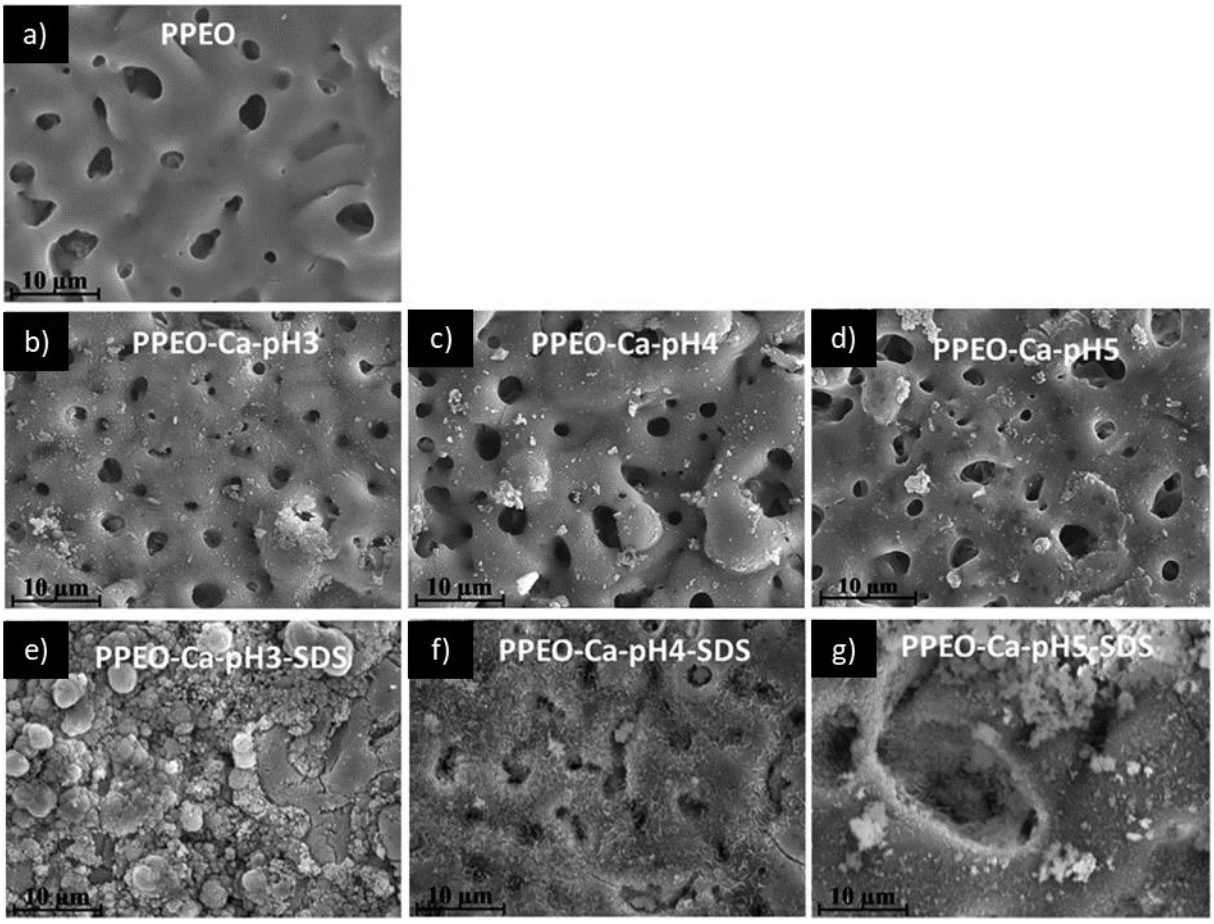

Figure 67. Surface micrographs of PEO coatings before and after post–treatment in different conditions.

As shown in Figure 68, the post–treatment has a slight influence on the coating thickness, being ~20 µm for all the specimens. The coatings reveal a double–layered microstructure with a porous outer part (pores being smaller near the substrate) and a dense micrometer–thick barrier layer adjacent to the substrate. The acidic conditions during the sealing treatments result in partial chemical dissolution of the coating material. However, the effect is not very significant. Therefore, the coatings maintain the double–layer structure without major changes in their morphology.

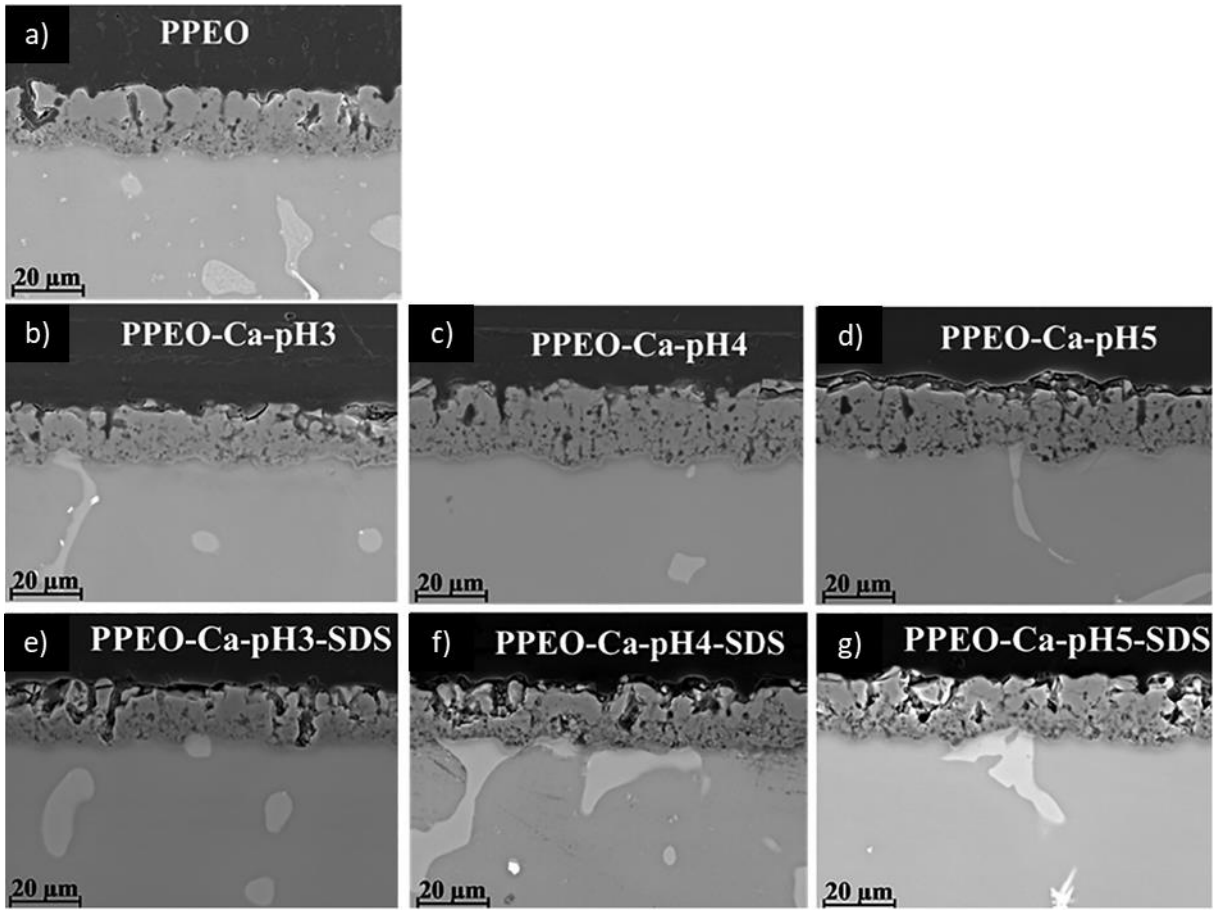

Figure 68. Cross–sectional micrographs of PEO coated Mg alloy before and after post–treatment in different conditions. (a) PPEO: (22.7 ± 1.6) µm, (b) PPEO–Ca–pH3: (20.1 ± 1.5) µm, (c) PPEO–Ca–pH4: (22.5 ± 1.5) µm, (d) PPEO–Ca–pH5: (20.5 ± 1.1) µm, (e) PPEO–Ca–pH3–SDS: (19.6 ± 1.3) µm, (f) PPEO–Ca–pH4–SDS: (21.7 ± 1.7) µm, (g) PPEO–Ca–pH5–SDS: (22.5 ± 2.2) µm.

Figure 69 allows for identifying the location of Ca–rich deposits that formed following partial dissolution of the coating material. As shown in the micrographs, the Ca signal is more evident for the specimens sealed in the presence of SDS. It is worth noting that the location of the Ca–rich deposits is also observed in the optical micrographs due to preferential adsorption or contamination of the blue dye–containing lubricant that was used for polishing (attempts to remove this contamination by ultrasonic cleaning were unsuccessful). As expected, Ca–rich deposits are mainly located within the pores and other coating defects.

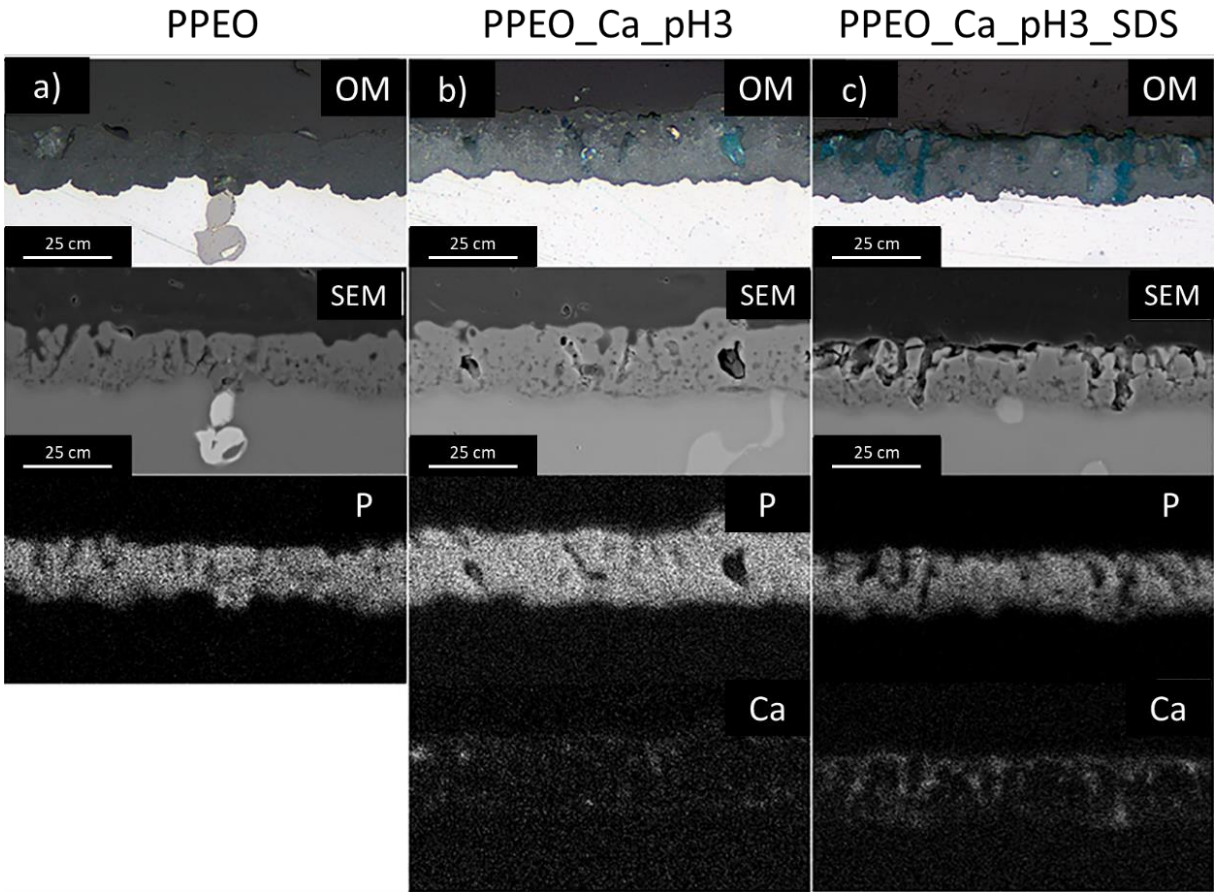

Figure 69. Cross–sectional micrographs and EDS mappings of PEO coated Mg alloy before and after post–treatment in different electrolytes. (a) PPEO, (b) PPEO–Ca–pH3 and (c) PPEO–Ca–pH3–SDS.

The chemical composition of the coatings (plan view area) before and after sealing treatment can be found in Table 37. The initial coating is mainly composed of O, Mg, P and F. After the sealing post–treatments, Mg and F contents are reduced while O levels increase. Ca is detected on the sealed surfaces, particularly when SDS is introduced into the sealing treatment solution. The concentration of P on the coating surface is slightly influenced by the sealing treatment.

Table 37. Results of the local EDS surface analysis of the coatings (at.%).

Element (at.%)	O	Mg	P	Al	Na	Ca	K	F
PPEO	51.1	27.7	12.2	1.8	2.5	/	0.1	4.6
PPEO–Ca–pH3	55.9	26.4	11.6	2.2	2.6	1.0	0.2	0.1
PPEO–Ca–pH4	53.2	28.7	12.1	2.1	3.0	0.5	0.3	0.1
PPEO–Ca–pH5	27.1	43.1	22.7	1.8	3.0	1.2	0.8	0.2
PPEO–Ca–pH3–SDS	56.2	8.2	14.9	2.1	1.0	17.4	0.1	0.1
PPEO–Ca–pH4–SDS	52.2	24.6	13.4	2.1	1.5	3.5	0.1	2.5
PPEO–Ca–pH5–SDS	53.8	20.3	14.2	1.1	2.8	4.3	0.4	3.0

Figure 70 gathers the XRD results for the studied systems. MgO peaks and a broad amorphous peak in the 20–35° range are the most distinct features in the patterns. This suggests that P and

F are incorporated as amorphous phases within the coating. Peaks corresponding to hydroxyapatite, $Ca_{10}(PO_4)_6(OH)_2$, were also detected in the PPEO–Ca–pH3–SDS specimen. The broad amorphous peak varied in intensity from one specimen to other, without a very clear trend. This could be related to a competition between dissolution of the coating material and precipitation of Ca–rich compounds on the surface.

Based on the above results, the following sealing mechanism is proposed. In the $Ca(NO_3)_2$ post–treatment solution, dissolution and precipitation processes compete during immersion: the original coating is dissolved due to the acidic conditions and, as a result, there is a local increase in pH and phosphate liberation, (17) and (18). This change in the electrolyte triggers the reaction between Ca^{2+} and phosphate ions (19, 20), resulting in precipitation of hydroxyapatite. When SDS is present, nucleation of hydroxyapatite is favoured [314] and a greater amount of sealing deposits are formed.

$$MgO(s) \xrightarrow{pH\ 3} Mg^{2+}(aq) + OH^{-}(aq) \quad (17)$$

$$Mg_3(PO_4)_2(s) \xrightarrow{pH\ 3} 3Mg^{2+}(aq) + 2PO_4{}^{3-}(aq) \quad (18)$$

$$10Ca^{2+}(aq) + 6H_2PO_4{}^{-}(aq) + 2OH^{-}(aq) \xrightarrow{SDS} Ca_{10}(PO_4)_6(OH)_2(s) + 12H^{+}(aq) \quad (19)$$

$$10Ca^{2+}(aq) + 6HPO_4{}^{2-}(aq) + 2OH^{-}(aq) \xrightarrow{SDS} Ca_{10}(PO_4)_6(OH)_2(s) + 6H^{+}(aq) \quad (20)$$

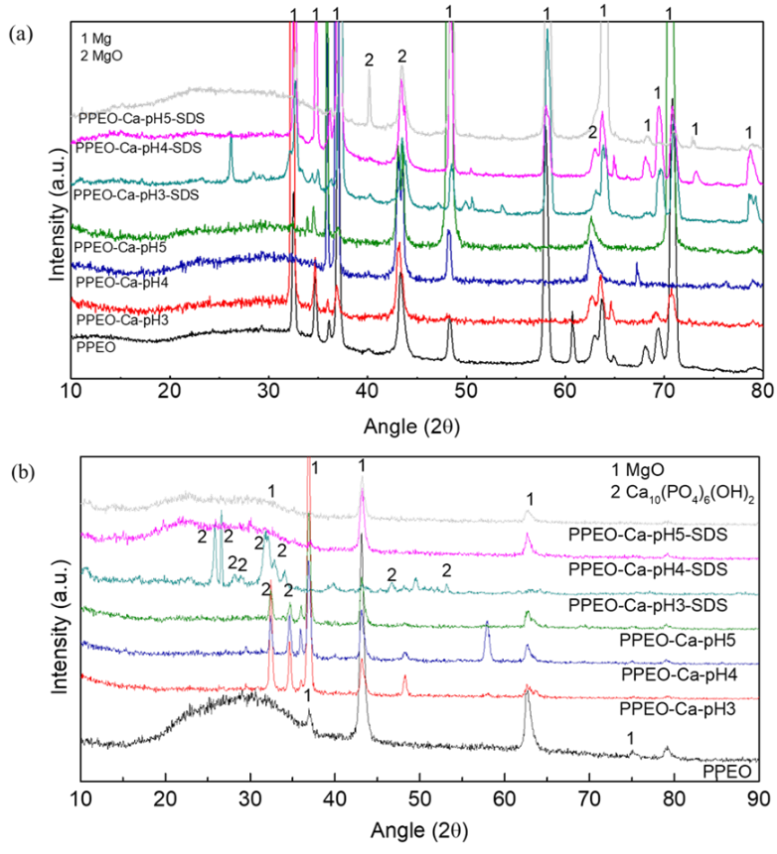

Figure 70. XRD patterns of different coatings (a) Bragg–Brentano, (b) Glancing angle (ω = 0.5º).

The survey XPS spectra and high–resolution Ca 2p, P 2p and S 2p spectra of the post–treated coatings are shown in Figure 71. The Ca peak located at 347.1 eV is consistent with the presence of $Ca_{10}(PO_4)_6(OH)_2$ (Figure 71b,c) [315]. The binding energy of P 2p (Figure 71d,e) at 131.5 eV corresponds to PO_4^{3-} and the one at 133.3 eV can be assigned to HPO_4^{2-} [316, 317]. The latter suggests the formation of additional phosphates in the coating (e.g. $CaHPO_4$). SDS is also detected on the coating surface after sealing post–treatment process. The spectrum of S 2p (Figure 71f) is attributed to SO_4^{2-} [318].

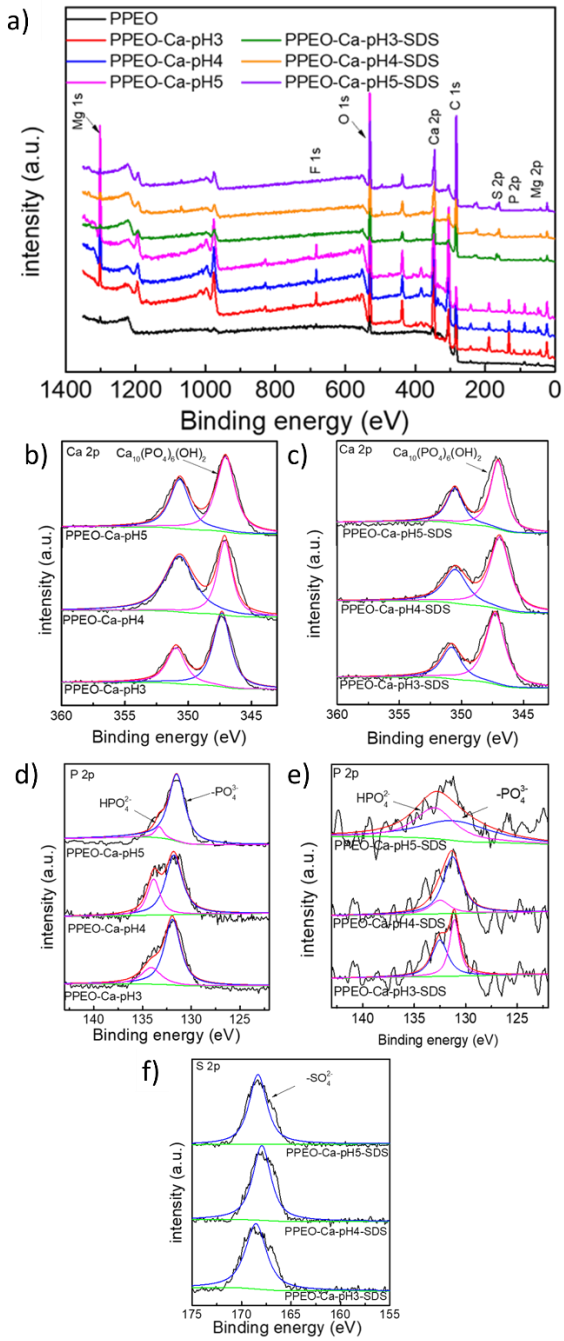

Figure 71. (a) XPS–survey spectra and (b–f) high–resolution spectra of the coatings. (b) Ca 2p; (c) Ca 2p, SDS; (d) P 2p; (e) P 2p, SDS; and (f) S 2p, SDS.

4.3.5.2 Corrosion Test: Polarization curves and EIS

The corrosion resistance of the coatings was evaluated by performing polarization tests in 3.5 wt.% NaCl solution at room temperature (Figure 72 and Table 38). It can be seen that the polarization curves are shifted to lower current densities and higher potentials for all the sealed coatings. The calculated corrosion current density (i_{corr}) of the unsealed coating is 0.57 μA/cm^2, whereas the i_{corr} of the coatings after post–treatment decreases by one order of magnitude. The lowest values were found for the coatings sealed in the presence of SDS. It is also worth noticing that the slope changes in the anodic branches (i.e. breakdown potentials) are higher in case of sealed specimens, indicating an improved passivation of the surfaces.

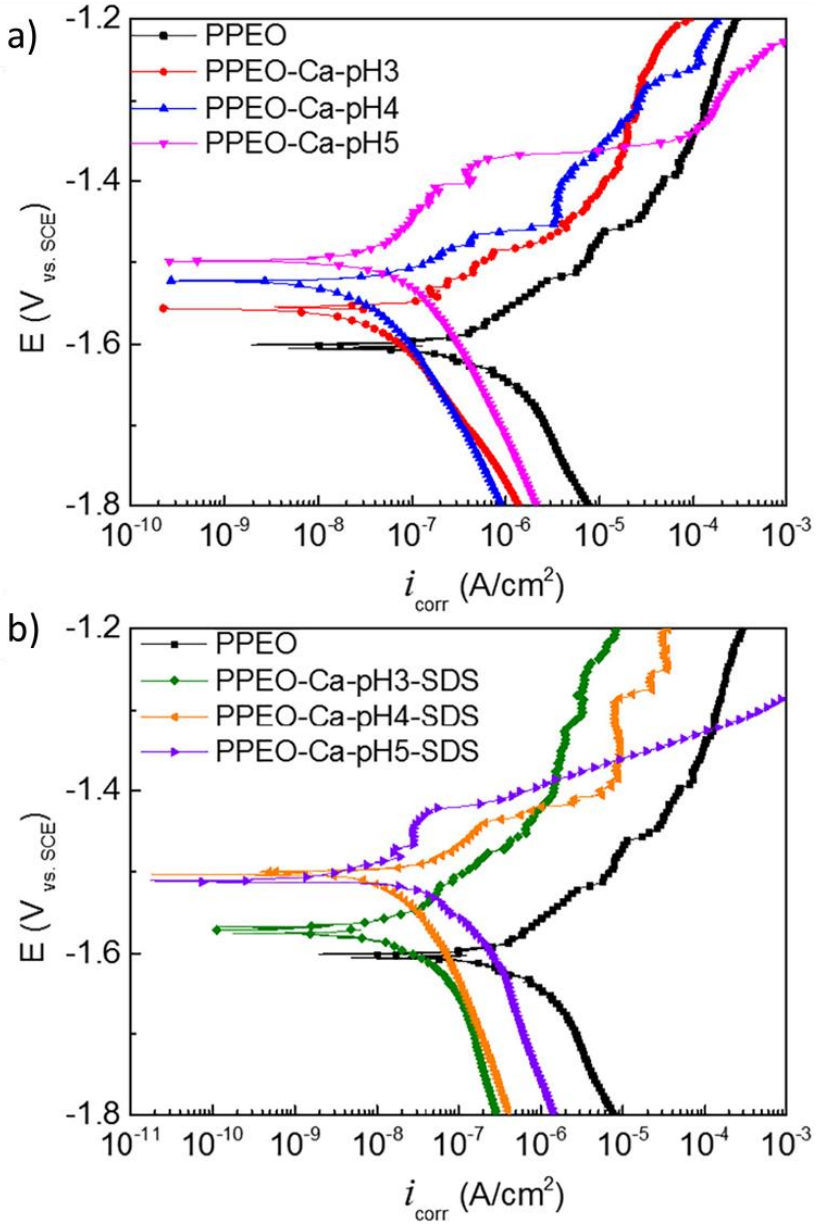

Figure 72. Polarization curves of the coatings in 3.5 wt.% NaCl solution.

Table 38. Electrochemical data of different coatings obtained from polarization test.

Sample	PPEO	PPEO–Ca–pH3	PPEO–Ca–pH4	PPEO–Ca–pH5	PPEO–Ca–pH3–SDS	PPEO–Ca–pH4–SDS	PPEO–Ca–pH5–SDS
E_{corr} (V_{SCE})	–1.60	–1.56	–1.52	–1.50	–1.57	–1.50	–1.51
i_{corr} (μA/cm^2)	0.572	0.032	0.023	0.085	0.014	0.012	0.028

EIS measurements were performed to investigate the long–term corrosion performance of the coatings, as shown in Figure 73 and Figure 74. According to the Nyquist plots, PEO–Ca–pH3–SDS and PEO–Ca–pH4–SDS show a large capacitive loop at low frequencies (Figure 73a,b), indicating superior corrosion resistance versus the coatings without corrosion inhibitor. It can be seen in the Bode plots in Figure 73c that the impedance modulus (|Z|) in the low frequency range increased significantly after sealing treatment. This enhancement was more noticeable for the coatings with the addition of corrosion inhibitor, which also show an additional time constant. The phase angle of PEO–Ca–pH3–SDS is close to 90°, suggesting that the open pores of the layer are blocked by SDS as well as by hydroxyapatite. SDS is suggested to be present at the surface of the coating by a mechanism of adsorption through its hydrophilic head.

It is worth mentioning that hydroxyapatite is more stable than MgO at neutral pH, thus enhancing the performance of the PEO coating in 3.5 wt.% NaCl solution. In Figure 74, the impedance values at low frequency decrease by one order of magnitude for all samples after 120 h immersion test, although the impedance of the sealed coatings is still higher than that of the unsealed coating. Equivalent circuits were used to fit the obtained EIS data (Figure 75). R_s represents the resistance of NaCl solution, R_{Ca} and CPE_{Ca} are the corrosion resistance and capacitance of the Ca–rich layer. R_{PEO} and CPE_{PEO} are the corrosion resistance and capacitance of the porous PEO coating. CPE_{dl} and R_p are related to the double layer capacitance and charge transfer resistance at the metal/electrolyte interface.

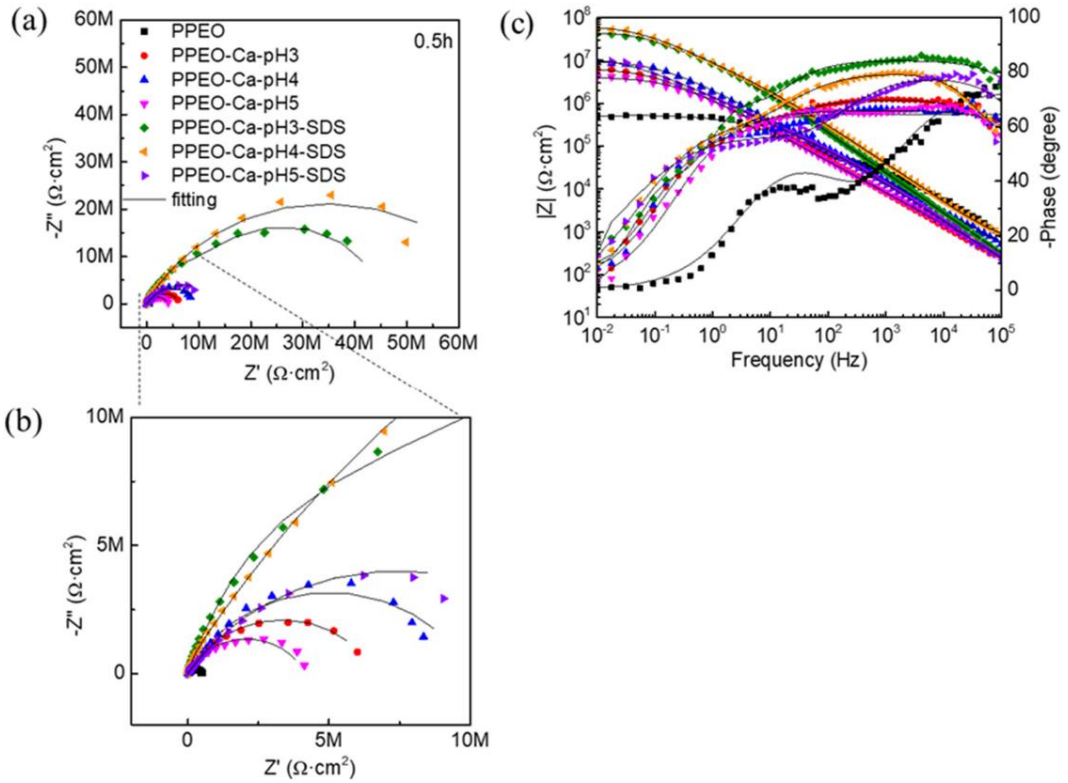

Figure 73. EIS plots of the coatings after immersion 0.5 h in 3.5 wt.% NaCl solution. (a) Nyquist plots, (b) enlarged Nyquist plots and (c) Bode plots.

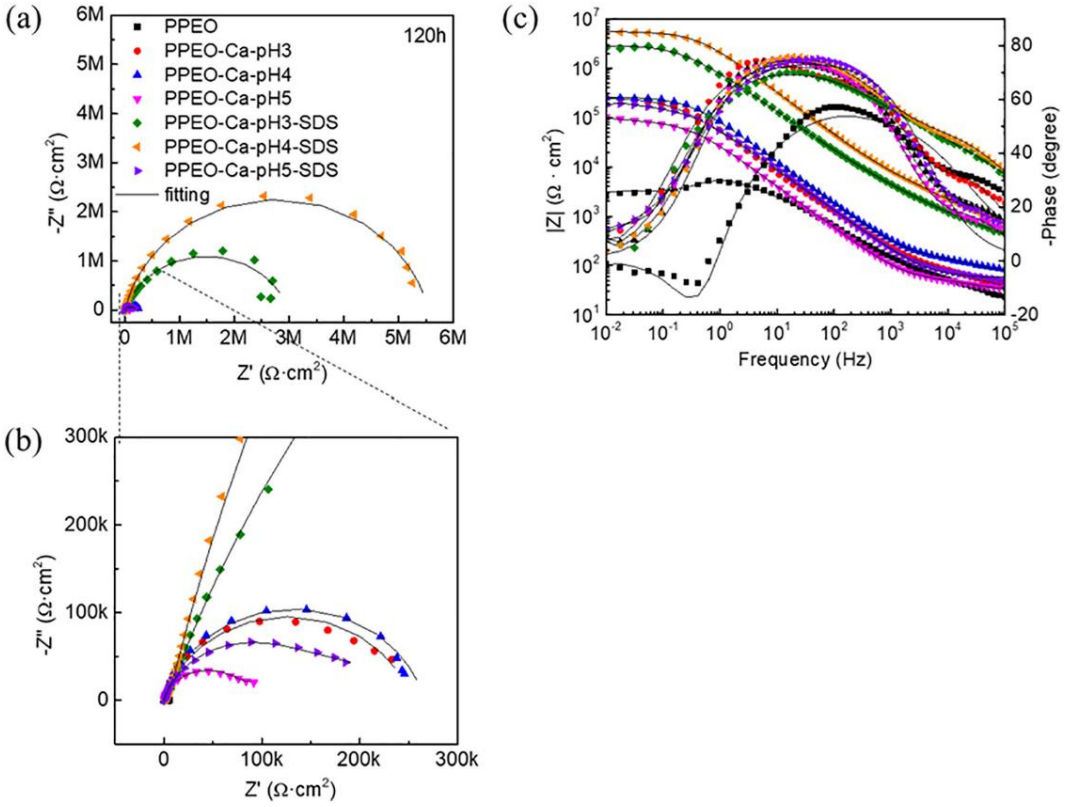

Figure 74. EIS plots of the coatings after immersion 120 h in 3.5 wt.% NaCl solution. (a) Nyquist plots, (b) enlarged Nyquist plots and (c) Bode plots.

The fitted electrochemical parameters are summarized in Table 39 and Table 40. The total corrosion resistance (R_{total}) is used to represent and evaluate the coating performance (Figure 76). The corrosion resistance of PPEO–Ca–pH4–SDS is significantly higher compared to that of other coatings, although more amounts of hydroxyapatite are deposited on the surface of PPEO–Ca–pH3–SDS. It can be inferred that the pH value of the post–treatment electrolyte has an effect on the corrosion resistance of the composite coatings, since the acidic post–treatment electrolyte also results in the partial dissolution of the composite coating and a decrease of corrosion resistance. Moreover, addition of SDS has a huge influence on improvement of the corrosion performance of the coatings, which is probably due to the enhanced nucleation of phosphates and the inhibition effect of SDS.

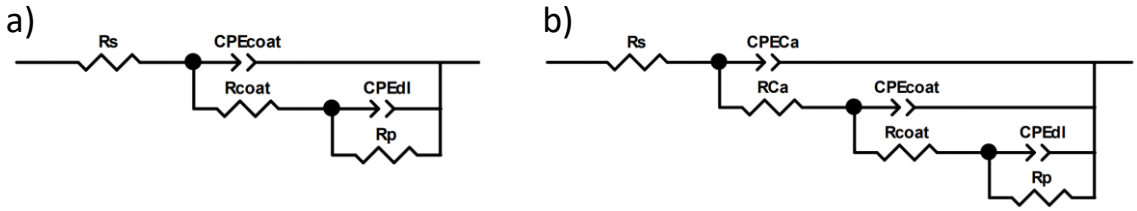

Figure 75. (a) Equivalent circuit used to fit PPEO and PPEO–Ca coatings and (b) equivalent circuit used to fit PPEO–Ca–SDS coatings.

Table 39. Fitted results of EIS plots of different coatings after immersion 0.5 h in 3.5 wt.% NaCl solution (R given in Ω cm^2; CPE given in S s^{-n} cm^{-2}; L given in Ω s cm^2).

Sample	R_s	CPE_{Ca}	n	R_{Ca}	CPE_{PEO}	n	R_{PEO}	CPE_{dl}	n	R_p
PPEO	36.5	–	–	–	21.2	0.81	4.28×10^4	21.7	0.68	4.90×10^5
PPEO–Ca–pH3	46.84	–	–	–	13.1	0.78	1.08×10^6	12.2	0.67	5.54×10^6
PPEO–Ca–pH4	38.85	–	–	–	12.0	0.72	1.07×10^7	7.06	0.96	1.56×10^5
PPEO–Ca–pH5	22.6	–	–	–	19.7	0.73	4.16×10^6	44.5	0.80	2.36×10^5
PPEO–Ca–pH3–SDS	37.76	233	0.95	9.73×10^6	6.25	0.92	3.49×10^7	3.34	0.94	5.51×10^5
PPEO–Ca–pH4–SDS	59.3	107	0.86	1.44×10^7	8.23	0.86	4.67×10^7	2.21	0.63	3.88×10^6
PPEO–Ca–pH5–SDS	31.03	132	0.87	6.62×10^4	24.5	0.83	1.01×10^7	14.7	0.86	5.73×10^5

Table 40. Fitted results of EIS plots of different coatings after immersion 120 h in 3.5 wt.% NaCl solution (R given in Ω cm^2; CPE given in S s^{-n} cm^{-2}; L given in Ω s cm^2).

Sample	R_s	CPE_{Ca}	n1	R_{Ca}	CPE_{PEO}	n2	R_{PEO}	CPE_{dl}	n3	R_p
PPEO	21.33	–	–	–	2.19	0.65	3209	22.26	0.88	4216
PPEO–Ca–pH3	32.17	–	–	–	10.88	0.83	2.53×10^5	2.93	0.82	1.36×10^4
PPEO–Ca–pH4	33.96	–	–	–	55.5	0.86	2.66×10^5	1.78	0.84	3.59×10^4
PPEO–Ca–pH5	25.62	–	–	–	7.53	0.90	6.07×10^4	24.58	0.72	5.71×10^4
PPEO–Ca–pH3–SDS	29.23	12.17	0.79	1.64×10^5	16.22	0.79	2.92×10^6	71.7	0.82	2.54×10^4
PPEO–Ca–pH4–SDS	35.2	62.71	0.87	2.97×10^5	13.32	0.55	5.54×10^6	57.71	0.78	2.88×10^4
PPEO–Ca–pH5–SDS	57.09	3.49	0.83	1.65×10^5	6.72	0.76	7.19×10^4	15.27	0.82	2.11×10^4

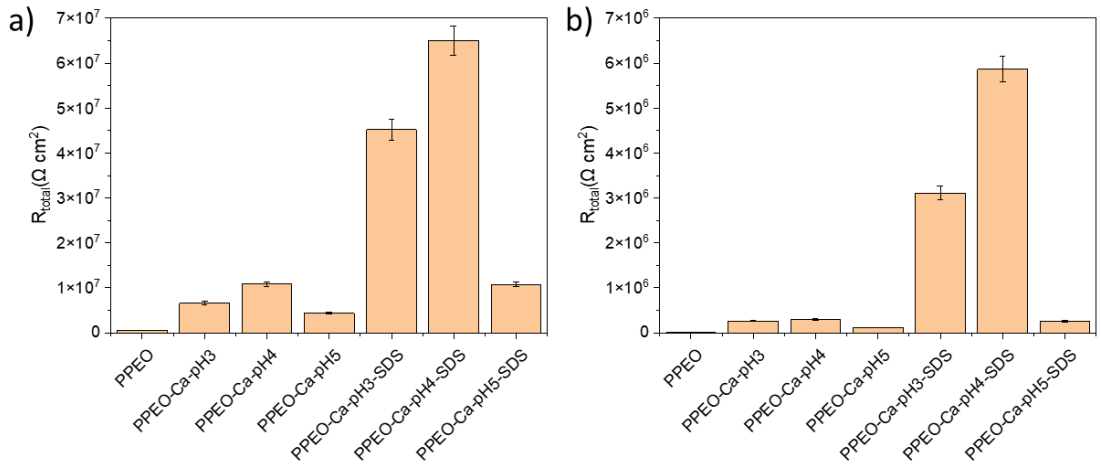

Figure 76. R_{total} of different coatings after immersion (a) 0.5 h and (b) 120 h in 3.5 wt.% NaCl solution.

4.3.5.3 Contact Angle and Paint Adhesion Test

Contact angle measurements are presented in Table 41 and images are gathered in Figure 77. The value of contact angle obtained for PPEO coating demonstrates the hydrophilic nature of the original oxide layer (i.e. <90°) mainly due to its inherent porosity. Coatings sealed at different pH slightly increase the values of contact angle. This might be associated with the presence of precipitates on the coating surface. The existence of SDS provides hydrophobicity for the coating surface with contact angle up to (111 ± 13°) in the case of PPEO–Ca–pH5–SDS. Similar findings were also reported for PEO coatings sealed with octadecylphosphonic acid [288]. Therefore, the obtained results indicate that the surface chemistry significantly influences the wettability for these particular layers.

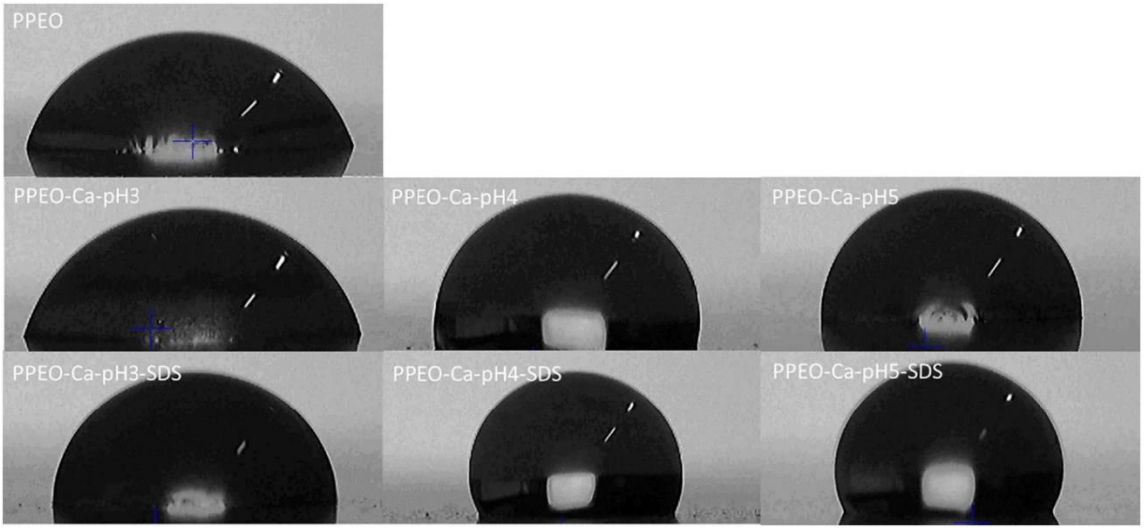

Figure 77. Water contact angle measurement of different coatings.

Table 41. Water contact angles of studied coatings.

Sample	Contact angle (°)
PPEO	46 ± 12
PPEO–Ca–pH3	62 ± 3
PPEO–Ca–pH4	52 ± 5
PPEO–Ca–pH5	57 ± 6
PPEO–Ca–pH3–SDS	84 ± 11
PPEO–Ca–pH4–SDS	106 ± 9
PPEO–Ca–pH5–SDS	111 ± 13

The results of the cross–cut paint adhesion test are shown in Figure 78. The rating system (from 0 to 5) is according to the detached surface (%) after the test considering no detachment (0) and complete detachment (5). The rating of PEO coatings without addition of corrosion inhibitors appears to be excellent from the adhesion point of view (as no paint pull–off occurred along the cross–cut lines).

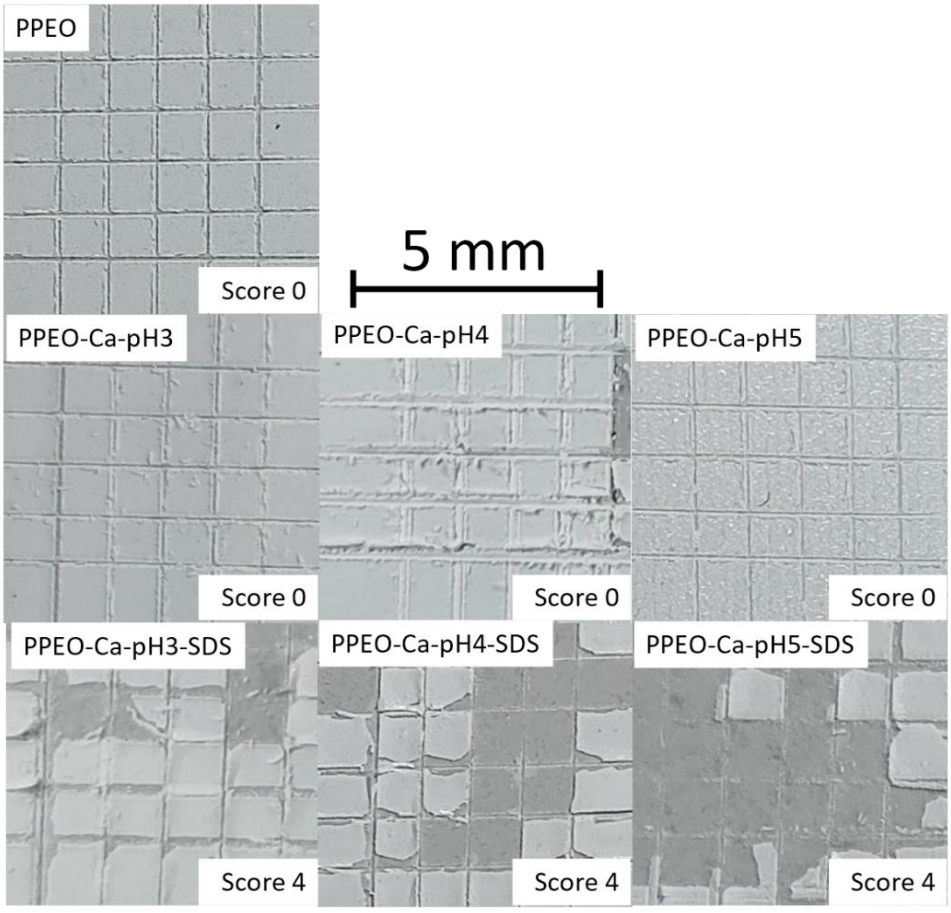

Figure 78. Appearance of painted PEO surfaces after the adhesion test.

Ca containing precipitates do not have a noticeable effect on paint adhesion. Considering the partial blocking of the pores with Ca containing precipitates, it is believed that the good

paintability of the sealed specimens (without SDS) is due to the good adsorption properties of hydroxyapatite. This is in accordance with the hydrophilic character of the layers even after performing post–treatment process. The increase in hydrophobicity of the coatings due to the presence of SDS has a negative influence on the paint adhesion of the layers with rating value up to 4. Only few data are available addressing the paint adhesion of PEO coatings, suggesting that the good adhesion property of the composite layers is ascribed to the outer porous layer [301, 319]. Findings obtained in the present work reveal that modification of the outer porous layer might decrease the adhesion between organic layer and inorganic PEO coating when painting is coated for long–term corrosion protection.

4.3.6 Concluding remarks on Ca–sealed PEO coating on AZ91D

Some conclusions can be drawn regarding the effects of studied sealings on PEO coated AZ91D alloy on PEO morphology and corrosion performance:

- The corrosion resistance of PEO coatings on AZ91D Mg alloy is enhanced by performing sealing post–treatment process in Ca–containing acidic solutions. Corrosion inhibitor (SDS) in the post–treatment electrolyte further improves the corrosion performance of the coatings.
- Ca–containing precipitates, i.e. hydroxyapatite, are deposited within the coatings pores following the partial dissolution during the post–treatment. Thus, blocking the access of aggressive species toward the substrate. The enhanced precipitation of calcium phosphates in the presence of SDS as well as the inhibiting effect of the latter further impede the corrosion process. SDS also provides hydrophobicity to the coating surface. However, this has negative influence on paint adhesion.

Chapter 4

Functionalization of hybrid PEO/Sol–Gel coatings on Mg alloys with corrosion inhibitors

4.4 Chapter 4. Context and aim

It is known that sol–gel sealing is an effective way to increase the corrosion resistance of Mg alloys. Inhibitor–loaded sol–gel formulations are becoming increasingly popular as a strategy for providing active protection. Chapter 4 is focused on the development of sol–gel sealings for PEO coatings on AZ31 alloy in combination with incorporation of corrosion inhibitor species. The chapter is organised in two sections: (i) post–treatment of the PEO layer by immersion in an inhibitor containing solution, and (ii) loading of the inhibitor into the sol–gel precursor. The goal is to identify the best strategy for improving the long–term corrosion protection of hybrid PEO/sol–gel coatings on AZ31 Mg alloy. Figure 79 shows the graphical abstract of Chapter 4.

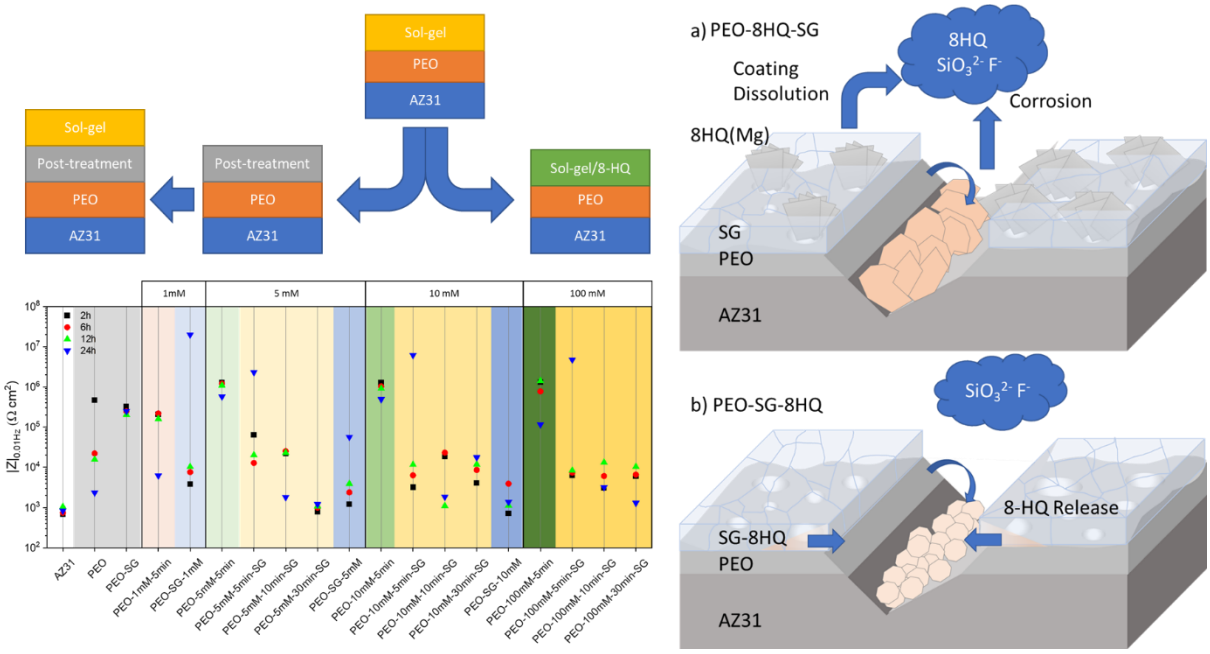

Figure 79. Chapter 4 graphical abstract: Functionalization of sol–gel–sealed PEO coatings on AZ31.

4.4.1 Introduction

PEO coatings on magnesium usually improve the corrosion resistance with respect to the bare substrate by up to 4 orders of magnitude in aqueous corrosion media such as NaCl [174, 320] and simulated body fluid (SBF) [321]. However, aggressive species eventually reach the substrate, leading to pitting or, alternatively, undercoating corrosion. Therefore, corrosion protection provided by PEO coatings usually only lasts up to 7 to 14 days [174, 288, 289, 291].

The use of sol–gel sealings has been gaining increasing interest in recent years and several papers on hybrid PEO/sol–gel coatings have already been reported [187, 188, 322, 323]. Sol–gel is highly valued for its capacity to penetrate through the PEO pores and cracks as well as for its versatility and low environmental impact [189, 324-326]. For instance, Malayoglu *et al.* [327] studied different post–treatments, including phosphate and silicate sealings, and concluded that the PEO/sol–gel system showed the best corrosion performance [189, 191].

Inorganic–organic sol–gel formulations, also known as hybrid sol–gels (HSGs), are highly suitable for enhancing the corrosion performance. The organic part lowers the curing temperature and provides elasticity, while the silane structure offers good mechanical properties and adhesion [186, 190-192, 328]. The use of hybrid sol—gel sealings for PEO coatings was positively reported by Pezzato *et al.* [329]. In all the studied cases, the sol–gel sealing produced an increase in the uniformity of the surface and, hence, a remarkable increase in the corrosion properties and durability of the coating system. Despite the good perspective of PEO/sol–gel systems, once the corrosion initiates there is lack of active protection.

To accomplish self–healing, the incorporation of inhibitor species is key. Corrosion inhibitors are chemical species that can protect actively the substrate from corrosion. Active protection has been widely studied in recent years and interesting results have been reported for 8–hydroxyquinoline (8HQ) [330] and 2–mercaprobenzothiazole (MBT) [331], as organic inhibitors, and Ca, Ce, and Zn [288, 332-335] as inorganic inhibitors. However, limited results have been published on PEO/sol–gel systems with incorporation of corrosion inhibitors. Chen *et al.* [336] developed a PEO/sol–gel system loaded with glycolic acid, 4–aminosalicylic sodium salt, and 2,6–pyridinedicarboxylic acid. Corrosion inhibitors were incorporated by impregnation of the PEO coating followed by sol–gel sealing. According to the reported results, inhibitors–containing coatings showed enhanced corrosion performance. The authors proposed a protection mechanism achieved by suppression of the re–deposition of detrimental Fe

impurity and inhibitor adsorption. Ivanou *et al.* [195] impregnated a PEO coating with 1,2,4–triazole followed by sol–gel sealing. High corrosion protection was reported during one month continuous exposure to the aggressive medium. This enhancement was attributed to the thin and porous PEO layer that secures the corrosion inhibitor close to the bulk metal where the corrosion process starts.

In this chapter, the approach is to evaluate the ability of sol–gel processes to seal the micropores of PEO coatings and to immobilise inhibitors with the aim of providing active corrosion protection. The suitability of the inhibitors was first assessed by screening their effect on the bare alloy. The chapter is divided into two sections. The first part evaluates the incorporation of organic inhibitors into the PEO/sol–gel system by using a post–treatment step after PEO. The second part is dedicated to inhibitor loading in the sol–gel precursor before its applied onto the PEO coating. The effects of inhibitors on the morphology, composition and corrosion resistance of hybrid PEO/sol–gel systems are studied. Electrochemical and immersion tests are used to evaluate the anti–corrosion performance and the degradation process of the coatings.

4.4.2 Results on PEO/inhibitor/Sol–Gel systems

4.4.2.1 Inhibitor Screening

Nine different corrosion inhibitors were preselected from the systematic study carried out by Lamaka *et al.* [98]. Note that most of the selected inhibitors are of the mixed type since they adsorb on the surface, blocking both the anodic and cathodic regions. Bare AZ31 Mg alloy was exposed to corrosive media containing the corrosion inhibitors in 0.05 M concentration and pH adjusted to 8. Hydrogen evolution testing (Figure 80) was carried out for comparison among species [203]. Table 42 summarises the information regarding the inhibitor type and conditions along with the kinetic laws calculated from the experimental data. Kinetic laws coefficients were calculated by the linear regression method [Eq. 9], where *V* coordinate represents the collected hydrogen in mL cm^{-2} and *t* is the immersion time in days.

$$V\ (mL\ cm^{-2}) = b_{cr} \cdot t\ (d) + a \qquad \text{[Eq. 9]}$$

As expected, the bare alloy generates significant amounts of hydrogen due to its high corrosion rate (Figure 80). Remarkably, some species (4–isopropilicbenzoic acid, 2–hydroxy–1,4–napothoquinone, and 4–methyl–3–salycilic acid) increased the corrosion rate, possibly due to formation of soluble complexes with Mg. 8–Hydroxyquinoline (8HQ) revealed the lowest

amount of collected hydrogen, followed closely by 5–methyl–2–nitrobenzoic acid and 3–methylsalycilic acid.

Table 42. Kinetic laws, with and without inhibitor, calculated from hydrogen measurements.

Inhibitor species	[I] (M)	NaCl (wt.%)	pH	b_{cr} (mL cm^{-2} d^{-1})	Formula
NaCl (reference)	0.05	0.5	8	0.21	
8–Hydroxyquinoline	0.05	0.5	8	0.02	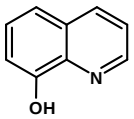
Dodecylbenzenesulphonic acid	0.05	0.5	8	0.05	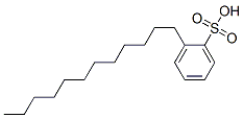
Fumaric acid	0.05	0.5	8	0.11	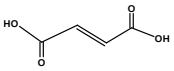
5–Methyl–2–nitrobenzoic acid	0.05	0.5	8	0.03	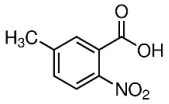
4–Isopropilicbenzoic acid	0.05	0.5	8	0.32	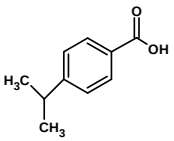
3–Methylsalycilic acid	0.05	0.5	8	0.03	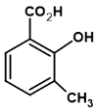
Quinaldic acid	0.05	0.5	8	0.16	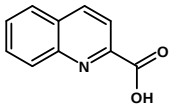
2–Hydroxy–1,4–napothoquinone	0.05	0.5	8	1.29	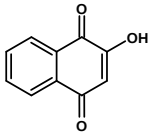
4–Methyl–3–salycilic acid	0.05	0.5	8	1.02	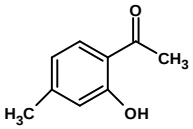

As shown in Figure 80, the surface of the reference sample was largely affected by corrosion. On the other hand, most of the surfaces exposed to the inhibitor showed a combination of corroded areas and inhibitor deposits. As the best candidate, 8HQ shows no corroded areas but a deposit covering the entire surface. This deposit limits the exposure of the metal to the corrosive environment, thus reducing the amount of evolved hydrogen. In agreement with several studies [337-341], 8HQ may behave as an inhibitor by the formation of a complex chelate ($Mg(8HQ)_2$) on the surface, blocking the action of aggressive ions. Based on this initial corrosion screening, 8HQ was selected for further evaluation. It is important to note that 8HQ

has already been used with good results as an additive in sol–gel systems for steel [342], Mg [343] and Al [341, 344-346], however, those systems did not include an intermediate PEO layer.

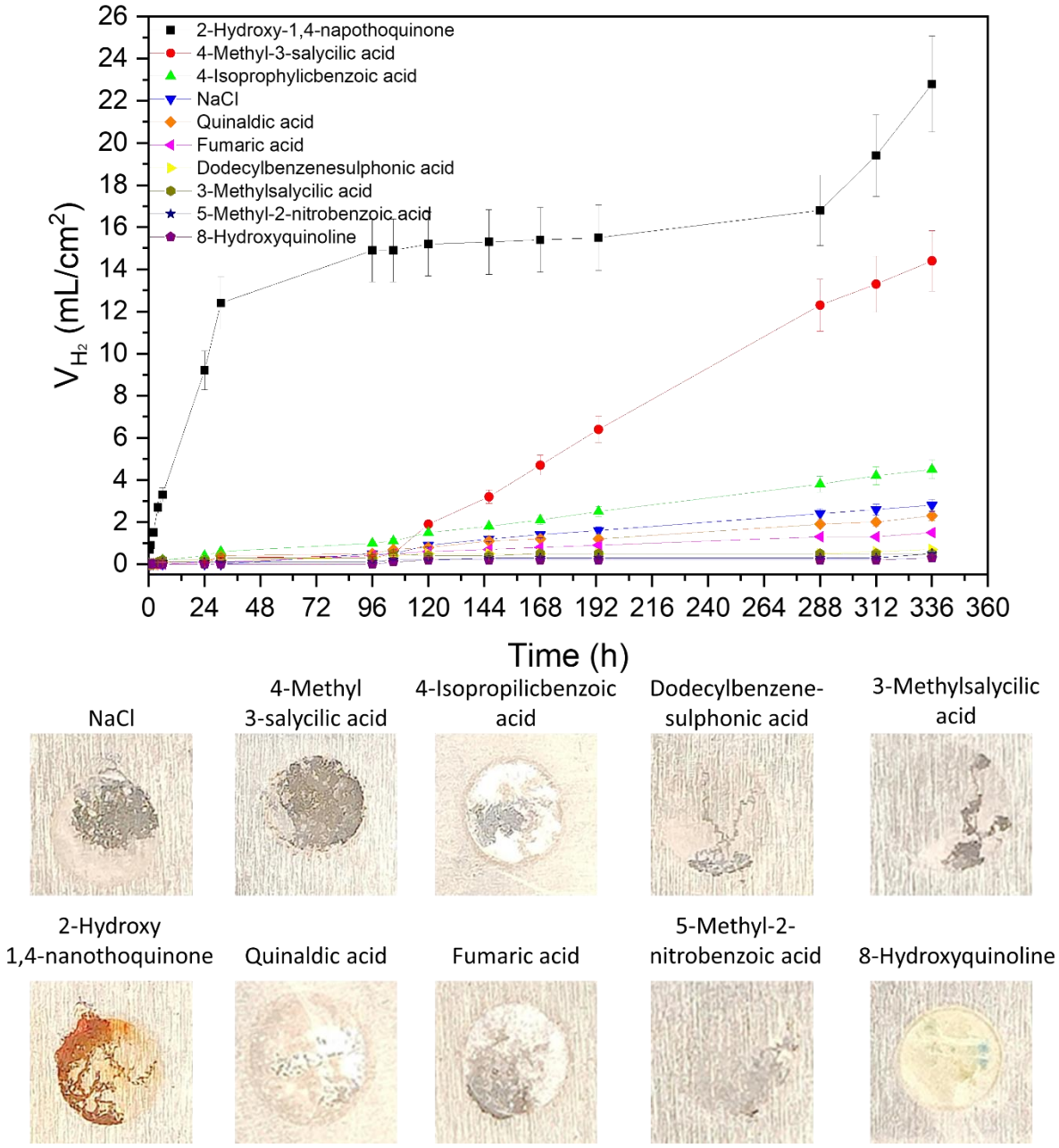

Figure 80. Volume of hydrogen evolved from the cathodic reaction during immersion in 0.5 wt.% NaCl solution and surface appearance of the exposed area after the test.

Figure 81 shows the SEM planar view characterization of the AZ31 surface after the hydrogen evolution test in the presence of 8HQ inhibitor. As demonstrated by the micrographs and the EDS analysis (Table 43), it is evident that the substrate is fully covered by the $Mg(8HQ)_2$ precipitates. The micrographs reveal that the flakes agglomerate to form islands. According to Vaghefinazari *et al.* [347], the liberation of H_2 bubbles promotes the formation of these islands;

hydrogen bubbles are trapped for a short time on the surface and the $Mg(8HQ)_2$ flakes precipitate around them. There are also agglomerates with a flower–like morphology that show a higher O content (Figure 81a, label 1, Table 43) suggesting the formation of $Mg(OH)_2$ [347].

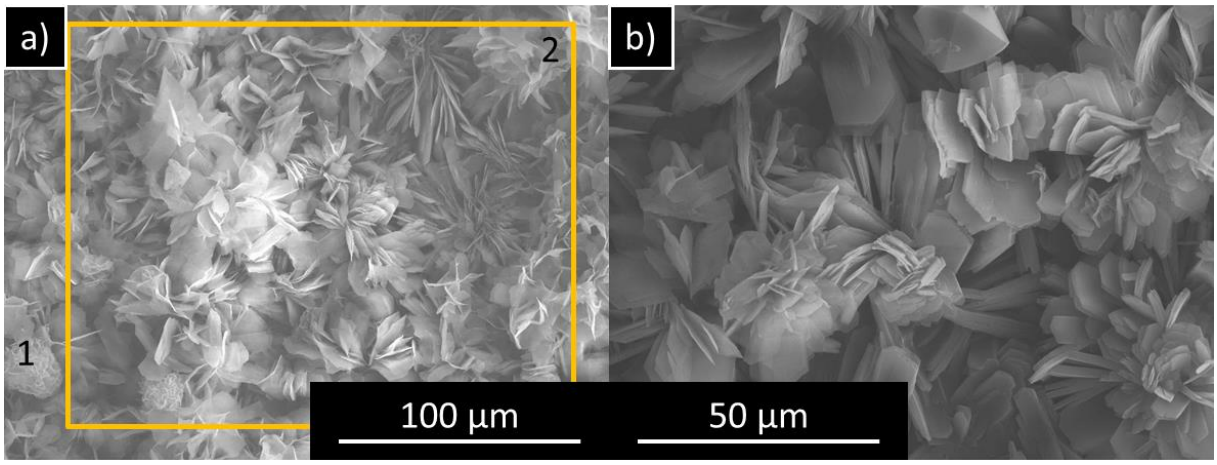

Figure 81. (a) Surface morphology of bare AZ31 exposed to 0.5 wt.% NaCl containing 8HQ after 14 days. A higher magnification view of the flakes is presented in (b). Marked areas corresponds to the EDS analysis collected in Table 43.

Table 43. Results of the local EDS surface analysis of the coatings (at.%).

	C	O	Na	Mg	Al	Cl	Zn
1	76.3	20.7	0.1	2.6	0.1	0.1	0.1
2	78.0	16.9	0.2	4.6	0.1	–	0.1

4.4.2.2 Optimization of inhibitor post–treatment

Once the most promising inhibitor was selected, several coating systems were defined for further analysis. These combined a PEO layer with a post–treatment in 8HQ just before a final sealing with sol–gel. PEO and sol–gel conditions are included in Table 44. Both PEO and sol–gel layers were produced by the author at UMONS (Belgium). The operating conditions were established considering previous studies [284, 348, 349] and the findings from previous section (Section 4.3.2). Table 45 shows the list of studied specimens. Only 8HQ was selected as inhibitor for this section, therefore, the names obviate the inhibitor in favour of the post–treatment conditions.

Electrochemical impedance screening was performed in order to identify the best candidates for further studies and detailed morphological and compositional characterization. Figure 82 shows the procedure followed for the evaluation of the coatings.

Table 44. PEO conditions for surface modification of AZ31 and details of the sol–gel sealing.

Electrolyte	Electrical signal	Sol–Gel solution	Sol–gel process
Na_2SiO_3 10.5 g/L KOH 8.5 g/L NaF 2 g/L	20 ± 1 °C 400/–30 V 100 mA cm^{-2} 50 Hz 4 min 60 s ramp	TEOS 20 % GPTMS 10 % Ethanol 10 % Water 58 % Acetic acid to adjust pH 2	10 mm/min immersion/withdraw 15 min air drying 150ºC 2h curing

Table 45. Designation of specimens and inhibitor post–treatment conditions. Colours are in correlation with those in Figure 83 for a better understanding.

Sample	Post–treatment [8HQ] and immersion time	Sol–gel solution
AZ31	–	–
PEO	–	–
PEO–SG	–	TEOS/GPTMS
PEO–1mM–5min	1 mM – 5 min	–
PEO–5mM–5min	5 mM – 5 min	–
PEO–10mM–5min	10 mM – 5 min	–
PEO–100mM–5min	100 mM – 5 min	–
PEO–5mM–5min–SG	5 mM – 5 min	TEOS/GPTMS
PEO–5mM–10min–SG	5 mM – 10 min	TEOS/GPTMS
PEO–5mM–30min–SG	5 mM – 30 min	TEOS/GPTMS
PEO–10mM–5min–SG	10 mM – 5 min	TEOS/GPTMS
PEO–10mM–10min–SG	10 mM – 10 min	TEOS/GPTMS
PEO–10mM–30min–SG	10 mM – 30 min	TEOS/GPTMS
PEO–100mM–5min–SG	100 mM – 5 min	TEOS/GPTMS
PEO–100mM–10min–SG	100 mM – 10 min	TEOS/GPTMS
PEO–100mM–30min–SG	100 mM – 30 min	TEOS/GPTMS

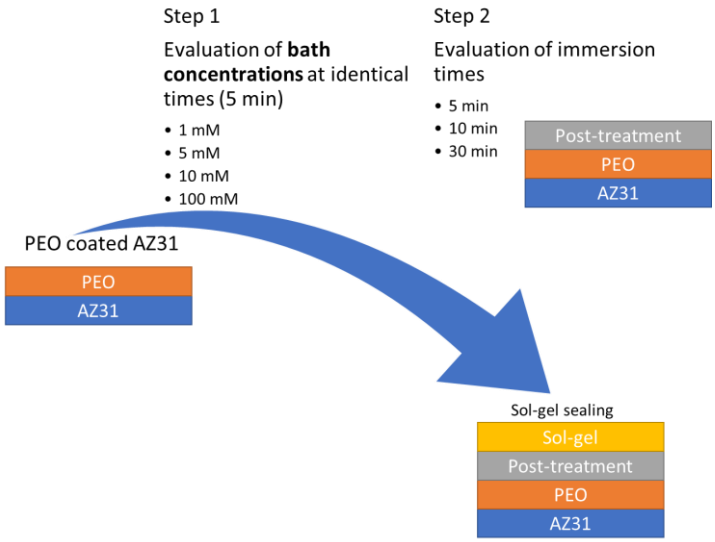

Figure 82. Steps for the optimization of the inhibitor post–treatment prior to sol–gel sealing.

The screening results are presented in Figure 83. All the combinations yielded higher impedance values than the reference bare alloy. Stand–alone PEO shows an impedance modulus 2 orders of magnitude higher than that of the substrate, but its protection is rapidly lost with time, reaching a modulus similar to that of the alloy after 24 hours. The hybrid system (PEO–SG) shows an initial impedance slightly lower than that of PEO, but the response remains practically constant with time. This long–term protection is attributed to the sealing of the PEO coating defects [186].

PEO post–treatments with different 8HQ concentrations improved the performance of the PEO coating with the only exception of one post–treatment (1mM 8HQ), which revealed a lower impedance value. 8HQ post–treatment is likely to form an insoluble deposit with magnesium, $Mg(8HQ)_2$, thus enhancing the corrosion resistance [350]. Contrary to expectations, the application of sol–gel on top of post–treated PEO produced lower impedance values than the reference PEO–SG film for all the tested combinations. The causes for this could be varied. For instance, 8HQ–rich precipitates may disrupt the continuity of the sol–gel film. Also the formation of Si–O–M bonds in the PEO/sol–gel interface could be affected in the presence of 8HQ and reduce the penetration of the sol–gel layer [347]. However, it is noteworthy that some coatings systems show an increase in the modulus with increasing immersion time. This improvement suggests active protection and recovery of the corrosion protection.

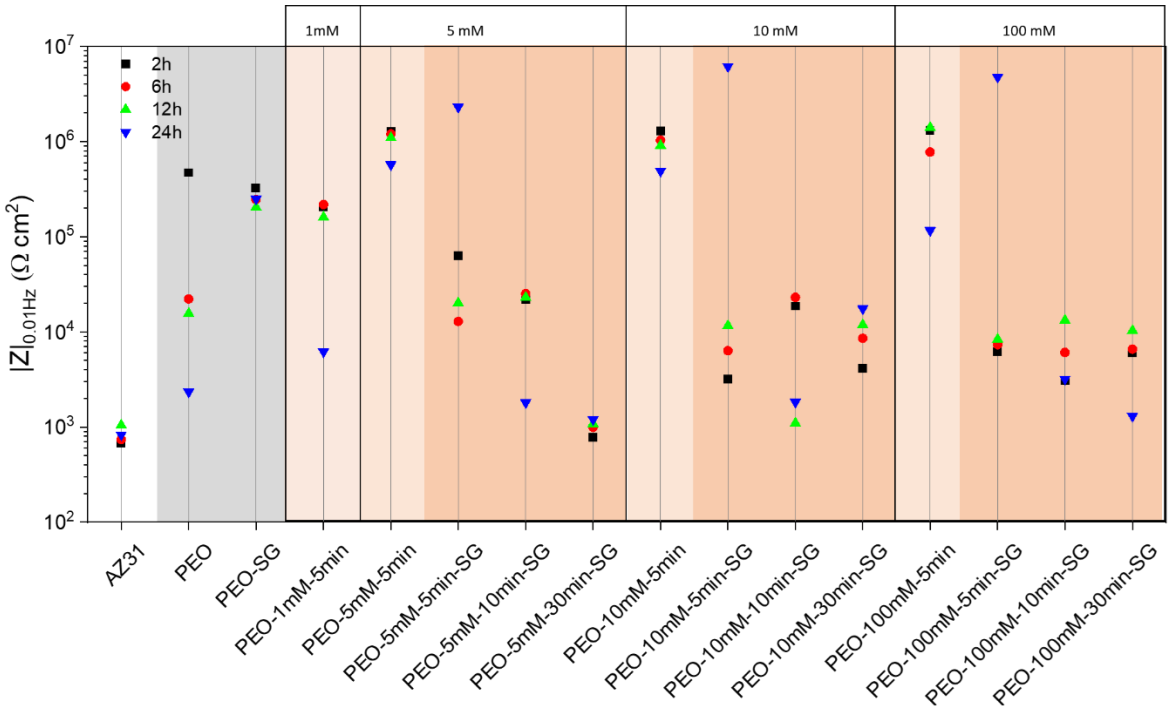

Figure 83. Scatter diagram of impedance modulus at 0.01 Hz in 0.5 wt.% NaCl of the selected coatings on AZ31 alloy.

With the exception of the PEO–1mM–5min specimen, there are no significant differences between the studied hybrid PEO/inhibitor/SG systems. Therefore, all the full systems with 5, 10 and 100 mM inhibitor concentrations were selected for further evaluation.

4.4.2.3 Coating Morphology and Composition

Several characterization techniques were used with the aim of elucidating the effect of the applied post–treatment on the PEO–SG system. In order to reduce the number of specimens, only representative systems were studied. FTIR spectra of 8HQ (powder), PEO–8HQ, PEO–SG and PEO–8HQ–SG coatings are presented in Figure 84.

Table 46. FTIR bands and their assignation for the 8HQ compound [351-353].

Band Wave Number (cm^{-1})	Assignation
3311	ν(OH) hydration of PEO
3150	stretching vibration for ν(OH) phenol
3049	aromatic ν(C–H) stretching
1625	ν(C=N) stretching
1579	ν(C=N) ring stretching vibration
1500	ν(C=C) stretching vibration
1471, 779	in–plane and out–of–plane deformations of CH_2 and CH_3 groups
1433	O–H plane bending
1274, 1246	ν(C–O) stretching vibrations
1165, 1138, 1093	N(C–N) stretching bands
1059, 1028	ν(N–O) stretching bands
974	–CH_2 rocking
896, 866	ν(C–C) bending vibration
740, 707	ν(C–H) out–of–plane bending band

Table 46 gathers the characteristic bands of the 8HQ compound (in powder form), which were identified in the FTIR spectrum presented in Figure 84. For a representative specimen (PEO–5mM–10min), the spectrum still shows bands corresponding to 8HQ, demonstrating the successful incorporation onto the surface (Figure 84b). However, there is a remarkable difference; the 3150 cm^{-1} band associated with the phenol group vanishes due to the formation of metal complexes between $8HQ^-$ and Mg^{2+} [354]. Note that the spectrum now also shows bands coming from the PEO layer. The most characteristic bands are the one at 3311 cm^{-1}, attributed to ν(H–O), due to hydration of the outermost region of the PEO layer, and several signals associated with Si–O–Si bonds (1493–960, 960–724 cm^{-1}) and Si–O–Mg (<700 cm^{-1}), due to incorporation of silicate from the electrolyte during PEO processing [186, 355, 356].

The spectra obtained for the PEO–SG and PEO–8HQ–SG coatings show characteristic bands of sol–gel layers. Signals at 3100–3600 cm^{-1} and 1585 cm^{-1} correspond to vibrations of the ν(H–O) bonds. These come from the Si–OH groups in the sol–gel layer and absorbed water molecules [186, 351, 352]. The intensity of this band increases with the number of polar groups, thereby acting like an indicator of the level of sol–gel polymerization. Vibrations of ν(C–H) bonds at 3000–2824 cm^{-1} correspond to the CH_3 and $–CH_2$ groups coming from the GPTMS precursor. Note the increased intensity of the Si–O–Si and Si–O–M signals which come from both the PEO and sol–gel layers. The intensity of the band centred at ~1034 cm^{-1} is generally associated with asymmetric Si–O–Si vibrations, which are also indicative of correct sol–gel formation.

It is important to mention that the inhibitor post–treatment with 8HQ results in less intense Si–O–Si and Si–O–Mg bands for the hybrid PEO–8HQ–SG system. Therefore, it can be concluded that the 8HQ post–treatment interferes with the sol–gel process: the hydrolysis and condensation reactions are restricted, and the formation of a 3D network is therefore limited. Very few studies have investigated the effect of an intermediate post–treatment step on sol–gel sealing of PEO coatings [357-359]. However, there are many examples where species incorporated in the sol–gel influence the degree of polymerisation associated with the inorganic and organic parts [360].

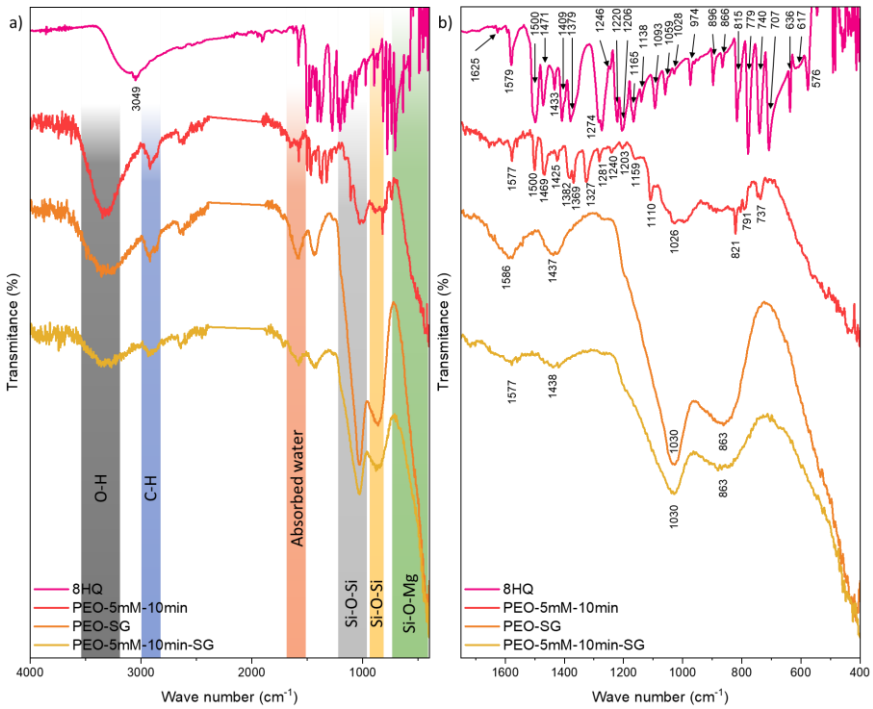

Figure 84. (a) FTIR spectra of 8HQ powder and studied coatings and (b) detail of the near IR region. A representative concentration of the 8HQ was used for FTIR study.

The SEM images of the surface of the PEO–coated AZ31 Mg alloy are presented in Figure 85 alongside with EDS maps. A crater–like morphology is revealed on the unsealed coating. Microcracks and micropores are located at the sites of the discharge channels caused by residual stresses and gas evolution during the coating formation (Figure 85a,b). As shown in the cross–section micrographs (Figure 85c,d), a well–defined barrier layer is observed in combination with a thicker and porous outer layer (thickness 7.3 ± 0.4 µm). The EDS Si map of the PEO layer show a significant contribution from Si, which is to be expected considering that the PEO coating was produced in an alkaline–silicate electrolyte [303, 361, 362]. The outer areas of the coating show some Al enrichment (this element comes from the substrate).

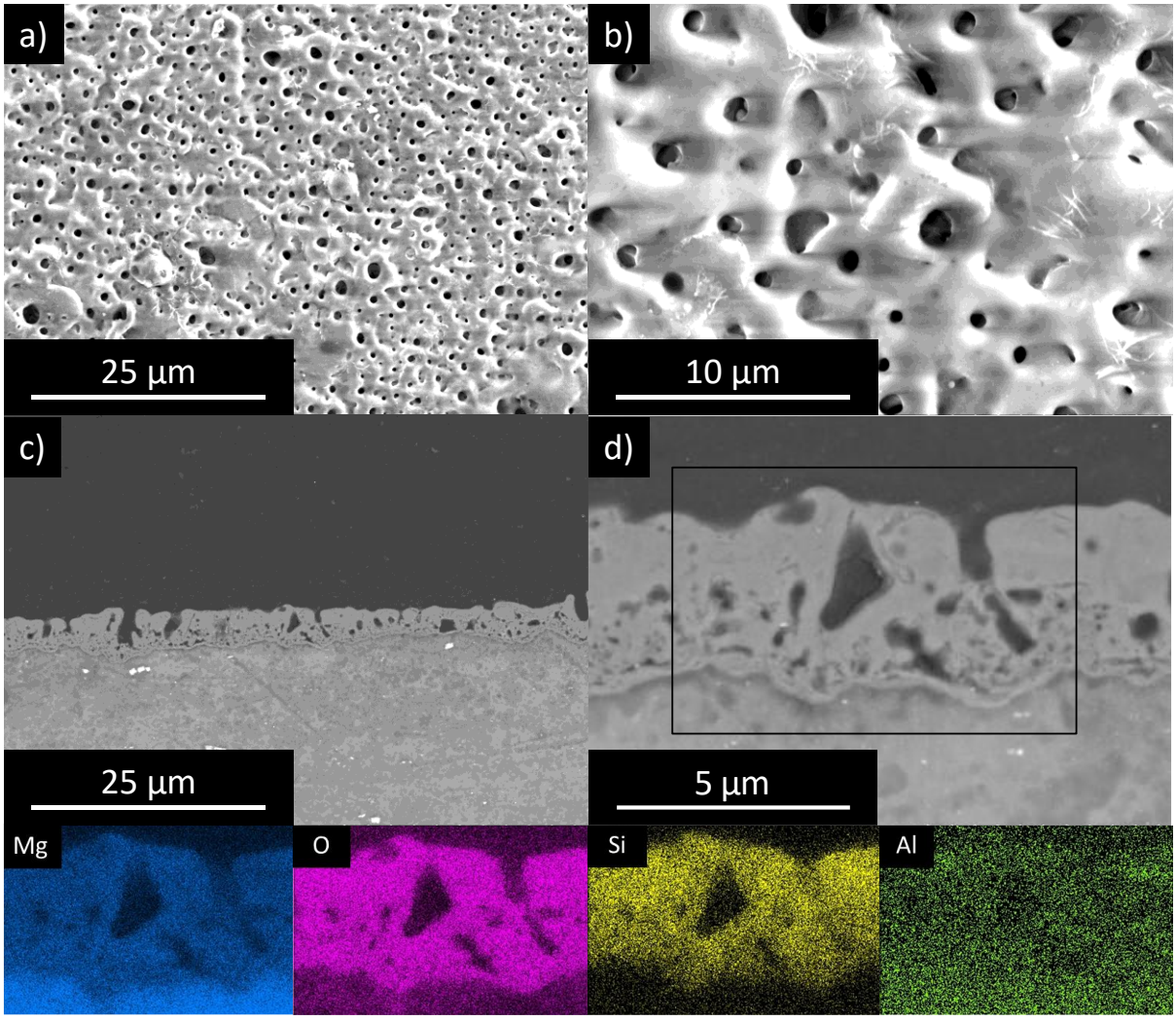

Figure 85. Scanning electron micrographs corresponding to the (a,b) planar and (c,d) cross views of PEO coated AZ31. Cross–section observation along with EDS mapping of the PEO layer.

XRD results of the unsealed PEO coating (Figure 86) shows the presence of magnesium oxide (MgO) and forsterite (Mg_2SiO_4). Aluminium crystalline phases (e.g. $MgAl_2O_4$) were not

detected. Therefore, the Al detected in the coating is mainly in the form of amorphous phases or doping the abovementioned compounds. Mg peaks come from the substrate due to penetration of the X–rays.

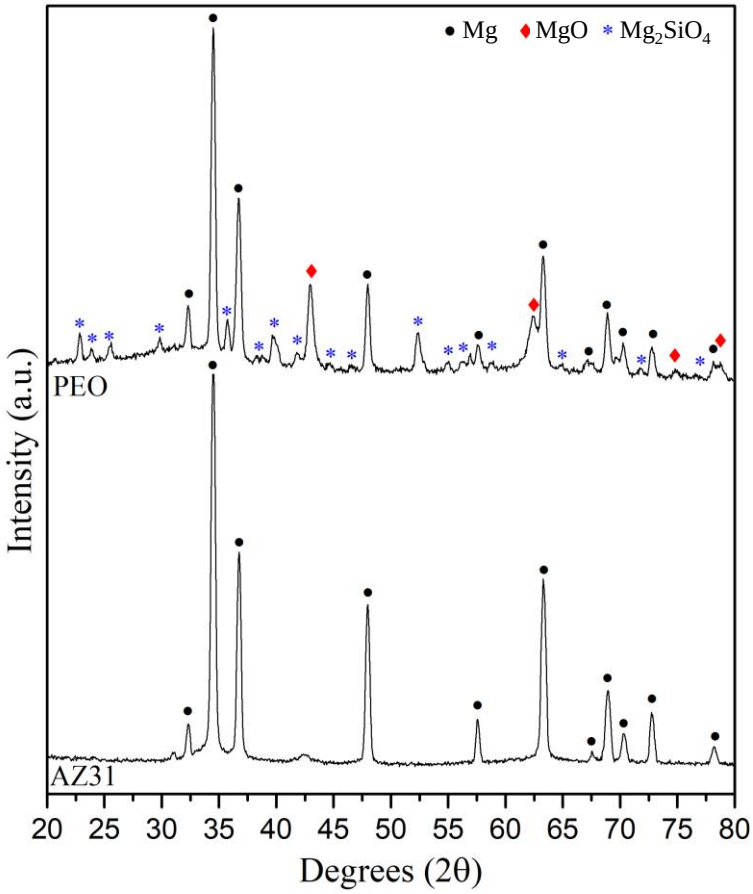

Figure 86. XRD patterns of bare alloy and the fabricated PEO coating.

Comparative SEM micrographs of PEO–coated AZ31 Mg alloy without and with post–treatment and sol–gel sealings are presented in Figure 87. Planar and cross view micrographs are included. After 10 min post–treatment, the surface of the PEO coating shows flakes of 8HQ complexes with two different morphologies (Figure 87c); (i) agglomerates of small flakes that are deposited on the flat surface of the PEO layer and surrounding smaller pores; and (ii) large flakes in the vicinity of bigger pores. Their morphology resembles that observed in Figure 81. No flakes were found in the cross–sectional micrographs as they were probably washed away during the cross–section preparation. Cross–view examination suggests a slight dissolution of the PEO coating after the inhibitor post–treatment (PEO 7.3 ± 0.4 µm *vs.* PEO–5mM–10min 6.7 ± 0.3 µm, Figure 87b,d).

The different size of the flakes is attributed here to the supply of Mg^{2+} ions. The dissolution of Mg is suggested to be more abundant inside the pores (supplied by substrate and PEO layer),

thus resulting in bigger flakes. According to EDS analysis, these flakes show high levels of C, O and Mg, suggesting the formation of $Mg(8HQ)_2$. These findings are in agreement with the results of Vaghefinazari *et al.* [347], who reported $Mg(8HQ)_2$ formation on a bare substrate exposed to a solution containing 8HQ.

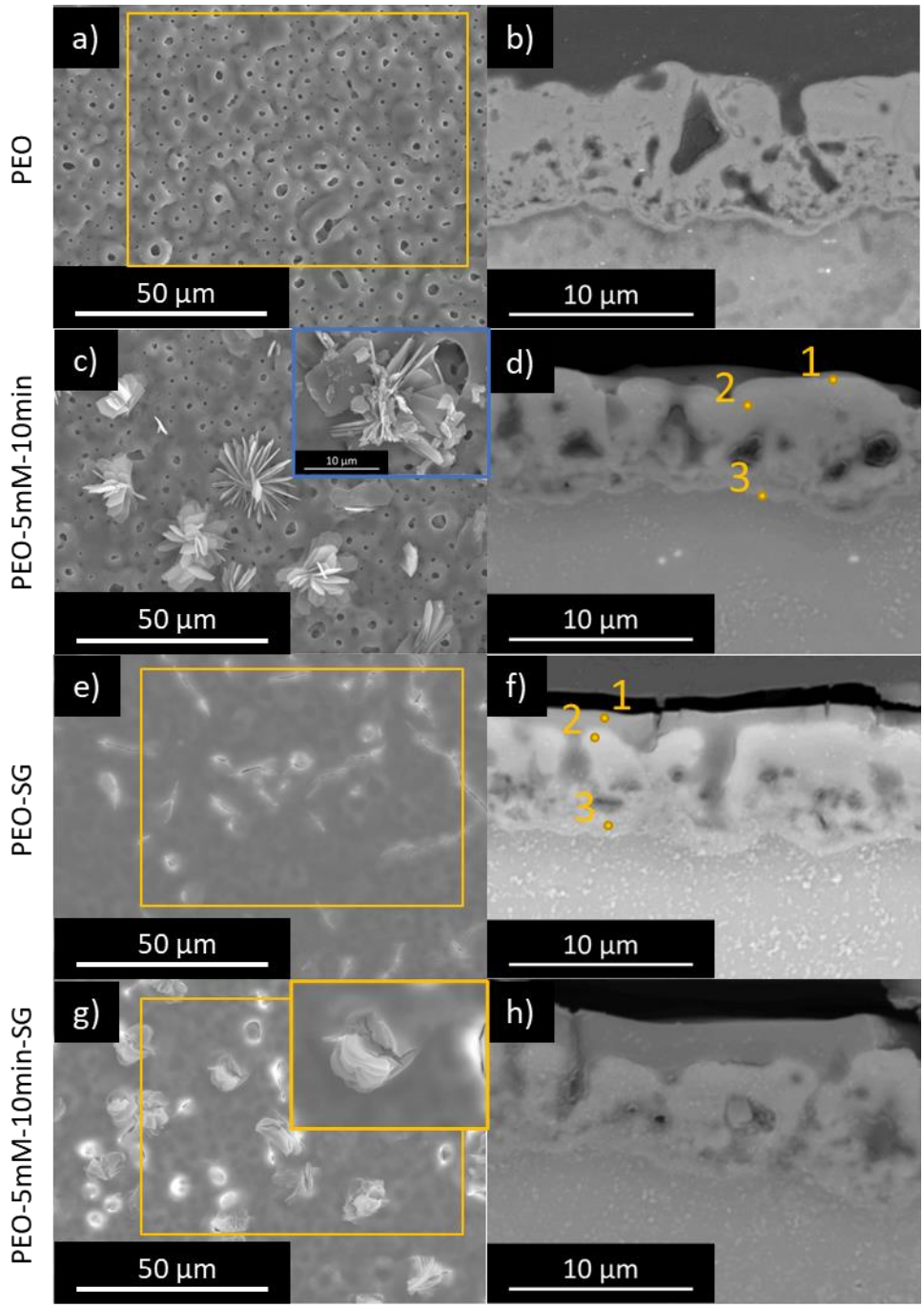

Figure 87. Scanning electron micrographs corresponding to the planar and cross views of (a,b) PEO, (c,d) PEO–5mM–10min, (e,f) PEO–SG and (g,h) PEO–5mM–10min–SG. Corresponding EDS analysis are collected in Table 47.

Figure 87e shows that the sol–gel sealing forms a homogeneous layer (1.8 ± 0.5 μm) that successfully fills up the pores and cracks in the PEO layer. However, some surface defects are observed, mostly cracks, caused by dehydration of the sol–gel layer during curing. These cracks are also observed in the cross–view (Figure 87f). PEO coating thickness decreased to 5.4 ± 0.5 μm due to the acidic conditions during sol–gel sealing. The total thickness of the PEO–SG system was 6.39 ± 0.09 μm. It is noteworthy that the inner barrier layer of the PEO coating is still intact.

Micrographs of the specimens with a sol–gel layer on top of 8HQ post–treated PEO layer are presented in Figure 87g and h. As it was observed in PEO–SG surface, the sol–gel layer fills up the pores and cracks in the PEO layer, but here $Mg(8HQ)_2$ deposits emerge from the surface of sol–gel layer at some points. Dehydration cracks in the sol–gel layer are also observed. Once again, no $Mg(8HQ)_2$ flaky deposits are observed in the cross–view, but minor bulky precipitates are visible inside the pores. The overall thickness increases to 8.2 ± 0.4 μm being the sol–gel layer thicker than in previous cases (2.9 ± 0.2 μm). The sol–gel thickening is attributed here to the increase in surface roughness due to the presence of the $Mg(8HQ)_2$ precipitates. It is noteworthy that the PEO layer showed some dissolution (5.5 ± 0.7 μm) with the inner dense layer being less evident than in previous cases.

Table 47. Results of the local EDS surface analysis of the studied coatings (at.%).

		Element (Atomic %)										
		C	N	O	F	Na	Mg	Al	Si	K	Mn	Zn
PEO	Area	8.8	–	54.3	–	1.0	24.6	0.7	10.4	0.2	–	–
PEO–5mM–10min	Area	13.0	0.6	52.1	0.9	1.0	20.6	1.0	10.0	0.2	0.5	0.1
	1	24.0	–	52.7	1.0	0.7	15.4	0.4	5.7	0.1	–	–
	2	22.7	–	47.9	0.8	0.8	19.0	0.6	8.1	0.1	–	–
	3	17.0	–	22.7	1.5	0.2	52.1	1.3	4.5	0.1	–	0.5
PEO–SG	Area	27.0	–	41.5	–	0.4	16.7	0.5	13.9	0.1	–	–
	1	46.7	–	43.0	0.5	0.2	4.6	0.1	4.8	0.1	–	–
	2	33.4	–	41.6	0.3	0.5	15.6	0.4	8.0	0.1	–	–
	3	18.4	–	29.7	2.0	0.2	42.1	1.2	5.9	0.1	–	0.3
PEO–5mM–10min–SG	Area	31.7	–	44.3	–	0.5	12.5	0.6	10.2	0.2	–	–

4.4.2.4 Corrosion Test: Immersion tests

Figure 88 shows the digital macrographs of the PEO–8HQ–SG specimens with an artificial scribe after 14 days of immersion in 0.5 wt.% NaCl solution. PEO and PEO–SG specimens are included as a reference.

The stand–alone PEO coating reveals corrosion all over the surface (Figure 88a), whereas PEO–SG system reveals a slightly better performance. However, there are evident signs of corrosion next to the scratch and some localized damage away from it.

The PEO–8HQ–SG systems reveal much less corrosion damage than the reference coatings (Figure 88c–k), although the 5 mM 8HQ post–treatments show some corrosion around the scratch. This coincides with the EIS results, where post–treatments with low 8HQ concentration showed lower modulus of impedance after 24 h. The PEO–10mM–30min–SG coating is among the best performers and was selected for further characterization (Figure 88h). Therefore, these results indicate a possitive effect of increasing the 8HQ concentration. It is suggested here that the dissolution of $Mg(8HQ)_2$ flakes and their redeposition in regions with high pH (above 7, [347]) provides self–healing ability, thus improving the long–term corrosion resistance of the hybrid systems.

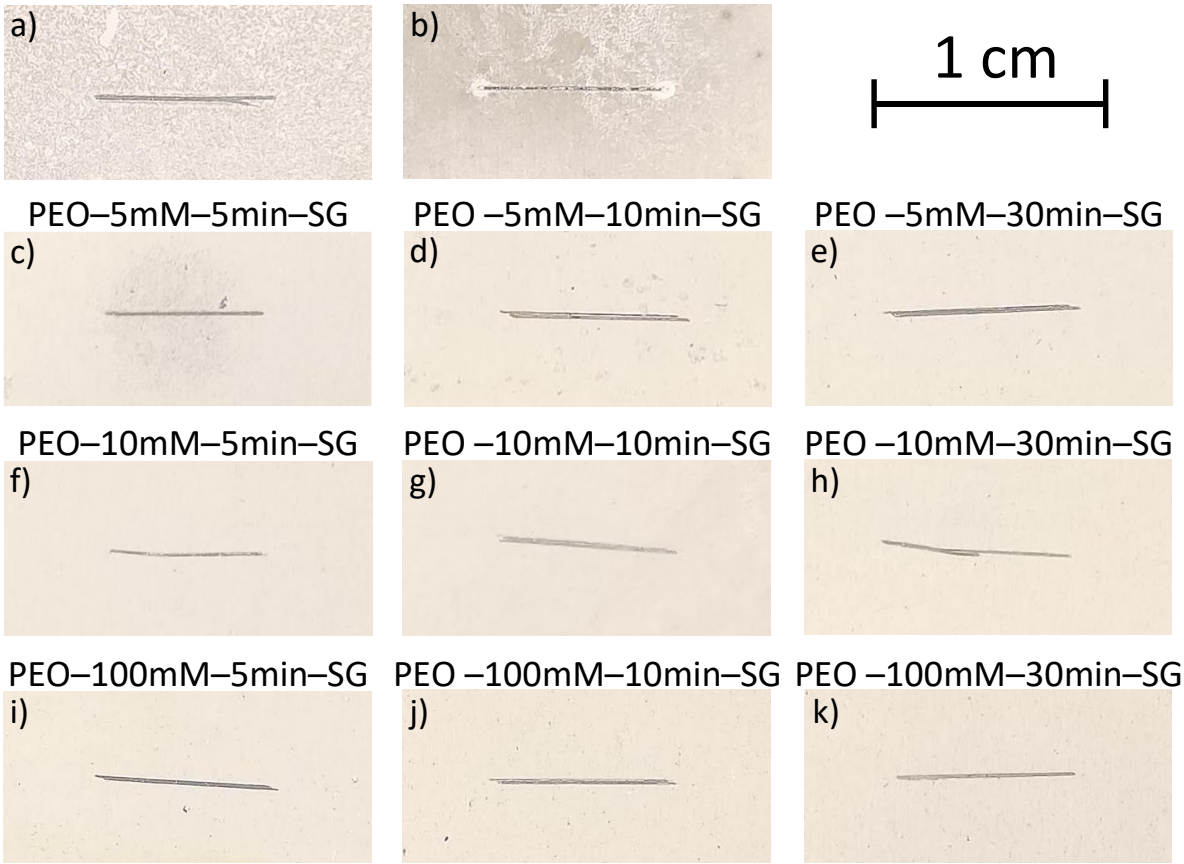

Figure 88. Digital images of (a) PEO, (b) PEO–SG and (c–k) PEO–8HQ–SG scribed coatings after 14 days of immersion in 0.5 wt.% NaCl solution at room temperature.

SEM/EDS results of the scribed systems after 14 days of immersion in 0.5 wt.% NaCl are presented in Figure 89 and Table 48. PEO–10mM–30min–SG was selected as a representative of PEO–8HQ–SG systems due to its superior corrosion performance.

The scratch in the PEO specimen shows voluminous corrosion products that are rich in O and Mg (Figure 89a, Table 48). As shown in Figure 89b, typical PEO micropores are no longer visible due to coating hydration (some cracks are formed as a consequence of partial dehydration). The cross–sectional view shows that the corrosion attack is quite deep, especially at the centre of the defect where small pits are revealed (inset in Figure 89c). The incorporation of F and Si in these corrosion products is noteworthy. These elements can only be released from the PEO coating. It is believed that SiO_3^{2-} anions that originate from dissolution of the PEO coating combine with Mg^{2+} in the solution and form precipitates such as $MgSiO_3$. Despite of this self–repairing properties, the level of protection is insufficient and some of the non–scribed areas also show corrosion damage, indicating failure of the inner barrier layer (Figure 89d).

In comparison with the stand–alone PEO coating, the PEO–SG system shows less amount of corrosion products (Figure 89e–h). Corrosion products are mostly present at the artificial defect and its surroundings. The cracked appearance of the sol–gel layer is particularly striking. The cross–sectional view of the defect (Figure 89g) shows the small amount of corrosion products within the scribe. The EDS analysis at the centre of the scribe also shows some Si, which can originate from both the PEO coating or the sol–gel layer.

The PEO–10mM–30min–SG shows the best corrosion behaviour as evidenced by the shallow depth of the scratch (Figure 89i–l). The initial depth of the scratch is 20 ± 2 µm and it reaches values of 49 ± 5 µm, 31 ± 2 µm and 22 ± 2 µm for PEO, PEO–SG and PEO–10mM–30min–SG, respectively, after 14 days of immersion. The presence of C and O along with Mg in EDS area 1 may be indicative of the presence of $Mg(8HQ)_2$ (Table 48).

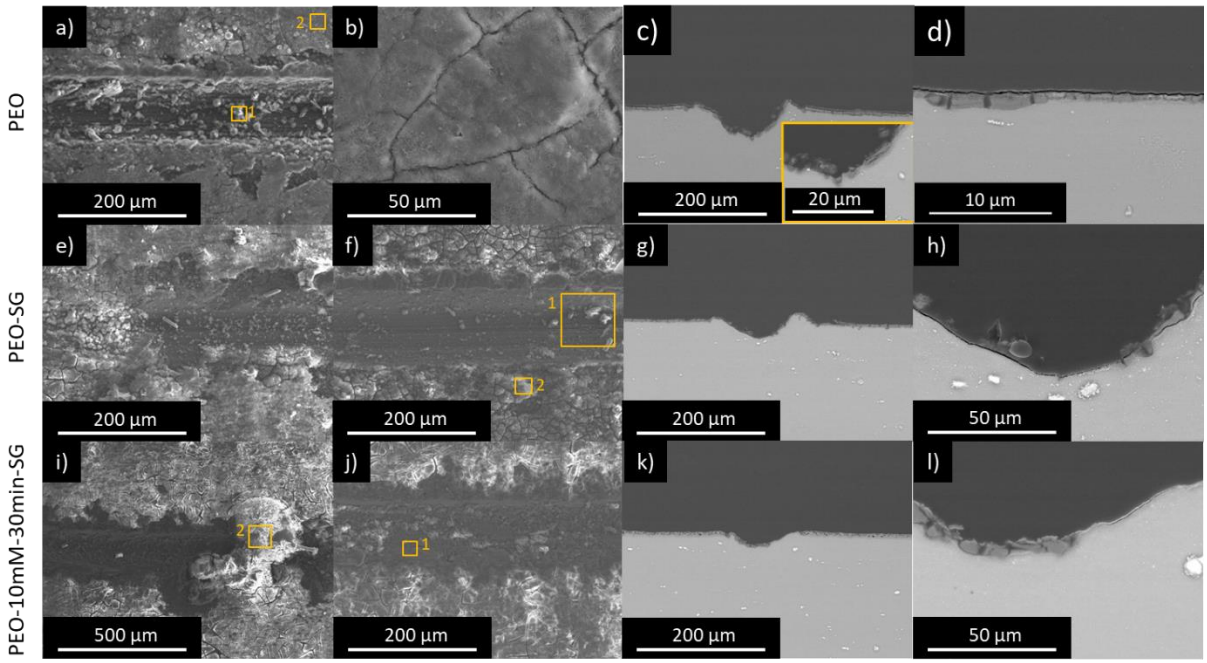

Figure 89. SEM microscopy images of (a–d) PEO, (e–h) PEO–SG and (i–l) PEO–10mM–30min–SG scribed coatings after 14 days immersion test in 0.5 wt.% NaCl solution at room temperature.

Table 48. EDS analysis performed of the scribed coatings after 14 days immersion in 0.5 wt.% NaCl (in at.%).

Sample	Area	Elements							
		C	O	F	Na	Mg	Al	Si	K
PEO	1	18.4	59.7	1.4	0.4	14.8	1.0	4.3	–
	2	20.5	59.0	–	0.2	15.9	0.3	4.1	–
PEO–SG	1	22.2	47.0	0.1	0.5	28.3	0.9	1.0	–
	2	19.9	58.5	0.3	0.7	12.0	0.6	8.0	–
PEO–10mM–30min–SG	1	32.1	26.7	0.3	0.2	39.2	0.8	0.7	–
	2	11.5	64.7	–	0.1	22.3	0.3	0.1	0.8

4.4.2.5 Contact Angle

Contact angle measurements were performed in order to assess the hydro–philicity/phobicity of the developed coatings (Figure 90). All the coatings show a hydrophilic behaviour with values below 66º. Minor differences are observed between the PEO and the sol–gel sealed samples. PEO coating inherent porosity is strongly related to the contact angle value obtained. Its hydration tendency also contributes to this behaviour. The sol–gel layer significantly reduces the contribution of surface defects, therefore the hydrophobic character is mostly related to the chemistry of the sol–gel surface rather than to its roughness.

According to SEM and FTIR results, the PEO–8HQ–SG specimens should be more hydrophilic due to the following two factors: (i) disrupted sol–gel layer in the presence of $Mg(8HQ)_2$ flakes; and (ii) lower degree of sol–gel polymerization in the presence of 8HQ resulting in an increased number of hydrophilic silanol groups and, therefore, increased hydrophilicity [186, 363]. However, as shown in Figure 90, the difference between specimens with and without treatment is not significant.

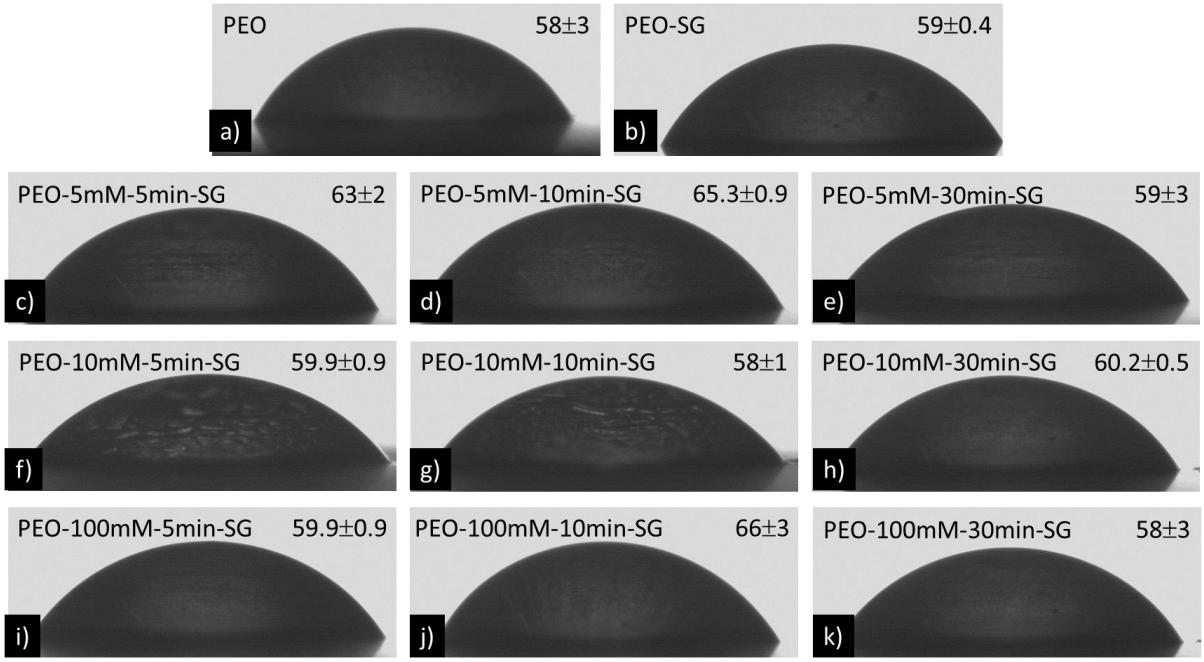

Figure 90. Water contact angle measurements: (a) PEO, (b) PEO–SG and (c–k) PEO–8HQ–SG.

4.4.3 Results on PEO/Sol–Gel(inhibitor) systems

4.4.3.1 Sol–gel precursors with incorporated 8HQ

Sol–gel precursors with different amounts of incorporated 8HQ corrosion inhibitor were prepared for sealing the PEO coating on the AZ31 alloy. The PEO processing was identical to that already described in section 4.4.2.2 (conditions are again included in Table 49). Therefore, the inhibitor loading approach in this hybrid PEO/sol–gel system differs from that of the section 4.4.2, where the inhibitor was incorporated after PEO and before the sol–gel sealing.

The inhibitor was incorporated into the precursor by means of dissolving 8HQ in the aqueous solution, which accounted for 58% of the sol–gel. Table 49 shows a summary of the studied systems.

Table 49. PEO conditions and sol–gel sealing precursors, with and without incorporated 8HQ, for surface modification of AZ31.

Coating	Conditions			
PEO	Na_2SiO_3 10.5 g/L	20 ± 1 °C	400/–30 V	5 min
	KOH 8.5 g/L		100 mA cm^{-2}	60 s
	NaF 2 g/L		50 Hz	ramp
PEO–SG	TEOS 20 %	Ethanol 10 %	Acetic acid to adjust pH 2	1 h
	GPTMS 10 %	Water 58 %		150 ºC
PEO–SG–1mM	8HQ 1 mM in the aqueous solution (58 %)			
PEO–SG–5mM	8HQ 5 mM in the aqueous solution (58 %)			
PEO–SG–10mM	8HQ 10 mM in the aqueous solution (58 %)			

**8HQ concentrations higher than 10 mM were discarded due to the precursor heterogeneity.*

Figure 91 depicts the rheological characterization of the sol–gel precursors before polymerization. The shear ratio increases with the shear stress for all cases, indicating a Newtonian behaviour. The presence of 8HQ causes a slight drop in viscosity, with the 10 mM concentration yielding the lowest values. The viscosity values in mPa·s were as follows: 3.87 ± 0.02, 3.74 ± 0.02, 3.74 ± 0.02 and 3.71 ± 0.02 for SG, SG–1mM, SG–5mM and SG–10mM, respectively. These values suggest that the addition of 8HQ may facilitate the penetration of the sol–gel precursor into the PEO coating. A different behaviour may also be expected in terms of film thickness and compactness for the inhibitor loaded specimens (i.e. lower viscosity should result in thinner sol–gel films).

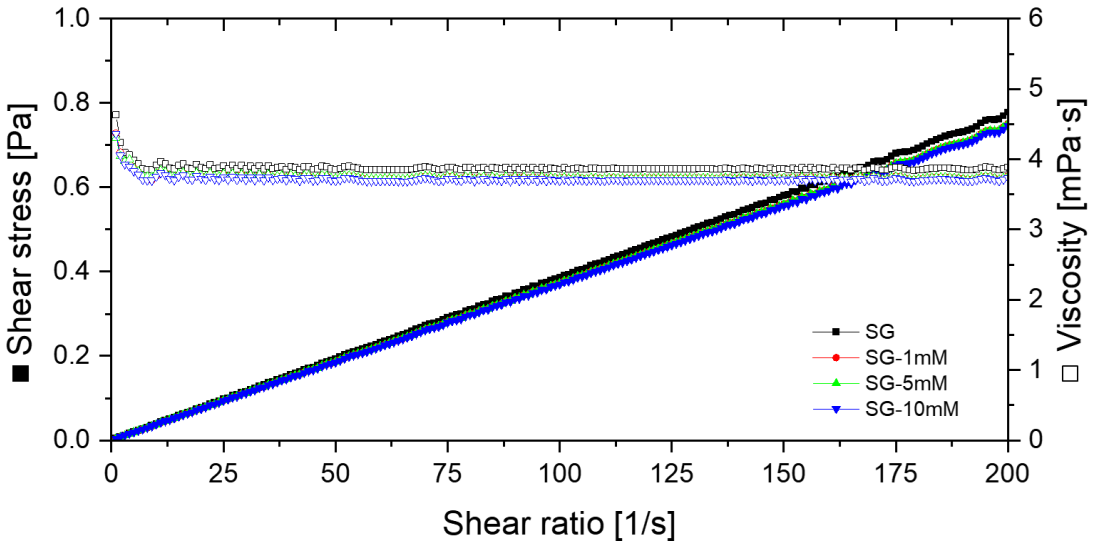

Figure 91. Flow curves for various 8HQ concentrations in the sol–gel solutions.

Figure 92 presents the UV–visible spectra of the sol–gel solutions with and without 8HQ. It should be taken into consideration that a 10 times dilution in deionized water was used to

minimize detector saturation. The 8HQ (0.05 M) aqueous solution is also included as a reference. The latter shows a saturated peak at ~250 nm and an absorption maximum at 305 nm, which is characteristic of the neutral prototropic species of 8HQ in water [364]. When 8HQ is incorporated into the acidic sol–gel precursor (pH 2.5) a new broad band arises at 358 nm. This corresponds to the lowest electronic transition of the acicid prototropic species of 8HQ (both O and N are protonated). Note that the intensity of this band is higher for the precursor with the highest amount of 8HQ. Therefore, UV–Vis spectra demonstrate the presence of 8HQ in the sol–gel precursor.

The SG solution without inhibitor presents an absorption maximum at ~263 nm which is attributed here to electronic transitions of SiO_2 [365] due to partial polymerization of the precursor.

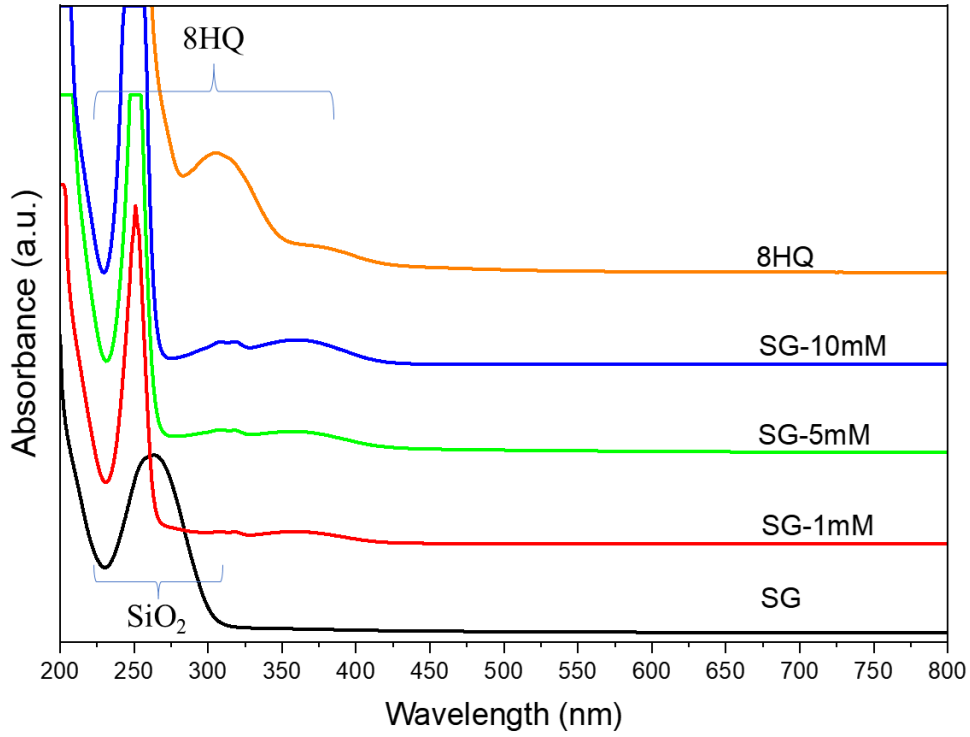

Figure 92. UV–Visible spectra of the sol–gel solutions for various concentrations of 8HQ corrosion inhibitor.

4.4.3.2 Coating Morphology and Composition

FTIR spectra of PEO–SG–8HQ systems are presented in Figure 93. The spectrum of 8HQ powder is included for reference. The spectra are like those presented in section 4.4.2.3. Si–O–Si bonds show their characteristic signals at 1493–960 and 960–724 cm^{-1} [186]. Again, the intense band at ~1034 cm^{-1}, associated with asymmetric vibrations, indicates successful sol–

gel polymerization. Comparatively, the presence of 8HQ results in less intense Si–O–Si signals. This suggests that 8HQ is detrimental for the polymerization process. Similarly, the band below 700 cm^{-1}, corresponding to Si–O–M bonds, is more intense for the PEO–SG which is attributed here to a better interaction between the PEO and the inhibitor–free sol–gel layer. Note that bands corresponding to the 8HQ molecule are almost invisible when incorporated into the sol–gel layer.

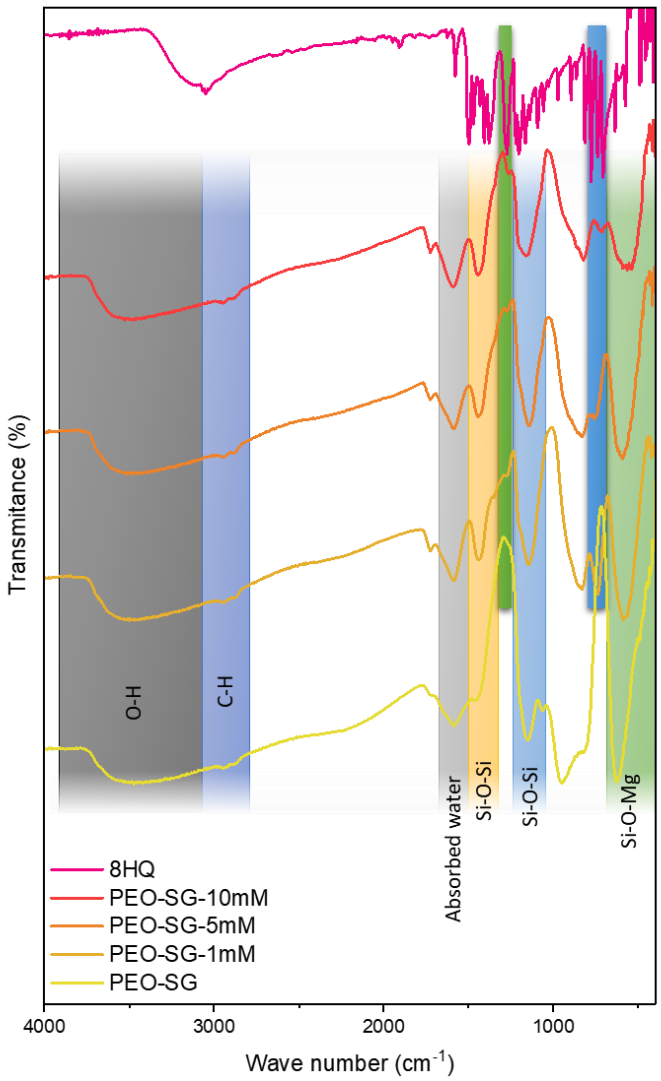

Figure 93. FTIR spectra of PEO–SG–8HQ systems on AZ31 alloy. The spectra of PEO–SG coating and 8HQ powder are included for reference.

The surface and cross–sectional SEM micrographs are shown in Figure 94 for the PEO–SG–1mM specimen, which is representative of the studied systems. As shown in Figure 94a, there are some cracks in the sol–gel layer, but the porosity of the PEO layer was almost completely sealed (Figure 94b). The thickness of the sol–gel film is 2.1 ± 0.7 μm (measured with the eddy current method) without a significant influence of 8HQ. The EDS analysis of the sol–gel layer

is consistent with previous results, but there is a relatively high amount of C, which is indicative of 8HQ incorporation in the sol–gel layer. Free system (~59º), possibly due to the small concentration of 8HQ in the sol–gel layer.

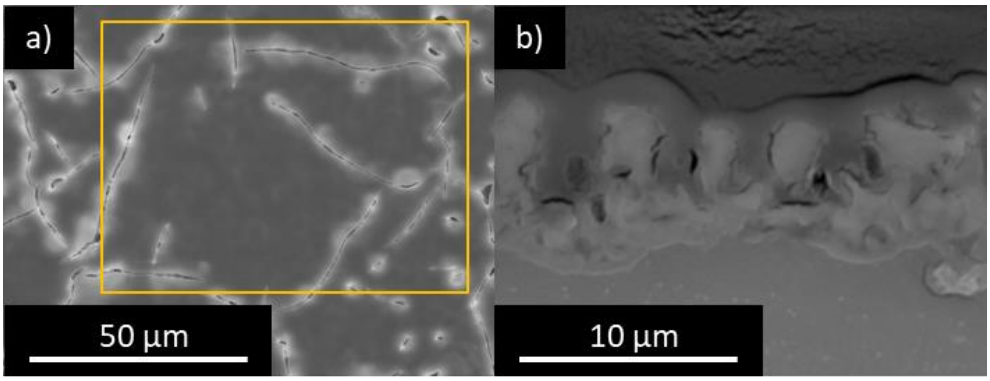

Figure 94. Scanning electron micrographs corresponding to the (a) planar and (b) cross views of PEO–SG–1mM coated AZ31. Results of the local EDS surface analysis of the coatings (at.%) are: C 36.3 , O 38.8, Na 0.3, Mg 9.9, Al 0.3, Si 13.4 and K 0.1.

4.4.3.3 Corrosion Test: Immersion test

Figure 95 depicts the impedance modulus for the studied coatings at 0.01 Hz in 0.5 wt.% NaCl up to 48 h of immersion. Impedance results for AZ31, PEO and PEO–SG are included as reference.

After 2h of immersion, PEO–SG–8HQ specimens show lower impedance modulus than the inhibitor–free PEO–SG system. Note that the impedance is the lowest for the highest 8HQ concentration (PEO–SG–10 mM) with lower values for increasing concentration of 8HQ in the sol–gel film. Despite this negative effect of 8HQ incorporation, PEO–SG–1 mM and PEO–SG–5 mM specimens show an improved performance after 24 h (e.g. $|Z| > 10^7$ **Ω** cm^2 for PEO–SG–1mM).

Therefore, findings reveal that 8HQ has opposing effects when incorporated into the sol–gel precursor. On the one hand, it hinders the sol–gel polymerization and makes the layer more susceptible to cracking, thus facilitating access of the corrosive medium. And, on the other hand, when added in small concentration (1 mM), 8HQ significantly improves the impedance response after long immersion times. Again, the positive effect is likely to be associated with the precipitation of complexes that form between the 8HQ molecules released from the sol–gel layer and the Mg^{2+} ions coming from the corroding substrate.

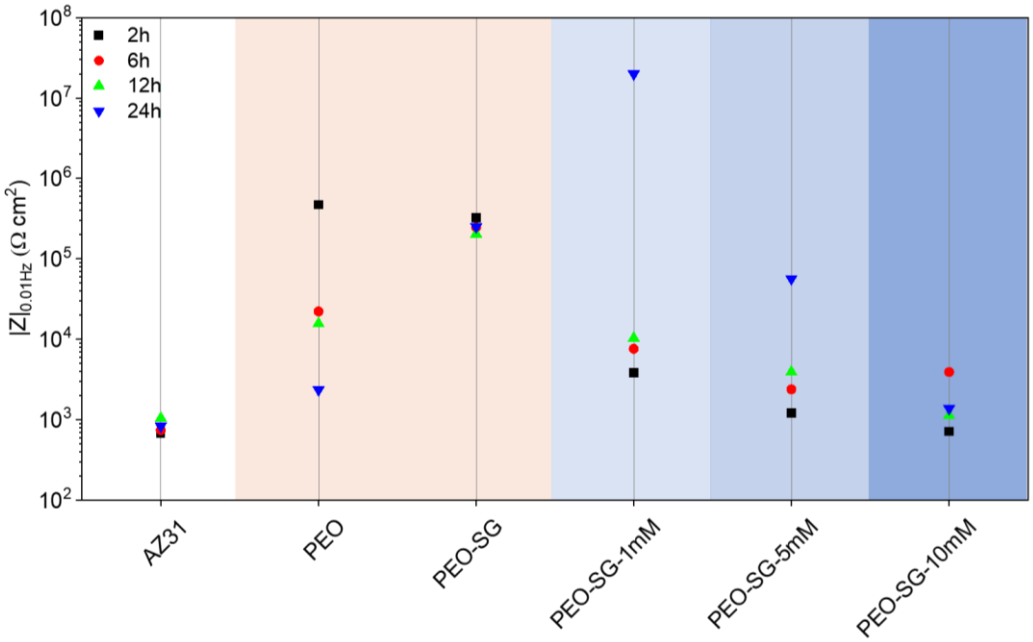

Figure 95. Scatter diagram of impedance modulus at 0.01 Hz in 0.5 wt.% NaCl of the PEO–SG coatings with 1, 5 and 10 mM 8HQ in the sol–gel layer. The diagram also includes the reference coatings (PEO and PEO–SG).

The surface appearance of PEO–SG–8HQ systems with an artificial scribe after 14 days in 0.5 wt.% NaCl is presented in Figure 96. Overall, the specimens show a much better corrosion performance than PEO and PEO–SG (see Figure 88a,b). However, some small corrosion spots are visible at the scratch for the PEO–SG–5mM and PEO–SG–10mM specimens. Therefore, additions of 8HQ into the sol–gel precursor improve the long–term corrosion resistance of hybrid PEO/SG systems, although their performance is slightly compromised when the concentration of 8HQ is above 1 mM.

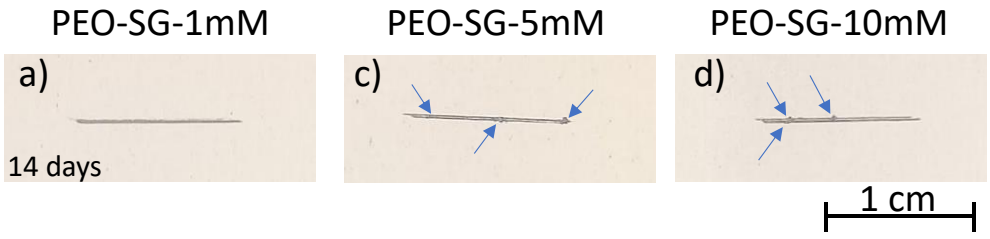

Figure 96. Digital images of PEO–SG–8HQ scribed coatings after 14 days of immersion in 0.5 wt.% NaCl solution at room temperature.

The PEO–SG–1mM specimen, which combines the highest |Z| value with best surface appearance after the scribe test, was selected for SEM/EDS examination (Figure 97 and Table 50). As shown in the plan–view, the scribe shows some corrosion products and there is cracking

of the sol–gel layer, which is due to water permeation and hydrolysis of the Si–O–Si bonds [366]. (Figure 97a,b). However, the depth of the attack is significantly less than that of the inhibitor–free systems (PEO, PEO–SG in Figure 89), being very similar to the original depth of the defect (~20 µm, Figure 97c). In the regions away from the scratch, it can be seen that the cracks penetrate the entire sol–gel thickness, although the PEO coatings remain relatively unaffected with only some signs of hydration (Figure 97d).

EDS analysis on the scribe's surface show a relatively high level of O, suggesting the formation of magnesium hydroxide as the main corrosion product. There is also some Si and F, which can originate from chemical dissolution of the PEO and/or sol–gel films (in case of Si), and C, although no $Mg(8HQ)_2$ flakes were detected on the surface of the scratch.

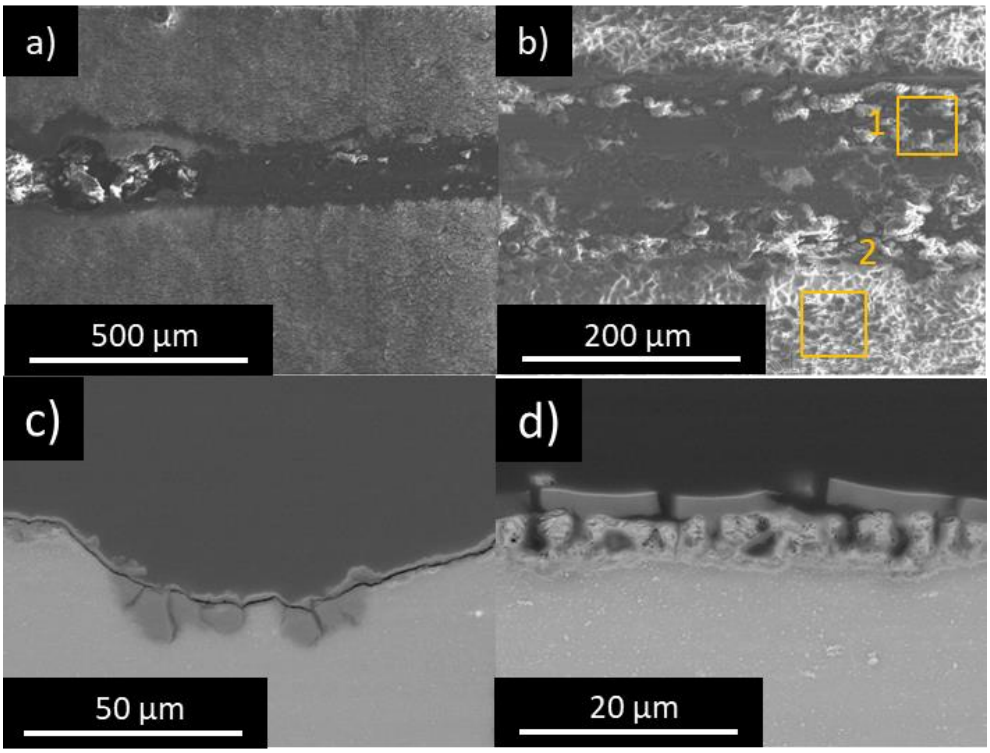

Figure 97. SEM microscopy images of PEO–SG–1mM scribed coatings after 14 days immersion test in 0.5 wt.% NaCl solution at room temperature.

Table 50. EDS analysis performed of the scribed coatings after 14 days immersion in 0.5 wt.% NaCl (in at.%).

Spectrum	Elements							
	C	O	F	Na	Mg	Al	Si	Cl
1	15.6	60.0	1.2	0.1	21.5	0.5	0.8	0.3
2	24.2	53.7	0.8	0.3	13.4	0.2	7.4	–

4.4.4 Discussion on the Protection mechanisms: PEO–8HQ–SG vs. PEO–SG–8HQ

PEO coatings are known to be highly susceptible to damage in saline media due to the relatively poor corrosion protection of MgO and the lack of self–healing ability. There are many strategies to incorporate inhibitors into PEO coatings in order to overcome this limitation. In this study, an immersion post–treatment and a modified sol–gel precursor based on 8HQ organic inhibitor were explored. This inhibitor was selected over a list of candidates after screening with EIS tests.

The inhibitory action of 8HQ is associated with the formation of insoluble metal chelates on the surface [340]. This mechanism has been demonstrated on materials such as aluminium [367] and copper [338]. In case of magnesium surfaces, $Mg(8HQ)_2$ precipitates in alkaline solutions in the form of large flakes [347]. In the present study, the flakes were clearly visible on the surface of the AZ31 after 14 days of immersion in a 0.5 wt.% NaCl solution that contained 0.05 M 8HQ. In a recent study by Vaghefinazari *et al.* [347] it was also reported that $Mg(8HQ)_2$ flakes can also form on the surface of a PEO–coated AZ21 alloy, resulting in improved corrosion resistance. Precisely, in the present work, this approach consisting in an immersion post–treatment was successfully applied for incorporation of 8HQ in the so–called hybrid PEO–8HQ–SG systems.

The second strategy for 8HQ incorporation, identified as PEO–SG–8HQ, follows the results from previous studies [343] where 8HQ–doped sol–gel formulations have demonstrated improved corrosion resistance on AZ31. The novelty in this study lies in the combination of the barrier properties of the PEO layer along with the sealing effect of the sol–gel as well as the active protection provided by the 8HQ inhibitor. In this scenario, 8HQ is suggested to act by a release–precipitation mechanism, therefore blocking corrosion in damaged areas.

In the present study, comparison between PEO–8HQ–SG and PEO–SG–8HQ strategies showed that, regardless of the approach, the incorporation of 8HQ improved the long–term corrosion resistance. This effect was more noticeable with scribed specimens, suggesting an active protection mechanism in the presence of 8HQ. PEO–8HQ–SG and PEO–SG–8HQ systems yielded similar results with a negligible depth of corrosion attack at the location of the scratch after 14 days of immersion in 0.5 wt.% NaCl. The influence of variables such as inhibitor post–treatment time and 8HQ concentration did not show a clear trend. In any case, the PEO–

100mM–30min–SG and PEO–SG–1mM were amongst the best performers when considering EIS results and corrosion tests with scribed specimens.

Figure 98 shows the schematics of the suggested protection mechanisms for the developed hybrid systems. The PEO–8HQ–SG combination, which is obtained by an immersion post–treatment in 8HQ solution followed by sol–gel sealing, produces a composite structure; flakes of $Mg(8HQ)_2$ are embedded in the sol–gel matrix and protrude at some locations (Figure 98a). The latter regions are more heterogeneous and show the presence of small cracks. The PEO–SG–8HQ combination does not show $Mg(8HQ)_2$ flakes (Figure 98b), however, UV–visible and FTIR spectra provided sufficient evidence of its successful incorporation into the sol–gel film. Remarkably, FTIR results indicated a lower degree of sol–gel polymerization and interaction between the sol–gel layer and the PEO coating when 8HQ was added to the precursor.

According to the findings in this study, when there is mechanical damage in PEO–8HQ–SG and PEO–SG–8HQ systems, the following steps are likely to take place:

1) Corrosion occurs at the location of the scribe with liberation of Mg^{2+} ions.

$$Mg(s) \rightarrow Mg^{2+}(aq) + 2e^{-} \quad (21)$$

2) Water uptake and hydrolysis of the Si–O–Si bonds causes cracking of the sol–gel layer and some Si release [368].

$$SiO_2(s) + 2H_2O(l) \rightarrow Si(OH)_4(aq) \quad (22)$$

3) Chemical dissolution of the PEO coating with liberation of SiO_3^{2-}, Mg^{2+} and F^{-} ions occurs when the solution penetrates across the sol–gel layer. Some dissolution is also expected to occur in the damaged regions next to the scratch. This chemical dissolution process is well documented in the literature [178, 288].

$$MgO(s) + 2H^{+}(aq) \rightarrow Mg^{2+}(aq) + H_2O(l) \quad (23)$$
$$Mg_2SiO_4(s) + 4H^{+}(aq) \rightarrow 2Mg^{2+}(aq) + SiO_3{}^{2-}(aq) + H_2O(l) \quad (24)$$

4) Under neutral or slightly acidic conditions, $8HQ^{-}$ ions are released from the $Mg(8HQ)_2$ flakes [343] in the PEO–8HQ–SG system and from the bulk of the sol–gel layer [369] in the PEO–SG–8HQ system. Then, when the pH rises over the cathodic regions due to the water reduction reaction, $8HQ^{-}$ combines with Mg^{2+} and forms $Mg(8HQ)_2$

precipitates. The latter will remain insoluble under the highly alkaline conditions that developed in the scratch region [347, 370].

5) The combination of Mg^{2+} and other species in the solution (SiO_3^{2-}, F^-, OH^-) results in additional precipitates that also contribute to delay the corrosion attack. This precipitation is more prominent at the location of the scratch due to a higher amount of Mg^{2+} ions and confinement of the solution. In this study, the presence of Si and F on the surface of the scribe has been demonstrated by EDS analysis, whereas further studies are required to confirm the precipitation of $Mg(8HQ)_2$ at the damaged areas (e.g. after testing for longer immersion times).

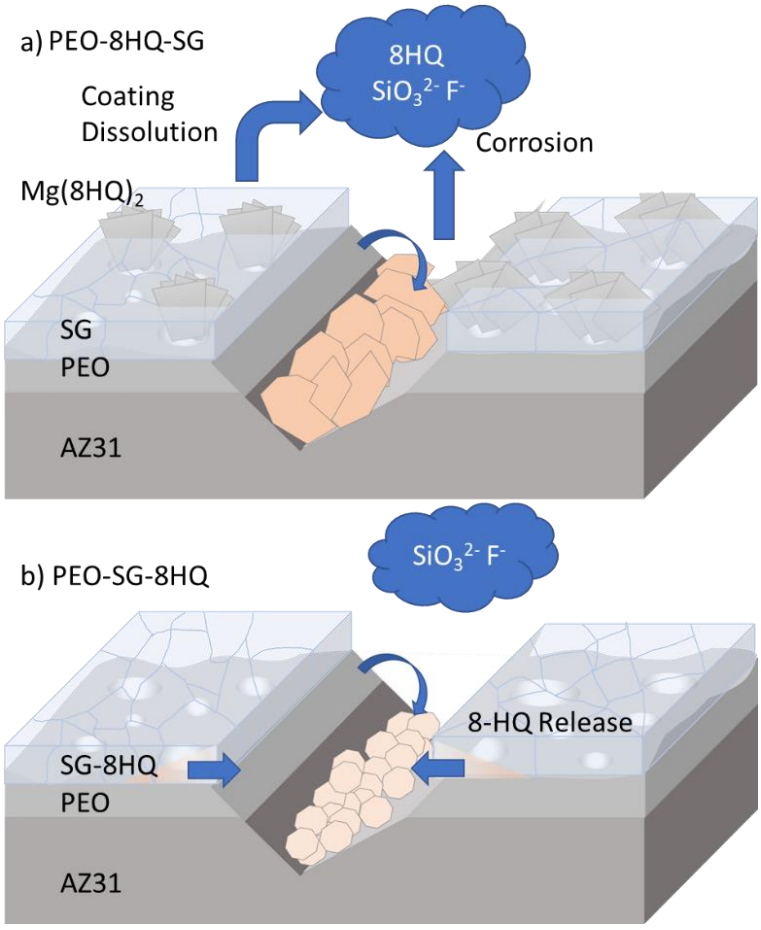

Figure 98. Schematic illustration of the corrosion mechanism for scratched (a) PEO–8HQ–SG and (b) PEO–SG–8HQ coatings on AZ31 Mg alloys.

4.4.5 Concluding Remarks on hybrid PEO/Sol–Gel coatings with corrosion inhibitors

The following conclusions were obtained from investigations on inhibitor loading on PEO/sol–gel systems:

- Hydrogen evolution tests showed that, among several organic corrosion inhibitors, 8HQ was the best performer for the AZ31 alloy in saline solution. The mechanism of protection is associated with formation of insoluble $Mg(8HQ)_2$ flakes.
- 8HQ inhibitor species were successfully incorporated into hybrid PEO/sol–gel systems following two strategies: i) inhibitor post–treatment before sol–gel sealing (PEO–8HQ–SG), and ii) inhibitor loading into the sol–gel precursor (PEO–SG–8HQ).
- The PEO–8HQ–SG system showed a composite structure with flakes of $Mg(8HQ)_2$ embedded in the SG film, whereas the PEO–SG–8HQ incorporated 8HQ into its structure, although it reduced the cross–linking of the sol–gel layer.
- PEO–8HQ–SG and PEO–SG–8HQ systems yielded similar results with a negligible depth of corrosion attack at the location of the scratch after 14 days of immersion in 0.5 wt.% NaCl. This improvement was mainly ascribed to an active protection mechanism involving the release and precipitation of 8HQ species and other species (SiO_3^{2-}, F^-).
- The PEO–10mM–30min–SG and PEO–SG–1mM coatings are amongst the best performers when tested by EIS and immersion with scribed specimens.

5 Conclusions

The development of environmentally friendly coatings for corrosion protection of Mg alloys is one of the main challenges for magnesium alloys in the transport industry. In this work, several strategies were investigated for the corrosion protection of Mg alloys. In Chapter 1, inhibitor–loaded LDH conversion coatings were investigated, whereas Chapters 2, 3 and 4 deal with plasma electrolytic oxidation coatings and their modification through inhibitor doping, sealing and hybrid combination with a sol–gel top layer. The following sections summarize the main conclusions of this work.

5.1 Chapter 1

LDH conversion coatings formed by *in–situ* growth method were investigated on AZ31 alloy. After an inhibitor screening stage, two systems were selected: Zn–Al– and Li–Al–LDHs loaded with inhibitors Na_2WO_4 and $LiNO_3$, respectively. Coatings showed a two–layer structure with an outer flaky layer and an inner denser layer. The applied inhibitor post–treatments resulted in the selective dissolution of the outermost layer of the LDH coatings, reducing hydrophilicity and paint adhesion of the coatings. The incorporation of W and Li was confirmed by several techniques. The incorporation of W species was mainly in the form of $MgWO_4$ precipitates, whereas Li^+ is suggested to attach to the top and bottom layers of the LDH flakes by electrostatic interaction with NO_3^- ions. The active corrosion properties of the developed coatings were confirmed by SVET analysis. The Zn–Al LDH W system revealed better active protection properties than Li–Al LDH Li. The inhibition corrosion mechanism is attributed to ion–exchange of Cl^- ions and dissolution–redeposition of protective deposits at the location of artificial defects.

5.2 Chapter 2

Ca–doped flash–PEO (FPEO) coatings with low energy consumption and enhanced corrosion resistance were developed on AZ31 alloy. Coatings (~1 µm–thick) were produced under low current densities (100 mA cm^{-2}) and short treatment times (20–45 s). Two Ca–based compounds, calcium oxide (CaO) and calcium glycerophosphate (CaGlyP), which is more soluble, were used as sources of Ca in the electrolyte. A chromium commercial conversion coating (CCC) was used as a landmark. Full–system evaluation with painted–and–scratched specimens, consisting of FPEO combined with an inhibitor–free epoxy primer, was performed in neutral salt spray and paint adhesion tests. The FPEO_CaGlyP coating revealed the best

performance, both as a stand–alone coating and as a full system, being superior to the CCC. This behaviour was attributed to the stronger interactions of Ca^{2+} ions with SiO_4^{4-} and PO_4^{3-} species within the MgO ceramic network.

5.3 Chapter 3

PEO coatings were successfully developed on Mg–Y–Zn and AZ91D alloys and sealed with Ce– and Ca–salts, respectively.

The Mg–Y–Zn alloy shows a recrystallized microstructure with a high–volume fraction of LPSO phases that act as cathodes according to SKPFM measurements. PEO processing resulted in a 5 µm–thick coating with a three layer structure where LPSO phases were oxidized without disrupting the continuity of the coating. The enhanced surface passivity after PEO treatment significantly reduced the corrosion rate in comparison to the untreated alloy. Sealing in an acidic Ce–containing solution led to accumulation of CeO_2 within the coating pores and cracks and, therefore, improved corrosion resistance. A 5 min sealing was enough to significantly improve the corrosion resistance of the PEO coating, whereas longer times (60 min) resulted in excessive dissolution of the coating and deterioration of the inner barrier layer.

A sealing treatment combining Ca species and SDS provided hydrophobicity and a significant inhibition effect for corrosion protection of PEO coatings on the AZ91D alloy. Low pH conditions and the presence of SDS as a nucleating agent promoted the precipitation of Ca–rich compounds. As shown by SEM, XRD and XPS, hydroxyapatite sealed the coating pores due to increased amount of released PO_4^{3-} at these locations. The adsorption of SDS is believed to greatly contribute to the enhanced corrosion performance, although it decreases the paintability due to its hydrophobic character.

5.4 Chapter 4

Screening of several organic corrosion inhibitors by hydrogen evolution test revealed that 8HQ was the best performer for the AZ31 alloy due to the formation of insoluble $Mg(8HQ)_2$ flakes. Two strategies were used to successfully incorporate 8HQ into hybrid PEO/sol–gel systems: i) inhibitor post–treatment before sol–gel sealing, which showed a composite structure with flakes of $Mg(8HQ)_2$ embedded in the SG film, and ii) inhibitor loading into the sol–gel precursor, in which 8HQ was incorporated into its structure. Both systems revealed similar corrosion performance after 14 days of immersion in 0.5 wt.% NaCl and the enhanced behaviour was

related to an active protection mechanism involving the release and precipitation of 8HQ species and other species (SiO_3^{2-}, F^-). The PEO–10mM–30min–SG and PEO–SG–1mM coatings are amongst the best performers when tested for short–time (EIS) and long–time (immersion test with scribed specimens).

6 Bibliography

Bibliography

[1] U.B. Pal, D.E. Woolley, A. Krishnan, T. Keenan, C.P. Manning, G.B. Kenney, Solid Oxide Oxygen Ion Conducting Membrane, in: H.E. Friedrich, B.L. Mordike (Eds.), Magnesium Technology, Springer, Berlin, 2002, pp. 19 - 24, 10.1007/3-540-30812-1.

[2] P. Duhaime, P. Mercille, M. Pineau, Electrolytic process technologies for the production of primary magnesium, Mineral Processing and Extractive Metallurgy 111(2) (2002), 53-55, 10.1179/mpm.2002.111.2.53.

[3] M. Fichtner, Motivation for a Magnesium Battery, in: M. Fichtner (Ed.), Magnesium Batteries: Research and Applications, The Royal Society of Chemistry, Cambridge, 2020, pp. 1-16, 10.1039/9781788016407-00001.

[4] C. Mendis, A. Singh, Magnesium Recycling: To the Grave and Beyond, The Journal of The Minerals, Metals & Materials Society 65(10) (2013), 1283-1284, 10.1007/s11837-013-0701-5.

[5] J. Tan, S. Ramakrishna, Applications of Magnesium and Its Alloys: A Review, Applied Sciences 11(15) (2021), 6861, 10.3390/app11156861.

[6] J. Durlach, Overview of Magnesium Research: History and Current Trends, in: Y. Nishizawa, H. Morii, J. Durlach (Eds.), New Perspectives in Magnesium Research, Springer, London, 2007, pp. 3-20, 10.1007/978-1-84628-483-0.

[7] I. Polmear, D. StJohn, J.F. Nie, M. Qian, Light Alloys : Metallurgy of the Light Metals, 5th ed., Butterworth-Heinemann, Boston, 2017.

[8] (EU) 2018/842, Regulation on binding annual greenhouse gas emission reductions by Member States from 2021 to 2030 contributing to climate action to meet commitments under the Paris Agreement and amending Regulation (EU) No 525/2013, European Parlament European Union

[9] M. Ashby, Material Property Charts, in: G.E. Dieter (Ed.), Materials Selection and Design, ASM International, Almere, 1997, pp. 418-454, 10.31399/asm.hb.v20.a0002452.

[10] Z. Yang, J.P. Li, J.X. Zhang, G.W. Lorimer, J. Robson, Review on Research and Development of Magnesium Alloys, Acta Metallurgica Sinica (English Letters) 21(5) (2008), 313-328, 10.1016/S1006-7191(08)60054-X.

[11] Y. Yang, X. Xiong, J. Chen, X. Peng, D. Chen, F. Pan, Research advances in magnesium and magnesium alloys worldwide in 2020, Journal of Magnesium and Alloys 9(3) (2021), 705-747, 10.1016/j.jma.2021.04.001.

[12] H. Liu, F. Cao, G.-L. Song, D. Zheng, Z. Shi, M.S. Dargusch, A. Atrens, Review of the atmospheric corrosion of magnesium alloys, Journal of Materials Science & Technology 35(9) (2019), 2003-2016, 10.1016/j.jmst.2019.05.001.

[13] A.S. Hamdy Makhlouf, Intelligent Stannate-Based Coatings of Self-Healing Functionality for Magnesium Alloys, in: A. Tiwari, J. Rawlins, L.H. Hihara (Eds.), Intelligent Coatings for Corrosion Control, Butterworth-Heinemann, Boston, 2015, pp. 537-555, 10.1016/B978-0-12-411467-8.00015-5.

Bibliography

[14] Y. Nie, J. Dai, X. Li, X. Zhang, Recent developments on corrosion behaviors of Mg alloys with stacking fault or long period stacking ordered structures, Journal of Magnesium and Alloys 9(4) (2021), 1123-1146, 10.1016/j.jma.2020.09.021.

[15] M. Razavi, M. Fathi, O. Savabi, M. Borouni, A review of degradation properties of Mg based biodegradable implants, Research and Reviews in Materials Science and Chemistry 1(1) (2012), 15-58.

[16] N.P. Papenberg, S. Gneiger, I. Weißensteiner, P.J. Uggowitzer, S. Pogatscher, Mg-Alloys for Forging Applications—A Review, Materials 13(4) (2020), 985, 10.3390/ma13040985.

[17] V. Tsakiris, C. Tardei, F.M. Clicinschi, Biodegradable Mg alloys for orthopedic implants – A review, Journal of Magnesium and Alloys 9(6) (2021), 1884-1905, 10.1016/j.jma.2021.06.024.

[18] S. Jayasathyakawin, M. Ravichandran, N. Baskar, C. Anand Chairman, R. Balasundaram, Mechanical properties and applications of Magnesium alloy – Review, Materials Today: Proceedings 27 (2020), 909-913, 10.1016/j.matpr.2020.01.255.

[19] V.K. Champagne, The Repair of Magnesium Rotorcraft Components by Cold Spray, Journal of Failure Analysis and Prevention 8(2) (2008), 164-175, 10.1007/s11668-008-9116-y.

[20] M. Esmaily, J.E. Svensson, S. Fajardo, N. Birbilis, G.S. Frankel, S. Virtanen, R. Arrabal, S. Thomas, L.G. Johansson, Fundamentals and advances in magnesium alloy corrosion, Progress in Materials Science 89 (2017), 92-193, 10.1016/j.pmatsci.2017.04.011.

[21] Q. Jiang, D.-z. Lu, C. Liu, N. Liu, B. Hou, The Pilling-Bedworth Ratio of Oxides Formed From the Precipitated Phases in Magnesium Alloys, Frontiers in Materials 8 (2021), 761052, 10.3389/fmats.2021.761052.

[22] A. Pardo, M.C. Merino, A.E. Coy, R. Arrabal, F. Viejo, E. Matykina, Corrosion behaviour of magnesium/aluminium alloys in 3.5wt.% NaCl, Corrosion Science 50(3) (2008), 823-834, 10.1016/j.corsci.2007.11.005.

[23] E. Gerashi, R. Alizadeh, T.G. Langdon, Effect of crystallographic texture and twinning on the corrosion behavior of Mg alloys: A review, Journal of Magnesium and Alloys 10(2) (2022), 313-325, 10.1016/j.jma.2021.09.009.

[24] G.L. Makar, J. Kruger, Corrosion Studies of Rapidly Solidified Magnesium Alloys, Journal of The Electrochemical Society 137(2) (1990), 414-421, 10.1149/1.2086455.

[25] G.R. Hoey, M. Cohen, Corrosion of Anodically and Cathodically Polarized Magnesium in Aqueous Media, Journal of The Electrochemical Society 105(5) (1958), 245, 10.1149/1.2428817.

[26] C. Wang, D. Mei, G. Wiese, L. Wang, M. Deng, S.V. Lamaka, M.L. Zheludkevich, High rate oxygen reduction reaction during corrosion of ultra-high-purity magnesium, Materials Degradation 4(1) (2020), 1-42, 10.1038/s41529-020-00146-1.

[27] E.L. Silva, S.V. Lamaka, D. Mei, M.L. Zheludkevich, The Reduction of Dissolved Oxygen During Magnesium Corrosion, ChemistryOpen 7(8) (2018), 664-668, 10.1002/open.201800076.

[28] R. Ambat, N. Aung, W. Zhou, Evaluation of microstructural effects on corrosion behaviour of AZ91D magnesium alloy, Corrosion Science 42(8) (2000), 1433-1455, 10.1016/S0010-938X(99)00143-2.

[29] M. Pourbaix, Atlas of Electrochemical Equilibria in Aqueous Solutions II, 2nd ed., National Association of Corrosion Engineers, Houston, 1974.

[30] J.A. Yuwono, N. Birbilis, C.D. Taylor, K.S. Williams, A.J. Samin, N.V. Medhekar, Aqueous electrochemistry of the magnesium surface: Thermodynamic and kinetic profiles, Corrosion Science 147 (2019), 53-68, 10.1016/j.corsci.2018.10.014.

[31] A. Pardo, M.C. Merino, A.E. Coy, F. Viejo, R. Arrabal, S. Feliú, Influence of microstructure and composition on the corrosion behaviour of Mg/Al alloys in chloride media, Electrochimica Acta 53(27) (2008), 7890-7902, 10.1016/j.electacta.2008.06.001.

[32] R.V. Allen, T.J. Johnson, W.E. Borbidge, D. Liang, Magnesium Technology 2001, TMS (2001), 75-80.

[33] G.L. Song, A. Atrens, Corrosion Mechanisms of Magnesium Alloys, Advanced Engineering Materials 1(1) (1999), 11-33, 10.1002/(SICI)1527-2648(199909)1:1<11::AID-ADEM11>3.0.CO;2-N.

[34] Y. Shao, G. Meng, C. Zhongyu, F. Wang, Corrosion of hot extrusion AZ91 magnesium alloy: I-relation between the microstructure and corrosion behavior, Corrosion Science 53 (2011), 1960–1968, 10.1016/j.corsci.2011.02.015.

[35] D. Song, A. Ma, J. Jiang, P. Lin, D.-h. Yang, J. Fan, Corrosion behavior of ultra-fine grained bulk AZ91D Mg alloy fabricated by equal-channel angular pressing, Corrosion Science 53 (2011), 362-373, 10.1016/j.corsci.2010.09.044.

[36] S. Sun, N. Deng, H. Zhang, L. He, H. Zhou, B. Han, K. Gao, X. Wang, Microstructure and mechanical properties of AZ31 magnesium alloy reinforced with novel sub-micron vanadium particles by powder metallurgy, Journal of Materials Research and Technology 15 (2021), 1789-1800, 10.1016/j.jmrt.2021.09.015.

[37] H. Liu, N. Gong, L. Pang, X. Zhang, Microstructure and mechanical properties of as-cast AZ31 with the addition of Sb, Materials Science and Engineering A-structural Materials Properties Microstructure and Processing 497(1) (2008), 254-259, 10.1016/j.msea.2008.07.010.

[38] Z. Yang, A. Ma, B. Xu, J. Jiang, J. Sun, Corrosion behavior of AZ91 Mg alloy with a heterogeneous structure produced by ECAP, Corrosion Science 187 (2021), 109517, 10.1016/j.corsci.2021.109517.

[39] D. Song, A.B. Ma, J.H. Jiang, P.H. Lin, D.H. Yang, J.F. Fan, Corrosion behaviour of bulk ultra-fine grained AZ91D magnesium alloy fabricated by equal-channel angular pressing, Corrosion Science 53(1) (2011), 362-373, 10.1016/j.corsci.2010.09.044.

[40] D. Orlov, K.D. Ralston, N. Birbilis, Y. Estrin, Enhanced corrosion resistance of Mg alloy ZK60 after processing by integrated extrusion and equal channel angular pressing, Acta Materialia 59(15) (2011), 6176-6186, 10.1016/j.actamat.2011.06.033.

Bibliography

[41] P. Minárik, R. Král, M. Janeček, Effect of ECAP processing on corrosion resistance of AE21 and AE42 magnesium alloys, Applied Surface Science 281 (2013), 44-48, 10.1016/j.apsusc.2012.12.096.

[42] L. Zhong, Y. Wang, H. Luo, X. Cui, Y. Zhang, B. Dou, J. Peng, Influence of aging prior to extrusion on the microstructure and corrosion resistance of Mg–8Sn–2Zn–0.2Mn alloy, Journal of Alloys and Compounds 780 (2019), 783-791, 10.1016/j.jallcom.2018.11.400.

[43] Y.-C. Zhao, M.-C. Zhao, R. Xu, L. Liu, J.-X. Tao, C. Gao, C. Shuai, A. Atrens, Formation and characteristic corrosion behavior of alternately lamellar arranged α and β in as-cast AZ91 Mg alloy, Journal of Alloys and Compounds 770 (2019), 549-558, 10.1016/j.jallcom.2018.08.103.

[44] M.-C. Zhao, M. Liu, G. Song, A. Atrens, Influence of the β-phase morphology on the corrosion of the Mg alloy AZ91, Corrosion Science 50(7) (2008), 1939-1953, 10.1016/j.corsci.2008.04.010.

[45] R. Zeng, E. Han, W. Ke, Corrosion of Artificial Aged Magnesium Alloy AZ80 in 3.5 wt pct NaCl Solutions, Journal of Materials Sciences and Technology 23(03) (2009), 353-358.

[46] Y. Wang, X. Wang, K. Wu, F. Wang, Role of β Phase during Microarc Oxidation of Mg Alloy AZ91D and Corrosion Resistance of the Oxidation Coating, Journal of Materials Science & Technology 29(12) (2013), 1129-1133, 10.1016/j.jmst.2013.10.014.

[47] J. Hao, J. Zhang, B. Li, R. Xie, Effects of 14H LPSO phase on the dynamic recrystallization and work hardening behaviors of an extruded Mg–Zn–Y–Mn alloy, Materials Science and Engineering: A 804 (2021), 140727, 10.1016/j.msea.2020.140727.

[48] S.M. Ramezani, A. Zarei-Hanzaki, A. Salandari-Rabori, H.R. Abedi, P. Minarik, K. Máthis, K.H. Fekete, Unraveling the effect of deformation-induced phase transformation on microstructure and micro-texture evolution of a multi-axially forged Mg-Gd-Y-Zn-Zr alloy containing the LPSO phase, Journal of Materials Research and Technology 15 (2021), 2088-2101, 10.1016/j.jmrt.2021.09.035.

[49] Y. Chen, L. Hu, L. Shi, T. Zhou, J. Tu, Q. Chen, M.-B. Yang, Effect of texture types on microstructure evolution and mechanical properties of AZ31 magnesium alloy undergoing uniaxial tension deformation at room temperature, Materials Science and Engineering A-structural Materials Properties Microstructure and Processing 769 (2020), 138497, 10.1016/j.msea.2019.138497.

[50] J.F. Nie, Y. Zhu, A.J. Morton, On the Structure, Transformation and Deformation of Long-Period Stacking Ordered Phases in Mg-Y-Zn Alloys, Metallurgical and Materials Transactions A 45 (2014), 3338-3348, 10.1007/s11661-014-2301-6.

[51] E. Abe, Y. Kawamura, K. Hayashi, A. Inoue, Long-period ordered structure in a high-strength nanocrystalline Mg-1 at% Zn-2 at% Y alloy studied by atomic-resolution Z-contrast STEM, Acta Materialia 50(15) (2002), 3845-3857, 10.1016/S1359-6454(02)00191-X.

[52] E. Abe, A. Ono, T. Itoi, M. Yamasaki, Y. Kawamura, Polytypes of long-period stacking structures synchronized with chemical order in a dilute Mg–Zn–Y alloy, Philosophical Magazine Letters 91(10) (2011), 690-696, 10.1080/09500839.2011.609149.

[53] J. Zhang, J. Xu, W. Cheng, C. Chen, J. Kang, Corrosion Behavior of Mg–Zn–Y Alloy with Long-period Stacking Ordered Structures, Journal of Materials Science & Technology 28(12) (2012), 1157-1162, 10.1016/S1005-0302(12)60186-8.

[54] F. Shi, C.-q. Wang, Z.-m. Zhang, Microstructures, corrosion and mechanical properties of as-cast Mg–Zn–Y–(Gd) alloys, Transactions of Nonferrous Metals Society of China 25(7) (2015), 2172-2180, 10.1016/S1003-6326(15)63829-8.

[55] C.Q. Li, D.K. Xu, Z.R. Zeng, B.J. Wang, L.Y. Sheng, X.B. Chen, E.H. Han, Effect of volume fraction of LPSO phases on corrosion and mechanical properties of Mg-Zn-Y alloys, Materials & Design 121 (2017), 430-441, 10.1016/j.matdes.2017.02.078.

[56] P. Cheng, Y. Zhao, R. Lu, H. Hou, Effect of the morphology of long-period stacking ordered phase on mechanical properties and corrosion behavior of cast Mg-Zn-Y-Ti alloy, Journal of Alloys and Compounds 764 (2018), 226-238, 10.1016/j.jallcom.2018.06.056.

[57] S. Fajardo, F.R. García-Galván, V. Barranco, J.C. Galvan, S. Jr, A Critical Review of the Application of Electrochemical Techniques for Studying Corrosion of Mg and Mg Alloys: Opportunities and Challenges, in: T. Tański, W. Borek, M. Król (Eds.), Magnesium Alloys, IntechOpen, Rijeka, 2018, pp. 6-28, 10.5772/intechopen.79497.

[58] S. Fajardo, C.F. Glover, G. Williams, G.S. Frankel, The Evolution of Anodic Hydrogen on High Purity Magnesium in Acidic Buffer Solution, Corrosion 73(5) (2017), 482-493, 10.5006/2247.

[59] D. Mei, S.V. Lamaka, X. Lu, M.L. Zheludkevich, Selecting medium for corrosion testing of bioabsorbable magnesium and other metals – A critical review, Corrosion Science 171 (2020), 108722, 10.1016/j.corsci.2020.108722.

[60] G. Williams, N. Birbilis, H.N. McMurray, The source of hydrogen evolved from a magnesium anode, Electrochemistry Communications 36 (2013), 1-5, 10.1016/j.elecom.2013.08.023.

[61] A. Samaniego, N. Birbilis, X. Xia, G. Frankel, Hydrogen Evolution During Anodic Polarization of Mg Alloyed with Li, Ca, or Fe, Corrosion 71 (2015), 224-233, 10.5006/1367.

[62] G.S. Frankel, A. Samaniego, N. Birbilis, Evolution of hydrogen at dissolving magnesium surfaces, Corrosion Science 70 (2013), 104-111, 10.1016/j.corsci.2013.01.017.

[63] A. Samaniego, B.L. Hurley, G.S. Frankel, On the evidence for univalent Mg, Journal of Electroanalytical Chemistry 737 (2015), 123-128, 10.1016/j.jelechem.2014.04.013.

[64] S. Bender, J. Goellner, A. Heyn, S. Schmigalla, A new theory for the negative difference effect in magnesium corrosion, Materials and Corrosion 63(8) (2012), 707-712, 10.1002/maco.201106225.

[65] W. Zhang, Q. Liu, Y. Chen, G. Wan, Anodic dissolution dictates the negative difference effect (NDE) of magnesium corrosion more in chemical pathway, Materials Letters 232 (2018), 54-57, 10.1016/j.matlet.2018.08.069.

Bibliography

[66] E. Dickinson, A. Wain, The Butler-Volmer equation in electrochemical theory: Origins, value, and practical application, Journal of Electroanalytical Chemistry 872 (2020), 114145, 10.1016/j.jelechem.2020.114145.

[67] S. Fajardo, G.S. Frankel, Effect of impurities on the enhanced catalytic activity for hydrogen evolution in high purity magnesium, Electrochimica Acta 165 (2015), 255-267, 10.1016/j.electacta.2015.03.021.

[68] J.A. Yuwono, C.D. Taylor, G.S. Frankel, N. Birbilis, S. Fajardo, Understanding the enhanced rates of hydrogen evolution on dissolving magnesium, Electrochemistry Communications 104 (2019), 106482, 10.1016/j.elecom.2019.106482.

[69] A. Samaniego, B.L. Hurley, G. Frankel, On the Evidence for Univalent Mg, Journal of Electroanalytical Chemistry 737 (2014), 123-128, 10.1016/j.jelechem.2014.04.013.

[70] N. Birbilis, A.D. King, S. Thomas, G.S. Frankel, J.R. Scully, Evidence for enhanced catalytic activity of magnesium arising from anodic dissolution, Electrochimica Acta 132 (2014), 277-283, 10.1016/j.electacta.2014.03.133.

[71] J. Huang, G.-L. Song, Y. Zhu, D. Zheng, Z. Wang, The anodically polarized Mg surface products and accelerated hydrogen evolution, Journal of Magnesium and Alloys 10(9) (2021), 1-19, 10.1016/j.jma.2021.05.008.

[72] S. Zhang, X. Zhang, C. Zhao, J. Li, Y. Song, C. Xie, H. Tao, Y. Zhang, Y. He, Y. Jiang, Y. Bian, Research on an Mg–Zn alloy as a degradable biomaterial, Acta Biomaterialia 6(2) (2010), 626-640, 10.1016/j.actbio.2009.06.028.

[73] T. Valente, Grain boundary effects on the behavior of WE43 magnesium castings in simulated marine environment, Journal of Materials Science Letters 20(1) (2001), 67-69, 10.1023/A:1006723016999.

[74] H.J. Martin, M.F. Horstemeyer, P.T. Wang, Comparison of corrosion pitting under immersion and salt-spray environments on an as-cast AE44 magnesium alloy, Corrosion Science 52(11) (2010), 3624-3638, 10.1016/j.corsci.2010.07.009.

[75] O. Lunder, J.E. Lein, S.M. Hesjevik, T.K. Aune, K. Nişancioğlu, Corrosion morphologies on magnesium alloy AZ 91, Materials and Corrosion 45(6) (1994), 331-340, 10.1002/maco.19940450603.

[76] S.P. Lynch, P. Trevena, Stress Corrosion Cracking and Liquid Metal Embrittlement in Pure Magnesium, Corrosion 44(2) (1988), 113-124, 10.5006/1.3583907.

[77] K. Gall, G. Biallas, H.J. Maier, P. Gullett, M.F. Horstemeyer, D.L. McDowell, In-situ observations of low-cycle fatigue damage in cast AM60B magnesium in an environmental scanning electron microscope, Metallurgical and Materials Transactions A 35(1) (2004), 321-331, 10.1007/s11661-004-0133-5.

[78] E. Lewis, O. Chamel, M. Mohsenin, E. Ots, E. White, REACH Regulation, 2018, pp. 219-219, 10.4324/9781315270326-156.

[79] J.E. Gray, B. Luan, Protective coatings on magnesium and its alloys — a critical review, Journal of Alloys and Compounds 336(1) (2002), 88-113, 10.1016/S0925-8388(01)01899-0.

[80] X.-B. Chen, M. Easton, N. Birbilis, H.Y. Yang, T. Abbott, Corrosion-resistant coatings for magnesium (Mg) alloys, 2013, pp. 282-312, 10.1533/9780857098962.2.282.

[81] S. Bender, J. Göllner, A. Heyn, C. Blawert, P. Srinivasan, Corrosion and surface finishing of magnesium and its alloys, in: F. Czerwinski (Ed.), Magnesium Alloys, IntechOpen, Rijeka, 2013, pp. 232-265, 10.1533/9780857097293.232.

[82] H. Hornberger, S. Virtanen, A. Boccaccini, Biomedical coatings on magnesium alloys - A review, Acta biomaterialia 8 (2012), 2442-2455, 10.1016/j.actbio.2012.04.012.

[83] G. Wu, J. Mohammed Ibrahim, P. Chu, Surface design of biodegradable magnesium alloys — A review, Surface and Coatings Technology 233 (2013), 2–12, 10.1016/j.surfcoat.2012.10.009.

[84] J. Tan, P. Balan, N. Birbilis, Advances in LDH coatings on Mg alloys for biomedical applications: A corrosion perspective, Applied Clay Science 202 (2020), 105948, 10.1016/j.clay.2020.105948.

[85] L.-y. Li, L.-Y. Cui, R. Zeng, S. li, X.-B. Chen, Y. Zheng, B.K. Mathan, Advances in functionalized polymer coatings on biodegradable magnesium alloys - A review, Acta Biomaterialia 79 (2018), 23-36, 10.1016/j.actbio.2018.08.030.

[86] W. Yao, L. Wu, G. Huang, B. Jiang, A. Atrens, F.-S. Pan, Superhydrophobic coatings for corrosion protection of magnesium alloys, Journal of Materials Science & Technology 52 (2020), 100-118, 10.1016/j.jmst.2020.02.055.

[87] Z. Ba, Y. Chen, Q. Dong, B. Ma, X. Lu, Research Progress on Corrosion Resistance of Hydrotalcite Films on Magnesium Alloys, Cailiao Daobao/Materials Review 31(11) (2017), 144-150, 10.11896/j.issn.1005-023X.2017.011.020.

[88] H. Tiyyagura, T. Mohan, S. Pal, K.-M. Mantravadi, Surface modification of Magnesium and its alloy as orthopedic biomaterials with biopolymers, in: P. Balakrishnan, M.S. Sreekala, S. Thomas (Eds.), Woodhead Publishing Series in Biomaterials, Woodhead Publishing Cambridge, 2018, pp. 197-210, 10.1016/B978-0-08-102205-4.00009-X.

[89] S. García Rodríguez, A. Riquelme Aguado, M. Muñoz, A.J. López, J. Rams, B. Torres, Coating of Mg Alloys and Composites, in: F.G. Caballero (Ed.), Encyclopedia of Materials: Metals and Alloys, Elsevier, Oxford, 2021, pp. 75-86, 10.1016/B978-0-12-819726-4.00068-5.

[90] M. Mohedano, X. Lu, E. Matykina, C. Blawert, R. Arrabal, M.L. Zheludkevich, Plasma Electrolytic Oxidation (PEO) of Metals and Alloys, in: K. Wandelt (Ed.), Encyclopedia of Interfacial Chemistry, Elsevier, Oxford, 2018, pp. 423-438, 10.1016/B978-0-12-409547-2.13398-0.

[91] S. Nibhanupudi, A. Manavbasi, Advanced Conversion Coatings for Magnesium alloys, in: W.H. Sillekens, S.R. Agnew, N.R. Neelameggham, S.N. Mathaudhu (Eds.), Magnesium Technology 2011 Springer, Cham, 2011, pp. 519-522, 10.1007/978-3-319-48099-2_95.

[92] Q. Li, Sol-gel coatings to improve the corrosion resistance of magnesium (Mg) alloys, in: G.-L. Song (Ed.), Woodhead Publishing Series in Metals and Surface Engineering, Woodhead Publishing, Cambridge, 2013, pp. 469-485, 10.1533/9780857098962.3.469.

Bibliography

[93] F.E.-T. Heakal, A.E. Elkholy, Smart coatings on magnesium alloys in transportation industries, in: A.S.H. Makhlouf, N.Y. Abu-Thabit (Eds.), Advances in Smart Coatings and Thin Films for Future Industrial and Biomedical Engineering Applications, Elsevier, Oxford, 2020, pp. 263-287, 10.1016/B978-0-12-849870-5.00003-3.

[94] (EC) No 1907/2006 Registration, evaluation, authorisation and restriction of chemicals (REACH), European Parlament Official Journal of the European Union.

[95] E. Wierzbicka, B. Vaghefinazari, S.V. Lamaka, M.L. Zheludkevich, M. Mohedano, L. Moreno, P. Visser, A. Rodriguez, J. Velasco, R. Arrabal, E. Matykina, Flash-PEO as an alternative to chromate conversion coatings for corrosion protection of Mg alloy, Corrosion Science 180 (2021), 109189, 10.1016/j.corsci.2020.109189.

[96] C. Monticelli, Corrosion Inhibitors, in: K. Wandelt (Ed.), Encyclopedia of Interfacial Chemistry, Elsevier, Oxford, 2018, pp. 164-171, 10.1016/B978-0-12-409547-2.13443-2.

[97] M. Forsyth, B. Hinton, Rare Earth-Based Corrosion Inhibitors, in: M. Forsyth, B. Hinton (Eds.), Woodhead Publishing Series in Metals and Surface Engineering, Woodhead Publishing, Cambridge, 2015, pp. 1-139, 10.1016/C2013-0-16231-9.

[98] S.V. Lamaka, B. Vaghefinazari, D. Mei, R. Petrauskas, D. Hoeche, M.L. Zheludkevich, Comprehensive screening of Mg corrosion inhibitors, Corrosion Science 128(Supplement C) (2017), 224-240, 10.1016/j.corsci.2017.07.011.

[99] I. Kartsonakis, S. Stanciu, M. Alecs Andrei, E. Karaxi, R. Hristu, A. Karantonis, C.A. Charitidis, Evaluation of the protective ability of typical corrosion inhibitors for magnesium alloys towards the Mg ZK30 variant, Corrosion Science 100 (2015), 194-208, 10.1016/j.corsci.2015.07.028.

[100] E. Slavcheva, G. Schmitt, Screening of new corrosion inhibitors via electrochemical noise analysis, Materials and Corrosion 53 (2002), 647-655, 10.1002/1521-4176(200209)53:9<647::AID-MACO647>3.0.CO;2-L.

[101] N.H. Helal, W. Badawy, Environmentally safe corrosion inhibition of Mg–Al–Zn alloy in chloride free neutral solutions by amino acids, Electrochimica Acta 56(19) (2011), 6581-6587, 10.1016/j.electacta.2011.04.031.

[102] M. Mosiałek, G. Mordarski, P. Nowak, W. Simka, G. Nawrat, M. Hanke, R. Socha, J. Michalska, Phosphate–permanganate conversion coatings on the AZ81 magnesium alloy: SEM, EIS and XPS studies, Surface and Coatings Technology 206 (2011), 51-62, 10.1016/j.surfcoat.2011.06.035.

[103] L. Kouisni, M. Azzi, M. Zertoubi, F. Dalard, S. Maximovitch, Phosphate coatings on magnesium alloy AM60. Part 1: study of the formation and the growth of zinc phosphate films, Surface & Coatings Technology 185(1) (2004), 58-67, 10.1016/j.surfcoat.2003.10.061.

[104] I. Mutlu, Production and fluoride treatment of Mg-Ca-Zn-Co alloy foam for tissue engineering applications, Transactions of Nonferrous Metals Society of China 28 (2018), 114-124, 10.1016/S1003-6326(18)64644-8.

[105] D. Kharitonov, M. Zimowska, J. Ryl, A. Zieliński, M. Osipenko, J. Adamiec, A. Wrzesińska, P. Claesson, I. Kurilo, Aqueous Molybdate Provides Effective Corrosion

Inhibition of WE43 Magnesium Alloy in Sodium Chloride Solutions, Corrosion Science 190 (2021), 109664, 10.1016/j.corsci.2021.109664.

[106] J. Hu, D. Huang, G.-L. Song, X. Guo, The synergistic inhibition effect of organic silicate and inorganic Zn salt on corrosion of Mg10Gd3Y magnesium alloy, Corrosion Science 53(17) (2011), 4093-4101, 10.1016/j.corsci.2011.08.017.

[107] D. Huang, J. Hu, G.-L. Song, X. Guo, Inhibition effect of inorganic and organic inhibitors on the corrosion of Mg–10Gd–3Y–0.5Zr alloy in an ethylene glycol solution at ambient and elevated temperatures, Electrochimica Acta 56 (2011), 10166-10178, 10.1016/j.electacta.2011.09.002.

[108] P. Tong, Y. Sheng, R. Hou, M. Iqbal, L. Chen, J. Li, Recent progress on coatings of biomedical magnesium alloy, Smart Materials in Medicine 3 (2022), 104-116, 10.1016/j.smaim.2021.12.007.

[109] S. Adsul, U. Bagale, S. Sonawane, R. Subasri, Release rate kinetics of corrosion inhibitor loaded halloysite nanotube-based anticorrosion coatings on magnesium alloy AZ91D, Journal of Magnesium and Alloys 9(1) (2020), 202-215, 10.1016/j.jma.2020.06.010.

[110] S. Adsul, K. Raju, S. Bulusu, S. Sonawane, R. Subasri, Evaluation of self-healing properties of inhibitor loaded nanoclay-based anticorrosive coatings on magnesium alloy AZ91D, 6 (2018), 299-308, 10.1016/j.jma.2018.05.003.

[111] X. Liu, H. He, T. Zhang, L. Ouyang, Y.-X. Zhang, S. Yuan, Superhydrophobic and self-healing dual-function coatings based on mercaptabenzimidazole inhibitor-loaded magnesium silicate nanotubes for corrosion protection of AZ31B magnesium alloys, Chemical Engineering Journal 404 (2021), 127106, 10.1016/j.cej.2020.127106.

[112] W. Li, Y. Su, L. Ma, S. Zhu, Y. Zheng, S. Guan, Sol-gel coating loaded with inhibitor on ZE21B Mg alloy for improving corrosion resistance and endothelialization aiming at potential cardiovascular application, Colloids and Surfaces B: Biointerfaces 207 (2021), 111993, 10.1016/j.colsurfb.2021.111993.

[113] K. Xue, L.-X. Liang, S.-C. Cheng, H.-P. Liu, L.-Y. Cui, R. Zeng, S. li, Z.-l. Wang, Corrosion resistance, antibacterial activity and drug release of ciprofloxacin-loaded micro-arc oxidation/silane coating on magnesium alloy AZ31, Progress in Organic Coatings 158 (2021), 106357, 10.1016/j.porgcoat.2021.106357.

[114] X. Wang, C. Jing, Y. Chen, X. Wang, G. Zhao, X. Zhang, L. Wu, X. Liu, B. Dong, Y. Zhang, Active corrosion protection of super-hydrophobic corrosion inhibitor intercalated Mg–Al layered double hydroxide coating on AZ31 magnesium alloy, Journal of Magnesium and Alloys 8 (2020), 291-300, 10.1016/j.jma.2019.11.011.

[115] Q. Dong, Z. Ba, Y. Jia, Y. Chen, X. Lv, X. Zhang, Z. Wang, Effect of solution concentration on sealing treatment of Mg-Al hydrotalcite film on AZ91D Mg alloy, Journal of Magnesium and Alloys 5 (2017), 320-325, 10.1016/j.jma.2017.08.005.

[116] B.L. Luan, D. Yang, X.Y. Liu, G.-L. Song, Corrosion protection of magnesium (Mg) alloys using conversion and electrophoretic coatings, in: G.-l. Song (Ed.), Corrosion of Magnesium Alloys, Woodhead Publishing, Cambridge, 2011, pp. 541-564, 10.1533/9780857091413.4.541.

Bibliography

[117] C. Vargel, Protection of aluminium, in: C. Vargel (Ed.), Corrosion of Aluminium, Elsevier, Amsterdam, 2020, pp. 383-443, 10.1016/B978-0-08-099925-8.00029-6.

[118] A. Sharma, Chemical Conversion Coatings on Magnesium Alloys - A Comparative Study, International Journal of Electrochemical Science 3 (2008), 993-1004.

[119] J.-H. Al-Fahemi, M. Abdallaha, E. Gad, B. Jahdaly, Experimental and theoretical approach studies for melatonin drug as safely corrosion inhibitors for carbon steel using DFT, Journal of Molecular Liquids 222 (2022), 1157-1163, 10.1016/j.molliq.2016.07.085.

[120] G. Eriksson, An algorithm for the computation of aqueous multi-component, multiphase equilibria, Analytica Chimica Acta 112(4) (1979), 375-383, 10.1016/S0003-2670(01)85035-2.

[121] N. Ingri, W. Kakolowicz, L.G. Sillén, B. Warnqvist, High-speed computers as a supplement to graphical methods—V1: Haltafall, a general program for calculating the composition of equilibrium mixtures, Talanta 14(11) (1967), 1261-1286, 10.1016/0039-9140(67)80203-0.

[122] X.-B. Chen, N. Birbilis, T. Abbott, Review of Corrosion-Resistant Conversion Coatings for Magnesium and Its Alloys, Corrosion -Houston Tx- 67 (2011), 035005-035001, 10.5006/1.3563639.

[123] S. Pommiers-Belin, J. Frayret, A. Uhart, J.-B. Ledeuil, J.-C. Dupin, A. Castetbon, M. Potin-Gautier, Determination of the chemical mechanism of chromate conversion coating on magnesium alloys EV31A, Applied Surface Science 298 (2014), 199–207, 10.1016/j.apsusc.2014.01.162.

[124] J. Drábiková, S. Fintová, P. Ptáček, I. Kuběna, M. Březina, J. Wasserbauer, P. Doležal, F. Pastorek, Structure and growth kinetic of unconventional fluoride conversion coating prepared on wrought AZ61 magnesium alloy, Surface and Coatings Technology 399 (2020), 126101, 10.1016/j.surfcoat.2020.126101.

[125] S.A. Salman, M.K. Gouda, Characterization and corrosion behavior of vanadium-based conversion coating on AZ31 magnesium alloy, Materials Today: Proceedings 62 (2022), 611-614, 10.1016/j.matpr.2022.03.618.

[126] T. Li, Z. Leng, S. Wang, X. Wang, R. Ghomashchi, Y. Yang, J. Zhou, Comparison of the effects of pre-activators on morphology and corrosion resistance of phosphate conversion coating on magnesium alloy, Journal of Magnesium and Alloys (2021), 11-18, 10.1016/j.jma.2021.03.012.

[127] S.-Y. Jian, K.-L. Chang, Effect of cerium ion on the microstructure and properties of permanganate conversion coating on LZ91 magnesium alloy, Applied Surface Science 509 (2020), 144767, 10.1016/j.apsusc.2019.144767.

[128] S. Fintová, J. Drábiková, F. Pastorek, J. Tkacz, I. Kuběna, L. Trško, B. Hadzima, J. Minda, P. Doležal, J. Wasserbauer, P. Ptáček, Improvement of electrochemical corrosion characteristics of AZ61 magnesium alloy with unconventional fluoride conversion coatings, Surface and Coatings Technology 357 (2019), 638-650, 10.1016/j.surfcoat.2018.10.038.

[129] L. Guo, W. Wu, Y. Zhou, F. Zhang, R. Zeng, J. Zeng, Layered double hydroxide coatings on magnesium alloys: A review, Journal of Materials Science & Technology 34(9) (2018), 1455-1466, 10.1016/j.jmst.2018.03.003.

[130] Y. Cao, D. Zheng, F. Zhang, J. Pan, C. Lin, Layered double hydroxide (LDH) for multi-functionalized corrosion protection of metals: A review, Journal of Materials Science & Technology 102 (2022), 232-263, 10.1016/j.jmst.2021.05.078.

[131] M.V. Bukhtiyarova, A review on effect of synthesis conditions on the formation of layered double hydroxides, Journal of Solid State Chemistry 269 (2019), 494-506, 10.1016/j.jssc.2018.10.018.

[132] J.K.E. Tan, P. Balan, N. Birbilis, Advances in LDH coatings on Mg alloys for biomedical applications: A corrosion perspective, Applied Clay Science 202 (2021), 105948, 10.1016/j.clay.2020.105948.

[133] D.E. Beving, A.M.P. McDonnell, W. Yang, Y. Yan, Corrosion Resistant High-Silica-Zeolite MFI Coating, Journal of The Electrochemical Society 153(8) (2006), B325, 10.1149/1.2207845.

[134] R.-G. Hu, S. Zhang, J.-F. Bu, C.-J. Lin, G.-L. Song, Recent progress in corrosion protection of magnesium alloys by organic coatings, Progress in Organic Coatings 73(2-3) (2012), 129-141, 10.1016/j.porgcoat.2011.10.011.

[135] J. Chen, Y. Song, D. Shan, E.-H. Han, Study of the corrosion mechanism of the in situ grown Mg–Al–CO32− hydrotalcite film on AZ31 alloy, Corrosion Science 65 (2012), 268-277, 10.1016/j.corsci.2012.08.026.

[136] L. Wang, K. Zhang, W. Sun, T. Wu, H. He, G. Liu, Hydrothermal synthesis of corrosion resistant hydrotalcite conversion coating on AZ91D alloy, Materials Letters 106 (2013), 111-114, 10.1016/j.matlet.2013.05.018.

[137] D. Li, X. Yu, X. Jing, M. Zhang, Z. Jiang, Hydrotalcite conversion coating on Mg alloy and its corrosion resistance, Journal of Alloys and Compounds 494 (2010), 271-274, 10.1016/j.jallcom.2010.01.007.

[138] F. Peng, H. Li, D. Wang, P. Tian, Y. Tian, G. Yuan, D. Xu, X. Liu, Enhanced Corrosion Resistance and Biocompatibility of Magnesium Alloy by Mg–Al-Layered Double Hydroxide, ACS Applied Materials & Interfaces 8(51) (2016), 35033-35044, 10.1021/acsami.6b12974.

[139] N. Kamiyama, G. Panomsuwan, E. Yamamoto, T. Sudare, N. Saito, T. Ishizaki, Effect of treatment time in the Mg(OH)2/Mg–Al LDH composite film formed on Mg alloy AZ31 by steam coating on the corrosion resistance, Surface and Coatings Technology 286 (2016), 172-177, 10.1016/j.surfcoat.2015.11.051.

[140] T. Ishizaki, S. Chiba, H. Suzuki, In Situ Formation of Anticorrosive Mg-Al Layered Double Hydroxide-Containing Magnesium Hydroxide Film on Magnesium Alloy by Steam Coating, ECS Electrochemistry Letters 2 (2013), C15-C17, 10.1149/2.006305eel.

[141] T. Ishizaki, N. Kamiyama, K. Watanabe, A. Serizawa, Corrosion resistance of Mg(OH)2/Mg–Al layered double hydroxide composite film formed directly on combustion-

resistant magnesium alloy AMCa602 by steam coating, Corrosion Science 92 (2015), 76-84, 10.1016/j.corsci.2014.11.031.

[142] J. Wang, D. Li, X. Yu, X. Jing, M. Zhang, Z. Jiang, Hydrotalcite conversion coating on Mg alloy and its corrosion resistance, Journal of Alloys and Compounds 494(1) (2010), 271-274, 10.1016/j.jallcom.2010.01.007.

[143] F. Zhang, Z.-G. Liu, R.-C. Zeng, S.-Q. Li, H.-Z. Cui, L. Song, E.-H. Han, Corrosion resistance of Mg–Al-LDH coating on magnesium alloy AZ31, Surface and Coatings Technology 258 (2014), 1152-1158, 10.1016/j.surfcoat.2014.07.017.

[144] J.-H. Syu, J.-Y. Uan, M.-C. Lin, Z.-Y. Lin, Optically transparent Li–Al–CO3 layered double hydroxide thin films on an AZ31 Mg alloy formed by electrochemical deposition and their corrosion resistance in a dilute chloride environment, Corrosion Science 68 (2013), 238–248, 10.1016/j.corsci.2012.11.023.

[145] R. Zeng, Z.-G. Liu, F. Zhang, S.-Q. Li, H.-Z. Cui, E.-H. Han, Corrosion of molybdate intercalated hydrotalcite coating on AZ31 Mg alloy, Journal of Materials Chemistry A 2 (2014), 13049–13057, 10.1039/C4TA01341G.

[146] Z. Gu, Y. Huang, Y. Wang, N. Yuan, J. Ding, An aluminum silicate modified Ni-Al LDHs film to improve the corrosion resistance of AZ31 Mg alloy, Materials Letters 252 (2019), 304-307, 10.1016/j.matlet.2019.06.010.

[147] J. Chen, L. Fang, F. Wu, J. Xie, J. Hu, B. Jiang, H. Luo, Corrosion resistance of a self-healing rose-like MgAl-LDH coating intercalated with aspartic acid on AZ31 Mg alloy, Progress in Organic Coatings 136 (2019), 105234, 10.1016/j.porgcoat.2019.105234.

[148] R.-c. Zeng, Z.-g. Liu, F. Zhang, S.-q. Li, Q.-k. He, H.-z. Cui, E.-h. Han, Corrosion resistance of in-situ Mg–Al hydrotalcite conversion film on AZ31 magnesium alloy by one-step formation, Transactions of Nonferrous Metals Society of China 25(6) (2015), 1917-1925, 10.1016/S1003-6326(15)63799-2.

[149] F. Zhang, Z.-G. Liu, R. Zeng, S.-Q. Li, H.-Z. Cui, L. Song, E.-H. Han, Corrosion resistance of Mg–Al-LDH coating on magnesium alloy AZ31, Surface and Coatings Technology 258 (2014), 1152-1158, 10.1016/j.surfcoat.2014.07.017.

[150] M.J. Anjum, J. Zhao, V. Zahedi Asl, G. Yasin, W. Wang, S. Wei, Z. Zhao, W. Qamar Khan, In-situ intercalation of 8-hydroxyquinoline in Mg-Al LDH coating to improve the corrosion resistance of AZ31, Corrosion Science 157 (2019), 1-10, 10.1016/j.corsci.2019.05.022.

[151] Y. Tang, F. Wu, L. Fang, T. Guan, J. Hu, S. Zhang, A comparative study and optimization of corrosion resistance of ZnAl layered double hydroxides films intercalated with different anions on AZ31 Mg alloys, Surface and Coatings Technology 358 (2019), 594-603, 10.1016/j.surfcoat.2018.11.070.

[152] J. Wang, D. Li, X. Yu, X. Jing, M. Zhang, Z. Jiang, Hydrotalcite conversion coating on Mg alloy and its corrosion resistance, Journal of Alloys and Compounds 494(1-2) (2010), 271-274, 10.1016/j.jallcom.2010.01.007.

[153] G. Barati Darband, M. Aliofkhazraei, P. Hamghalam, N. Valizade, Plasma electrolytic oxidation of magnesium and its alloys: Mechanism, properties and applications, Journal of Magnesium and Alloys 5(1) (2017), 74-132, 10.1016/j.jma.2017.02.004.

[154] G. Darband, M. Aliofkhazraei, P. Hamghalam, N. Valizade, Plasma electrolytic oxidation of magnesium and its alloys: Mechanism, properties and applications, Journal of Magnesium and Alloys 5 (2017)10.1016/j.jma.2017.02.004.

[155] Research Centre Geesthacht GmbH 2006. https://www.hereon.de/about_us/history/history/index.php.en. (Accessed April 15 2022).

[156] A. Yerokhin, X. Nie, A. Leyland, A. Matthews, S.J. Dowey, Plasma Electrolysis for Surface Engineering, Surface and Coatings Technology 122 (1999), 73-93, 10.1016/S0257-8972(99)00441-7.

[157] W. Krysmann, P. Kurze, K.H. Dittrich, H. Schneider, Process characteristics and parameters of Anodic Oxidation by spark discharge (ANOF), Crystal Research and Technology 19 (1984), 973-979, 10.1002/crat.2170190721.

[158] A. Hickling, M. Ingram, Contact glow-discharge electrolysis, Transactions of The Faraday Society 60 (1964), 783-793, 10.1039/tf9646000783.

[159] C.S. Dunleavy, I.O. Golosnoy, J. Curran, B. Clyne, Characterisation of discharge events during plasma electrolytic oxidation, Surface and Coatings Technology 203 (2009), 3410-3419, 10.1016/j.surfcoat.2009.05.004.

[160] E. Kostic, S.J. Kis, S. Boskovic, S. Zec, Mechanically Activated Transition of Anatase into Rutile, American Ceramic Society Bulletin 76 (1997), 60-64.

[161] B. Duane, L. Brian, W. Earl, Hard anodic coating for magnesium alloys, National Center for Biotechnology Information, Technology Applic Group INC (US), Grand Forks, N. Dak., United States, 1995, p. 9.

[162] E.L. Schmeling, B. Röschenbleck, M.H. Weidemann, Method for producing corrosion and wear resistant protective coatings on magnesium and magnesium alloys, Electro Chemical Engineering GmbH Germany, 1988, p. 8.

[163] M. Molaei, A. Fattah-alhosseini, M. Nouri, A. Nourian, Systematic optimization of corrosion, bioactivity, and biocompatibility behaviors of calcium-phosphate plasma electrolytic oxidation (PEO) coatings on titanium substrates, Ceramics International 48(5) (2021), 6322-6337, 10.1016/j.ceramint.2021.11.175.

[164] B. Hamrahi, B. Yarmand, A. Massoudi, Improved in-vitro corrosion performance of titanium using a duplex system of plasma electrolytic oxidation and graphene oxide incorporated silane coatings, Surface and Coatings Technology 422 (2021), 127558, 10.1016/j.surfcoat.2021.127558.

[165] Y. Li, X. Lu, M. Serdechnova, C. Blawert, M.L. Zheludkevich, K. Qian, F. Wang, Incorporation of LDH nanocontainers into plasma electrolytic oxidation coatings on Mg alloy, Journal of Magnesium and Alloys (2021), 19-56, 10.1016/j.jma.2021.07.015.

Bibliography

[166] K. Mojsilović, N. Božovića, S. Stojanović, L. Damjanović-Vasilić, M. Serdechnova, C. Blawert, M.L. Zheludkevich, S. Stojadinović, R. Vasilic, Zeolite-containing photocatalysts immobilized on aluminum support by plasma electrolytic oxidation, Surfaces and Interfaces 26 (2021), 101307, 10.1016/j.surfin.2021.101307.

[167] X. Lu, J. Ma, M. Mohedano, B. Pillado Ríos, R. Arrabal, K. Qian, Y. Li, F. Wang, Ca-based sealing of plasma electrolytic oxidation coatings on AZ91 Mg alloy, Surface and Coatings Technology 417 (2021), 127220, 10.1016/j.surfcoat.2021.127220.

[168] X. Wang, X. Lu, P. Ju, Y. Chen, F. Wang, Influence of ZnO on thermal control property and corrosion resistance of plasma electrolytic oxidation coatings on Mg alloy, Surface and Coatings Technology 409 (2021), 126905, 10.1016/j.surfcoat.2021.126905.

[169] S. Stojadinović, A. Ćirić, Effect of Eu2+ doping on photoluminescence of Al2O3:Tb3+ functional coatings formed by plasma electrolytic oxidation, Journal of Luminescence 239 (2021), 118323, 10.1016/j.jlumin.2021.118323.

[170] H. Du, Z. Wei, X. Liu, E. Zhang, Effects of Zn on the microstructure, mechanical property and bio-corrosion property of Mg-3Ca alloys for biomedical application, Materials Chemistry and Physics 125 (2011), 568-575, 10.1016/j.matchemphys.2010.10.015.

[171] M. Tang, Z. Feng, G. li, Z. Zhang, R. Zhang, High-corrosion resistance of the microarc oxidation coatings on magnesium alloy obtained in potassium fluotitanate electrolytes, Surface and Coatings Technology 264 (2015), 105-113, 10.1016/j.surfcoat.2015.01.013.

[172] Z. Li, Q. Ren, X. Wang, Q. Kuang, D. Ji, R. Yuan, X. Jing, Effect of phosphate additive on the morphology and anti-corrosion performance of plasma electrolytic oxidation coatings on magnesium—lithium alloy, Corrosion Science 157 (2019), 295-304, 10.1016/j.corsci.2019.06.005.

[173] R. Arrabal, E. Matykina, P. Skeldon, G. Thompson, Incorporation of Zirconia Particles into Coatings Formed on Magnesium by Plasma Electrolytic Oxidation, Journal of Materials Science 43 (2008), 1532-1538, 10.1007/s10853-007-2360-9.

[174] E. Matykina, I. Garcia, R. Arrabal, M. Mohedano, B. Mingo, J. Sancho, M.C. Merino, A. Pardo, Role of PEO coatings in long-term biodegradation of a Mg alloy, Applied Surface Science 389 (2016), 810-823, 10.1016/j.apsusc.2016.08.005.

[175] R. del Olmo, M. Mohedano, P. Visser, E. Matykina, R. Arrabal, Flash-PEO coatings loaded with corrosion inhibitors on AA2024, Surface and Coatings Technology 402 (2020), 126317, 10.1016/j.surfcoat.2020.126317.

[176] R. Puscaselu, G. Gutt, S. Amariei, Biopolymer-Based Films Enriched with Stevia rebaudiana Used for the Development of Edible and Soluble Packaging, Coatings 9(6) (2019), 1-13, 10.3390/coatings9060360.

[177] A. Gnedenkov, S. Sinebryukhov, D. Mashtalyar, S. Gnedenkov, Localized corrosion of the Mg alloys with inhibitor-containing coatings: SVET and SIET studies, Corrosion Science 102 (2015), 269-278, 10.1016/j.corsci.2015.10.015.

[178] M. Mohedano, C. Blawert, M.L. Zheludkevich, Cerium-based sealing of PEO coated AM50 magnesium alloy, Surface and Coatings Technology 269 (2015), 145-154, 10.1016/j.surfcoat.2015.01.003.

[179] M. Wu, Effects of Deposition Thickness on Electrochemical Behaviors of AZ31B Magnesium Alloy with Composite Coatings Prepared by Micro-arc Oxidation and Electrophoretic Deposition, International Journal of Electrochemical Science 15 (2020), 1378-1390, 10.20964/2020.02.08.

[180] C.-Y. Li, X.-L. Fan, L.-Y. Cui, R. Zeng, Corrosion resistance and electrical conductivity of a nano ATO-doped MAO/methyltrimethoxysilane composite coating on magnesium alloy AZ31, Corrosion Science 168 (2020), 108570, 10.1016/j.corsci.2020.108570.

[181] J. Han, C. Blawert, S. Tang, J. Yang, J. Hu, M.L. Zheludkevich, Formation and corrosion behaviors of calcium phosphate coatings on plasma electrolytic oxidized Mg under changing chemical environment, Surface and Coatings Technology 412 (2021), 127030, 10.1016/j.surfcoat.2021.127030.

[182] Z. Li, W. Yang, Q. Yu, W. Yang, D. Wang, J. Liang, F. Zhou, A New Method for the Corrosion Resistance of AZ31 Mg Alloy with Porous Micro-arc Oxidation Membrane as Ionic Corrosion Inhibitor Container, Langmuir 35 (2018), 1134-1145, 10.1021/acs.langmuir.8b01637.

[183] M. Toorani, M. Aliofkhazraei, M. Mahdavian, R. Naderi, Effective PEO/Silane Pretreatment of Epoxy Coating Applied on AZ31B Mg Alloy for Corrosion Protection, Corrosion Science 169 (2020), 108608, 10.1016/j.corsci.2020.108608.

[184] F. Peng, D. Wang, Y. Tian, H. Cao, Y. Qiao, X. Liu, Sealing the Pores of PEO Coating with Mg-Al Layered Double Hydroxide: Enhanced Corrosion Resistance, Cytocompatibility and Drug Delivery Ability, Scientific Reports 7 (2017), 1-12, 10.1038/s41598-017-08238-w.

[185] M. Mohedano, M. Serdechnova, M. Starykevich, S. Karpushenkov, A. Bouali, M. Ferreira, M.L. Zheludkevich, Active protective PEO coatings on AA2024: Role of voltage on in-situ LDH growth, Materials & Design 120 (2017), 36-46, 10.1016/j.matdes.2017.01.097.

[186] S. Akbarzadeh, L. Santos, V. Vitry, Y. Paint, M.G. Olivier, Improvement of the corrosion performance of AA2024 alloy by a duplex PEO/clay modified sol-gel nanocomposite coating, Surface and Coatings Technology 434 (2022), 128168, 10.1016/j.surfcoat.2022.128168.

[187] E. Merino, A. Durán, Y. Castro, Integrated corrosion-resistant system for AZ31B Mg alloy via Plasma Electrolytic Oxidation (PEO) and sol-gel processes, International Journal of Applied Glass Science 12(4) (2021), 519-530, 10.1111/ijag.16536.

[188] J.P. Fernández-Hernán, A.J. López, B. Torres, E. Martínez-Campos, E. Matykina, J. Rams, Anticorrosion and Cytocompatibility Assessment of Graphene-Doped Hybrid Silica and Plasma Electrolytic Oxidation Coatings for Biomedical Applications, ACS Biomaterials Science & Engineering 7 (2021), 5861-5877, 10.1021/acsbiomaterials.1c00326.

[189] S. Zheng, J. Li, Inorganic–organic sol gel hybrid coatings for corrosion protection of metals, Journal of Sol-Gel Science and Technology 54 (2010), 174-187, 10.1007/s10971-010-2173-1.

Bibliography

[190] R. Olmo, U. Tiringer, I. Milošev, P. Visser, R. Arrabal, E. Matykina, J.M.C. Mol, Hybrid sol-gel coatings applied on anodized AA2024-T3 for active corrosion protection, Surface and Coatings Technology 419 (2021), 127251, 10.1016/j.surfcoat.2021.127251.

[191] R. Figueira, C. Silva, E. Pereira, Organic–inorganic hybrid sol–gel coatings for metal corrosion protection: a review of recent progress, Journal of Coatings Technology and Research 12 (2014), 1–35, 10.1007/s11998-014-9595-6.

[192] D. Balgude, A. Sabnis, Sol–gel derived hybrid coatings as an environment friendly surface treatment for corrosion protection of metals and their alloys, Journal of Sol-Gel Science and Technology 64 (2012), 124-134, 10.1007/s10971-012-2838-z.

[193] L. Pezzato, R. Babbolin, P. Cerchier, M. Marigo, P. Dolcet, M. Dabalà, K. Brunelli, Sealing of PEO coated AZ91magnesium alloy using solutions containing neodymium, Corrosion Science 173 (2020), 108741, 10.1016/j.corsci.2020.108741.

[194] S.V. Lamaka, G. Knörnschild, D.V. Snihirova, M.G. Taryba, M.L. Zheludkevich, M.G.S. Ferreira, Complex anticorrosion coating for ZK30 magnesium alloy, Electrochimica Acta 55(1) (2009), 131-141, 10.1016/j.electacta.2009.08.018.

[195] D. Ivanou, K. Yasakau, S. Kallip, A.D. Lisenkov, M. Starykevich, S.V. Lamaka, M. Ferreira, M.L. Zheludkevich, Active corrosion protection coating for ZE41 magnesium alloy created by combining PEO and sol-gel techniques, RSC Advances 6(15) (2016), 12553-12560, 10.1039/C5RA22639B.

[196] A.S. Gnedenkov, S.L. Sinebryukhov, D.V. Mashtalyar, S.V. Gnedenkov, Protective properties of inhibitor-containing composite coatings on a Mg alloy, Corrosion Science 102 (2016), 348-354, 10.1016/j.corsci.2015.10.026.

[197] L. Newton, N. Senin, C. Gomez, R. Danzl, F. Helmli, L. Blunt, R. Leach, Areal topography measurement of metal additive surfaces using focus variation microscopy, Additive Manufacturing 25 (2019), 365-389, 10.1016/j.addma.2018.11.013.

[198] S. Sinha Ray, 3 - Structure and Morphology Characterization Techniques, in: S. Sinha Ray (Ed.), Clay-Containing Polymer Nanocomposites, Elsevier, Amsterdam, 2013, pp. 39-66, 10.1016/B978-0-444-59437-2.00003-X.

[199] S. Sinha Ray, 4 - Techniques for characterizing the structure and properties of polymer nanocomposites, in: S. Sinha Ray (Ed.), Environmentally Friendly Polymer Nanocomposites, Woodhead Publishing, 2013, pp. 74-88, 10.1533/9780857097828.1.74.

[200] Comité técnico CTN 112 Corrosión y protección de los materailes metálicos UNE-EN ISO 2360, Recubrimientos no conductores sobre metales base conductores no magnéticos Medición de recubrimientos Método por corrientes inducidas sensibles a la variación de amplitud, AENOR, 2017, p. 5.

[201] Comité técnico CTN 48 Pinturas y barnices ISO 2409:2020, Pinturas y barnices Ensayo de corte por enrejado, AENOR, Madrid, Spain, 2021, p. 4.

[202] S. Ebnesajjad, Fabrication and Processing of Polytetrafluoroethylene Dispersions, in: S. Ebnesajjad (Ed.), Introduction to Fluoropolymers, William Andrew Publishing, Oxford, 2021, pp. 149-167, 10.1016/B978-0-12-819123-1.00009-4.

[203] S. Fajardo, G.S. Frankel, Gravimetric method for hydrogen evolution measurements on dissolving magnesium, Journal of The Electrochemical Society 162(14) (2015), C693-C701, 10.1149/2.0241514jes.

[204] G. Song, A. Atrens, D. Suohn, An Hydrogen Evolution Method for the Estimation of the Corrosion Rate of Magnesium Alloys, in: S.N. Mathaudhu, A.A. Luo, N.R. Neelameggham, E.A. Nyberg, W.H. Sillekens (Eds.), Essential Readings in Magnesium Technology, Springer Cham, 2014, pp. 565-572, 10.1002/9781118859803.ch90.

[205] S. Hiromoto, Corrosion of metallic biomaterials, in: M. Niinomi (Ed.), Metals for Biomedical Devices, Woodhead Publishing, Cambridge, 2010, pp. 99-121, 10.1016/B978-0-08-102666-3.00004-3.

[206] A.C. Bastos, M. Quevedo, O. Karavai, M. Ferreira, Review—On the Application of the Scanning Vibrating Electrode Technique (SVET) to Corrosion Research, Journal of The Electrochemical Society 164 (2017), C973-C990, 10.1149/2.0431714jes.

[207] B117-18 Standard Practice for Operating Salt Spray (Fog) Apparatus, ASTM International, 2019, p. 11, 10.1520/B0117-19.

[208] D1654-08(2016)e1 Standard Test Method for Evaluation of Painted or Coated Specimens Subjected to Corrosive Environments, ASTM International, 2000, p. 4, 10.1520/D1654-08R16E01.

[209] C. Forano, T. Hibino, F. Leroux, C. Taviot-Guého, Layered Double Hydroxides, in: F. Bergaya, B.K.G. Theng, G. Lagaly (Eds.), Developments in Clay Science, Elsevier, Oxford, 2006, pp. 1021-1095, 10.1016/S1572-4352(05)01039-1.

[210] Z. Lü, F. Zhang, X. Lei, L. Yang, S. Xu, X. Duan, In situ growth of layered double hydroxide films on anodic aluminum oxide/aluminum and its catalytic feature in aldol condensation of acetone, Chemical Engineering Science 63(16) (2008), 4055-4062, 10.1016/j.ces.2008.05.007.

[211] J.-K. Lin, J.-Y. Uan, C.-P. Wu, H.-H. Huang, Direct growth of oriented Mg–Fe layered double hydroxide (LDH) on pure Mg substrates and in vitro corrosion and cell adhesion testing of LDH-coated Mg samples, Journal of Materials Chemistry 21(13) (2011), 5011-5020, 10.1039/C0JM03764H.

[212] J. Tedim, M.L. Zheludkevich, A.C. Bastos, A.N. Salak, J. Carneiro, F. Maia, A.D. Lisenkov, A.B. Oliveira, M.G.S. Ferreira, Effect of surface treatment on the performance of LDH conversion films, ECS Electrochemistry Letters 3(1) (2014), C4-C8, 10.1149/2.005401eel].

[213] Y. Li, S. Li, Y. Zhang, M. Yu, J. Liu, Fabrication of superhydrophobic layered double hydroxides films with different metal cations on anodized aluminum 2198 alloy, Materials Letters 142 (2015), 137-140, 10.1016/j.matlet.2014.11.148.

[214] D.E. Beving, A.M.P. McDonnell, W. Yang, Y. Yan, Corrosion resistant high-silica-zeolite MFI coating: One general solution formulation for aluminum alloy AA-2024-T3, AA-5052-H32, AA-6061-T4, and AA-7075-T6, Journal of the Electrochemical Society 153(8) (2006), B325-B329, 10.1149/1.2207845.

Bibliography

[215] V. Zahedi Asl, J. Zhao, M.J. Anjum, S. Wei, W. Wang, Z. Zhao, The effect of cerium cation on the microstructure and anti-corrosion performance of LDH conversion coatings on AZ31 magnesium alloy, Journal of Alloys and Compounds 821 (2020), 153248, 10.1016/j.jallcom.2019.153248.

[216] S.C. Jun, P. Shinde, Review on Recent Progress in the Development of Tungsten Oxide Based Electrodes for Electrochemical Energy Storage, ChemSusChem 13(1) (2019), 11-38, 10.1002/cssc.201902071.

[217] A.C. Cursino, F. da Silva Lisboa, A. dos Santos Pyrrho, V.P. de Sousa, F. Wypych, Layered double hydroxides intercalated with anionic surfactants/benzophenone as potential materials for sunscreens, Journal of Colloid and Interface Science 397 (2013), 88-95, 10.1016/j.jcis.2013.01.059.

[218] T. Shulha, M. Serdechnova, M.H. Iuzviuk, I.A. Zobkalo, P. Karlova, N. Scharnagl, D.C.F. Wieland, S.V. Lamaka, A.A. Yaremchenko, C. Blawert, M.L. Zheludkevich, In situ formation of LDH-based nanocontainers on the surface of AZ91 magnesium alloy and detailed investigation of their crystal structure, Journal of Magnesium and Alloys 10(5) (2022), 1268-1285, 10.1016/j.jma.2021.10.006.

[219] J.T. Kloprogge, D. Wharton, L. Hickey, R.L. Frost, Infrared and Raman study of interlayer anions CO32–, NO3–, SO42– and ClO4– in Mg/Al-hydrotalcite, American Mineralogist 87(5-6) (2002), 623-629, 10.2138/am-2002-5-604.

[220] P.E. Kleyi, P. Mudaly, S. Kesavan Pillai, M. de Beer, Zn/Al Layered double hydroxides nanostructure as effective controlled release vehicle of nicotinic acid for topical applications, Applied Clay Science 215 (2021), 106304, 10.1016/j.clay.2021.106304.

[221] J.H. Saska Romero, G.P. Saito, F. Cagnin, M.A. Cebim, M.R. Davolos, Europium-doped Zn-Al-LDH intercalated with 4-biphenylcarboxylate anion and undoped Zn-Al-LDH intercalated with its anionic Eu(III) complex: Structural and UV or X-ray excited luminescence properties, Optical Materials 124 (2022), 111703, 10.1016/j.optmat.2021.111703.

[222] P. Kumari, B. Pal, R.K. Das, Superior adsorptive removal of eco-toxic drug diclofenac sodium by Zn–Al LDH·xBi2O3 layer double hydroxide composites, Applied Clay Science 208 (2021), 106119, 10.1016/j.clay.2021.106119.

[223] Y. Bouvier, B. Mutel, J. Grimblot, Use of an Auger parameter for characterizing the Mg chemical state in different materials, Surface and Coatings Technology 180-181 (2004), 169-173, 10.1016/j.surfcoat.2003.10.062.

[224] A. Head, J. Schnadt, UHV and Ambient Pressure XPS: Potentials for Mg, MgO, and Mg(OH)2 Surface Analysis, The Journal of The Minerals, Metals & Materials Society 69(12) (2016), 3070–3077, 10.1007/s11837-016-2112-x.

[225] S. Ardizzone, C.L. Bianchi, M. Fadoni, B. Vercelli, Magnesium salts and oxide: an XPS overview, Applied Surface Science 119(3) (1997), 253-259, 10.1016/S0169-4332(97)00180-3.

[226] Z. Li, M. Chen, H. Hu, Q. Zhang, D. Tao, Mechanochemical synthesis of novel Pt modified ZnAl-LDH for effective ciprofloxacin photodegradation, Journal of Solid State Chemistry 290 (2020), 121594, 10.1016/j.jssc.2020.121594.

[227] P.V. Krasovskii, O.S. Malinovskaya, A.V. Samokhin, Y.V. Blagoveshchenskiy, V.A. Kazakov, A.A. Ashmarin, XPS study of surface chemistry of tungsten carbides nanopowders produced through DC thermal plasma/hydrogen annealing process, Applied Surface Science 339 (2015), 46-54, 10.1016/j.apsusc.2015.02.152.

[228] J. Brillo, H. Kuhlenbeck, H.J. Freund, Interaction of O2 with WC(0001), Surface Science 409(2) (1998), 199-206, 10.1016/S0039-6028(98)00193-9.

[229] X. Zhang, R. Li, X. Feng, X. Pang, X. He, Z. Jin, H. Ren, D. Wang, K. Li, X. Dai, Z. Du, Q. Zhou, Y. Zhang, Influence of Li+/Al3+on the corrosion behavior of Li-Al layered double hydroxides (LDHs) film on LA51 magnesium alloys, Journal of Magnesium and Alloys 48(5) (2022), 1-11, 10.1016/j.jma.2022.03.019.

[230] P. Visser, Y. Liu, X. Zhou, T. Hashimoto, G.E. Thompson, S.B. Lyon, L.G.J. van der Ven, A. Mol, H.A. Terryn, The corrosion protection of AA2024-T3 aluminium alloy by leaching of lithium-containing salts from organic coatings, Faraday Discussions 180(0) (2015), 511-526, 10.1039/C4FD00237G.

[231] Y. Liu, P. Visser, X. Zhou, S. Lyon, T. Hashimoto, A. Gholinia, G. Thompson, G. Smyth, S. Gibbon, D. Graham, J.M.C. Mol, H. Terryn, An investigation of the corrosion inhibitive layers generated from lithium oxalate-containing organic coating on AA2024-T3 aluminium alloy, Surface and Interface Analysis 48 (2016), 798-803, 10.1002/sia.5972.

[232] P. Visser, Y. Liu, H. Terryn, J.M.C. Mol, Lithium salts as leachable corrosion inhibitors and potential replacement for hexavalent chromium in organic coatings for the protection of aluminum alloys, Journal of Coatings Technology and Research 13 (2016), 1-10, 10.1007/s11998-016-9784-6.

[233] P. Visser, A. Lutz, J.M.C. Mol, H. Terryn, Study of the formation of a protective layer in a defect from lithium-leaching organic coatings, Progress in Organic Coatings 99 (2016), 80-90, 10.1016/j.porgcoat.2016.04.028.

[234] K. Marcoen, P. Visser, G.F. Trindade, M.L. Abel, J.F. Watts, J.M.C. Mol, H. Terryn, T. Hauffman, Compositional study of a corrosion protective layer formed by leachable lithium salts in a coating defect on AA2024-T3 aluminium alloys, Progress in Organic Coatings 119 (2018), 65-75, 10.1016/j.porgcoat.2018.02.011.

[235] R. Kurosawa, M. Takeuchi, J. Ryu, Comparison of the Effect of Coaddition of Li Compounds and Addition of a Single Li Compound on Reactivity and Structure of Magnesium Hydroxide, ACS Omega 4(18) (2019), 17752-17761, 10.1021/acsomega.9b02189.

[236] R. Arrabal, E. Matykina, P. Skeldon, G. Thompson, A. Pardo, Transport of Species during Plasma Electrolytic Oxidation of WE43-T6 Magnesium Alloy, Journal of The Electrochemical Society 155 (2008), C101, 10.1149/1.2823374.

[237] G. Zhang, L. Wu, A.-t. Tang, X. Ding, B. Jiang, A. Atrens, F.-S. Pan, Smart epoxy coating containing zeolites loaded with Ce on a plasma electrolytic oxidation coating on Mg alloy AZ31 for active corrosion protection, Progress in Organic Coatings 132 (2019), 144-147, 10.1016/j.porgcoat.2019.03.046.

[238] G. Zhang, L. Wu, A. Tang, Y. Ma, G.-L. Song, D. Zheng, B. Jiang, A. Atrens, F.-S. Pan, Active corrosion protection by a smart coating based on a MgAl-layered double hydroxide on

a cerium-modified plasma electrolytic oxidation coating on Mg alloy AZ31, Corrosion Science 139 (2018), 370-382, 10.1016/j.corsci.2018.05.010.

[239] P. Srinivasan, J. Liang, C. Blawert, M. Störmer, W. Dietzel, Characterization of calcium containing plasma electrolytic oxidation coatings on AM50 magnesium alloy, Applied Surface Science 256 (2010), 4017-4022, 10.1016/j.apsusc.2010.01.069.

[240] J. Dou, Y. Zhao, L. Lu, G. Gu, H. Yu, C. Chen, Effect of the second-step voltages on the structural and corrosion properties of silicon-calcium-phosphate (Si-CaP) coatings on Mg-Zn-Ca alloy, Royal Society Open Science 5 (2018), 1-14, 10.1098/rsos.172410.

[241] A. Bordbar-Khiabani, A. Ghanbari, B. Yarmand, A. Zamanian, M. Mozafari, Improving corrosion behavior and in-vitro bioactivity of plasma electrolytic oxidized AZ91 magnesium alloy using calcium fluoride containing electrolyte, Materials Letters 212 (2017), 98-102, 10.1016/j.matlet.2017.10.072.

[242] H. Tang, G. Yang, Preparation and characterization of hydroxyapatite containing coating on AZ31 magnesium alloy by micro-arc oxidation, Journal of Alloys and Compounds 688(A) (2016), 699-708, 10.1016/j.jallcom.2016.07.079.

[243] L. Chen, L. Liu, S. Liu, B. Hou, Q. Liu, H. Ding, Effect of ultrasonic cold forging technology as the pretreatment on the corrosion resistance of MAO Ca/P coating on AZ31B Mg alloy, Journal of Alloys and Compounds 635 (2015), 278-288, 10.1016/j.jallcom.2015.02.086.

[244] Y. Pan, C.Z. Chen, D. Wang, T.G. Zhao, Effects of phosphates on microstructure and bioactivity of micro-arc oxidized calcium phosphate coatings on Mg-Zn-Zr magnesium alloy, Colloids and surfaces. B, Biointerfaces 109C (2013), 1-9, 10.1016/j.colsurfb.2013.03.026.

[245] Y. Gao, A. Yerokhin, E. Parfenov, A. Matthews, Application of Voltage Pulse Transient Analysis during Plasma Electrolytic Oxidation for Assessment of Characteristics and Corrosion Behaviour of Ca- and P-containing Coatings on Magnesium, Electrochimica Acta 149 (2014), 218-230, 10.1016/j.electacta.2014.10.063.

[246] J. Yang, X. Lu, C. Blawert, S. Di, M.L. Zheludkevich, Microstructure and corrosion behavior of Ca/P coatings prepared on magnesium by plasma electrolytic oxidation, Surface and Coatings Technology 319 (2017), 359-369, 10.1016/j.surfcoat.2017.04.001.

[247] Y. Pan, C. Chen, D. Wang, Z. Lin, Preparation and bioactivity of micro-arc oxidized calcium phosphate coatings, Materials Chemistry and Physics 141 (2013), 842-849, 10.1016/j.matchemphys.2013.06.013.

[248] Y. Pan, C. Chen, D. Wang, X. Yu, Microstructure and biological properties of micro-arc oxidation coatings on ZK60 magnesium alloy, Journal of Biomedical Materials Research. Part B, Applied Biomaterials 100 (2012), 1574-1586, 10.1002/jbm.b.32726.

[249] P. Srinivasan, J. Liang, C. Blawert, M. Störmer, W. Dietzel, A preliminary study of calcium containing plasma electrolytic oxidation coatings on AM50 magnesium alloy, Journal of Materials Science 45 (2010), 1406–1410, 10.1007/s10853-009-4093-4.

[250] Y. Gao, A. Yerokhin, A. Matthews, Effect of current mode on PEO treatment of magnesium in Ca- and P-containing electrolyte and resulting coatings, Applied Surface Science 316 (2014), 558-567, 10.1016/j.apsusc.2014.08.035.

[251] S. Gnedenkov, S. Sinebryukhov, O. Khrisanfova, A. Zavidnaya, V. Egorkin, A. Puz', N. Sergienko, Formation of bioactive anticorrosion coatings on resorbable implants by plasma electrolytic oxidation, Protection of Metals and Physical Chemistry of Surfaces 49 (2013), 874-879, 10.1134/S2070205113070071.

[252] M.C. Kuo, S. Yen, The Process of Electrochemical-Deposited Hydroxyapatite Coatings on Biomedical Titanium at Room Temperature, Materials Science and Engineering: C 20 (2002), 153-160, 10.1016/S0928-4931(02)00026-7.

[253] Z. Chun-Yan, R. Zeng, L. Cheng-Long, G. Jia-Cheng, Comparison of calcium phosphate coatings on Mg–Al and Mg–Ca alloys and their corrosion behavior in Hank's solution, Surface and Coatings Technology 204 (2010), 3636-3640, 10.1016/j.surfcoat.2010.04.038.

[254] C. Wen, S. Guan, L. Peng, C. Ren, X. Wang, Z. Hu, Characterization and degradation behavior of AZ31 alloy surface modified by bone-like hydroxyapatite for implant applications, Applied Surface Science 255 (2009), 6433-6438, 10.1016/j.apsusc.2008.09.078.

[255] S. Goss, K. Lemons, J. Kerstetter, R. Bogner, Determination of calcium salt solubility with changes in pH and P(CO(2)), simulating varying gastrointestinal environments, The Journal of Pharmacy and Pharmacology 59 (2007), 1485-1492, 10.1211/jpp.59.11.0004.

[256] R. Zeng, F. Zhang, Z.-D. Lan, H.-Z. Cui, E.-H. Han, Corrosion resistance of calcium-modified zinc phosphate conversion coatings on magnesium–aluminium alloys, Corrosion Science 88 (2014), 452–459, 10.1016/j.corsci.2014.08.007.

[257] D. Sreekanth, N. Rameshbabu, Development and characterization of MgO/hydroxyapatite composite coating on AZ31 magnesium alloy by plasma electrolytic oxidation coupled with electrophoretic deposition, Materials Letters 68 (2011), 439-442, 10.1016/j.matlet.2011.11.025.

[258] L. Chang, T. Lifeng, W. Liu, X. Duan, Formation of dicalcium phosphate dihydrate on magnesium alloy by micro-arc oxidation coupled with hydrothermal treatment, Corrosion Science 72 (2013), 118–124, 10.1016/j.corsci.2013.03.017.

[259] S. Dorozhkin, Calcium orthophosphate coatings on magnesium and its biodegradable alloys, Acta biomaterialia 10 (2014)10.1016/j.actbio.2014.02.026.

[260] L. Miller, J. Witt, Solubility of Calcium Hydroxide, The Journal of Physical Chemistry A 33 (1928), 285-289, 10.1021/j150296a010.

[261] M. Laleh, F. Kargar, A. Sabour Rouh Aghdam, R. Aca, Occa, Formation of a compact oxide layer on AZ91D magnesium alloy by microarc oxidation via addition of cerium chloride into the MAO electrolyte, Journal of Coatings Technology and Research 8 (2011), 765-771, 10.1007/s11998-011-9357-7.

[262] C.E. Barchiche, E. Rocca, J. Hazan, Corrosion behaviour of Sn-containing oxide layer on AZ91D alloy formed by plasma electrolytic oxidation, Surface and Coatings Technology 202 (2008), 4145–4152, 10.1016/j.surfcoat.2008.03.010.

Bibliography

[263] L. Pezzato, K. Brunelli, E. Napolitani, M. Magrini, M. Dabalà, Surface properties of AZ91 magnesium alloy after PEO treatment using molybdate salts and low current densities, Applied Surface Science 357(Part A) (2015), 1031-1039, 10.1016/j.apsusc.2015.09.107.

[264] F. Zhao, A.-d. Liao, R.-f. Zhang, S.-f. Zhang, H.-x. Wang, X.-m. Shi, M.-j. Li, X.-m. He, Effects of sodium tungstate on properties of micro-arc coatings on magnesium alloys, Transactions of Nonferrous Metals Society of China 20 (2010), s683-s687, 10.1016/S1003-6326(10)60562-6.

[265] X.-J. Cui, C.-h. Liu, R.-s. Yang, M.-t. Li, X.-z. Lin, Self-sealing micro arc oxidation coating on AZ91D Mg alloy and its formation mechanism, Surface and Coatings Technology 269 (2014), 228-237, 10.1016/j.surfcoat.2014.09.071.

[266] D. Hwang, J. Cho, D. Lee, B. Yoo, D. Shin, Plasma Electrolytic Oxidation of AZ91 Mg Alloy in the Sodium Stannate Electrolyte, Materials Transactions 49 (2008), 1600-1605, 10.2320/matertrans.MC200797.

[267] Y. Ko, S. Namgung, D. Shin, Correlation between KOH concentration and surface properties of AZ91 magnesium alloy coated by plasma electrolytic oxidation, Surface & Coatings Technology 205 (2010), 2525-2531, 10.1016/j.surfcoat.2010.09.055.

[268] A. Ghasemi, V.s. Raja, C. Blawert, W. Dietzel, K. Kainer, The role of anions in the formation and corrosion resistance of the plasma electrolytic oxidation coatings, Surface and Coatings Technology 204 (2010), 1469-1478, 10.1016/j.surfcoat.2009.09.069.

[269] B. Srinivasan, J. Liang, R. Balajee, C. Blawert, M. Störmer, W. Dietzel, Effect of pulse frequency on the microstructure, phase composition and corrosion performance of a phosphate-based plasma electrolytic oxidation coated AM50 magnesium alloy, Applied Surface Science 256 (2010), 3928-3935, 10.1016/j.apsusc.2010.01.052.

[270] T. Clyne, S. Troughton, A review of recent work on discharge characteristics during plasma electrolytic oxidation of various metals, International Materials Reviews 64 (2018), 1-36, 10.1080/09506608.2018.1466492.

[271] X. Lu, S. Sah, N. Scharnagl, M. Störmer, M. Starykevich, M. Mohedano, C. Blawert, M.L. Zheludkevich, K. Kainer, Degradation behavior of PEO coating on AM50 magnesium alloy produced from electrolytes with clay particle addition, Surface and Coatings Technology 269 (2014), 155-169, 10.1016/j.surfcoat.2014.11.027.

[272] S. Lee, K. Ueda, T. Narushima, T. Nakano, T. Kasuga, Preparation of orthophosphate glasses in the MgO–CaO–SiO2–Nb2O5–P2O5 system, Bio-Medical Materials and Engineering 28 (2017), 23-30, 10.3233/BME-171652.

[273] M. Karakassides, A. Saranti, I. Koutselas, Preparation and Structural Study of Binary Phosphate Glasses with High Calcium and/or Magnesium Content, Journal of Non-crystalline Solids 347 (2004), 69-79, 10.1016/j.jnoncrysol.2004.08.111.

[274] S. Lee, T. Nakano, T. Kasuga, Formation and structural analysis of 15MgO–15CaO–8P2O5–4SiO2 glass, Journal of Non-Crystalline Solids 457 (2017), 73-76, 10.1016/j.jnoncrysol.2016.11.020.

[275] J.-s. Cheng, W. Deng, M.-t. Wang, Structure of Na2O·MO·SiO2·CaF2 (M=Mg, Ca) oxyfluoride glasses, Physica B: Condensed Matter 407 (2012), 2778–2783, 10.1016/j.physb.2012.04.026.

[276] A.K. Yadav, P. Singh, A Review on Structure of Glasses by Raman Spectroscopy, RSC Advances 5 (2015), 67583-67609, 10.1039/C5RA13043C.

[277] R. Kirkpatrick, J. Yarger, P. McMillan, P. Yu, X. Cong, Raman Spectroscopy of C-S-H, Tobermorite, and Jennite, Advanced Cement Based Materials 5 (1997), 93-99, 10.1016/S1065-7355(97)00001-1.

[278] S. Agathopoulos, D. Tulyaganov, J.M. Ventura, K. Sanjeevi, A. Saranti, M.A. Karakassides, J. Ferreira, Structural analysis and devitrification of glasses based on the CaO–MgO–SiO2 system with B2O3, Na2O, CaF2 and P2O5 additives, Journal of Non-Crystalline Solids 352 (2006), 322-328, 10.1016/j.jnoncrysol.2005.12.003.

[279] H. Yu, Q. Dong, J. Dou, Y. Pan, C. Chen, Structure and in vitro bioactivity of ceramic coatings on magnesium alloys by microarc oxidation, Applied Surface Science 388 (2016), 114-119, 10.1016/j.apsusc.2016.03.028.

[280] H. Gao, M. Zhang, X. Yang, P. Huang, K.W. Xu, Effect of Na2SiO3 solution concentration of micro-arc oxidation process on lap-shear strength of adhesive-bonded magnesium alloys, Applied Surface Science 314 (2014), 447-452, 10.1016/j.apsusc.2014.06.117.

[281] L.-Y. Cui, S.-D. Gao, P.-P. Li, R. Zeng, F. Zhang, S. li, E.-H. Han, Corrosion resistance of a self-healing micro-arc oxidation/polymethyltrimethoxysilane composite coating on magnesium alloy AZ31, Corrosion Science 118 (2017), 84-95, 10.1016/j.corsci.2017.01.025.

[282] H. Aguiar, E. Solla, J. Serra, P. González, B. León, N. Almeida, S. Cachinho, E. Davim, R. Correia, J. Oliveira, M. Fernandes, Orthophosphate nanostructures in SiO2-P2O5-CaO-Na2O-MgO bioactive glasses, Journal of Non-Crystalline Solids 354 (2008), 4075-4080, 10.1016/j.jnoncryso1.2008.05.031.

[283] H. Bakhsheshi-Rad, E. Hamzah, M. Daroonparvar, M.A. Mat Yajid, M. Medraj, Fabrication and corrosion behavior of Si/HA nano-composite coatings on biodegradable Mg–Zn–Mn–Ca alloy, Surface and Coatings Technology 258 (2014), 1090-1099, 10.1016/j.surfcoat.2014.07.025.

[284] R. Arrabal, E. Matykina, A. Pardo, M.C. Merino, K. Paucar, M. Mohedano, P. Casajús, Corrosion behaviour of AZ91D and AM50 magnesium alloys with Nd and Gd additions in humid environments, Corrosion Science 55 (2012), 351-362, 10.1016/j.corsci.2011.10.038.

[285] B. Genevieve, G. Galicia, C. Deslouis, N. Pébère, B. Tribollet, V. Vivier, An Impedance Investigation of the Mechanism of Pure Magnesium Corrosion in Sodium Sulfate Solutions, Journal of The Electrochemical Society 154 (2007), C108, 10.1149/1.2401056.

[286] A.D. King, N. Birbilis, J.R. Scully, Accurate Electrochemical Measurement of Magnesium Corrosion Rates; a Combined Impedance, Mass-Loss and Hydrogen Collection Study, Electrochimica Acta 121 (2014), 394-406, 10.1016/j.electacta.2013.12.124.

Bibliography

[287] K. Giju, Effect of coordinated water on the mechanism of neutral hydrolysis of silicon dioxide in gas phase: A first principles study, Journal of Molecular Structure-theochem 592 (2002), 53-60, 10.1016/S0166-1280(02)00226-9.

[288] B. Mingo, R. Arrabal, M. Mohedano, Y. Llamazares, E. Matykina, A. Yerokhin, A. Pardo, Influence of sealing post-treatments on the corrosion resistance of PEO coated AZ91 magnesium alloy, Applied Surface Science 433 (2018), 653-667, 10.1016/j.apsusc.2017.10.083.

[289] A. Castellanos, A. Altube, J.M. Vega, E. García-Lecina, J.A. Díez, H.J. Grande, Effect of different post-treatments on the corrosion resistance and tribological properties of AZ91D magnesium alloy coated PEO, Surface and Coatings Technology 278 (2015), 99-107, 10.1016/j.surfcoat.2015.07.017.

[290] M. Sun, A. Matthews, A. Yerokhin, Plasma electrolytic oxidation coatings on cp-Mg with cerium nitrate and benzotriazole immersion post-treatments, Surface and Coatings Technology 344 (2018), 330-341, 10.1016/j.surfcoat.2018.02.078.

[291] T. Seop Lim, H. Sam Ryu, S.-H. Hong, Plasma Electrolytic Oxidation/Cerium Conversion Composite Coatings for the Improved Corrosion Protection of AZ31 Mg Alloys, Journal of The Electrochemical Society 160(2) (2012), C77-C82, 10.1149/2.005303jes.

[292] M. Laleh, F. Kargar, A.S. Rouhaghdam, Investigation of rare earth sealing of porous micro-arc oxidation coating formed on AZ91D magnesium alloy, Journal of Rare Earths 30(12) (2012), 1293-1297, 10.1016/s1002-0721(12)60223-3.

[293] N.V. Phuong, B.R. Fazal, S. Moon, Cerium- and phosphate-based sealing treatments of PEO coated AZ31 Mg alloy, Surface and Coatings Technology 309 (2017), 86-95, 10.1016/j.surfcoat.2016.11.055.

[294] Y. Li, X. Lu, K. Wu, L. Yang, T. Zhang, F. Wang, Exploration the inhibition mechanism of sodium dodecyl sulfate on Mg alloy, Corrosion Science 168 (2020), 108559, 10.1016/j.corsci.2020.108559.

[295] X. Lu, Y. Li, P. Ju, Y. Chen, J. Yang, K. Qian, T. Zhang, F. Wang, Unveiling the inhibition mechanism of an effective inhibitor for AZ91 Mg alloy, Corrosion Science 148 (2019), 264-271, 10.1016/j.corsci.2018.12.025.

[296] G. Garces, P. Perez, S. Cabeza, H.K. Lin, S.K. Kim, W. Gan, P. Adeva, Reverse tension/compression asymmetry of a Mg-Y-Zn alloys containing LPSO phases, 647 (2015), 287-293, 10.1016/j.msea.2015.09.003.

[297] P. Pérez, S. Cabeza, G. Garcés, P. Adeva, Influence of long period stacking ordered phase arrangements on the corrosion behaviour of extruded Mg97Y2Zn1 alloy, Corrosion Science 107 (2016), 107-112, 10.1016/j.corsci.2016.02.024.

[298] J. Liu, L. Yang, C. Zhang, B. Zhang, T. Zhang, Y. Li, K. Wu, F. Wang, Role of the LPSO structure in the improvement of corrosion resistance of Mg-Gd-Zn-Zr alloys, Journal of Alloys and Compounds 782 (2019), 648-658, 10.1016/j.jallcom.2018.12.233.

[299] A.E. Coy, F. Viejo, P. Skeldon, G.E. Thompson, Susceptibility of rare-earth-magnesium alloys to micro-galvanic corrosion, Corrosion Science 52(12) (2010), 3896-3906, 10.1016/j.corsci.2010.08.006.

[300] S. Mu, J. Du, H. Jiang, W. Li, Composition analysis and corrosion performance of a Mo–Ce conversion coating on AZ91 magnesium alloy, Surface and Coatings Technology 254 (2014), 364-370, 10.1016/j.surfcoat.2014.06.044.

[301] R. Arrabal, J.M. Mota, A. Criado, A. Pardo, M. Mohedano, E. Matykina, Assessment of duplex coating combining plasma electrolytic oxidation and polymer layer on AZ31 magnesium alloy, Surface and Coatings Technology 206(22) (2012), 4692-4703, 10.1016/j.surfcoat.2012.05.091.

[302] M. Mohedano, R. Arrabal, B. Mingo, A. Pardo, E. Matykina, Role of particle type and concentration on characteristics of PEO coatings on AM50 magnesium alloy, Surface and Coatings Technology 334 (2018), 328-335, 10.1016/j.surfcoat.2017.11.058.

[303] M. Mohedano, C. Blawert, M.L. Zheludkevich, Silicate-based Plasma Electrolytic Oxidation (PEO) coatings with incorporated CeO2 particles on AM50 magnesium alloy, Materials & Design 86 (2015), 735-744, 10.1016/j.matdes.2015.07.132.

[304] H. Habazaki, K. Fushimi, K. Shimizu, P. Skeldon, G.E. Thompson, Fast migration of fluoride ions in growing anodic titanium oxide, Electrochemistry Communications 9(5) (2007), 1222-1227, 10.1016/j.elecom.2006.12.023.

[305] J. Martin, A.V. Nominé, J. Stef, A. Nominé, J.X. Zou, G. Henrion, T. Grosdidier, The influence of metallurgical state of substrate on the efficiency of plasma electrolytic oxidation (PEO) process on magnesium alloy, Materials & Design 178 (2019), 107859, 10.1016/j.matdes.2019.107859.

[306] J. Wang, W. Jiang, Y. Ma, Y. Li, S. Huang, Substantial corrosion resistance improvement in heat-treated Mg–Gd–Zn alloys with a long period stacking ordered structure, Materials Chemistry and Physics 203 (2018), 352-361, 10.1016/j.matchemphys.2017.09.035.

[307] M. Yamasaki, S. Izumi, Y. Kawamura, H. Habazaki, Corrosion and passivation behavior of Mg–Zn–Y–Al alloys prepared by cooling rate-controlled solidification, Applied Surface Science 257(19) (2011), 8258-8267, 10.1016/j.apsusc.2011.01.046.

[308] J.A. Mejias, A.J. Berry, K. Refson, D.G. Fraser, The kinetics and mechanism of MgO dissolution, Chemical Physics Letters 314(5) (1999), 558-563, 10.1016/S0009-2614(99)00909-4.

[309] D.Y. Hwang, Y.M. Kim, D.H. Shin, Corrosion Resistance of Plasma-Anodized AZ91 Mg Alloy in the Electrolyte with/without Potassium Fluoride, Materials Transactions 50(3) (2009), 671-678, 10.2320/matertrans.MER2008345.

[310] J. Carneiro, J. Tedim, S.C.M. Fernandes, C.S.R. Freire, A.J.D. Silvestre, A. Gandini, M.G.S. Ferreira, M.L. Zheludkevich, Chitosan-based self-healing protective coatings doped with cerium nitrate for corrosion protection of aluminum alloy 2024, Progress in Organic Coatings 75(1) (2012), 8-13, 10.1016/j.porgcoat.2012.02.012.

Bibliography

[311] H. Shi, E.-H. Han, S.V. Lamaka, M.L. Zheludkevich, F. Liu, M.G.S. Ferreira, Cerium cinnamate as an environmentally benign inhibitor pigment for epoxy coatings on AA 2024-T3, Progress in Organic Coatings 77(4) (2014), 765-773, 10.1016/j.porgcoat.2014.01.003.

[312] J.-B. Cambon, J. Esteban, F. Ansart, J.-P. Bonino, V. Turq, S.H. Santagneli, C.V. Santilli, S.H. Pulcinelli, Effect of cerium on structure modifications of a hybrid sol–gel coating, its mechanical properties and anti-corrosion behavior, Materials Research Bulletin 47(11) (2012), 3170-3176, 10.1016/j.materresbull.2012.08.034.

[313] R.H.U. Khan, A. Yerokhin, X. Li, H. Dong, A. Matthews, Surface characterisation of DC plasma electrolytic oxidation treated 6082 aluminium alloy: Effect of current density and electrolyte concentration, Surface and Coatings Technology 205(6) (2010), 1679-1688, 10.1016/j.surfcoat.2010.04.052.

[314] M.Y. Koroleva, E.Y. Karakatenko, E.V. Yurtov, Synthesis of Hydroxyapatite Nanoparticles by Controlled Precipitation in the Presence of Sodium Dodecyl Sulfate, Colloid Journal 82(3) (2020), 275-283, 10.1134/S1061933X20030059.

[315] H.-L. Yao, H.-T. Wang, X.-B. Bai, G.-C. Ji, Q.-Y. Chen, Improvement in mechanical properties of nano-structured HA/TiO2 multilayer coatings deposited by high velocity suspension flame spraying (HVSFS), Surface and Coatings Technology 342 (2018), 94-104, 10.1016/j.surfcoat.2018.02.058.

[316] K. McLeod, S. Kumar, R.S.C. Smart, N. Dutta, N.H. Voelcker, G.I. Anderson, R. Sekel, XPS and bioactivity study of the bisphosphonate pamidronate adsorbed onto plasma sprayed hydroxyapatite coatings, Applied Surface Science 253(5) (2006), 2644-2651, 10.1016/j.apsusc.2006.05.031.

[317] L. Wu, L. Zhao, J. Dong, W. Ke, N. Chen, Potentiostatic Conversion of Phosphate Mineral Coating on AZ31 Magnesium Alloy in 0.1MK2HPO4 Solution, Electrochimica Acta 145 (2014), 71-80, 10.1016/j.electacta.2014.08.100.

[318] X. Li, S. Deng, H. Fu, G. Mu, N. Zhao, Synergism between rare earth cerium(IV) ion and vanillin on the corrosion of steel in H2SO4 solution: Weight loss, electrochemical, UV–vis, FTIR, XPS, and AFM approaches, Applied Surface Science 254(17) (2008), 5574-5586, 10.1016/j.apsusc.2008.03.026.

[319] H. Sharifi, M. Aliofkhazraei, G.B. Darband, S. Shrestha, A review on adhesion strength of PEO coatings by scratch test method, Surface Review and Letters 25(03) (2017), 1830004, 10.1142/S0218625X18300046.

[320] X. Guo, K. Du, Q. Guo, Y. Wang, F. Wang, Experimental study of corrosion protection of a three-layer film on AZ31B Mg alloy, Corrosion Science 65 (2012), 367–375, 10.1016/j.corsci.2012.08.055.

[321] O. Oleshko, V. Kornienko, S. Kyrylenko, W. Simka, Y. Husak, T. Oleshko, B. Dryhval, J. Dudko, P. Maksym, Physical and Chemical Characterization of the Magnesium Surface Modified by Plasma Electrolytic Oxidation – Influence of Immersion in Simulated Body Fluid, 2020 IEEE 10th International Conference Nanomaterials: Applications & Properties (NAP), IEEE, Sumy, Ukraine, 2020, pp. 02BA11-01, 10.1109/NAP51477.2020.9309586.

[322] C. Liu, X. Lu, Y. Li, Q. Chen, T. Zhang, F. Wang, Influence of post-treatment process on corrosion and wear properties of PEO coatings on AM50 Mg alloy, Journal of Alloys and Compounds 870 (2021), 159462, 10.1016/j.jallcom.2021.159462.

[323] D. Zeng, Z. Liu, S. Bai, J. Wang, Influence of Sealing Treatment on the Corrosion Resistance of PEO Coated Al-Zn-Mg-Cu Alloy in Various Environments, Coatings 9(12) (2019), 867, 10.3390/coatings9120867.

[324] T. Li, L. Li, J. Qi, F. Chen, Corrosion protection of Ti6Al4V by a composite coating with a plasma electrolytic oxidation layer and sol-gel layer filled with graphene oxide, Progress in Organic Coatings 144 (2020), 105632, 10.1016/j.porgcoat.2020.105632.

[325] J. Joo, D. Kim, H.-S. Moon, K. Kim, J. Lee, Durable Anti-Corrosive Oil-Impregnated Porous Surface of Magnesium Alloy by Plasma Electrolytic Oxidation with Hydrothermal Treatment, Applied Surface Science 509 (2020), 145361, 10.1016/j.apsusc.2020.145361.

[326] M. Toorani, M. Aliofkhazraei, Review of electrochemical properties of hybrid coating systems on Mg with plasma electrolytic oxidation process as pretreatment, Surfaces and Interfaces 14 (2019), 262-295, 10.1016/j.surfin.2019.01.004.

[327] U. Malayoglu, K. Tekin, S. Shrestha, Influence of post-treatment on the corrosion resistance of PEO coated AM50B and AM60B Mg alloys, Surface & Coatings Technology 205 (2010), 1793-1798, 10.1016/j.surfcoat.2010.08.022.

[328] J. Wen, G. Wilkes, Organic/Inorganic Hybrid Network Materials by the Sol−Gel Approach, Chemistry of Materials 8 (1996), 1667-1681, 10.1021/cm9601143.

[329] L. Pezzato, M. Rigon, A. Martucci, K. Brunelli, M. Dabalà, Plasma Electrolytic Oxidation (PEO) as pre-treatment for sol-gel coating on aluminum and magnesium alloys, Surface and Coatings Technology 366 (2019), 114-123, 10.1016/j.surfcoat.2019.03.023.

[330] A.F. Galio, S.V. Lamaka, M.L. Zheludkevich, L.F.P. Dick, I.L. Müller, M.G.S. Ferreira, Inhibitor-doped sol–gel coatings for corrosion protection of magnesium alloy AZ31, Surface and Coatings Technology 204(9-10) (2010), 1479-1486, 10.1016/j.surfcoat.2009.09.067.

[331] I.A. Kartsonakis, A.C. Balaskas, E.P. Koumoulos, C.A. Charitidis, G. Kordas, Evaluation of corrosion resistance of magnesium alloy ZK10 coated with hybrid organic–inorganic film including containers, Corrosion Science 65 (2012), 481-493, 10.1016/j.corsci.2012.08.052.

[332] M.F. Montemor, M.G.S. Ferreira, Electrochemical study of modified bis-[triethoxysilylpropyl] tetrasulfide silane films applied on the AZ31 Mg alloy, Electrochimica Acta 52(27) (2007), 7486-7495, 10.1016/j.electacta.2006.12.086.

[333] F. Zanotto, V. Grassi, A. Frignani, F. Zucchi, Protection of the AZ31 magnesium alloy with cerium modified silane coatings, Materials Chemistry and Physics 129(1) (2011), 1-8, 10.1016/j.matchemphys.2011.05.013.

[334] V. Barranco, N. Carmona, J.C. Galván, M. Grobelny, L. Kwiatkowski, M.A. Villegas, Electrochemical study of tailored sol–gel thin films as pre-treatment prior to organic coating for AZ91 magnesium alloy, Progress in Organic Coatings 68(4) (2010), 347-355, 10.1016/j.porgcoat.2010.02.009.

Bibliography

[335] T.S. Lim, H.S. Ryu, S.-H. Hong, Electrochemical corrosion properties of CeO2-containing coatings on AZ31 magnesium alloys prepared by plasma electrolytic oxidation, Corrosion Science 62 (2012), 104-111, 10.1016/j.corsci.2012.04.043.

[336] Y. Chen, X. Lu, S.V. Lamaka, P. Ju, C. Blawert, F. Wang, M.L. Zheludkevich, Active protection of Mg alloy by composite PEO coating loaded with corrosion inhibitors, Applied Surface Science 504 (2019), 144462, 10.1016/j.apsusc.2019.144462.

[337] S. Shangyi, Y. Zuo, X. Zhao, The effects of 8-hydroxyquinoline on corrosion performance of a Mg-rich coating on AZ91D magnesium alloy, Corrosion Science 76 (2013), 275-283, 10.1016/j.corsci.2013.06.050.

[338] G.P. Cicileo, B.M. Rosales, F.E. Varela, J.R. Vilche, Inhibitory action of 8-Hydroxyquinoline on the copper corrosion process, Corrosion Science 40(11) (1998), 1915-1926, 10.1016/S0010-938X(98)00090-0.

[339] L. Tang, X. Li, Y. Si, G. Mu, G. Liu, The synergistic inhibition between 8-hydroxyquinoline and chloride ion for the corrosion of cold rolled steel in 0.5M sulfuric acid, Materials Chemistry and Physics 95(1) (2006), 29-38, 10.1016/j.matchemphys.2005.03.064.

[340] S.V. Lamaka, M.L. Zheludkevich, K.A. Yasakau, M.F. Montemor, M.G.S. Ferreira, High effective organic corrosion inhibitors for 2024 aluminium alloy, Electrochimica Acta 52(25) (2007), 7231-7247, 10.1016/j.electacta.2007.05.058.

[341] K.A. Yasakau, M.L. Zheludkevich, O.V. Karavai, M.G.S. Ferreira, Influence of inhibitor addition on the corrosion protection performance of sol–gel coatings on AA2024, Progress in Organic Coatings 63(3) (2008), 352-361, 10.1016/j.porgcoat.2007.12.002.

[342] A. Stankiewicz, Self-healing nanocoatings for protection against steel corrosion, in: F. Pacheco-Torgal, M.V. Diamanti, A. Nazari, C.G. Granqvist, A. Pruna, S. Amirkhanian (Eds.), Nanotechnology in Eco-efficient Construction, Woodhead Publishing, Cambridge, 2019, pp. 303-335, 10.1016/B978-0-08-102641-0.00014-1.

[343] A.F. Galio, S.V. Lamaka, M.L. Zheludkevich, L.F.P. Dick, I.L. Müller, M.G.S. Ferreira, Inhibitor-doped sol–gel coatings for corrosion protection of magnesium alloy AZ31, Surface and Coatings Technology 204(9) (2010), 1479-1486, 10.1016/j.surfcoat.2009.09.067.

[344] D. Snihirova, S.V. Lamaka, P. Taheri, J.M.C. Mol, M.F. Montemor, Comparison of the synergistic effects of inhibitor mixtures tailored for enhanced corrosion protection of bare and coated AA2024-T3, Surface and Coatings Technology 303 (2016), 342-351, 10.1016/j.surfcoat.2015.10.075.

[345] Z. Tian, H. Shi, F. Liu, S. Xu, E.-H. Han, Inhibiting effect of 8-hydroxyquinoline on the corrosion of silane-based sol–gel coatings on AA 2024-T3, Progress in Organic Coatings 82 (2015), 81-90, 10.1016/j.porgcoat.2015.01.018.

[346] M. Arunoday, K.P. Premkumar, R. Kumar, R. Subasri, Multifunctional, environmental coatings on AA2024 by combining anodization with sol-gel process, Ceramics International 48(8) (2022), 10969-10978, 10.1016/j.ceramint.2021.12.316.

[347] B. Vaghefinazari, S.V. Lamaka, C. Blawert, M. Serdechnova, N. Scharnagl, P. Karlova, D.C. Wieland, M. Zheludkevich, Exploring the corrosion inhibition mechanism of 8-

hydroxyquinoline for a PEO-coated magnesium alloy, Corrosion Science 203 (2022), 110344, 10.1016/j.corsci.2022.110344.

[348] R. Arrabal, E. Matykina, T. Hashimoto, P. Skeldon, G.E. Thompson, Characterization of AC PEO coatings on magnesium alloys, Surface and Coatings Technology 203(16) (2009), 2207-2220, 10.1016/j.surfcoat.2009.02.011.

[349] A. Pardo, P. Casajús, M. Mohedano, A.E. Coy, F. Viejo, B. Torres, E. Matykina, Corrosion protection of Mg/Al alloys by thermal sprayed aluminium coatings, Applied Surface Science 255(15) (2009), 6968-6977, 10.1016/j.apsusc.2009.03.022.

[350] S.V. Lamaka, D.G. Shchukin, D.V. Andreeva, M.L. Zheludkevich, H. Möhwald, M.G.S. Ferreira, Sol-Gel/Polyelectrolyte Active Corrosion Protection System, Advanced Functional Materials 18(20) (2008), 3137-3147, 10.1002/adfm.200800630.

[351] A. Jarad, I. Nafliu, A. Nechifor, R. Al Tahan, Synthesis, Characterization and Antibacterial Activity from Mixed Ligand Complexes of 8-Hydroxyquinoline and Tributylphosphine for Some Metal Ions, Revista de Chimie -Bucharest- Original Edition- (2019), 36-40.

[352] A. Karuppanan, A.b. Govindan, R. Perumalsamy, Growth of <201> 8-hydroxyquinoline organic crystal by Czochralski method and its characterizations, Journal of Thermal Analysis and Calorimetry volume 110 (2012), 1333-1339, 10.1007/s10973-011-2121-5.

[353] S. Kumar, B. Kumar, Growth of an 8-hydroxyquinoline single crystal by a modified Czochralski growth technique, and crystal characterization, CrystEngComm 20(5) (2018), 624-630, 10.1039/C7CE01857F.

[354] R. Abbas, A. Jarad, I. Nafliu, A. Nechifor, Synthesis, Characterization and Antibacterial Activity from Mixed Ligand Complexes of 8-Hydroxyquinoline and Tributylphosphine for Some Metal Ions, Revista de Chimie 70 (2019), 36-40, 10.37358/RC.19.1.6846.

[355] C.A. Hernández-Barrios, C.A. Cuao, M.A. Jaimes, A.E. Coy, F. Viejo, Effect of the catalyst concentration, the immersion time and the aging time on the morphology, composition and corrosion performance of TEOS-GPTMS sol-gel coatings deposited on the AZ31 magnesium alloy, Surface and Coatings Technology 325 (2017), 257-269, 10.1016/j.surfcoat.2017.06.047.

[356] S. Narayanan, M.H. Lee, A simple strategy to modify the porous structure of plasma electrolytic oxidation coatings on magnesium, RSC Advances 6(19) (2016), 16100-16114, 10.1039/c5ra20647b.

[357] J. Xu, Q. Yu, J. Liu, Y. Yin, Y. Han, B. Li, Preparation and characterization of polyfluoroaniline/organosiloxane hybrid films, Journal of Sol-Gel Science and Technology 69 (2013), 580-585, 10.1007/s10971-013-3260-x.

[358] P. Molaeipour, M. Ramezanzadeh Karati, B. Ramezanzadeh, Stachys byzantina extract: A green biocompatible molecules source for graphene skeletons generation on the carbon steel for superior corrosion mitigation, Bioelectrochemistry 143 (2021), 107970, 10.1016/j.bioelechem.2021.107970.

Bibliography

[359] A. Tan, A. Soutar, I.F. Annergren, Y.N. Liu, Multilayer Sol–Gel Coatings for Corrosion Protection of Magnesium, Surface and Coatings Technology 198 (2005), 478-482, 10.1016/j.surfcoat.2004.10.066.

[360] S. Akbarzadeh, L. Sopchenski Santos, V. Vitry, Y. Paint, M.-G. Olivier, Improvement of the corrosion performance of AA2024 alloy by a duplex PEO/clay modified sol-gel nanocomposite coating, Surface and Coatings Technology 434 (2022), 128168, 10.1016/j.surfcoat.2022.128168.

[361] A. Alabbasi, M. Bobby Kannan, R. Walter, M. Störmer, C. Blawert, Performance of pulsed constant current silicate-based PEO coating on pure magnesium in simulated body fluid, Materials Letters 106 (2013), 18-21, 10.1016/j.matlet.2013.04.047.

[362] S.V. Gnedenkov, O.A. Khrisanfova, A.G. Zavidnaya, S.L. Sinebryukhov, V.S. Egorkin, M.V. Nistratova, A. Yerokhin, A. Matthews, PEO coatings obtained on an Mg–Mn type alloy under unipolar and bipolar modes in silicate-containing electrolytes, Surface and Coatings Technology 204(14) (2010), 2316-2322, 10.1016/j.surfcoat.2009.12.024.

[363] V.N. Nguyen, F. Perrin, J.L. Vernet, Water permeability of organic/inorganic hybrid coatings prepared by sol-gel method: A comparison between gravimetric and capacitance measurements and evaluation of non-Fickian sorption models, Corrosion Science 47 (2005), 397-412, 10.1016/j.corsci.2004.06.028.

[364] S.-Y. Park, P. Ghosh, S.O. Park, Y.M. Lee, S.K. Kwak, O.-H. Kwon, Origin of ultraweak fluorescence of 8-hydroxyquinoline in water: photoinduced ultrafast proton transfer, RSC Advances 6(12) (2016), 9812-9821, 10.1039/C5RA23802A.

[365] W. Zhao, W. Ji, Y. Zhang, L. Du, S. Wang, A competitive fluorescence quenching-based immunoassay for bisphenol A employing functionalized silica nanoparticles and nanogold, RSC Advances 6(45) (2016), 38950-38956, 10.1039/C5RA26366B.

[366] M. Hernández-Escolano, M. Juan-Díaz, M. Martínez-Ibáñez, A. Jiménez-Morales, I. Goñi, M. Gurruchaga, J. Suay, The design and characterisation of sol–gel coatings for the controlled-release of active molecules, Journal of Sol-Gel Science and Technology 64 (2012), 442–451, 10.1007/s10971-012-2876-6.

[367] L. Garrigues, N. Pebere, F. Dabosi, An investigation of the corrosion inhibition of pure aluminum in neutral and acidic chloride solutions, Electrochimica Acta 41(7) (1996), 1209-1215, 10.1016/0013-4686(95)00472-6.

[368] A. Spinthaki, M. Kamaratou, J. Matheis, D. Disci, W. Hater, The precipitation of “aluminum silicate” under geothermal stresses: Identifying its idiosyncrasies, Geothermics 92 (2021), 102060, 10.1016/j.geothermics.2021.102060.

[369] M. El Ojaimi, R.P. Thummel, Polydentate Analogues of 8-Hydroxyquinoline and Their Complexes with Ruthenium, Inorganic Chemistry 50(21) (2011), 10966-10973, 10.1021/ic201524j.

[370] V. Prachayasittikul, S. Prachayasittikul, S. Ruchirawat, V. Prachayasittikul, 8-Hydroxyquinolines: A review of their metal chelating properties and medicinal applications, Drug design, Development and Therapy 7 (2013), 1157-1178, 10.2147/DDDT.S49763.